

Searching for Anisotropies in the Arrival Directions of Electromagnetic Air Showers at TeV energies with H.E.S.S.

Dissertation

zur Erlangung des Doktorgrades Dr. rer. nat.
an der Fakultät für Mathematik, Informatik und
Naturwissenschaften
des Fachbereichs Physik der Universität Hamburg

vorgelegt von

Franziska Caroline Spies (geb. Laatz)
aus Norderstedt

Hamburg,
September 2015

Tag der Disputation: 10.12.2015

Gutachter der Dissertation:

1. Prof. Dr. Dieter Horns
2. Prof. Dr. Günter Hans Walter Sigl

Mitglieder der Prüfungskommission:

1. Prof. Dr. Caren Ines Hagner
2. Prof. Dr. Dieter Horns
3. Prof. Dr. Günter Hans Walter Sigl
4. Prof. Dr. Jürgen Schmitt
5. Jun.-Prof. Christian Oliver Sander

Vorsitzende/r des Prüfungsausschusses:

Prof. Dr. Caren Ines Hagner

Vorsitzender des Promotionsausschusses:

Prof. Dr. Jan Louis

Dekan der MIN Fakultät:

Prof. Dr. Heinrich Graener

Abstract

The measurements of cosmic-ray electrons and positrons with PAMELA (Adriani et al. 2009), *Fermi*-LAT (Ackermann et al. 2012) and AMS-02 (Aguilar et al. 2013) have established the existence of an additional component of cosmic-ray positrons below 200 GeV. The origin of this additional component has not been clearly resolved. Two possible scenarios are mainly considered. In the first case positrons and electrons are accelerated in a nearby source (or a few sources) for example a pulsar or (aged) shell-type supernova remnant (e.g. di Bernardo et al. 2011). In the second scenario they are produced by self-annihilating or decaying dark matter (DM) (e.g. Borriello et al. 2012). In both scenarios anisotropies in the arrival directions of cosmic-ray electrons of different magnitudes are expected. The measurement or constraint of these anisotropies, therefore, serves as a valuable tool to unravel electron production scenarios and investigate propagation models of charged particles in the local Galactic environment.

In this study one of the first searches for such anisotropies with a ground based Imaging Atmospheric Cherenkov Telescope (IACT) was performed. The analysis is based on an unprecedented data set of 1178 hours of high quality data taken with the H.E.S.S. telescopes located in Namibia. These events were analyzed at energies above 600 GeV using an advanced image analysis and gamma/hadron separation (de Naurois and Rolland 2009) technique. Systematic effects in the data were quantified and minimized employing a unique approach taking advantage of the large amount of hadronic background events available.

Several different large-scale anisotropy models employing spherical harmonic functions up to the hexadecapole were fit to the data in an energy range between 0.64 and 1.04 TeV. None of these models was able to explain the measured electron arrival rates well. Two conclusions were drawn from extensive statistical and systematic studies. First, the characteristics of cosmic-ray electron arrival rate fluctuations (relative standard deviation of 34 %) differs significantly from the arrival rate scatter found in hadronic background events (relative standard deviation of 8 %). Second, the fluctuations of electron arrival rates are dominant at angular scales significantly smaller than the hexadecapole ($l = 4$).

An upper limit on the dipole amplitude in the arrival directions of cosmic-ray electrons was derived. Due to the irregular exposure available in the different directions of the sky the upper limits vary between 2.5 % and 56 % over the sky. These are the first upper limits at TeV energies.

Additionally, an upper limit on the cosmic-ray electron spectrum is presented at energies up to 14 TeV. This measurement accesses an energy range, where no measurement of the cosmic-ray electron spectrum was previously possible. Even an upper limit at these energies puts considerable constraints on models of cosmic-ray electron acceleration and propagation.

Kurzfassung

Messungen kosmischer Elektronen und Positronen mit PAMELA (Adriani et al. 2009), *Fermi-LAT* (Ackermann et al. 2012) und AMS-02 (Aguilar et al. 2013) haben die Existenz einer zusätzlichen Positron-Komponente unterhalb von 200 GeV nachgewiesen, deren Herkunft bisher unklar ist. Zwei unterschiedliche Szenarien werden aktuell am häufigsten diskutiert. Im ersten Fall werden Positronen und Elektronen von einem (oder einigen wenigen) sehr nahen kosmischen Beschleuniger z.B. einem Pulsar oder einem gealterten Supernovaüberrest des Schalentyps beschleunigt (z.B. di Bernardo et al. 2011). Im zweiten Fall werden sie von selbst-annihilierender oder zerfallender dunkler Materie (DM) erzeugt (z.B. Borriello et al. 2012). In beiden Szenarien wird eine Anisotropie in der Verteilung der Ankunftsrichtungen der kosmischen Elektronen und Positronen vorhergesagt. Beide Fälle unterscheiden sich jedoch in der erwarteten Stärke dieser Anisotropie. Der Nachweis bzw. die Einschränkung einer solchen Anisotropie wäre somit ein wertvolles Werkzeug zur Erforschung der Produktionsmechanismen kosmischer Elektronen sowie bei Untersuchungen von Propagationsmodellen geladener Teilchen durch die Galaxie.

In der vorgelegten Arbeit wird eine der ersten detaillierten Suchen nach einer Anisotropie in der Verteilung der Ankunftsrichtungen kosmischer Elektronen und Positronen mit einem Imaging Atmospheric Cherenkov Teleskop (IACT) vorgestellt. Zu diesem Zweck wurden 1178 Stunden Daten besonders hoher Qualität, aufgezeichnet mit dem H.E.S.S. Teleskop in Namibia, analysiert. Dazu wurde eine hochentwickelte Methode zur Luftschauer-Rekonstruktion und zur Separation von Gamma-Strahlung von hadronischer Strahlung verwendet (de Naurois and Rolland 2009). Der betrachtete Energiebereich dieser Analyse liegt oberhalb von 600 GeV.

Die in den Daten vorhandenen systematischen Effekte wurden quantifiziert und minimiert. Dazu wurde eine neue Methode, basierend auf der großen Menge an in den Daten enthaltenen hadronischen Ereignissen, entwickelt.

Im Energiebereich zwischen 0.64 und 1.04 TeV wurden verschiedene Anisotropie-Modelle, die Kugelflächenfunktionen bis zur Ordnung $l = 4$ (Hexadekapol) beinhalten, an die Daten gefittet, jedoch konnten die gemessenen Elektron-Raten nicht zufriedenstellend beschrieben werden. Detaillierte statistische und systematische Untersuchungen ergaben einen signifikanten Unterschied zwischen den Charakteristiken der Fluktuationen in den Elektron-Raten (relative Standardabweichung von 34 %) und den Fluktuationen der hadronischen Untergrundraten (relative Standardabweichung von 8 %). Darüber hinaus werden die Fluktuationen der Elektron-Raten von Winkelskalen signifikant kleiner als $l = 4$ dominiert.

Zudem wurde eine obere Schranke auf die Dipolamplitude der kosmischen Elektron-Rate berechnet. Sie variiert richtungsabhängig zwischen 2.5 % und 56 % auf Grund der ungleichmäßigen Himmelsabdeckung der Beobachtungen.

Des Weiteren wurde eine obere Schranke auf das Elektron Spektrum bis zu Energien von 14 TeV berechnet. Dadurch wurde ein Energiebereich jenseits aller bisherigen Messungen des Flusses kosmischer Elektronen erschlossen. Bereits diese obere Schranke auf den Elektronenfluss ist ausreichend um Beschleunigungs- und Propagationsmodelle von kosmischen Elektronen stark einzuschränken.

Contents

1	Introduction	6
2	The Physics of Cosmic-Ray Electrons	10
2.1	Hadronic Cosmic Rays	11
2.1.1	Spectrum of Cosmic-Ray Hadrons	11
2.1.2	Anisotropies in CR Hadrons	14
2.2	Cosmic-Ray Electrons	16
2.2.1	Spectrum of Cosmic-Ray Electrons	16
2.2.2	The Positron Fraction	17
2.2.3	Anisotropies in CR Electrons	19
2.3	Production of Cosmic Rays	21
2.3.1	Particle Acceleration in Supernova Remnants	21
2.3.2	Particle Acceleration by Pulsars	24
2.3.3	Dark Matter as a Source of Cosmic-Ray Electrons and Positrons	27
2.4	Propagation of Cosmic-Ray Electrons	30
3	Detecting Cosmic-Ray Electrons	34
3.1	Direct Detection	34
3.2	Indirect Detection	38
3.2.1	Air Shower Physics	38
3.2.2	Cherenkov Light	43
3.3	The H.E.S.S. Telescope	45
3.3.1	Experimental Setup	45
3.3.2	The Trigger System	48
3.3.3	Data Acquisition	48
3.3.4	Data Analysis with H.E.S.S.	49
4	Statistical Basics	56
4.1	Data Modeling	56
4.1.1	χ^2 -Fitting	56
4.1.2	Log-Likelihood-Fitting	57
4.1.3	Confidence Intervals and Upper Limits	58
4.2	Hypothesis Testing	60

4.2.1	χ^2 - and $\Delta\chi^2$ -Test	61
4.2.2	F -Test	62
4.2.3	Requirements on Hypothesis Tests	63
4.2.4	Other Interesting Tests and their Applications	64
4.3	Correlation	65
4.3.1	Pearson Correlation	65
4.3.2	Spearman's Rank Correlation	66
5	Analysis of Cosmic-Ray Electrons	67
5.1	Data Selection and Reconstruction	67
5.1.1	Run Quality Selection	67
5.1.2	Shower Reconstruction with Model++	73
5.1.3	Event Selection	79
5.2	Upper Limit on the Cosmic-Ray Electron Spectrum	81
5.2.1	Computing the Electron Flux	81
5.2.2	Simulating Diffuse CR Electrons	82
5.2.3	Exposure Calculation	95
5.2.4	UL on the CR Electron Spectrum	99
5.2.5	The Electron Fraction between 0.64 and 1.04 TeV	103
5.3	Search for Anisotropies in CR Electron Arrival Rates	105
5.3.1	Electron Arrival Rates	105
5.3.2	Dipole Model	107
5.3.3	Systematic Effects	119
5.3.4	Split Analysis	130
5.3.5	Dependency on Gamma-Hadron Separation Cuts	137
5.3.6	Dependency on the Electron Fraction	141
5.3.7	Cross Check	143
5.3.8	Multipole Fits	148
5.3.9	Power Spectrum	152
5.3.10	The Two-Point-Correlation Function	156
5.3.11	Upper Limit on the Dipole Amplitude	171
6	Conclusion: Summary and Outlook	173
	Bibliography	179
A	Q-factor	194
B	Electron Spectrum	196
C	Systematic Error	198
D	Split Analysis	200

E	Multipole Fits	204
F	Run Selection	207

Chapter 1

Introduction

Astronomy, the science of studying celestial objects such as stars, galaxies, planets and the like, has been a cornerstone of human striving for understanding since the ancient Greeks, Egyptians, Babylonians and others. All of these early civilizations already had a recorded history of methodical observations of the night sky. Most modern astronomy concentrates not only on the qualitative study of the positions and motions of celestial objects, but also on physical interpretations of observed phenomena. Thus, modern astronomy is usually synonymous with astrophysics, a former branch of astronomy that focused on the physics of the universe, while classical astronomy also included disciplines such as astrometry, celestial navigation and making calendars. Astrophysics includes observing the emissions of celestial objects across the whole range of the electromagnetic spectrum. Radiation at wavelengths above a few millimeters (radio emissions) emitted by cold objects, e.g. the interstellar gas, is studied as well as the most energetic photons at energies above 100 keV (corresponding to wavelengths of the order of 10^{-12} m) called gamma rays.

In 1912 Victor Hess (Hess 1912) discovered a radiation of great penetrating power entering our atmosphere from above. This highly ionizing radiation originating from outside the Earth's atmosphere, nowadays called cosmic rays, are high-energy particles of intrinsic mass, for example protons, atomic nuclei and electrons. The energies of cosmic rays range over 10 orders of magnitude from 10^9 eV to 10^{20} eV. Thus, the energies of the most energetic particles are up to 40 million times the energy of particles accelerated by the most powerful collider ever built by humans, the Large Hadron Collider.

Studying these particles of astronomical origin and their relation to astrophysics and cosmology has become a new branch of scientific research emerging at the intersection between astronomy, astrophysics, particle physics and related branches such as detector physics. Today, astroparticle physicists study not only cosmic rays, but also gamma rays, neutrinos and search for the hypothetical dark matter particle. An example for the important findings of the field is the discovery of neutrino oscillations which resulted in a rapid development of the field in the early 2000's. Major topics in astroparticle physics are the questions of dark matter, dark energy and the inequality of the number densities of matter and antimatter in the universe (Baryogenesis). Another question concerns the origin and production mechanisms of cosmic rays themselves. What kind of objects are able to accelerate cosmic-ray particles to the highest

energies? More precisely, the acceleration mechanisms attached to which objects are able to explain experimental observations, such as the shape of the cosmic-ray spectrum? Supernova remnants (SNR), pulsars, active galactic nuclei (AGN), quasars and gamma-ray bursts (GRB) are debated among others.

No matter which messenger particle is chosen to observe astrophysical objects, it will have difficulties attached to it. Neutrinos point directly towards a hypothetical source, but their interaction cross sections are very small so they are difficult to detect. Gamma rays are thought to be produced in cosmic accelerators either via pion decay in hadronic scenarios or via Inverse-Compton scattering by relativistic electrons interacting with target photon fields in electromagnetic acceleration scenarios. Gamma rays are absorbed by dense environments, e.g. in the interstellar medium, and additionally they interact with photons of the microwave background. Charged particles such as protons have an uncertainty on the directional information they deliver, since they are deflected by magnetic fields on their way to Earth.

A messenger particle lately receiving a lot of attention are cosmic-ray electrons. Cosmic-ray electrons may also suffer from deflection of galactic magnetic fields, but additionally they lose energy much more rapidly than, e.g., protons due to synchrotron losses and inverse Compton scattering. Thus, high-energy cosmic-ray electrons are expected to originate from distances closer than approximately 1 kpc (model dependent). This leaves fewer objects as possible sources, among those being the Vela SNR and the pulsars Monogem and Geminga. Observations of cosmic-ray electrons up to 10 TeV with the ground-based gamma-ray telescope H.E.S.S. suggest the existence of at least one such nearby source of cosmic-ray electrons (Aharonian et al. 2008).

Observations conducted with the PAMELA detector (Adriani et al. 2009) have triggered further attention, because it found an unexpected rise in the positron fraction (positron flux divided by the total flux of electrons plus positrons). Such a rise suggests that an additional source of positrons exists, because from the *conventional* model a continuous drop of the positron fraction was expected. In the *conventional* model electrons are accelerated by diffuse shock acceleration in SNRs only while positrons are of secondary origin produced by the interaction of cosmic-ray protons with protons of the interstellar medium. To explain the PAMELA results high energy positrons must be produced in addition to the secondary process. They could be either produced by a nearby source, e.g. a pulsar or aged shell-type SNR, or by self-annihilating or decaying dark matter. In both scenarios some type of anisotropy is expected. The difference lies in the magnitude of the predicted anisotropies. In dark matter scenarios the expected dipole amplitude is smaller than 2% (Borriello et al. 2012), while in the close-by source scenarios amplitudes of 20% (di Bernardo et al. 2011) are possible. The observation of a dipole anisotropy would strongly constrain possible models of electron and positron production, acceleration and propagation.

This PhD thesis is dedicated to the first ever extensive search for anisotropies in the arrival direction of cosmic-ray electrons with a ground-based Imaging Atmospheric Cherenkov Telescope (IACT). It is a continuation of the initial diploma thesis by Marco Prüser (Prüser 2012), who derived an upper limit on the dipole amplitude of cosmic-ray electrons based on a data set of gold-plated events (events of very high quality). IACTs do not detect the primary cosmic rays directly, but measure the Cherenkov light emitted by secondary particles of the

cascade they have initiated in the Earth's atmosphere. The only other two experiments ever conducting similar searches at energies below 500 GeV were the *Fermi*-LAT (Ackermann et al. 2010a) and AMS-02 (Aguilar et al. 2013) telescopes using direct measurement techniques. Both are located in space and are limited to energies below 1 TeV due to their small physical size and consequently limited collection area ($\mathcal{O}(\text{m}^2)$). IACTs have the advantage of a much larger collection area ($\sim 10^5 \text{ m}^2$) so that they detect a much larger number of particles, which becomes especially important at high energies. On the other hand there is an unavoidable lower limit on the energy of the particles that can be observed given by the energy of the particles required to emit Cherenkov light (the speed of the particle must be larger than c/n). For electrons traveling through air this threshold energy is approximately 20 MeV (260 keV in water).

Further, for IACTs there is no obvious way to directly discriminate electrons from gamma rays and hadrons, as for direct detection methods. Gamma rays (or electrons) and hadrons are separated based on the shower images they produce in the cameras of the telescope. Nevertheless, this method only gives a likelihood of the particle being a gamma ray or a hadron. Thus, events are called gamma-like or hadron-like. Gammas and electrons produce almost identical shower images since both initiate electromagnetic showers. Thus, up to now they cannot be discriminated. It is possible to exclude regions of known gamma-ray emission from the data sample. The crucial challenge is to determine the residual hadronic-background level. This was a major difficulty when the electron spectrum was measured with H.E.S.S. (Aharonian et al. 2008). In that study the separation was done on statistical basis simulating the distributions of the used gamma-hadron separation parameter for electron and proton events, fitting the obtained distributions to the actually measured distribution of the parameter and finding the number of electrons and hadrons in the data set. This method has different problems attached: the first being the large amount of proton simulations required, and the second being the uncertainties that exist in currently available hadron interaction models.

In this study an experimentally driven approach was applied calculating the background level from the electron spectrum measured with *Fermi*-LAT and the H.E.S.S. electron collection area. The electron flux is not reconstructed individually for every direction of the sky, but instead the arrival rates of cosmic-ray electrons at Earth are used directly (number of electrons measured with H.E.S.S. per unit time). Since dependencies on the zenith angle and optical efficiency of the observations are not corrected the assessment of systematic effects is crucial. The treatment of systematics is based on the idea that systematic effects are the same for electron and hadron events. The method takes advantage of the large number of hadron-like events from which the systematic error is derived. It ensures at least that all systematic effects that are present in the hadron-like event sample are also taken into account in the analysis of the gamma-like event sample. The remaining rate fluctuations are studied in the anisotropy analysis. This thesis is structured as follows:

- **Chapter 2** is dedicated to experimental results concerning hadronic cosmic rays and cosmic-ray electrons. It includes a summary of experimental results concerning spectra and anisotropies of both types of cosmic rays. Further, the electron fraction is discussed. Additionally, the theoretical background of cosmic-ray electron production and propagation is introduced including a discussion of possible sources of cosmic-ray electrons and positrons.

- **Chapter 3** focuses on detection principles of cosmic-ray electrons. Direct and indirect detection methods are discussed. The H.E.S.S. experiment is introduced in more detail, while the *Fermi*-LAT and AMS-02 detectors are discussed as examples of direct detection instruments.
- **Chapter 4** gives a short summary of the statistical basics required to understand the data analysis in this study. Topics such as data modeling, hypothesis testing and correlations between variables are covered.
- **Chapter 5** is dedicated to the actual data analysis. It covers three main parts. First, the selection of the data set used in this study is discussed. Second, the determination of the level of hadronic background including the calculation of the collection area (here exposure) for electrons is considered. As a side product an upper limit on the electron spectrum is presented. Further, extensive anisotropy studies are performed including the analysis of a dipole model as well as higher order multipole models, such as the calculation of the two-point correlation function. The employed methods include standard statistical tests as well as Monte Carlo simulations. The treatment of systematic effects is also discussed. Finally an upper limit on the dipole amplitude is presented.
- **Chapter 6** gives a summary of the obtained results. Further, they are discussed in terms of possibly un-accounted systematic effects, in the context of previously found experimental results and physical implications. An outlook is given at the end of the Chapter.

Chapter 2

The Physics of Cosmic-Ray Electrons

The underlying physics of cosmic rays is discussed in this Section. Major attention is given to cosmic-ray electrons and topics connected to this thesis such as the small and medium scale anisotropy of galactic cosmic rays. First, experimental results on cosmic rays and in particular cosmic-ray electrons are discussed with emphasis on their spectra and arrival direction. Second, the most widely discussed sources of cosmic-ray electrons are introduced and connected to the previously mentioned experimental results. At last, the propagation mechanisms relevant for cosmic-ray electrons are explained by the use of simple analytic solutions to the transport equation.

This short introduction aims to give an overview of experimental results as well as of the theoretical models of acceleration and propagation of cosmic-ray electrons (and positrons). Related topics as certain aspects and experimental results concerning hadronic cosmic rays are shortly discussed but this introduction does not aim to give a full overview on cosmic rays. For more information on cosmic rays the interested reader is referred to several review articles. Blümer et al. (2009) discuss experimental results and theoretical interpretations at energies above the *knee* and give a comprehensive picture until 2009. Even though, some of the most current experimental results are missing the basic ideas are explained well. Hörandel (2013) gives an update on the composition of galactic cosmic rays between 10^{14} and 10^{18} eV. Blasi and Amato (2012) focuses on supernova remnants as the most plausible source of galactic cosmic rays. Aloisio (2012) gives a short review on ultra-high-energy cosmic rays (UHECR) at energies above 10^{19} eV. Cosmic-ray electrons are covered by Panov et al. (2011). Many aspects of cosmic rays, cosmic-ray electrons and their physics are also covered by Spurio (2015).

2.1 Hadronic Cosmic Rays

2.1.1 Spectrum of Cosmic-Ray Hadrons

Cosmic rays (CRs) are high-energy particles between 10^9 eV and 10^{20} eV bombarding the Earth from outside its atmosphere. They originate from outside the Solar System, but also from the Sun. When CRs enter the Earth's atmosphere they interact with nuclei in the atmosphere and initiate hadronic and electromagnetic showers of secondary particles. CRs are mainly composed of protons ($\sim 89\%$) and atomic nuclei ($\sim 10\%$), but also electrons ($\sim 1\%$) and antiparticles such as antiprotons and positrons contribute by a small fraction. The flux F of CRs arriving at Earth has been measured over several decades in energy by detectors that were carried by balloons or satellites (up to 10^5 GeV) and air shower detectors on the ground (above 10^5 GeV). Figure 2.1 shows the CR spectrum for all charged CRs giving the number of particles arriving per unit interval of time, area, solid angle and kinetic energy. Additionally, the spectra of electrons, positrons, protons and antiprotons up to 100 GeV are shown.

The number of electrons is much smaller than the number of protons. At 1 GeV they contribute only between 1% and 2% to the total CR flux and even less at higher energies. The flux of positrons and antiprotons is even smaller. The differential CR flux $\frac{dF}{dE}$, where E is the particle energy, follows a power law with a spectral index of -2.7 ($\frac{dF}{dE} \sim E^{-2.7}$) up to the *knee* at approximately $10^{15.5}$ eV. Above the *knee* the spectrum bends downward (index ~ 3.1) for three decades in energy to the *ankle* at $10^{18.5}$ eV, where the spectrum breaks upwards again. The entire spectrum reaches up to approximately 10^{11} GeV where only one particle per square-kilometer and century is expected. Here, the statistics and possibly also the flux peter out. All elements of the periodic table were found in CRs. The abundance of the elements in CRs differs somewhat from the abundance found in the solar system. E.g. the light elements such as lithium, beryllium and boron are more abundant in CRs than in the solar system. They are assumed to be produced during spallation processes of the CNO, iron and lead groups while propagating through the Galaxy (Blümer et al. 2009).

It was found by the KASCADE experiment that the *knee* is measured at higher and higher energies for continuously heavier nuclei (Apel et al. 2013). Thus, the shape of the *knee* measured in the spectrum of all CRs appears to be a superposition of the spectra of protons and heavier nuclei. This behavior at the *knee* can be explained in the model of diffuse shock acceleration in strong magnetic fields of young supernova remnants (SNR) (see Section 2.3.1 for details). The idea that CRs are accelerated by SNRs goes back to (Baade and Zwicky 1934) who found that 3 supernovae per galaxy and century are sufficient to release enough kinetic energy to deliver the required power to generate the observed CR flux (CR energy density is ~ 1 eV/cm³). Due to the limited lifetime ($\sim 10^5$ years) of a shock the energy attainable via diffuse acceleration in shock fronts is given by $E_{\max} \sim Z \cdot (0.1 - 5)$ PeV.

However, alternative explanations are under debate, e.g. the leakage of particles from the Galaxy (Hörandel 2005). CRs propagate through the Galaxy approximately 20×10^6 years. During this time they are deflected many times by the magnetic field. The galactic magnetic field is oriented mainly parallel to the galactic plane and has an average intensity of 3 to 4 μ G (see Durrer and Neronov 2013 for a review on cosmological magnetic fields). With increasing energy the Larmor radius (Equation 2.1) of CRs in the Galaxy increases until it exceeds the

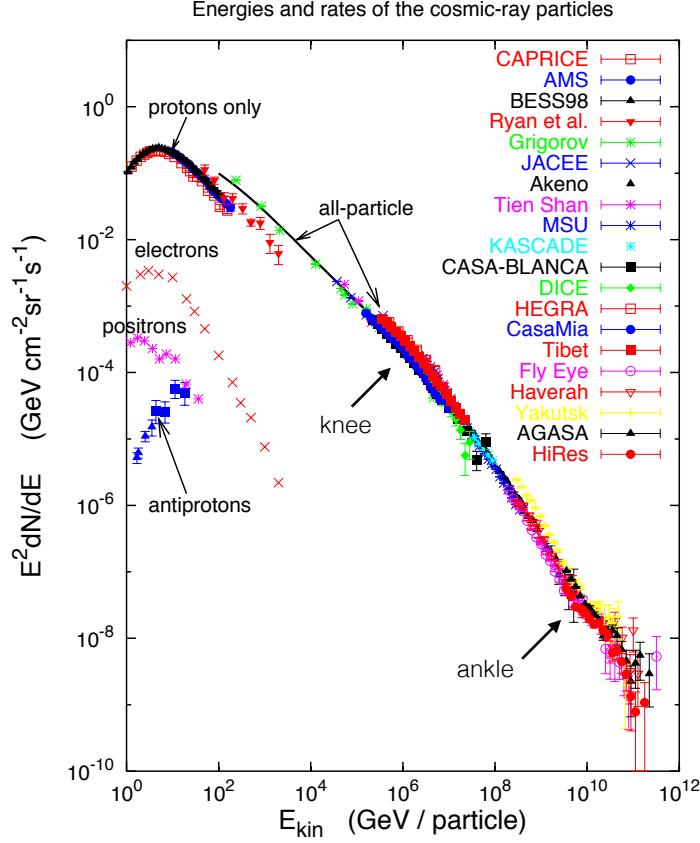


Figure 2.1: Spectrum of CRs as observed by several experiments at Earth. On the x-axis the kinetic energy E_{kin} of the particles is given. The differential CR flux $\frac{dN}{dE}$ times E^2 , where E is the energy of the particles, is given on the y-axis. This representation of the differential flux was chosen to make the features (*knee* and *ankle*) of the CR spectrum clearly visible. Adapted from Hillas 2006.

thickness of the galactic disk (~ 150 pc). For protons with an energy of 10^{18} eV the Larmor radius r_L is 300 pc (for $B = 4 \mu\text{G}$) so that they are no longer constrained to the Galaxy. In this model the energy spectra of the individual nuclei would similarly exhibit a cutoff at an energy given by the cutoff energy of protons and the elemental charge Z .

The origin (and, thus, also the acceleration mechanism) of CRs at even higher energies is less clear. Figure 2.2 shows an overview of objects possibly capable of accelerating particles to energies up to 10^{20} eV. The objects on the right-hand side of the locus are possibly capable of accelerating protons/nuclei up to the highest energies. These include active galactic nuclei (AGN) and gamma-ray bursts (GRBs). Since CRs at these energies are no longer constrained to the Galaxy, in this picture, the *ankle* could be a feature of an extragalactic cosmic ray component that is less intense, but has a harder spectrum and, thus, starts to dominate over the galactic component at energies above 10^{19} eV (Hillas 2005 and Erlykin and Wolfendale

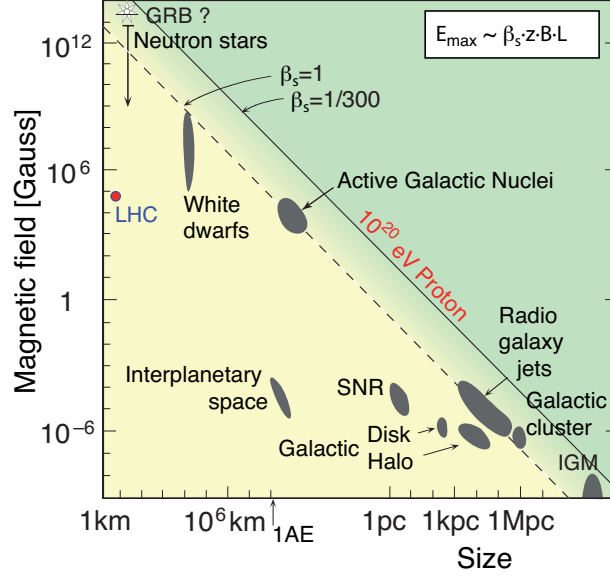


Figure 2.2: Hillas plot of astrophysical objects that could possibly accelerate CR particles to the highest energies. The magnetic field strength responsible for acceleration in these objects is given on the y-axis. The size of the objects is given on the x-axis. The black lines separate the regions in the plot where protons can be accelerated up to 10^{20} eV from those where they cannot. The solid line indicates this boundary for non relativistic shocks and the dashed line for relativistic shocks. The relation of the maximum energy achievable by the objects to their properties such as the magnetic field strength B , the size L , the charge of the accelerated particle Z and the speed of the shock front normalized to the speed of light β_s is shown in the upper right corner. Adapted from Blümer and Kampert 2000.

2005). Naturally, a heavy composition would be expected at the higher end of the galactic component ending just below 10^{19} eV. Consequently, the measurement of the composition of the highest energy CRs (ultra-high-energy cosmic rays UHECR) is crucial for understanding the origin of the *ankle*.

If UHECRs are protons an acceleration in active galaxies is most likely due to their isotropic arrival directions (no large scale anisotropy was found at energies above 10^{18} eV by, e.g. Armengaud 2008 and Swain 2006) and correlation with relatively nearby AGNs at energies above 5.7×10^{19} eV as found by Auger (Pierre Auger Collaboration et al. 2007 and Abraham et al. 2008b). However, the HiRes collaboration did not find a significant correlation (Abbasi et al. 2008b) and, thus, this point is still unclear. If the highest energy particles are iron nuclei the velocities of the shock front involved must not be relativistic and other sources become reasonable.

Experimental results on the composition of UHECRs are contradictory. While data taken by the HiRes experiment point towards a proton dominated composition of UHECRs at energies above 10^{18} eV (Jui and Telescope Array Collaboration 2012), the Auger collaboration finds a

proton dominated composition at 10^{18} eV with a gradual transition to a composition dominated by heavy nuclei above 10^{19} eV (Abraham et al. 2010). In these measurements there is a strong dependence on the hadron interaction models employed and conclusions cannot be drawn safely. Above 4×10^{19} eV a suppression of the CR flux was observed by HiRes and Auger (Abbasi et al. 2008a and Abraham et al. 2008a). Composition information may also help to decide whether the flux suppression is due to interactions of CRs with the microwave background (GZK effect) or due to a maximum injection energy of the sources.

2.1.2 Anisotropies in the Arrival Directions of Galactic Cosmic-Ray Hadrons

The distribution of the arrival directions of CRs at Earth can give additional information about their origin and propagation in the Galaxy. The existence of a directional variation of the flux (anisotropy) of CRs at different angular scales gives information about different aspects of CR acceleration and transport. A large scale anisotropy would be connected to the propagation of CRs in the Galaxy (diffusion and magnetic field structure), while small scale anisotropies (up to roughly 20°) could point towards CR sources. When CRs travel from the location of their source to Earth they are scattered on the random and irregular component magnetic field. This should isotropize the arrival direction of CRs since the radius (Larmor radius, Blümer et al. 2009) of the circular motion of a proton in the galactic magnetic field ($B=3 \mu\text{G}$) is given by

$$r_L = 1.08 \text{ pc} \frac{E/\text{PeV}}{Z \cdot B/\mu\text{G}}. \quad (2.1)$$

Thus, for a proton with an energy of 1 PeV the Larmor radius is only 0.4 pc and for a proton with an energy of 100 GeV even only 3×10^{-5} pc. This radius is much smaller than the typical distance to a nearby source (roughly 100 pc) so that it is not expected to see any point sources at these energies or below. Only at the highest energies it could be possible to find point sources of CRs.

In the last years several experiments have measured relative CR anisotropies of the order of 10^{-3} at energies between a few and a few hundred TeV. A large scale anisotropy compatible with the movement of the Earth around the Sun (Compton Getting effect) has been found. Further, there is clear evidence for small to medium scale anisotropies (a few to twenty degrees). First, the Milagro experiment reported localized hot-spots at an angular scale of 10° (Abdo et al. 2008). Among others also the IceCube ($E \sim 20$ TeV), Tibet III (4 - 50 TeV) and ARGO-YBJ (up to 20 TeV) collaborations have reported such small to medium scale anisotropies (Abbasi et al. 2011, Amenomori and Tibet AS γ Collaboration 2006, ARGO-YBJ Collaboration 2013). Figure 2.3 shows the combined significance map of anisotropy observed with IceCube in the southern hemisphere and Milagro in the northern hemisphere. The CR anisotropy sky maps of the northern hemisphere measured by the ARGO-YBJ (shown later in Figure 5.48), Milagro and Tibet collaborations show clear similarities. Additionally, anisotropies up to median energies of 400 TeV have been measured by IceCube and IceTop and up to 2 PeV by IceTop. The large scale structure of the anisotropy changes at an energy above roughly 100 TeV (Abbasi et al. 2012, Aartsen et al. 2013).

Since the diffusion approximation only predicts a simple dipole anisotropy, theoretical explanations for the observed medium to small scale anisotropies are still strongly debated. A

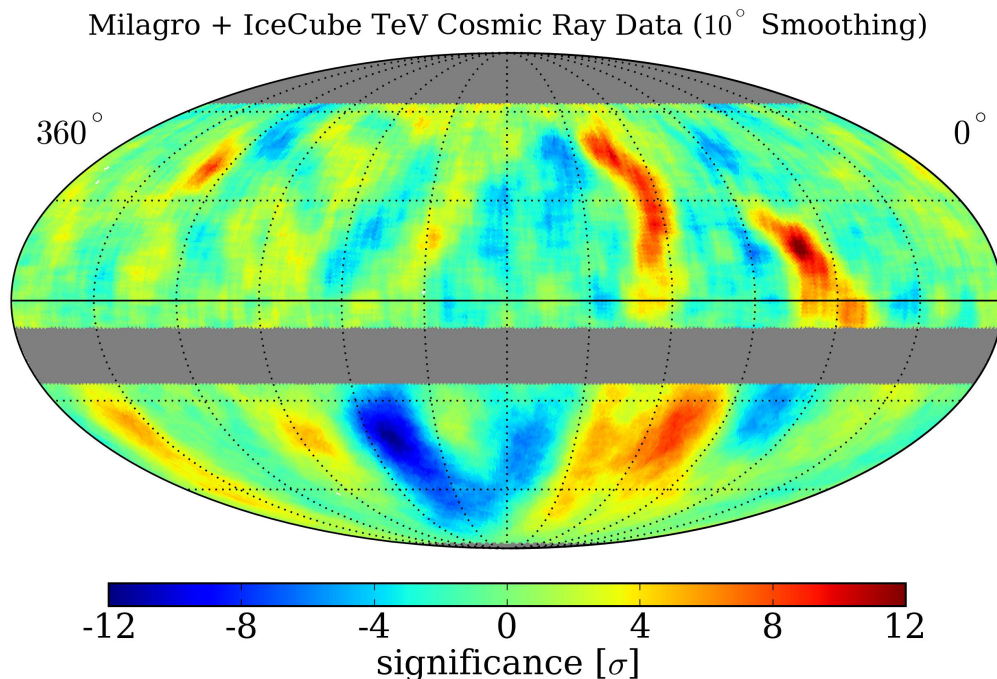


Figure 2.3: Combined sky map of significance in Gaussian sigma of the anisotropy in the CR arrival distribution measured by Milagro in the northern hemisphere and IceCube in the southern hemisphere. Both maps have been smoothed with a 10° radius. The figure was adapted from Abbasi et al. (2011).

wide range of approaches has been suggested. Here, two fundamentally different explanations are discussed exemplarily.

Since the location of the more prominent of the Milagro hot-spots coincides with the direction of the heliotail (the shocked solar wind and interstellar medium trailing behind the solar system) ideas promoting a connection with the heliotail have been proposed. For example O’C. Drury (2013) has argued that the small scale anisotropy could in part be a reflection of the electric field structure of the outer heliosphere.

In contrast Giacinti and Sigl (2012) have argued that the local magnetic field configuration within the mean free path of the CR traveling to Earth may naturally result in small to medium scale anisotropies provided that a large scale dipole anisotropy is present as predicted by the diffusion approximation.

Further ideas are covered in the recent literature, e.g. by Ptuskin et al. (2006), Drury and Aharonian (2008), Amenomori and Tibet As γ Collaboration (2010), Malkov et al. (2010), Lazarian and Desiati (2010), Blasi and Amato (2012) and Desiati and Lazarian (2013).

2.2 Cosmic-Ray Electrons

2.2.1 Spectrum of Cosmic-Ray Electrons

As for hadronic cosmic rays the shape of the cosmic-ray electron spectrum can help to understand acceleration mechanisms and propagation of cosmic-ray electrons. In this context usually the term electrons refers to both positrons and electrons.

Figure 2.4 shows a summary of the current state of the art (except the recent data from AMS-02 and Magic) of the measurements of the cosmic-ray electron spectrum. Much attention was dedicated to the cosmic-ray electron measurement of the Antarctic long-duration balloon-borne ATIC-2 experiment in 2005 which reported a bump in the electron spectrum between 300 - 800 GeV (Chang et al. 2005, Chang et al. 2008, Panov et al. 2011). ATIC-2 found a spectral index close to 3.0 between 30 GeV and 300 GeV and a hint at a cutoff at 1 TeV. The Antarctic PP-BETS experiment discovered also a bump in the spectrum, but with less statistical significance, different position and broader shape (Yoshida et al. 2008).

No bump like feature was found with the *Fermi*-LAT instrument (Abdo et al. 2009), which

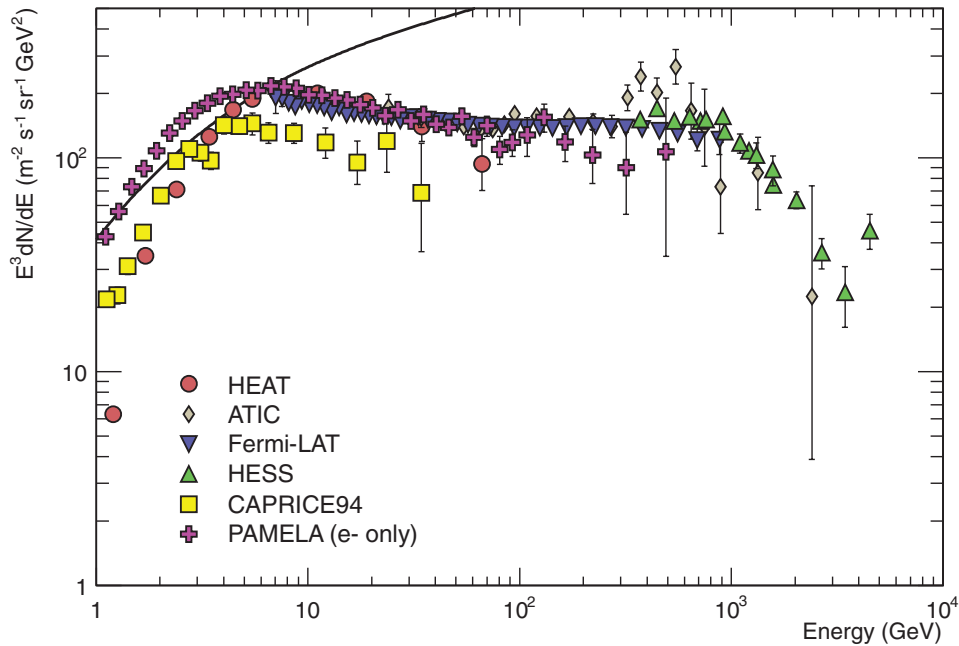


Figure 2.4: Differential spectrum of cosmic-ray electrons plus positrons (except the PAMELA data, which are electrons only) as observed by several experiments at Earth and multiplied by E^3 . The black line indicates the proton spectrum multiplied by 0.01. The figure was adapted from Olive et al. 2014.

on the other hand confirmed the spectral index previously measured by ATIC. *Fermi*-LAT extended the energy range of the electron spectrum up to 1 TeV. The High Energy Stereoscopic System (H.E.S.S.) experiment published the first cosmic-ray electron spectrum measured with a ground-based Imaging Atmospheric Cherenkov Telescope (Aharonian et al. 2008). This measurement extended the spectrum of cosmic-ray electrons up to 5 TeV and confirmed the high-energy cutoff previously measured by ATIC. The spectrum was fit by an exponentially cutoff power law with a spectral index of 3.05 and a cutoff at 2.1 TeV. H.E.S.S. also published a low energy cosmic-ray electron spectrum down to an energy of 340 GeV (Aharonian et al. 2009), which is consistent with ATIC data within statistical and systematic errors, but excluded a pronounced peak as suggested for interpretation by ATIC. The data follow a power-law spectrum with a spectral index of 3.0, which steepens at about 1 TeV. At these energies the H.E.S.S. spectrum overlaps with the *Fermi*-LAT energy range. Notably, the *Fermi* and H.E.S.S. electron spectra connect nicely after cross-correlating the energy scales (Meyer et al. 2010).

Further measurements of the cosmic-ray electron spectrum have been recently made by the PAMELA space spectrometer (Adriani et al. 2011a), the MAGIC telescope (Borla Tridon 2011) and the AMS-02 experiment (Aguilar et al. 2014a). AMS-02 presented the most precise measurement of the electron plus positron spectrum between 0.5 GeV and 1 TeV. The measured flux is smooth and can be described, above approximately 30 GeV, by a single power law with a spectral index of 3.17. Thus, the spectral shape appears softer than the previous measured spectra, e.g. with *Fermi*-LAT. The flux measured by AMS-02 is consequently higher at energies below approximately 100 GeV and lower above this value than previously measured. Figure B.1 in Appendix B shows the differential electron spectrum measured with AMS-02 and other experiments up to 1 TeV.

Overall, even though most measurements agree in principle about the spectral index of the cosmic-ray electron spectrum at least below approximately 250 GeV the question has not been finally resolved whether a bump like feature exists between 250 GeV - 700 GeV. Unaccounted systematic effects may play a significant role in understanding these discrepancies. If the cosmic-ray electron spectrum has a spectral index of ~ 3.0 it is harder than the one expected in *conventional* models (index ~ 3.1 to 3.5). Further, the cutoff found at approximately 1 TeV is not expected in *conventional* models (see Section 2.4 for details).

2.2.2 The Positron Fraction

The ratio of the positron flux to the total number of electrons and positrons allows the decomposition of the total electron and positron flux, giving a second important parameter capable of testing source and propagation models of cosmic-ray electrons and positrons. In the *conventional* picture (discussed in more detail in Section 2.4) electrons are accelerated in supernova remnants (SNR), while positrons originate from the interaction of CR protons with protons in the interstellar medium (secondary origin). In this model the positron fraction is expected to decrease continuously at energies above 1 GeV. Early measurements between 1970's and 1980's (for an overview see review of Panov et al. 2011) already showed deviations from this simple model above 10 GeV. Nonetheless, statistics were not sufficient to draw meaningful conclusions.

The situation changed with the gain in statistics and precision of data provided by the PAMELA collaboration. The positron fraction shown in Figure 2.5 indeed increases above 10

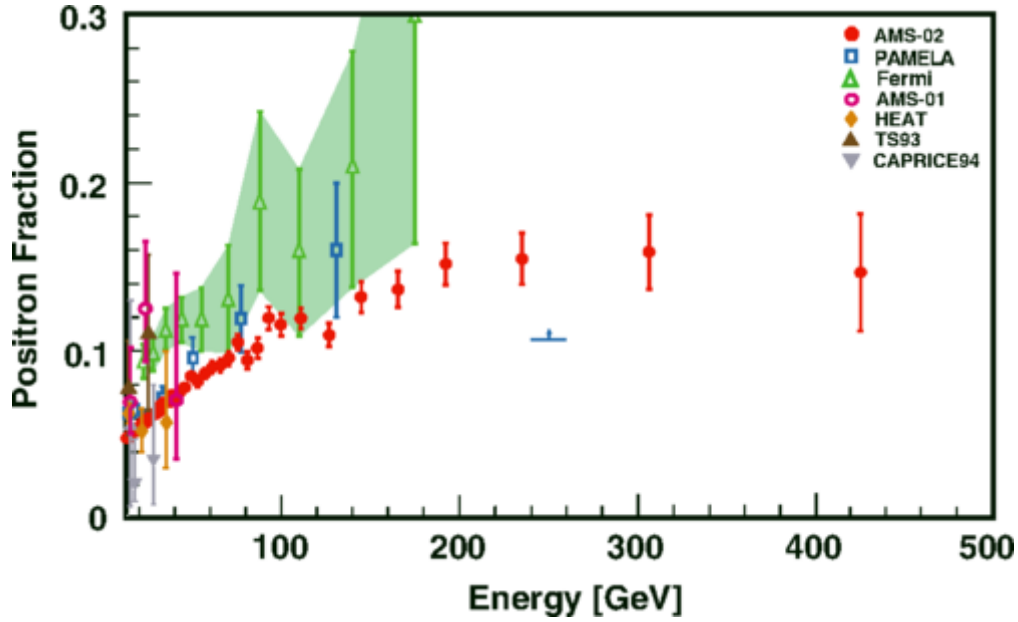


Figure 2.5: The positron fraction measured with PAMELA, *Fermi*-LAT, AMS-02 and a few other experiments. Adapted from (Accardo et al. 2014).

GeV (Adriani et al. 2009). The positron fraction measured with PAMELA was overall lower than the results from previous experiments, but this can be explained by different charge sign dependent solar modulation at different epochs of solar magnetic polarity. The PAMELA results were first confirmed by measurements with *Fermi*-LAT (Ackermann et al. 2012), which measured the positron fraction by indirectly taking advantage of the Earth’s magnetic field for separating electrons and positrons. Lately, the PAMELA result was also confirmed by a high precision measurement with the AMS-02 experiment onboard the International Space Station (Aguilar et al. 2013). The AMS-02 experiment measured the positron fraction with even higher resolution than PAMELA and up to 500 GeV (Accardo et al. 2014). Despite the high resolution of the AMS-02 data no substructure was found in the positron fraction. Further, it was found that the positron fraction does not further increase above 200 GeV. The state of the art of positron fraction measurements is presented in Figure 2.5.

The *conventional* model, discussed in Section 2.4, predicts a continuously decreasing positron fraction with increasing energy. It is clear that the *conventional* model cannot explain the results above, which in turn point towards new physical phenomena. To produce the rise of the positron fraction new sources of positrons are needed. In literature two different scenarios are most widely discussed. The first scenario suggests that electrons and positrons are accelerated by one or a few nearby sources either (aged) shell-type SNRs (see Section 2.3.1) or pulsars (Section 2.3.2). In the second scenario electron-positron pairs are produced by self-annihilating or decaying dark matter (DM) as discussed in Section 2.3.3.

2.2.3 Anisotropies in the Arrival Direction of Cosmic-Ray Electrons

Both the pulsar (or SNR) and the DM scenario possibly able to explain the electron spectrum and positron fraction measurements predict some type of large-scale anisotropy in the arrival direction of cosmic-ray electrons. In contrast to hadronic CRs cosmic-ray electrons lose energy rapidly through synchrotron radiation and inverse Compton scattering, so that an electron with an observed energy of 100 GeV must originate from a location within 1.6 kpc (see Section 2.4). Thus, the electrons measured at Earth possibly originate from one or a few nearby sources, e.g. pulsars or SNRs (Hooper et al. 2009). Following Mao and Shen (1972) the dipole anisotropy parameter for a single source in the case of isotropic diffusion is given by

$$\delta_i = \frac{I_{\max} - I_{\min}}{I_{\max} + I_{\min}} = \frac{3D}{c} \frac{|\nabla N_i|}{N_i} = \frac{3r_i}{2ct_i}, \quad (2.2)$$

here I_{\max} and I_{\min} are the minimum and maximum electron intensities over the whole sky. The concentration of electrons from a source i with age t_i and at distance r_i is given by N_i . The diffusion coefficient D is discussed in more detail in Section 2.4. In such a scenario a dipole anisotropy with an amplitude up to 20 % at 1-2 TeV is expected (left-hand panel in Figure 2.6, di Bernardo et al. 2011).

In the DM scenario the anisotropy usually originates from fluctuations of the number density of DM substructures in the vicinity of the observer as discussed in Borriello et al. (2012). Even though the DM mass is roughly equally distributed into a smooth halo component and into clustered DM substructures (found in N-body simulations), the halo component gives only a relatively small dipole anisotropy pointing towards the Galactic Center. Anisotropies generated by DM clumps lead to rather large fluctuations of possible dipole amplitudes and directions due to the stochastic nature of the distribution of high mass DM clumps. The resulting anisotropy reaches values up to 1% at 500 GeV (right-hand panel in Figure 2.6) and is, thus, much smaller than in a pulsar/SNR scenario¹.

Other studies discussing the distinguishability of an exotic origin from an astrophysical origin were also performed by for example Cernuda (2010) and Profumo (2015). Cernuda (2010) found the dipole anisotropy to be a useful tool for discrimination between the two scenarios, but the differences in amplitude are not as striking as in the studies above. Profumo (2015) even argues that a dipole anisotropy found in cosmic-ray electrons with the current instrumental sensitivity would unavoidably point towards an astrophysical origin, because otherwise a clear signal from the nearby dark matter clump would have to be visible in gamma rays.

One caveat in all discussions is that isotropic diffusion is assumed. In principle a local magnetic field structure will influence the observed anisotropy and possibly even produce an *artificial* anisotropy in cosmic-ray electrons. Nonetheless, the measurement or constraint of a dipole anisotropy in the arrival directions of cosmic-ray electrons is a powerful tool to constrain models and possibly able to distinguish between a dark matter and an astrophysical scenario.

The first study of anisotropies of cosmic-ray electrons was published by the *Fermi*-LAT collaboration (Ackermann et al. 2010a). They searched for anisotropies at angular scales between

¹The authors mention that anisotropies up to 10^{-1} due to a single massive clump being the only source of cosmic-ray electrons are in principle possible. However, in the relevant regions of the parameter space large boost factors would be required to reproduce the measured electron flux.

10° and 90° at minimum energies between 60 GeV and 480 GeV. No significant anisotropy was found at any of the searched angular scales. Thus, upper limits on the value of the dipole amplitude were derived and are superimposed in Figure 2.6. The AMS-02 collaboration also searched for an anisotropy in the ratio of the positron to electron flux between 16 and 500 GeV. The coefficients of the power spectrum were found to be consistent with isotropy at all energies and an upper limit on the dipole amplitude of $\delta \leq 0.030$ at 95 % C.L. for energies above 16 GeV (see Aguilar et al. 2013 and Accardo et al. 2014) was derived (integrated over the whole energy range). A more detailed study of the upper limit on the dipole amplitude measured with AMS-02 is presented in the PhD thesis of Cangas 2013-2014. Over its lifetime AMS will reach a dipole sensitivity of $\delta \sim 0.01$. AMS-02 and *Fermi*-LAT upper limits are also shown in the right-hand panel of Figure 5.55.

The study of Linden and Profumo (2013) is recommended to the interested reader, because the sensitivity of current and future IACTs, AMS and *Fermi*-LAT to a possible dipole anisotropy is discussed.

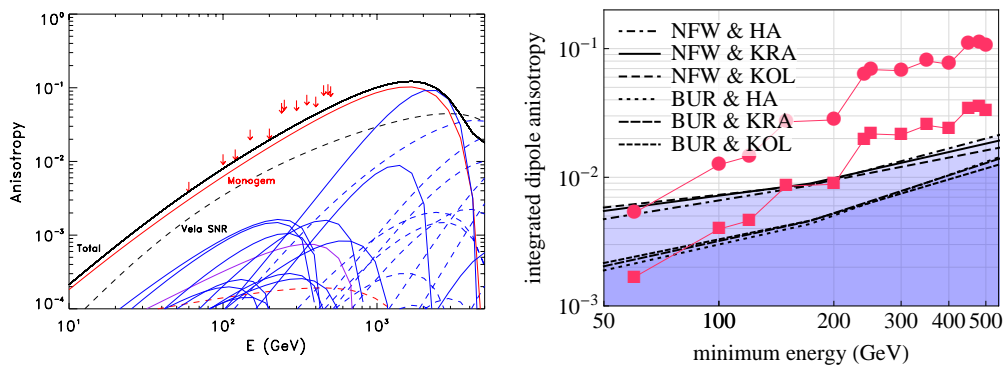


Figure 2.6: Left: Expectation of the integrated anisotropy as a function of minimum energy in a scenario where the cosmic-ray electron flux originates from few nearby sources (mainly pulsars but also a few SNRs) as derived by di Bernardo et al. (2011). The blue solid lines indicates nearby pulsars and the blue dashed lines SNRs. The black solid line represents the total anisotropy dominated by Monogem (red solid line) and the Vela SNR (black dashed line). The red arrows indicate the 95 % C.L. upper limit published by the *Fermi*-LAT collaboration. Right: Upper limit on the intrinsic anisotropy (maximum possible dipole amplitude) derived by Borriello et al. (2012). The results are shown for different combinations of DM density profiles (Navarro-Frenk-White NFW, Burkert BUR) and propagation models (Kraichnan KRA, Kolmogorov KOL and another HA). The different upper limits are indicated by black lines of different styles and the allowed values for the dipole amplitude are colored dark blue and light blue for Burkert and NFW DM density profiles. The upper limit on the dipole amplitude measured by *Fermi*-LAT (95 % C.L. red circles) and the expected *Fermi*-LAT sensitivity after 10 years of data taking (red squares) are also shown.

2.3 Production of Cosmic Rays

There are several different objects that are discussed to produce high-energy cosmic rays. Among those are supernova remnants, which are known to accelerate cosmic-ray particles, but do not accelerate antiparticles in the standard picture. In context of the positron-fraction problem discussed in Section 2.2.2 pulsars are often discussed as possible sources of cosmic-ray electrons and positrons, because they naturally accelerate also positrons. Often, also a dark matter origin of cosmic-ray electrons and positrons is debated. These three most popular source candidates of cosmic-ray electrons and positrons are introduced below in more detail.

2.3.1 Particle Acceleration in Supernova Remnants

One candidate for the acceleration of cosmic-ray electrons (and charged cosmic rays in general) are shock fronts of shell-type supernova remnants (SNR). The mechanism probably responsible for CR acceleration in SNRs is called diffusive shock acceleration and was first developed by Axford et al. (1978), Krymskii (1977), Bell (1978) and Blandford and Ostriker 1978 based on ideas by Fermi (1949). Such a shock front occurs as the result of a supernova explosion and can be described as a compression wave that moves supersonically into the surrounding medium (see e.g. Longair 2011 for an overview). A discontinuity forms at the wave front which resembles the shock. Gas before and behind the shock front is characterized by individual pressure, energy and momentum conditions. At the shock front, mass, energy and momentum must be conserved. In the case of a strong shock this leads to a jump of the density by a factor of 4 at the shock front leading to a change of velocities of the gas in the regions in front and behind the shock front.

Figure 2.7 illustrates the situation in a shock front moving at speed u . The shock front moves forward relative to the interstellar gas. In the rest frame of the shock front the observer sees the unshocked gas ahead of the shock front moving at speed u towards the observer (the shock front). The gas in the shocked region behind the shock is streaming away from the shock at speed $1/4 u$ in the case of a strong shock. This speed results from energy, momentum and mass conservation (Longair 2011). An electron initially at rest in the unshocked gas frame sees the shock front approaching at speed u , but also the shocked gas at $3/4 u$. When the electron crosses the shock front it is accelerated to $3/4 u$ and is thermalized to a high temperature. Now the electron is scattered back on magnetic inhomogeneities. With respect to the shocked frame where the electron is coming from the shocked gas moves at a speed of $3/4 u$ towards the electron and, thus, the electron receives a small amount of energy. In this manner the electron can be scattered across the shock front several times gaining energy with every crossing. The electrons are scattered back and forth at magnetic inhomogeneities. In the unshocked gas region they are produced by turbulences initiated by the shock front itself. In the shocked gas region they originate from streaming instabilities produced by the relativistic particles themselves (Bell 1978).

The scattering of a particle in the unshocked gas region by the shock front is shown in Figure 2.8. The energy gain of this particle can be calculated by Lorentz transformation of the particle into the frame of the shock front and back into the laboratory frame and averaging over the scattering angles (θ_1, θ_2) taking into account that the shock front has a defined direction

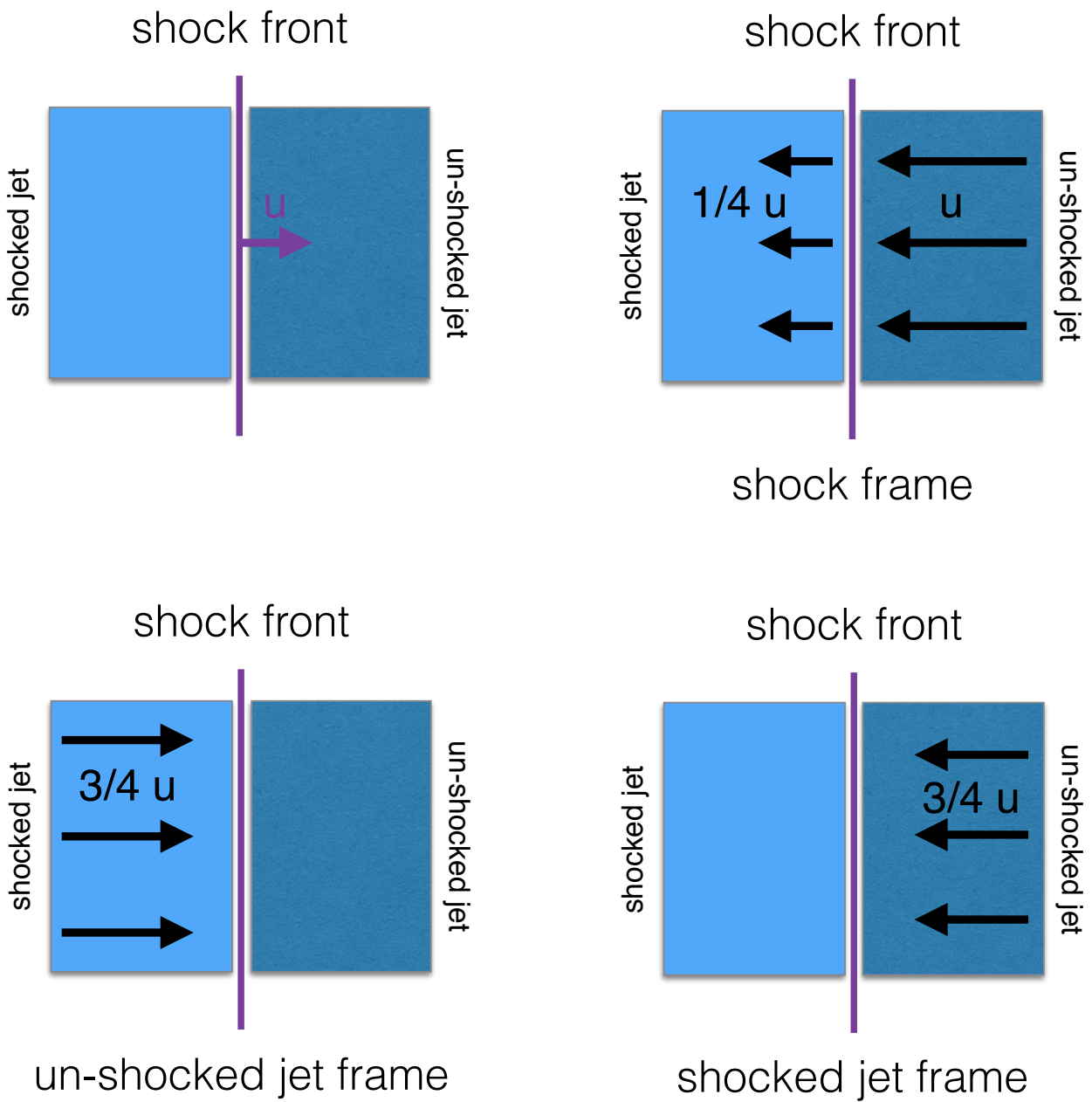


Figure 2.7: Hydrodynamics of a shock front. Upper Left: Shock front traveling at speed u . Upper right: View in the rest frame of the shock front. Lower left: View in the frame of the unshocked jet. Lower right: View in the frame of the shocked jet. Drawing inspired by lectures of M. Longair at IMPRES summer school 2013 in Heidelberg.

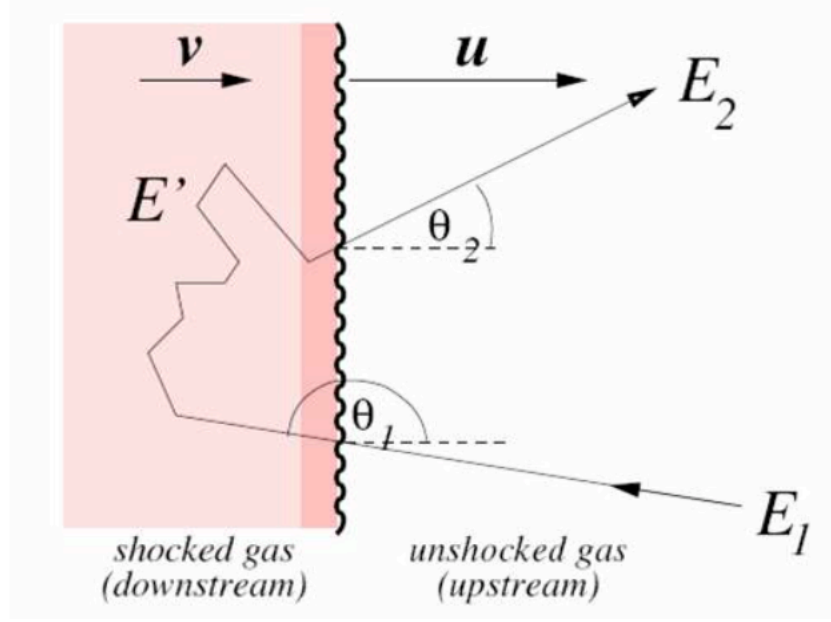


Figure 2.8: First order Fermi acceleration at a shock front. Adapted from Kolanoski (2006).

of motion and that particles scattered to the wrong hemisphere are lost to the acceleration process. Following Longair (2011) the mean energy gain per round trip in a shock front is given by

$$\left\langle \frac{\Delta E}{E} \right\rangle = \frac{4}{3} \beta = \frac{4}{3} \frac{v}{c} = \frac{4}{3} \frac{3}{4} \frac{u}{c} = \frac{u}{c}. \quad (2.3)$$

Here, $v = 3/4 u$ is the speed at which the particle in the unshocked gas region (upstream) sees the shocked gas moving towards it. Thus, the energy after k round trips is given by

$$E_k = E_0 \left(1 + \frac{4}{3} \frac{v}{c} \right)^k = E_0 \xi^k. \quad (2.4)$$

E_k is the energy after k round trips and E_0 is the original energy of the particle. $\xi = 1 + \frac{4}{3} \frac{v}{c}$ is the energy gain parameter. Assuming a constant probability P for a particle to stay in the system after a round trip, the number of particles left after k round trips is given by

$$N_k = N_0 P^k. \quad (2.5)$$

From Equations 2.4 and 2.5 the energy spectrum expected from diffusive shock acceleration can be obtained by solving the equations for k and then combining them

$$\frac{\ln \frac{N_k}{N_0}}{\ln \frac{E_k}{E_0}} = \frac{\ln P}{\ln \xi} \rightarrow \frac{N}{N_0} = \left(\frac{E}{E_0} \right)^{\ln(P)/\ln \xi}. \quad (2.6)$$

Thus, the differential energy spectrum of charged particles accelerated in diffuse shock fronts is a power law with spectral index $\alpha = -1 + \ln(P)/\ln\xi$

$$\frac{dN}{dE} = \frac{dN}{dE}(E_0) \left(\frac{E}{E_0} \right)^\alpha. \quad (2.7)$$

Assuming that the number of particles crossing the shock is given by $1/4 N c$ (N is the number density of particles) and that particles are swapped away from the shock downstream (shocked gas region) at a rate $N v = 1/4 N u$ the fraction of particles lost per unit time is given by u/c (Longair 2011). Thus, $P = 1 - u/c$ and $\ln(P)/\ln\xi = -1$ and $\alpha = -2$ can be derived. This differs from the measured spectral index of cosmic rays $\alpha = -2.7$, but is reasonable when considering the fact that cosmic rays suffer significant energy losses propagating through the interstellar medium. Chapter 2.4 discusses the propagation mechanisms in the related case of cosmic-ray electrons briefly.

Energies above the knee cannot be explained in this model, because the return rate to the shock front due to scattering on magnetic fields is too low at these high energies (Lagage and Cesarsky 1983, Berezhko 1996). In this standard picture of diffuse shock acceleration only particles and no antiparticles are accelerated, because supernova explosions only produce particles and no antiparticles. Consequently, SNRs are exclusive candidates for electron (proton) and not for positron (antiproton) acceleration. Recently, strong evidence that protons are actually accelerated in SNRs was found. The *Fermi*-LAT telescope discovered a characteristic pion decay feature in the gamma-ray spectra of two SNRs, IC 443 and W 44, which is unlikely produced by Bremsstrahlung or inverse Compton scattering of high-energy electrons (Ackermann et al. 2013). Previously, a similar observation was already made with Italy's AGILE spacecraft (Giuliani et al. 2011). Complimentary evidence was found by a group of physicists in Heidelberg studying the spectrum of visible light emitted by hydrogen atoms in the shock region of SNR 1006 (Nikolić et al. 2013). From the hydrogen line (two-component $H\alpha$ line) intensity and width the speed of the atoms can be deduced, which suggests the existence of suprathermal protons in the SNR.

Long before these recent developments, the electron source spectrum had been determined by X-ray (and also radio) observations of synchrotron radiation produced by electrons in SNRs and was found to have a power law index of -2.2 (Allen 1999). Nevertheless, the idea that unusual SNRs could produce not only electrons, but also positrons has been discussed as well. Suprathermal positrons could be produced in the beta decay chains of radioactive nuclei ejected during the supernova explosion (e.g. Zirakashvili and Aharonian 2011, Ramaty and Lingenfelter 1979). Possibly, reverse shocks play an important role in the acceleration process of electrons and positrons (e.g. Zirakashvili and Aharonian 2011, Zirakashvili 2011).

2.3.2 Particle Acceleration by Pulsars

Pulsars are fast rotating neutron stars equipped with extremely high corotating magnetic fields (for an introduction see Weigert et al. 2005, Spurio 2015 or Longair 2011). A neutron star is formed after the supernova explosion at the end of the lifetime of a main sequence star with an initial mass larger than $8 M_\odot$ (solar masses). Neutrons make up most of the mass of the

neutron star, while a small amount of protons and electrons ($\sim 1\%$ of the stellar mass), due to the process $n \leftrightarrow e^- + p$, exist.

The density in the neutron star is extremely high with core densities possibly up to 10^{18} kg/m³, while the radius of the neutron star is only 10-15 km. The neutron star retains most of the angular momentum and magnetic field flux of its progenitor star. Since the radius of the neutron star is much smaller than the radius of its progenitor this leads to extremely large rotational frequencies ω and strong magnetic fields (up to 10^8 T). Usually the rotational axis and the axis of the dipolar magnetic field are not aligned, so that a pulsed radiation can be detected at Earth (if the alignment is right). The rotational velocity declines with time (called spin down) due to the radiation occurring in a fast rotating magnetic dipole. The spin down velocity is proportional to ω^3 . For details on pulsars and their acceleration mechanisms see the reviews of, e.g. Manchester and Taylor (1977) and Kaspi et al. (2006).

The phenomena leading to particle acceleration in the magnetosphere of pulsars are in general rather complex (Figure 2.9 shows exemplarily a sketch of the magnetosphere of the Crab pulsar.), but the simple Goldreich-Julian model (Goldreich and Julian 1969) describes the basic mechanisms. In this model the pulsar is an aligned rotator, meaning that the magnetic field axis and the rotation axis are aligned parallel to each other. The magnetic field is static and described by a point-like dipole. The star is a perfectly conducting sphere and the magnetic field is frozen into the sphere. Charged particles moving through the material experience a Lorentz force, which separates the charges and, thus, induces an electric field. The electric charges reorganize themselves and cancel out the induced electric field. As a result there is a charge distribution within the star. The electric potential must be continuous at the surface of the star. Thus, the potentials in the stellar interior and outside the star must be matched to each other. The electric potential outside the star is described by the vacuum solution of the Laplace equation and is a superposition of a monopole and a quadrupole.

The radial component of the induced electric field at the surface is much stronger than the gravitational forces pulling the charged particles downwards. Thus, the charged particles are pulled out of the surface and make up the plasma around the neutron star. The charge density in the magnetosphere of the pulsar is called *Goldreich-Julian density* and is given by $\rho_{GJ} = -2\epsilon_0 \vec{\omega} \vec{B}$. Here, ϵ_0 is the electric permittivity, $\vec{\omega}$ the angular velocity vector and \vec{B} the magnetic field vector. This charge distribution has the important property of separating positive and negative charges along zero charge cones.

The plasma is moving alongside the neutron star, but the particles cannot travel faster than the speed of light. This condition defines the light cylinder. Within this cylinder the magnetic field lines are closed, the charged particles gyrate around them, but are preserved within the magnetosphere. If the magnetic field lines cross the light cylinder they leave the magnetosphere. Thus, it is assumed that the particles are pulled from the areas of the pole cap region (see e.g. Ruderman and Sutherland 1975, Baring 2004) and are accelerated along the open magnetic field lines. For acceleration of charged particles the component of the electric field parallel to the magnetic field lines cannot be vanishing. The main problem with this simple model is that in stationary equilibrium the electric fields are screened by electric charges leading to a vanishing parallel component of the electric field.

In reality, the axis of the rotation of the neutron star and the magnetic field are not aligned.

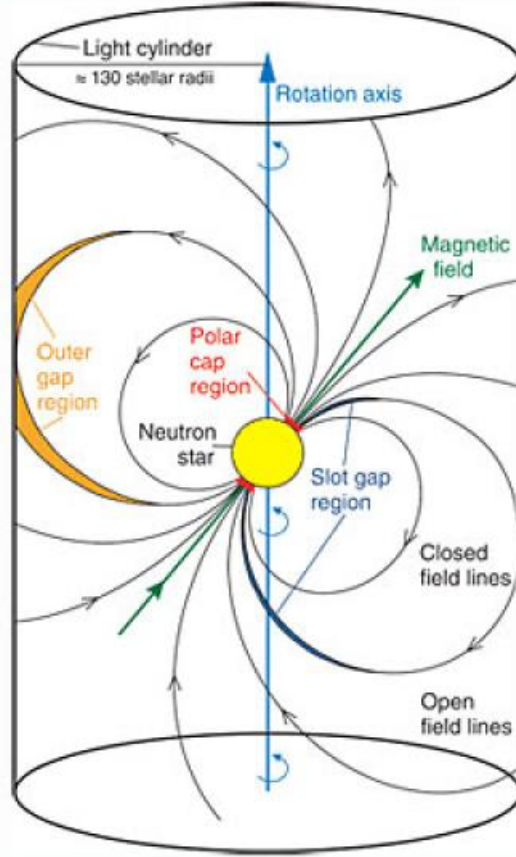


Figure 2.9: A sketch of the Crab pulsar’s magnetosphere (exemplarily also for other pulsars) by Aliu et al. (2008). The rotation axis (blue) and magnetic field axis (green) are indicated. In this case they are not aligned. The light cylinder is also illustrated. Electrons are trapped and accelerated along the magnetic field lines. Vacuum gaps/regions occur near the polar cap close to the surface of the neutron star, in a thin layer on the boundary of the closed magnetic field lines (called slot gap region) and in a region close to the light cylinder (outer gap region). In these regions the plasma density is lower than the Goldreich-Julian density and, thus, electrons can be accelerated.

In these more complicated models the charges are not only accelerated in the polar cap region, but additionally in a region close to the field line closest to the light cylinder where the charge density changes sign ($\vec{\omega} \cdot \vec{B} = 0$) called outer gap (see e.g. Cheng et al. 1986 or Tang et al. 2008) or in a thin layer close to the last closed magnetic field line called slot gap (see e.g. Arons and Scharlemann 1979 or Harding et al. 2008). Figure 2.9 illustrates the general structure of the pulsar magnetosphere (exemplarily for the Crab pulsar) and regions in which acceleration

is predicted.

If charged particles are accelerated they start emitting synchrotron and curvature radiation. The emerging photons interact with the transverse component of the magnetic field producing electron-positron pairs. The resulting electrons and positrons are again accelerated and a cascade is initiated. This plasma forms the pulsar wind nebula (PWN), which expands through the ambient medium until it reaches the expanding shell of the SNR and a stationary termination shock is formed. At the termination shock the relativistic pulsar wind is forced to join the slowly expanding outer nebula and the particles are again accelerated (Slane 2002).

In distinction to the acceleration in SNRs not only electrons but also positrons are accelerated in the magnetospheres of pulsars.

When the charged cosmic rays move through the strong magnetic fields and the radiation field they can produce high energy gamma rays by inverse Compton scattering, which makes them interesting objects for gamma-ray astronomy. In 'outer gap' models the probability that high energy gammas are produced and not immediately absorbed again is even larger than in 'polar cap' models.

2.3.3 Dark Matter as a Source of Cosmic-Ray Electrons and Positrons

It was noticed quickly after the measurement of the ATIC peak in the electron spectrum and the anomaly in the positron fraction measured by PAMELA (see Sections 2.2.1 and 2.2.2) that self-annihilating or decaying dark matter (DM) could simultaneously explain both features. In this context the DM particles are usually assumed to be *weakly interacting massive particles* (WIMPs), one of the most promising and popular DM particle candidates (for a review see e.g. Griest 1996 and Hooper 2009). In principle, two different scenarios are discussed.

First, the annihilation and decay of DM in a smooth Galactic halo. In the left-hand panel of Figure 2.10 the electron spectrum expected from DM annihilation in a smooth Galactic halo is shown (dashed line). The spectrum exhibits a peak-like feature, but the flux amplitude is three orders of magnitude smaller than the actually measured spectrum so that the DM contribution is negligible compared to the expectation from the *conventional* background (solid line, discussed in detail in Section 2.4). This is caused by the value of the thermally averaged velocity weighted annihilation cross section $\langle\sigma v\rangle \sim 3 \cdot 10^{-26} \text{cm}^3 \text{s}^{-1}$ (Jungman et al. 1996), which corresponds to the value expected from the cosmological abundance of DM. This value strongly influences the annihilation rate

$$R = \frac{1}{2} k n^2 \langle\sigma v\rangle \quad (2.8)$$

and, thus, the amplitude of the spectrum. Here, k is the number of electrons and positrons produced per annihilation process and n the WIMP number density. While the spectrum in the left-hand panel of Figure 2.10 shows a peak in the electron spectrum a cross section boost factor is required to reproduce the amplitude of the flux. Mechanisms possibly producing such a boost are a Sommerfeld effect and a Breit-Wigner enhancement (for a review see He 2009). Such a model is shown in the right-hand panel of Figure 2.10. Electrons and positrons are produced in equal parts by DM annihilation so that such a model almost automatically

produces a behavior of the positron fraction very similar to the one found in experimental data (Panov 2013).

Further, it was found from numerical N-body simulations that DM forms substructures often called subhalos or clumps with masses between 10^5 and $10^{10} M_\odot$ inhomogeneously distributed within the Galactic halo (see e.g. Ghigna et al. 1998, Diemand et al. 2008 and Springel et al. 2008). The different simulations roughly agree that the mass density of the substructures scales approximately as $\frac{dN}{dM} \sim M^{-2}$, where M is the mass of the clump and N the number of clumps. The distribution of DM clumps within the smooth halo is less certain. Via Lactae II (Diemand et al. 2008) and Aquarius subhalos (Springel et al. 2008) simulations disagree on the number of substructures, the amount of (sub)substructures within subhalos and the density profile of the subhalos.

In the Via Lactea II simulations by Diemand et al. (2008) roughly 10 clumps with $10^9 M_\odot$ and 10^4 clumps with $10^6 M_\odot$ were found. The mean distance between small $10^6 M_\odot$ clumps is of the order of 10 kpc, which also corresponds to the expected distance from the Sun to the nearest clump. The number density within such a clump is expected to be several hundred times (mean density in the whole clump) to several thousand times (mean density in the central region of the clump) larger than the density in a smooth DM halo. Since the annihilation rate scales with the square of the DM density it is, thus, much larger in a DM clump than in the smooth DM halo. In the case of DM clumps it is in principle possible to get the correct magnitude of the spectrum without a boost factor, but only for a clump located very close to the Sun (< 0.1 kpc) (Panov 2013). For the more realistic distance of 10 kpc between clump and Earth again high boost factors are required. In general, the electron spectrum

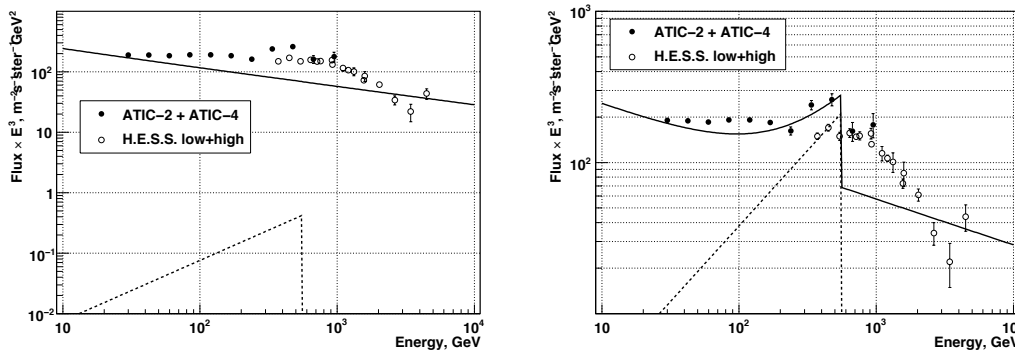


Figure 2.10: Simple analytical models of the electron spectrum produced by a homogenous DM halo without a boost factor (left-hand panel) and with a boost factor of 500 (right-hand panel). The electron spectra measured with the ATIC and H.E.S.S. experiments are shown (markers). The dashed line gives the spectrum expected from DM annihilation in a smooth Galactic halo. The solid line gives the sum of *conventional* background and DM spectrum. The following parameters were used for the DM model: $M_{\text{WIMP}} = 1.1$ TeV, $k = 4$, $\langle\sigma v\rangle = 3 \cdot 10^{-26} \text{cm}^3 \text{s}^{-1}$, $n = 0.3 \text{GeV cm}^{-3} / M_{\text{WIMP}}$. Adapted from Panov (2013).

produced by a DM clump is expected to be much harder than the one produced by a smooth DM halo. This leads to difficulties in reproducing the positron fraction. In combination with DM annihilation in the Galactic halo also the positron fraction is reproduced (for a review see Fan et al. 2010). Decaying DM can also produce similar behaviors of the electron spectrum and the positron fraction as annihilating DM. Since the mechanisms are very similar decaying DM is not discussed here, but a review is given by Bae and Kye (2009).

One drawback of the DM explanation, already mentioned above, is the necessity for strong boost factors. But, there are more troubles attached to DM models. They naturally predict an anomaly in the antiproton to proton ratio analogue to the one found in the positron fraction. Such an anomaly is not seen in experimental data by PAMELA (Adriani et al. 2009 and Adriani et al. 2010). Thus, the annihilation of DM particles must be restricted to leptophilic channels (Yin et al. 2009). Further, constraints on the thermally averaged and velocity weighted annihilation cross section $\langle\sigma v\rangle$ from gamma-ray observations exclude Galactic halo DM as the only source of anomalies in the ATIC spectrum and the positron fraction measurement (Zavala et al. 2011 and Abramowski et al. 2011). However, this is not the case for clumpy DM so that DM annihilation or decay is still discussed as source of the measured anomalies.

2.4 Propagation of Cosmic-Ray Electrons

The propagation of cosmic-ray electrons is generally described by the diffusion equation first proposed in a paper by Syrovatskii 1959. The solution of the diffusion equation will be discussed by illustrating the main properties of cosmic-ray electron propagation via simplified models following the approach of Panov (2013) and then discussing more complicated cases briefly and qualitatively. In the simple case of a homogenous and isotropic medium the diffusion equation is given by

$$\frac{\partial \rho}{\partial t} = \frac{\partial}{\partial E} [b(E)\rho] + D(E)\nabla^2 \rho + Q, \quad (2.9)$$

where $\rho = \rho(\mathbf{r}, t, E)$ is the number density of cosmic-ray electrons at location \mathbf{r} , time t and with energy E . $D(E)$ is the energy dependent diffusion coefficient which is given by $D = D_0 \cdot (E/\text{GeV})^\delta$. Typical values of the diffusion coefficient D_0 found from fitting diffusion models to CR data lie between $1 \cdot 10^{28} \text{cm}^2/\text{s}$ and $5 \cdot 10^{28} \text{cm}^2/\text{s}$. The parameter δ takes values between 0.3 and 0.6 depending on the type of magnetic hydrodynamic (MHD) turbulence considered (Strong et al. 2007). The source function $Q = Q(\mathbf{r}, t, E)$ depends on the location of the electron source, the time t at which the electrons are emitted by the source and the energy spectrum (dependence on E) of the emission. $b(E)$ resembles the continuous energy loss rate of the electrons while propagating through the ISM. In general, for relativistic electrons ionization losses, bremsstrahlung losses, adiabatic losses as well as synchrotron and inverse Compton losses must be considered. At energies up to a few TeV and at time scales smaller than 10^7 years only inverse Compton and synchrotron losses are important. Thus, the energy loss is given by

$$b(E) = \frac{\partial E}{\partial t} = -b_0 E^2, \quad (2.10)$$

with

$$b_0 = \frac{4}{3} \frac{\sigma_T c}{(m_e c^2)^2} \left(\omega_{\text{photon}} + \frac{B^2}{8\pi} \right). \quad (2.11)$$

In Equation 2.11 ω_{photon} resembles the energy densities of all photons contributing to inverse Compton scattering. This includes photons from the cosmic microwave background (CMB), infrared photons emitted by dust and optical starlight photons. All three contributions add up to a total photon energy density of roughly $\omega_{\text{photon}} = 1 \text{eV}/\text{cm}^3$. The mean strength of the magnetic field adopts typical values between 3 and 4 μG . The Thompson cross section is $\sigma_T = 6.65 \cdot 10^{-25} \text{cm}^2$, c is the speed of light and m_e is the electron mass. This gives a value of b_0 lying between 1.2 and $1.6 \cdot 10^{-16} (\text{GeV} \cdot \text{s})^{-1}$. The energy of an electron with initial energy E_0 after traveling a time t is given by

$$E(t) = \frac{E_0}{1 + b_0 E_0 t}. \quad (2.12)$$

From this equation it can be inferred that a particle with initially infinitely high energy $E(t) \rightarrow \infty$ cooling down to energy E_0 cannot have traveled longer than a maximum timespan of $T_{\text{max}} = 1/(b_0 E_0)$ because in this case $t \rightarrow -1/(b_0 E_0)$. Thus, the maximum distance an electron with energy E_0 can have traveled is approximately $d_{\text{max}} \approx \sqrt{2 D T_{\text{max}}}$ (see definition of the cooling

length in Equation 2.16). For an electron measured today at 1 TeV this maximum travelled distance is given by 1.5 kpc (for $D_0 = 3 \cdot 10^{28} \text{ cm}^2/\text{s}$ and $\delta = 0.6$). Thus, a cosmic-ray electron measured at Earth probably originates from a maximum distance of the order of one to a few kpcs so that potentially only a few nearby sources contribute to the cosmic-ray electron flux measured at Earth.

The diffusion equation for an arbitrary source function can be solved by convoluting the source function with Green's function (Syrovatskii 1959)

$$\rho(\mathbf{r}, t, E) = \int G(\mathbf{r}, t, E | \mathbf{r}', t', E') Q(\mathbf{r}', t', E') d^3\mathbf{r}' dt' dE'. \quad (2.13)$$

The Green function $G(\mathbf{r}, t, E | \mathbf{r}', t', E')$ is given by

$$G(\mathbf{r}, t, E | \mathbf{r}', t', E') = \frac{\exp \left[-\frac{(\mathbf{r}-\mathbf{r}')^2}{2\lambda^2(E, E')} \right] \delta(t - t' - \tau(E, E'))}{|b(E)|(2\pi)^{3/2}\lambda^3(E, E')}. \quad (2.14)$$

Here, the cooling time $\tau(E, E')$ of an electron from energy E' to E is given by

$$\tau(E, E') = \int_E^{E'} \frac{dE''}{|b(E'')|} = \frac{1}{b_0 E} - \frac{1}{b_0 E'} \quad (2.15)$$

and the mean square of the cooling length $\lambda^2(E, E')$ is given by

$$\lambda^2(E, E') = 2 \int_E^{E'} \frac{D(E'') dE''}{|b(E'')|} = 2D \left[\frac{1}{b_0 E} - \left(\frac{E'}{E} \right)^\delta \frac{1}{b_0 E'} \right]. \quad (2.16)$$

Even in the case of a simple power law source function this approach does not lead to any convenient analytical solution. For realistic distributions of the matter in the Galaxy the solution of the diffusion equation is usually found numerically, e.g. by employing the GALPROP system (Strong and Moskalenko 1998). This method was used for calculating the electron spectrum of the *conventional* model calculated by Moskalenko and Strong (1998). In this conservative approach the electrons and positrons originate from two different sources. Electrons (such as protons and heavier nuclei) are accelerated in SNRs, while positrons are produced in collisions of cosmic-ray protons with protons of the interstellar medium ($p+p \rightarrow \pi+X$). In these interactions mainly pions are produced, which decay into muons and gamma rays (see Equations 3.1 to 3.3). Afterwards muons decay into electrons and positrons (Equations 3.4 and 3.5).

The main predictions of the *conventional* model can be illustrated by considering a simple model called thin disk approximation. In this model the depth of the galactic halo is indefinitely large, while the Galactic disk within which the sources of electrons are distributed is assumed to be indefinitely thin. Further, since the Sun is located rather close to the Galactic plane the flux of cosmic-ray electrons at height $z=0$ is assumed to be representative for the location of the Earth. In this model the source function is given by

$$Q(\mathbf{r}, t, E) = Q(E) \delta(z). \quad (2.17)$$

Here, $Q(E)$ is the electron spectrum at the source, which is constant in time. In this case the solution of the diffusion equation is given by

$$\rho(E)|_{z=0} = \frac{1}{b_0\sqrt{2\pi}} \frac{1}{E^2} \int_E^\infty \frac{Q(E')}{\lambda(E, E')} dE'. \quad (2.18)$$

Considering a power law source spectrum $Q(E) = Q_0 E^{-\alpha}$ (where Q_0 is a constant, that could be calculated) and the previous definitions of λ and the diffusion coefficient D , the integral can be solved and the following spectrum is expected:

$$\rho(E)|_{z=0} = Q_0 E^{-(\alpha+\Delta)} \quad \text{where} \quad \Delta = \delta + \frac{1}{2}. \quad (2.19)$$

From this equation it is obvious that the initial source electron spectrum steepens by Δ due to the propagation mechanisms of cosmic-ray electrons. Since $0.3 < \delta < 0.6$ the source spectrum and the measured electron spectrum differ by $\Delta \approx 1$. In the two component *conventional* model the spectral index of the SNR source of cosmic-ray electrons is not exactly known, but is probably similar to that of protons (Blandford and Ostriker 1980, Müller 2001) and lies approximately between $2.1 < \alpha_0 < 2.5$. The spectral index of the source spectrum of cosmic-ray electrons was observed via the measurement of synchrotron radiation in SNRs in X-ray and radio observations (e.g. Allen 1999, Reynolds and Gilmore 1986 and Anderson and Rudnick 1995). The source spectrum of secondary electrons and protons is given by the spectral index of the observed spectrum of cosmic-ray protons $\alpha_s \approx 2.7$, since they are produced in interactions of these protons. The total spectrum of electrons plus positrons $Q_{e^++e^-}(E)$ is, thus, given by

$$Q_{e^++e^-}(E) = Q_0 E^{-(\alpha_0+\Delta)} + Q_{s,el} E^{-(\alpha_s+\Delta)} + Q_{s,pos} E^{-(\alpha_s+\Delta)}. \quad (2.20)$$

Here, Q_0 is the amplitude of the primary electron flux and $Q_{s,el}$, $Q_{s,pos}$ are the amplitudes of the secondary flux of electrons and positrons. When comparing these results to the data it is found that the primary component strongly dominates over the secondary and mainly determines the shape of the actually measured spectrum. In this model a prediction of the positron to electron plus positron flux ratio $R(E) = \frac{Q_{e^+}(E)}{Q_{e^++e^-}(E)}$, called positron fraction, is calculated by

$$R(E) = \frac{Q_{e^+}(E)}{Q_{e^++e^-}(E)} = \frac{Q_{s,pos}}{Q_{s,el} + Q_{s,pos} + Q_0 E^{(\alpha_s-\alpha_0)}}. \quad (2.21)$$

Thus, the *conventional* model predicts a decrease of the positron fraction with energy.

As shown in Sections 2.2.1 and 2.2.2 the measured electron spectrum and positron fraction cannot be explained by the *conventional* model of electron and positron diffusion. Many authors have suggested other approaches for solving the diffusion equation. Here, only a few selected shall be mentioned briefly. Atoyan et al. (1995) found an analytical solution to the diffusion equation for the case of a burst-like injection of electrons into the ISM, which exhibits a cutoff of the electron spectrum at high energies. Kobayashi et al. (2004) modified the source function of burst-like injection by an exponential cutoff term. It was found that the strength of the contributions of the considered sources (Vela, Monogem, Cygnus Loop) varied strongly with the chosen diffusion parameters such as diffusion coefficient and release time of the electrons.

Overall, the shape of the electron spectrum varies strongly with the diffusion parameters, the assumed distribution of sources that are contributing and the injection history of the sources (e.g. burst-like or continuous injection).

Chapter 3

Detection Principles of Cosmic-Ray Electrons

3.1 Direct Detection

The detection technique applicable to detect cosmic-ray electrons depends strongly on the energy range considered. At low energies the flux of cosmic-ray electrons is comparably large, approximately $10^1 \text{ GeV}^{-1}\text{cm}^{-2}\text{sr}^{-1}\text{s}^{-1}$ at 1 GeV as compared to $10^{-7} \text{ GeV}^{-1}\text{cm}^{-2}\text{sr}^{-1}\text{s}^{-1}$ at a few 100 GeV and $10^{-10} \text{ GeV}^{-1}\text{cm}^{-2}\text{sr}^{-1}\text{s}^{-1}$ at 4 TeV (see Figure 2.4), but the particles are absorbed in the upper atmosphere. Thus, they have to be detected directly at the top of the atmosphere or in space, with instruments located aboard a balloon, rocket or satellite. Particle detectors similar to the ones used on Earth at particle accelerators are employed. The particles are detected by measuring the energy/momentum the particle transfers to the detector material. For example the first cosmic rays were measured with electroscopes aboard a balloon by Victor Hess (Hess 1912). Modern detectors usually contain different parts/layers that are designed for measuring different properties of the particle including energy (momentum), mass, charge and arrival direction. In the following, three of the currently operating detectors will be presented exemplarily to demonstrate their functionality. The list of presented instruments is not complete, but aims to shortly introduce the most important instruments that appear at some point in this study.

PAMELA (Payload for Antimatter Matter Exploration and Light-nuclei Astrophysics) is an instrument detecting cosmic-ray particles on board the Resurs-DK1 satellite (Picozza et al. 2007). It was designed to measure charged cosmic rays (electrons, protons and light nuclei) from tens of MeV to several hundred GeV. It was optimized for the identification of antiparticles. The scientific accomplishments so far include the measurements of energy spectra of electrons, positrons, protons, antiprotons, helium, carbon and boron. Another goal is the search for antimatter, e.g. antihelium. The high statistics measurement of the excess of cosmic-ray positrons shown in Figure 2.5 was one of the PAMELA results.

The setup of the PAMELA detector is shown in Figure 3.1. The magnetic spectrometer is composed of a permanent magnet and a silicon tracker. With the information from both

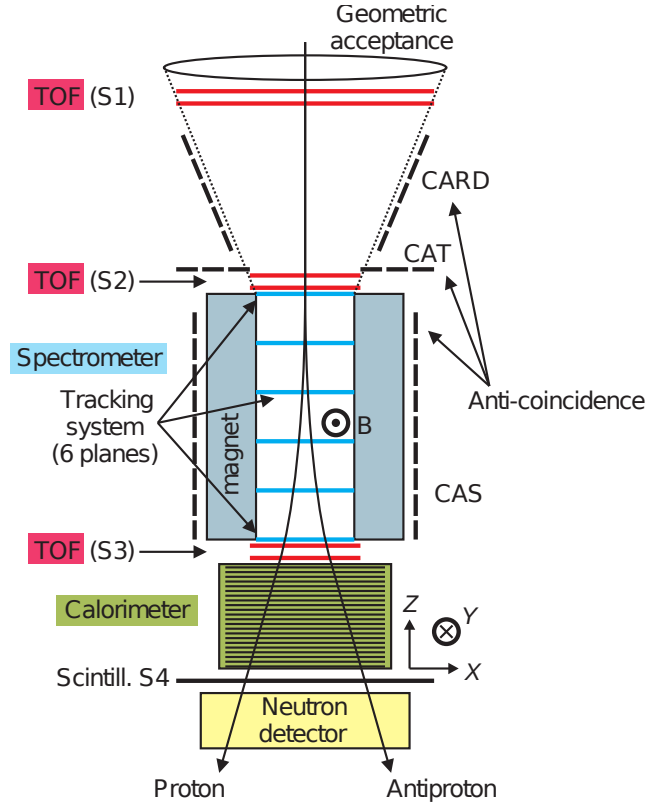


Figure 3.1: Schematic drawing of the components of the PAMELA detector. Measured from top to bottom the detector is roughly 1.3 m high. It consists of a Time-of-Flight system (ToF), which comprises the three scintillator planes S1, S2 and S3, an anticoincidence shield system, a permanent magnet spectrometer, a silicon-tungsten electromagnetic calorimeter, shower tail scintillator S4 and a neutron detector. The figure was adapted from Adriani et al. (2013).

components the absolute charge, the sign of the charge and the rigidity (momentum per unit charge) can be obtained. The anticoincidence detector consists of five scintillators covering the sides and the top of the magnet and is used to identify particles that have not cleanly entered the detector for example through the magnet. The Time-of-Flight system (ToF) consists of three planes of fast plastic scintillators. The time of flight information between the first (S1) and the last plane (S3) is used together with information about the track length from the magnetic spectrometer to calculate the velocity of the particles and to reject albedo particles. The particle charge is determined by measuring the ionization in the scintillator layers. The electromagnetic sampling imaging calorimeter consists of silicon sensors alternated with tungsten absorbers. The energy released by the interacting particle is measured and the interaction topology of

the particle in the calorimeter is reconstructed. This allows to distinguish leptons (e^+, e^-) from hadrons (p, \bar{p}). Additionally, the calorimeter allows to reconstruct the energy of the electromagnetic shower and, thus, of the incoming particle. The neutron detector is also used to distinguish between electromagnetic and hadronic cascades coming from the calorimeter (and, thus, electrons and protons) and consists of 36 ^3He counters and polyethylene neutron moderators. Before particles can reach the neutron detector they must pass through the bottom scintillator S4, which on the one hand is a high energy trigger for the neutron detector and on the other hand improves the electron-hadron discrimination by measuring shower leakage from the calorimeter.

Fermi-LAT The second instrument presented here is the Fermi Large Area Telescope (*Fermi-LAT*) pair conversion gamma-ray telescope (Atwood et al. 2009), because the measurement of the electron spectrum by *Fermi-LAT* was used in Section 5.2.5. The *Fermi-LAT* gamma-ray telescope aims to resolve the gamma-ray sky concerning both unidentified sources and the diffuse gamma-ray emission. The gamma rays emitted by active galactic nuclei (AGN), pulsars and supernova remnants (SNR) are studied to improve the understanding of particle acceleration mechanisms in these objects. Many more topics are studied for example the high-energy behavior of gamma-ray bursts and the search for an excess of gamma rays from the center of the Milky Way which is expected in dark matter scenarios. Additionally, studies of cosmic-ray electrons and positrons are carried out by the *Fermi-LAT* collaboration.

The *Fermi-LAT* has a field of view (FOV) of 2.4 sr and is designed to detect gamma rays between 200 MeV and 300 GeV on board the *Fermi* satellite orbiting the Earth within roughly every 1.5 hours. Most of the time *Fermi-LAT* operates in an all-sky survey mode scanning the whole sky almost uniformly within two orbits by alternating the boresight of the telescope between northern and southern hemisphere.

A schematic drawing of *Fermi-LAT* is shown in Figure 3.2. It consists of a 4x4 array of 16 identical towers each containing a tracker module and a calorimeter module. The tracker module consists of 16 tungsten converter layers that are interleaved with 18 single-sided silicon strip detectors. The incoming gamma ray interacts with an atom in one of the tungsten conversion layers and produces an electron-positron pair. The two charged particles proceed and interact with the silicon strip detectors creating electron-hole pairs. The strip detectors track the path of the particles through the detector, since they are arranged alternating in x- and y-directions. The tracker is divided into two regions called *front* and *back*. The 12 tungsten converter foils in the front region are thin (0.03 radiation lengths) in order to optimize the resolution of the direction reconstruction of the incident photons at low energies, which is limited mainly by scattering of the electrons and positrons going with $\sim 1/E$. At high energies scattering processes do not play an important role, but due to the lower fluxes a high effective area is required. Thus, the converters in the back tracker section (last 4 x, y planes) are 6 times thicker. Moreover, the pair conversion signature in the tracker can also be used for rejecting cosmic-ray background.

Afterwards the electron-positron pair enters the segmented caesium iodide (CSI) calorimeter, where it initiates an electromagnetic particle shower. Each calorimeter module consists of 96 CSI(Tl) crystals that are arranged in 8 layers of 12 crystals each. Each layer is rotated by

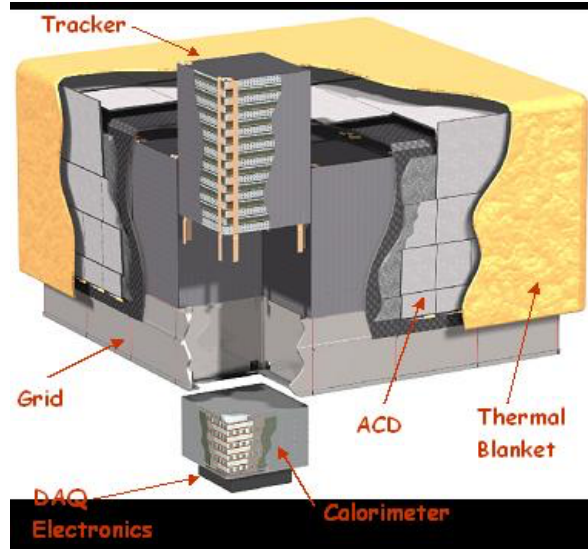


Figure 3.2: Schematic drawing of the components of the Fermi-LAT gamma-ray telescope. The main parts of the instrument are 16 silicon tungsten tracker modules, 16 segmented caesium iodide calorimeter modules, as well as segmented anticoincidence detectors (ACDs), which are composed of plastic scintillators. All components are marked in the Figure by arrows. Picture credit goes to NASA 2015.

90° with respect to its neighboring layers. Their total vertical depth is 8.6 radiation lengths (total instrument 10.1). At both ends of the crystals a photodiode measures the scintillation light. The position of the energy deposition along the crystal can be determined from the difference of light intensities measured on both ends. Thus, the profile of energy deposition of the shower in the segmented calorimeter can be determined. From this profile the energy of the initial electron can be derived. Additionally, the shower profile in the calorimeter can be used for discriminating hadronic background from signal events (usually gamma rays). The whole instrument is surrounded by a segmented anticoincidence detector (ACD), which tags charged particles producing a flash of light in the plastic scintillators of the ACD in order to provide a charged-particle background rejection with an efficiency of 99.97 %.

The information of all three components discussed previously are combined to estimate the parameters characterizing the measured event. During the reconstruction process the energy of the particle, the track through the instrument, the vertex and the direction of the incident particle are determined. Based on this information background particles are identified and can be rejected. This can be illustrated on the basis of the following two examples. If two tracks point back to the same vertex this is a clear indicator for an electron-positron pair initiated by an incident gamma ray. On the other hand, if a lot of hits or tracks occur that are not associated with a track this is a clear indication that the incident particle was probably a hadronic background event. Further, information from the calorimeter is used to distinguish between background and gamma-ray events, since the shower morphologies look different. By

combining the data from all LAT subsystems the energy reconstruction quality, the track reconstruction quality and the probability that the incident particle was a gamma ray can be derived. Overall, *Fermi*-LAT achieves a relative energy resolution $< 15\%$ at energies above 100 MeV, an angular resolution $< 0.15^\circ$ at energies above 10 GeV and $< 3.5^\circ$ at 100 MeV (68 % space angle containment radius) and a background rejection with less than 10% residual contamination (high latitude diffuse sample between 100 MeV and 300 GeV).

Not only gamma rays can be distinguished from charged background particles, but it is also possible to identify electrons (Abdo et al. 2009, Ackermann et al. 2010b). A charged particle will cause a signal in the ACD tile aligned with its track, which can be used to separate electrons from photons. In general electromagnetic tracks are much closer confined than hadronic tracks, which makes their lateral distributions the most powerful separator. Thus, electrons can be separated from hadrons by the signature they leave in the tracker and calorimeter. E.g. in the tracker they leave more clusters in the close vicinity of the track and the average energy deposition in the silicon foils is larger. In the calorimeter the transverse shower size for hadrons is much larger than for electrons and the average energy in the ACD tiles is significantly higher. Additionally, a classification tree (CT) analysis is employed combining different quantities sensitive to differences in hadronic and electromagnetic event topologies into a single variable and improving the hadron rejection power.

3.2 Indirect Detection of Cosmic-Ray Electrons with IACTs

The energy spectrum of cosmic-ray electrons follows a power law with index close to 3.0 as shown in Section 2.2.1. At energies above a few hundred GeV the effective collection area of direct detection instruments gets too small to detect enough electrons for spectral reconstruction. Consequently, other detection techniques must be employed at higher energies. Indirect detection techniques take advantage of high-energy cosmic rays producing showers of secondary particles when entering the Earth's atmosphere. Most of these secondary particles never reach the Earth, but they produce fluorescence and Cherenkov light, that can be detected. Some of the particles reach the ground and can be detected with, e.g. scintillation counters, drift chambers or Geiger tubes. In this study data from the Imaging Air Cherenkov Telescope (IACT) H.E.S.S. was analyzed. In the following, first the physics of particle showers in the Earth's atmosphere and the origin of Cherenkov light will be discussed and then the H.E.S.S. telescopes will be introduced in detail.

3.2.1 Air Shower Physics

When cosmic rays, either charged (electrons, protons, nuclei or their antiparticles) or neutral gamma rays (photons) enter the Earth's atmosphere they interact with atoms therein and initiate a shower of secondary particles. These showers can be separated into two different types, i.e. hadronic and electromagnetic air showers. The former type is initiated by protons and charged nuclei and the latter by gamma rays and cosmic-ray electrons (and positrons).

Hadronic Air Showers Figure 3.3 shows a schematic drawing of an hadronic air shower. The mean free path λ_I^p of protons in air corresponds to roughly $\lambda_I^p = 90 \text{ g/cm}^2$ (Table 3.1 from Spurio 2015), which means on average cosmic-ray protons initiate air showers roughly at a height of 16 km. There, they interact via inelastic scattering, producing charged and neutral mesons (mainly pions but also kaons) and atomic nuclei. The pions decay mainly in the three following channels (Spurio 2015)

$$\pi^0 \rightarrow \gamma + \gamma, \quad (3.1)$$

$$\pi^+ \rightarrow \mu^+ + \nu_\mu, \quad (3.2)$$

$$\pi^- \rightarrow \mu^- + \bar{\nu}_\mu. \quad (3.3)$$

Neutral pions account for roughly one third of the pions and decay almost instantaneously (lifetime $\tau_{\pi^0} = 8.4 \cdot 10^{-17} \text{ s}$) into two photons, which initiate an electromagnetic cascade. This component of the hadronic air shower, called soft component, contains mainly particles at relatively low energies and the details of it's development will be discussed below (Paragraph Electromagnetic Air Showers). Charged pions have much longer lifetimes ($\tau_{\pi^{+/-}} = 2.6 \cdot 10^{-8} \text{ s}$), so that they can in principle interact via inelastic scattering before they decay. Which process dominates strongly depends on the energy of the particle and the density of the medium it traverses. If the pion scatters inelastically it again produces pions of which a third are neutral

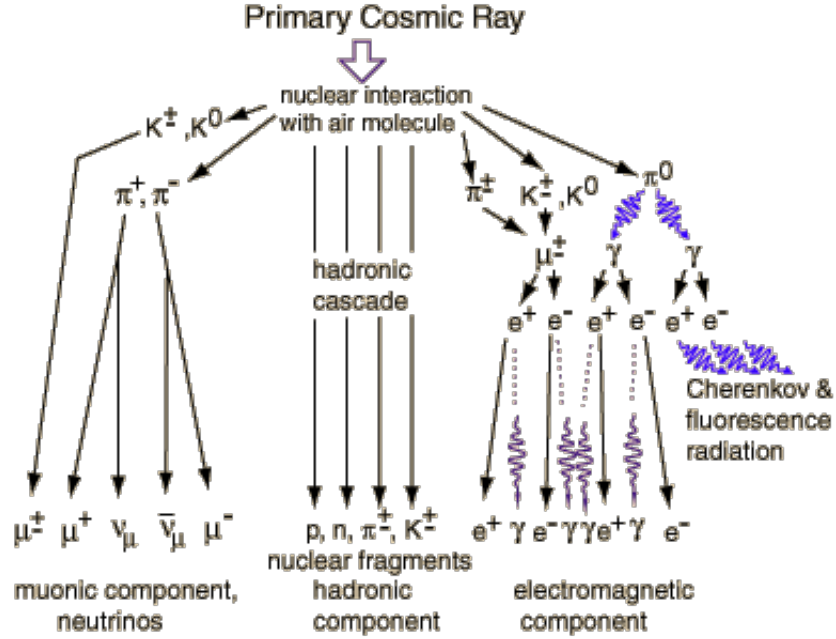


Figure 3.3: Schematic drawing of an hadronic cascade. The particles are grouped in electromagnetic (soft spectrum), muonic (hard spectrum) and hadron components. Adapted from Hyperphysics (2015).

and, thus, contribute to the soft component. If charged pions decay they produce muons with a lifetime 100 times longer than that of pions. Thus, e.g. a 1 GeV muon has a good chance to reach the Earth's surface. This muonic component of the hadronic shower consequently contains more particles at relatively high energies (above a few GeV) and is called the hard component. Muons decay into electrons and neutrinos via the channels

$$\mu^+ \rightarrow e^+ + \bar{\nu}_\mu + \nu_e, \quad (3.4)$$

$$\mu^- \rightarrow e^- + \nu_\mu + \bar{\nu}_e. \quad (3.5)$$

At ground level an air shower initiated by a 10^{15} eV (1 PeV) proton consists of roughly 80% photons, 18% electrons and positrons (soft component), 1.7 % muons (hard component) and 0.3% hadrons (hadronic component) (Kampert 2001). Overall, such a PeV proton produces 10^6 secondary particles (including photons). In general the composition of the air shower depends strongly on the height considered.

Electromagnetic Interactions In addition to strong interactions (inelastic scattering) and weak interactions (pion and muon decay) that were discussed previously also electromagnetic interactions play a role in the development of hadronic air showers. All charged particles lose energy via ionization. Electrons and positrons also produce bremsstrahlung and photons undergo pair production. Ionization losses most important for moderately relativistic charged particles other than electrons are described by the Bethe-Bloch formula (Landau 1944, Vavilov 1957). The ionization losses for positive muons are shown exemplarily in Figure 3.4. The energy loss depends on the mass and the energy of the particle. In practice, most relativistic particles (e.g. cosmic-ray muons) have a mean energy loss rate close to the minimum at $2 \text{ MeV cm}^2/\text{g}$ and are, thus, called minimal ionizing particles.

Bremsstrahlung occurs when an electron is accelerated in the Coulomb-Field of a charged nucleus when traversing matter. The energy at which bremsstrahlung becomes dominant depends strongly on the type of material (Chapter 32.4 in Olive et al. 2014 and references therein). For electrons bremsstrahlung becomes dominating in lead at 7 MeV and in air at 100 MeV. At energies above 100 GeV bremsstrahlung becomes also important for muons. The energy loss $\frac{dE}{dx}$ via bremsstrahlung is proportional to the distance x traveled

$$\frac{dE}{dx} = -\frac{E}{x_0}. \quad (3.6)$$

The energy of the particle after traveling the distance x is given by

$$E(x) = E_0 \cdot e^{-x/x_0}, \quad (3.7)$$

where x_0 is the radiation length giving the distance after which the electron has lost $1/e$ of its initial energy. For electrons in air the radiation length for bremsstrahlung is roughly $x_0 = 36.7 \text{ g/cm}^2$.

Both ionization and bremsstrahlung losses depend on the energy of the particle, the mass of the particle and the atomic number of the material. Ionization losses are proportional to $Z \ln(E)/m$ and bremsstrahlung losses are proportional to $Z^2 \cdot (E/m^2)$. The critical energy E_c

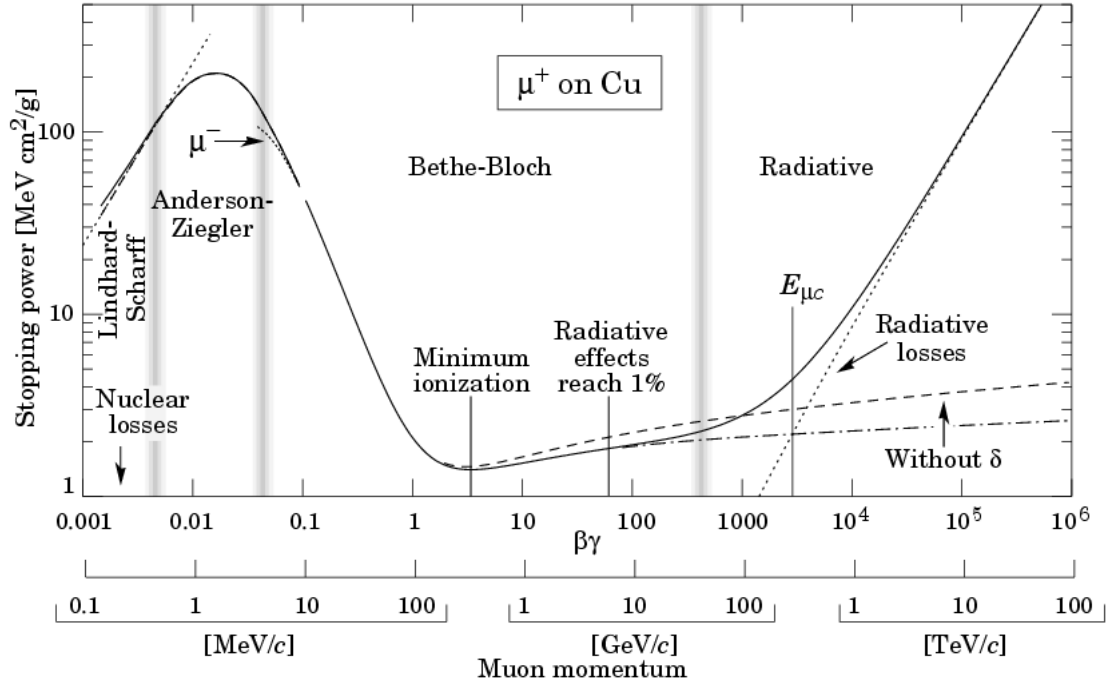


Figure 3.4: The energy loss for positive muons in copper in dependence on $\beta\gamma = E/m$ is shown over 12 orders in kinetic energy. The solid curves indicate the total stopping power. The Bethe-Bloch and radiative loss approximation regimes are indicated among others. Vertical bands indicate boundaries between different approximations. More details about the different approximation regimes can be found in Olive et al. 2014. The Figure is adapted from Figure 32.1 in Olive et al. (2014).

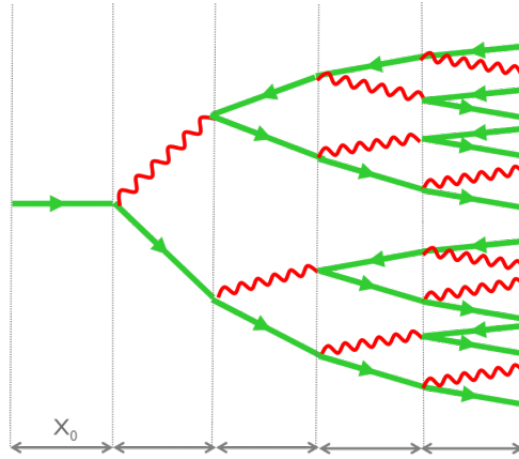


Figure 3.5: Simplified picture of the development of an electromagnetic cascade initiated by an electron. Adapted from <http://www.borborigni.org>.

is the energy at which both energy loss types become equally important. As mentioned, before this is 100 MeV for electrons in air.

During the shower development photons undergo three types of interactions. First, the photoelectric effect (Einstein 1905) where its total energy is transferred to an electron in the shell of an atom. Second, the Compton effect (Compton 1923), where the photon scatters elastically on a shell electron and transfers part of its energy to the electron. The last type is pair production where the photon converts into an electron-positron pair in the Coulomb field of an atomic nucleus (Bethe and Heitler 1934). For photons with energies larger than two times the electron mass ($2m_e$) the pair production process dominates. The mean free path for pair production is proportional to the radiation length of electrons ($9/7 x_0$).

Electromagnetic Air Showers Electromagnetic air showers are either initiated by a primary electron or photon or originate from the decay of neutral pions and are, thus, sub-showers of air showers initiated by hadrons. Bremsstrahlung and pair production processes are most important in the development of these electromagnetic cascades. The schematic development of such an electromagnetic shower is shown in Figure 3.5. A primary photon produces an electron-positron pair in the Coulomb field of an atomic nucleus. The electron and positron both produce bremsstrahlung and, thus, new photons which again produce an electron-positron pair. This process continues until ionization losses dominate over bremsstrahlung losses for all electrons. Thus, the maximum number of shower particles is given by $N_{\max} \approx E_0/E_c$, where E_0 is the initial particle energy and E_c the critical energy introduced above. In the simple Heitler model (Heitler 1944) it is assumed that on average two particles are produced over a splitting distance of roughly $s = \ln(2) x_0$, which is the distance after which an electron loses 1/2 of its energy via bremsstrahlung (Spurio 2015). Consequently, the number of particles in the shower is $2^n = E_0/E_c$, where n is the number of splittings. Thus, the depth of the shower maximum

t_{\max} is proportional to the logarithm of the fraction of the initial energy of the particle and the critical energy, which can be seen from

$$t_{\max} = x_0 \ln(E_0/E_c). \quad (3.8)$$

In comparison to hadronic showers gamma-ray (or electron) initiated showers are much more even and less broad, because the scattering on atomic nuclei produce much larger scattering angles than the radiation processes involved in electromagnetic cascades.

3.2.2 Cherenkov Light

In the atmosphere the charged shower particles emit Cherenkov light if they travel faster than the phase velocity of light in air (Čerenkov 1937). This effect is not only observed in air, but can in principle occur in every dielectric medium. The traversed medium (here air) is polarized by the charged particle and electromagnetic light is emitted. When the particle travels slower than the phase velocity of light in the medium the electromagnetic waves interfere destructively and no light is emitted macroscopically. If the particle is fast enough the electromagnetic waves of neighboring atoms cannot interfere destructively and a spherical wave is emitted. The Cherenkov light is emitted into a cone (analogous to the supersonic cone) along the track of the particle as shown in Figure 3.6. For the angle at which the light is emitted the following condition holds

$$\cos \varphi = \frac{c/n}{v} = \frac{1}{\beta n}. \quad (3.9)$$

Here, $v = \beta c$ is the speed of the particle, c/n the speed of light in the medium determined by the refraction index n and the speed of light in vacuum c . From $\cos \varphi < 1$ follows, that

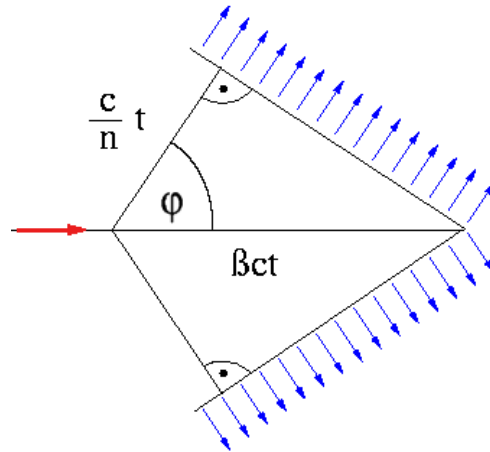


Figure 3.6: Schematic drawing of the Cherenkov cone. The wave front is indicated by blue arrows. The distance travelled by the particle $\beta c t$ and the light $\frac{c}{n} t$ and the opening angle of the Cherenkov light cone are shown. Adapted from (Horvath 2006).

Cherenkov light is only emitted if $1/n \leq \beta$. This results in a threshold energy for particles emitting Cherenkov photons, which is given by

$$E_{\min} = m_0 c^2 \left(\frac{1}{\sqrt{1 - 1/n^2}} - 1 \right). \quad (3.10)$$

Here, m_0 is the rest mass of the particle. For electrons the threshold energy is 20 MeV in air and 260 keV in water.

In the visible frequency range the spectrum is almost proportional to the frequency, so that most of the Cherenkov light is emitted in the ultraviolet. The atmosphere strongly absorbs ultraviolet radiation, so that the maximum intensity is observed at approximately 330 nm (blue light). The Cherenkov light is emitted into a cone of roughly 1° . Due to Coulomb scattering of electrons it is not emitted along a single axis but diffused over an area with a radius of approximately 120 m on the ground (Völk and Bernlöhr 2009). A flash of Cherenkov light lasts only a few nanoseconds.

3.3 The H.E.S.S. Telescope

3.3.1 Experimental Setup

The High Energy Stereoscopic System H.E.S.S. is an array of five Imaging Atmospheric Cherenkov Telescopes located in the Khoma Highlands of Namibia (Hofmann and H.E.S.S. Collaboration 2001) an area that was chosen due to the excellent optical quality. Phase-1 (H.E.S.S. I) of the experiment consisted of four identical telescopes that can be pointed at any position in the sky using a mount consisting of a base frame rotating around a vertical axis and carrying the dish, which rotates around the elevation axis (altazimuth mount). The telescopes are equipped with Davies-Cotton reflectors (Davies and Cotton 1957) with a flat-to-flat width of 13 m (Bernlöhr et al. 2003). The mirror is divided into 382 round segments and has a total mirror area of 108 m². Due to its excellent reflectivity aluminized glass mirrors were employed. Each of the mirror facets can be aligned by two actuators. The optics lead to a point spread function (PSF) with a width of 0.4 mrad at the camera center (radius containing 80% of the light, Cornils et al. 2003). Each telescope has a camera (Vincent et al. 2003) mounted at a focal length of 15 m. Each camera consists of 960 photomultipliers (PMTs) with a hexagonal pixel size of 42 mm (equivalent to 0.16°). The camera provides a field of view of 5° on the sky. 16 PMTs are packed in one drawer, which also contains the electronics for signal storage, signal digitalization, triggering and readout. The four telescopes are placed in a square with a side length of 120 m. Figure 3.7 shows a H.E.S.S. I telescope including the mirrors, camera and the supporting steel space frame. This array of four 13 m telescopes has been fully operational since December 2003 and was inaugurated in September 2004.

In order to lower the energy threshold (down to 15-25 GeV), to improve the sensitivity at low energies and the reconstruction quality at high energies (typical H.E.S.S. I energies) a fifth, larger telescope, called CT5, was built in the center of the original array (Punch et al. 2005). The new array consisting of four small and one large telescope is called H.E.S.S. II and was inaugurated in September 2012. The large telescope is equipped with a reflector of parabolic shape with a size of 32.6 m by 24.3 m. The mirror consists of 875 hexagonal facets and has a total area of 614 m². The alignment technique is the same as for the H.E.S.S. I telescopes. The PSF of CT5 is also comparable to the one of the small telescopes (Abramowski 2015). The camera is mounted at a focal length of 36 m and consists of 2048 PMTs. It provides a field of view of 3.2°. The PMTs are again packed into drawers of 16 containing the corresponding electronics. A close up picture of CT5 is shown in Figure 3.8. The complete H.E.S.S. II array is shown in Figure 3.9 illustrating the large difference in size between the large telescope and the small telescopes.

For more details on the design of the H.E.S.S. telescopes see Bernlöhr et al. (2003) for the H.E.S.S. I layout and components, Cornils et al. (2003) for the mirror alignment and the point spread function, Funk et al. (2004) for the trigger system and Punch et al. (2005) for the layout of the H.E.S.S. II telescope.

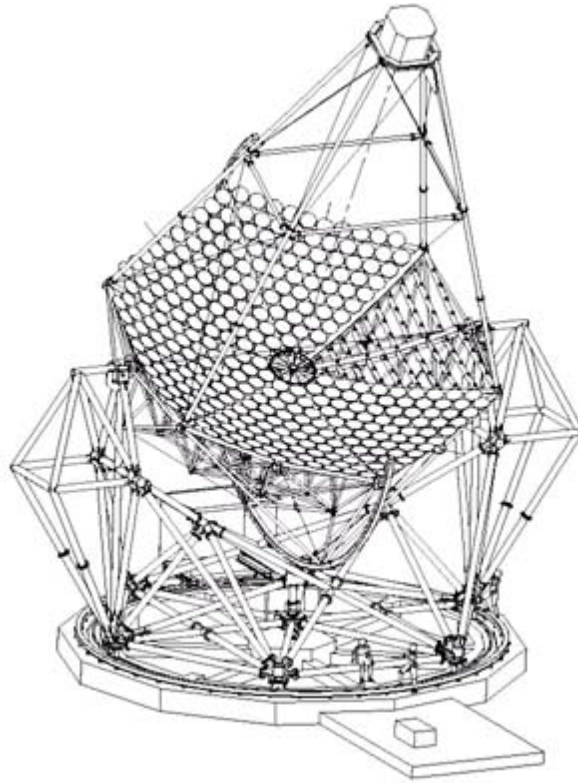


Figure 3.7: H.E.S.S. telescope showing the steel space frame of the dish and the telescope mount. Also the round mirror facets, the Davies-Cotton reflector design and the camera are shown. Mirrors are removed in one section of the dish to view the support beams. Adapted from Bernlöhr et al. (2003).



Figure 3.8: Large central telescope (CT5) showing the steel space frame of the dish and the telescope mount. Also the hexagonal mirror facets, the parabolic reflector design and the camera are shown. Picture was taken by Christian Föhr, MPIK.

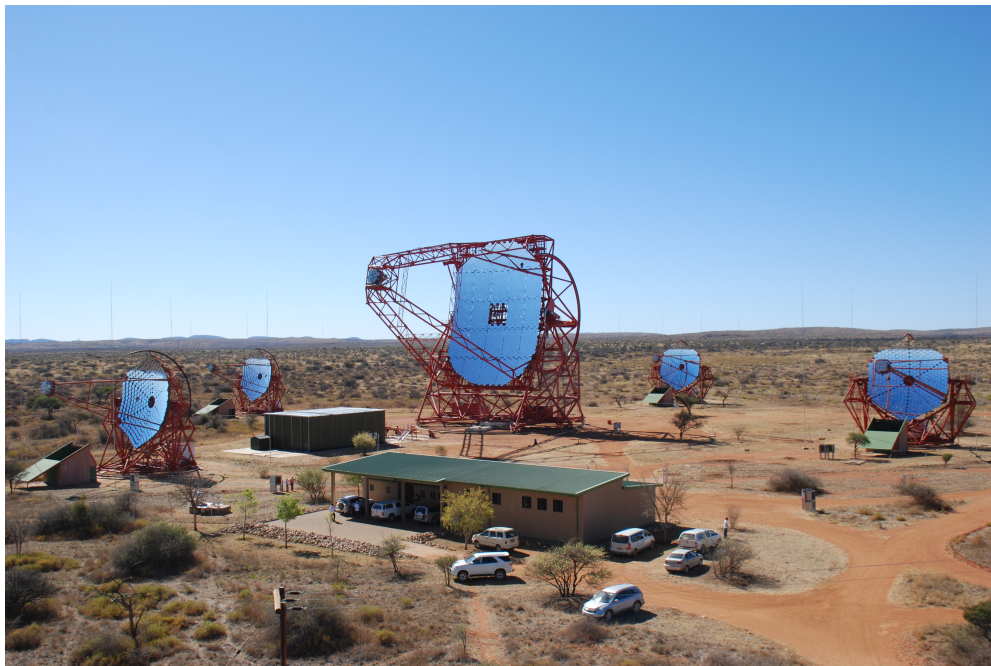


Figure 3.9: The complete H.E.S.S. II telescope array. All five telescopes are shown. Picture was taken by Christian Föhr, MPIK.

3.3.2 The Trigger System

The trigger system of the H.E.S.S. telescopes was designed in order to take advantage of the stereoscopic nature of the array (Funk et al. 2004). Typically, the rate at which a single Cherenkov telescope triggers is dominated by background events (hadrons and muons) because those are much more numerous than gamma events. In a stereoscopic system this background is reduced at the trigger level by requiring that an event triggers at least two telescopes. This requirement reduces the coincident triggers due to the night sky background (NSB) and almost completely removes muon triggers. For this reason H.E.S.S. uses a two level trigger system, with a local trigger for each telescope and a central trigger for identifying coincidence events.

Local trigger: The pixels in each H.E.S.S. camera are divided into overlapping sectors each containing 64 pixels. The camera is triggered if a certain number M (sector threshold, usually between 2-4) of pixels within a sector exceed a threshold of N photoelectrons (p.e.) (pixel threshold, e.g. 4 p.e.) within a 1.3 ns time window. Both, sector and pixel threshold are programmable. The signals from the PMTs are sampled by 1 GHz Analogue Ring Samplers. When a camera trigger occurs the sampling is stopped and the ring buffer content is digitized within a 16 ns time window around the signal. The length of the time window is also programmable.

Central Trigger System (CTS): In the central trigger system the coincidence decision is made. If a telescope triggers another trigger from a second telescope must occur within 80 ns otherwise a reset signal is sent to the telescope. If this requirement is met the CTS assigns a unique system wide event number to the event and distributes it to all telescopes. Each camera connects the event number with the corresponding pixel data for building a system event. After including the larger H.E.S.S. II telescope this trigger requirement has been modified, so that also events, where only the large telescope triggered, are recorded in order to provide a minimal energy threshold.

3.3.3 Data Acquisition

Data are taken with the H.E.S.S. telescopes in runs of 28 minutes (Aharonian et al. 2006). Usually the telescopes do not point directly at the source but are operated in *Wobble* mode meaning that the telescopes point to a position with a little offset from the source. Thus, it is possible to use the parts of the field of view that do not contain the source but have the same distance to the camera center for background subtraction. By using these regions systematics are reduced that originate from a radial drop of the acceptance in the camera. In order to further reduce systematics the direction of the *Wobble* offset relative to the source region is varied between different runs. Often the offset direction is mirrored between consecutive runs. The region around a (potential) source is called *ON* region, because this is the region expected to contain a signal. Regions with the same distance to the camera center that are used for background determination are called *OFF* regions. The *ON* region is usually circular, while the shape and exact positions of the *OFF* regions depend on the background subtraction method employed. Figure 3.10 shows the *ON* region (blue) and the corresponding *OFF* regions (green) exemplarily for the reflected region background method (Berge et al. 2007). In this method

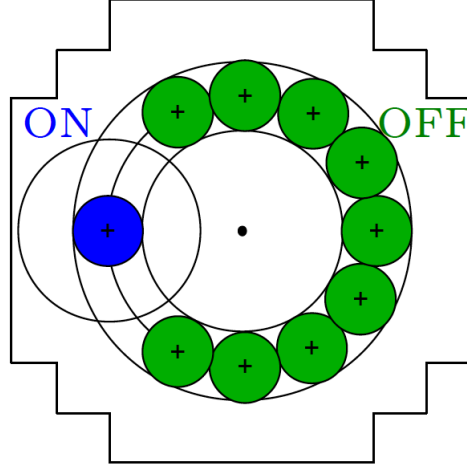


Figure 3.10: Schematic drawing illustrating the reflected region background estimation method. The *ON* region containing the potential source is colored blue, while the *OFF* regions are colored green. Adapted from Jahn (2013).

multiple *OFF* regions of the same shape and distance to the observation position as the *ON* region are defined. They are placed in a ring around the observation position, but at a certain safety distance to the *ON* region.

3.3.4 Data Analysis Method: Direction and Energy Reconstruction

For the analysis of H.E.S.S. data different methods have been developed by the H.E.S.S. collaboration. The classical method uses the Hillas technique calculating the moments of the camera images (Hillas 1985, Aharonian et al. 2006). The second most established method is based on a semi-analytical shower model and called Model++ analysis. It was developed by de Naurois and Rolland (2009). Other methods are also used including a 3D Model analysis, where the shower is modeled as a Gaussian photosphere in the atmosphere leading to a three dimensional generalization of the Hillas parameters (Lemoine-Goumard et al. 2006). Some methods use output parameters from Hillas or Model++ analysis and combine them with a *Boosted Decision Tree* (BDT) approach, e.g. Ohm et al. (2009), where the TMVA multivariate analysis package is used (Hoecker et al. 2007). In this study Model++ is used and described in Section 5.1.2, while some of the data used for cross checking the results of this study were analyzed with the Hillas technique combined with a BDT.

Every data analysis with H.E.S.S. requires the following steps. The data must be calibrated, meaning that the measured analogue to digital converter (ADC) counts must be translated to

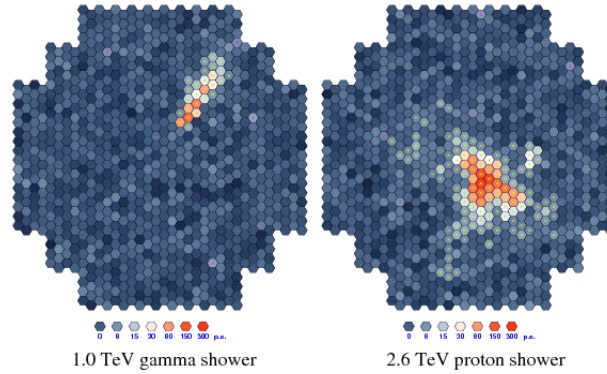


Figure 3.11: Camera images of a gamma ray shower of 1 TeV (left-hand panel) and a proton shower of 2.6 TeV (right-hand panel). Adapted from Völk and Bernlöhr 2009.

image amplitudes in photoelectrons (p.e.). For this purpose the pedestal (base line level of ADC counts in the absence of Cherenkov light) and the conversion factor between ADC counts and pixel charge in photoelectrons must be determined. Further, differences between optical and quantum efficiencies of the PMTs must be accounted for (flat-fielding). Afterwards, the parameters of the primary incoming event must be reconstructed. This is done by reconstructing direction, energy, impact distance and sometimes also other parameters of the air shower (and consequently of the primary particle) from the camera image of the Cherenkov light emitted by the particle shower.

The H.E.S.S. telescopes were designed to detect gamma rays, but not only gamma rays produce air showers and Cherenkov light, but also muons, electrons and hadrons. Muons do not initiate an air shower (at least this is extremely unlikely) and can be seen as rings or fragments of rings in the camera. These ring fragments look very similar to gamma-ray showers. However, muon events usually trigger only one telescope and are removed from the data by the requirement that at least two telescopes must trigger. Hadrons usually produce much broader images in the cameras than gammas as shown in Figure 3.11. Nevertheless, hadronic showers can have a large fraction of electromagnetic sub-showers (soft component) so that they can also produce camera images very similar to the image of a gamma-ray initiated shower. Thus, in the last step the analysis must provide parameters that can be used for separating gamma events from hadronic background events. In the following the basic principles of direction and energy reconstruction with H.E.S.S. will be explained exemplarily using the standard Hillas method. The Hillas method is the most simple and illustrative method. In Section 5.1.2 the advanced reconstruction technique Model++ is also discussed in detail, because it is used in this study.

Calibrating the Camera

Before the parameters of the air shower can be reconstructed the PMTs and the electronic response must be calibrated (Aharonian et al. 2004). The PMT signal is measured across a

resistor and amplified into acquisition channels. The low-gain channel detects charges between 15 and 1600 p.e. and the high-gain channel detects charges between 1 and 200 p.e. After the analogue signal from the PMTs has been amplified it is sampled in an Analogue Ring Sampler (ARS) at a rate of 1 GHz. Finally, the signal is converted by an Analogue to Digital Converter to digital counts (ADC counts), so that for every pixel two ADC count values are stored (one for the low-gain channel and one for the high-gain channel).

Standard Cherenkov analysis requires the signal amplitude per camera pixel. This signal is the charge induced by light on every PMT corrected by differences between the pixels due to varying optical and quantum efficiencies and variations of the amplification of the signal within the PMTs. Thus, the number of ADC counts must be translated into the valid signal amplitude measured in photoelectrons. Therefore, besides the measured number of ADC counts three additional quantities must be known. These three quantities are explained below.

Pedestal The pedestal P is the mean number of ADC counts recorded in a pixel in the absence of a signal (baseline level) due to electronic noise and the night sky background (NSB). The pedestal due to electronic noise (dark pedestal) is Gaussian and can be obtained for every channel by measuring the ADC distributions in the absence of background light (all lids of the camera are closed).

During observations, the NSB contributes to the pedestal and modifies the shape of the pedestal ADC count distribution. The distribution depends on the level of NSB. At small NSB frequencies possibly no NSB photoelectron arrives within the 16 ns integration window. The pedestal ADC count distribution exhibits a negative shift relative to the dark pedestal distribution (larger absolute value), while the pedestal shape and width remain similar to the dark pedestal values.

At higher frequencies, e.g. 50 MHz, one or more photoelectrons are contained or partially contained in the integration window. The number of photoelectrons contained in the integration window follows a Poisson distribution resulting in an asymmetric pedestal shape. The shape of the pedestal is a superposition of a rise and a peak at the position of the shifted dark pedestal followed by a smeared single-photoelectron peak and a tail towards higher values.

At even higher NSB frequencies, well above 100 MHz, the pedestal distribution is dominated by NSB photoelectron peaks and is, thus, much broader, but again Gaussian. The width of this distribution is determined by the mean number of NSB photoelectrons (except small corrections for the electronic noise, the width of the single-photoelectron amplitude distribution and the effect of photoelectron signals truncated by the integration window).

Since the overall pedestal depends on the temperature of the camera and the level of the NSB it must be determined for every observation run if possible. For the determination only the pixels not belonging to the shower image are used. The pedestal is calculated separately for both acquisition channels.

Conversion Factor The conversion factor¹ between ADC counts and the signal charge in units of photoelectrons γ_e^{ADC} includes the PMT gain, the signal amplification in both readout channels and the integration of the signal in the Analogue Ring Sampler (ARS). It is determined

¹The conversion factor is sometimes also slangily called gain as for example by Aharonian et al. (2004).

roughly every two days by illuminating each camera with an LED pulser with an intensity of approximately one photoelectron in each pixel. In the measured ADC count distribution a peak originating from the single photoelectron can be clearly identified. For each pixel the measured ADC count distribution is fit by the theoretical ADC distribution fit function. In the theoretical model the number of photoelectrons follows a Poisson distribution, the single photoelectron distribution is described by a Gaussian and the electronic pedestal is also approximated by a Gaussian. Consequently, the light distribution of a given signal of n photoelectrons is described by a Gaussian with a standard deviation of $\sqrt{n} \sigma_{\gamma_e}$, where σ_{γ_e} is the root-mean-square (RMS) of the charge induced by a single photoelectron, and a mean position in ADC counts $P + n \gamma_e^{ADC}$, here P is the electronic pedestal. The conversion factor γ_e^{ADC} is one of the free parameters of this fit and the best-fit value is used for each pixel. This procedure is solely followed for the high gain channel, because only the high gain channel is sensitive to single photoelectrons. The conversion factor for the low gain channel is given by the amplification ratio between the high gain and the low gain channels (HG/LG) and the conversion factor of the HG channel. Thus, it is given by $\gamma_{e,LG}^{ADC} = (LG/HG) \gamma_{e,HG}^{ADC}$.

Flat-Fielding The flat-fielding coefficient FF is used to correct the above mentioned difference between the pixels due to varying optical and quantum efficiencies. This is done by comparing the relative efficiency of the considered pixel to the mean efficiency of the whole camera. The FF coefficients are determined in special flat-fielding runs roughly every two days. In these runs LED flashers illuminate the cameras uniformly in short pulses with a wavelength around the PMT peak quantum efficiency. The FF coefficients are calculated by comparing the pixel amplitudes without flat-fielding to the mean amplitude of the camera. The efficiency of the pixel is given by the ratio of the pixel amplitude and the mean amplitude over the whole camera. The mean of the inverse of this ratio for this pixel over the whole run is used as the final flat-fielding coefficient FF .

The final pixel amplitude for each channel is calculated as follows

$$A_i = \frac{ADC_i - P_i}{\gamma_{e,i}^{ADC}} \cdot FF, \quad (3.11)$$

where the ADC counts, the pedestal and the conversion factor depend on the chosen acquisition channel $i = (LG, HG)$. The conversion factor of the LG channel is calculated from the conversion factor of the HG channel as shown above.

Hillas Reconstruction Technique

The Hillas reconstruction technique is based on reducing the image properties into a few parameters, reflecting the modeling of the image by a two-dimensional ellipse (Hillas 1985). Before calculating the parameters of this ellipse the camera pixels that actually belong to the shower image must be identified in order to remove pixels that only contain NSB. During this cleaning procedure only pixels are kept where the pixel itself contains more than k p.e. and a neighbor pixel more than j p.e., usually $k = 5$ and $j = 10$ (Aharonian et al. 2006). The shape of the leftover image pixels approximates an ellipse, while the images of hadrons are much wider and more uneven.

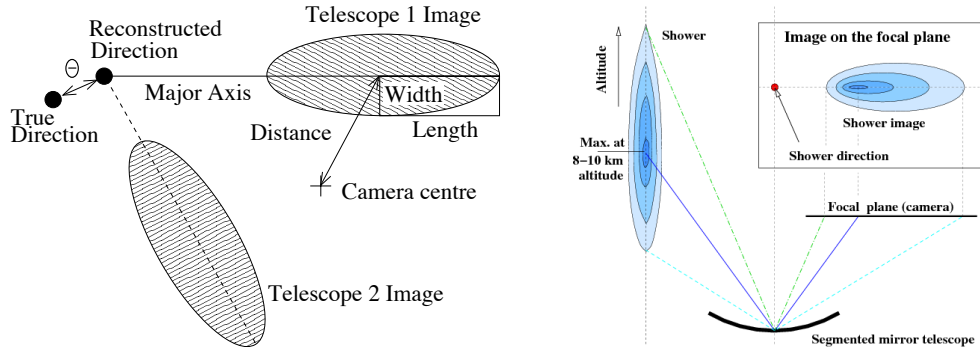


Figure 3.12: Left: Schematic drawing of the Hillas reconstruction technique. The superimposed ellipses from two telescopes are shown. The width and length of the Hillas ellipse are illustrated. Additionally, the camera center, the major axis and the reconstructed direction are shown. Figure adapted from Aharonian et al. (2006). Right: Shower imaging by a Cherenkov telescope. The shower ellipse is reflected by the mirrors of the telescope into the focal plane of the camera. Despite some asymmetry, the shower image has the shape of an ellipse. The direction of the shower is located on the extension of the major axis of the ellipse. Adapted from Völk and Bernlöhr (2009).

The Hillas parameters illustrated in the left-hand panel of Figure 3.12 are calculated from the image. This includes the **length** and the **width** of the shower, the distance of the center of gravity of the ellipse to the camera center (**nominal distance**) and the **orientation** of the image in the camera coordinate system. Further, the **image size**, which is the sum over the charges of all pixels left after image cleaning, is needed. These parameters are first extracted individually for every telescope that triggered (two to four).

Direction Reconstruction With H.E.S.S. the **direction** of each event is reconstructed using stereoscopy. The major axis of the ellipse is basically an image of the shower axis. Thus, it points in one direction towards the image of the source (the direction where the primary event came from) and in the other direction towards the point where the shower axis intersects the plane of the telescope dish (Hofmann et al. 1999). The direction of the event is retrieved by first superimposing the images of the shower taken by two different cameras and then intersecting the major axes. In the most simple method the intersection point of the two major axes gives the direction of the primary particle estimated from these two images. The intersection points of all possible pairs (up to six if all four telescopes have triggered) is calculated and averaged. With this method the quality of the images is not taken into account. The algorithm is improved by taking the error ellipse on the center of gravity and the error on the image orientation for every camera image into account. Employing these errors an error ellipse for the image of the source can be calculated. Additionally, other methods exist that for example take the quality of the images into account (Hofmann et al. 1999). The location of the center of the Cherenkov light pool, which corresponds to the projected impact point of the original particle track on the ground (also called shower core location), is obtained by

intersecting the image axes, projected into the plane perpendicular to the system observing direction. An angular resolution of 0.1° to 0.2° is obtained.

Energy Reconstruction For a given **energy** of the primary particle, the measured image size depends on the impact parameter² and the zenith angle. Monte Carlo simulations are used to estimate the energy of the primary particle $E_{\text{reco}}(IP, s, z)$ in dependence on the impact parameter IP , the image size s and zenith angle z so that the corresponding energy is obtained from look-up tables containing these information. The energy of the shower is given by the weighted average of the energy reconstructed for each telescope. The error on the energy obtained by this method E_{reco} is given by $\Delta E = (E_{\text{reco}} - E_{\text{true}})/E_{\text{true}}$, where E_{true} is the true energy of the particle. The expectation value of ΔE is called energy bias and increases towards lower energies. Usually, only the energy range, where the energy bias is smaller than 10% is used. The energy resolution is given by the width of the ΔE distribution and is around 20% for the Hillas analysis (Aharonian et al. 2006).

Gamma-Hadron Separation The Hillas parameters are not only used for reconstructing the energy and direction of the primary particle. They are also employed for distinguishing between showers that have been initiated by gamma rays, which H.E.S.S. wants to measure, and hadrons, which constitute an unwanted background contamination. Thus, a parameter for classifying the events into gamma-like or hadron-like events is needed. Parameters based on the width (and possibly length) of the shower are defined and called mean reduced scaled width and mean reduced scaled length (MRSW or MRSWL). These are calculated by comparing the measured value of the parameter (e.g. the width) to the parameter value expected from Monte Carlo simulations and normalizing it to the uncertainty obtained in these simulations. For the width w of the image the RSW is defined as

$$RSW = \frac{w - \langle w \rangle}{\sigma_w}. \quad (3.12)$$

Here, $\langle w \rangle$ is the mean value of the width obtained from MC simulations and σ_w the corresponding scatter. Both quantities depend on the impact parameter, the image amplitude and the zenith angle of the observation and are stored in look-up tables. The MRSW is obtained by averaging the RSW values of all telescopes. This parameter is finally used for gamma-hadron separation.

Figure 3.13 shows the expected distributions of the MRSW for gamma rays and protons obtained from simulations (left-hand panel). As expected from the definition of the MRSW the distribution for gammas follows closely a Gaussian and is centered around zero. The MRSW distribution of a simulated proton exhibits a very different behavior with much larger MRSW values. Additionally, a distribution of the MRSW from an *OFF* region (region in the FOV without a source see Section 3.3.3) is shown. The proton and *OFF* distributions are very similar. In the right-hand panel of Figure 3.13 the MRSW distribution of the Crab nebula

²The impact parameter is the projected (perpendicular) distance of the extrapolated shower track to a telescope (Aharonian et al. 2006). It is calculated as the perpendicular distance between a line (track) and a point (telescope) in space.

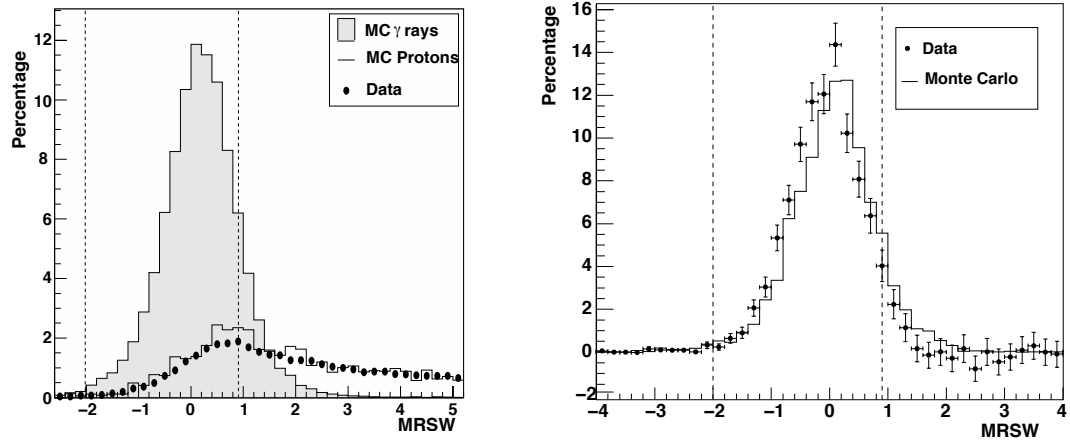


Figure 3.13: Left: Distribution of the MRSW from gamma-ray MC simulations (gray histogram) compared to the MRSW distribution from proton MC simulations (white histogram) and data obtained from an *OFF* region (black markers). Right: Distribution of the MRSW from gamma-ray MC simulations (white histogram) compared to the MRSW distribution of the Crab Nebula signal region after applying selection cuts (including MRSL cut, but not MRSW) and subtracting the background. Adapted from Aharonian et al. (2006).

signal region after background subtraction and application of selection cuts (cuts including a cut on the MRSL but not on the MRSW) is shown. The MRSW distribution of the source data behaves very similar to the MC gamma-ray distribution. In the H.E.S.S. standard Hillas reconstruction usually cuts on the MRSW and MRSL are applied.

Chapter 4

Statistical Basics

4.1 Data Modeling

In physics reality is described by simplified models of the measured data. The question is: Which model is correct? Or in other words: Which model explains the data best? A model usually contains adjustable parameters, which are varied until the parameter set is found describing the data in the best possible way. The figure-of-merit function (also called merit function or function of merit) is a measure of how well a certain model (particular choice of parameters) describes the data (Press et al. 2002). It reduces the data and the model to a single numerical value from which the ability of the model to describe the data is judged (goodness-of-fit). Usually small values of this function correspond to a good agreement between model prediction and measured data. Larger values usually indicate that the model does not explain the data. The *best-fit* model is the model with the parameter set leading to the minimum value of the merit function. The process of finding these *best-fit* parameters is a minimization problem in many dimensions. There are several different possibilities of choosing the merit function and the appropriate choice often depends on the requirements the different methods set on the data and the distribution the random variable follows. In the following the two methods used in this study are summarized.

4.1.1 χ^2 -Fitting

One of the many applications of χ^2 statistics is in the context of finding the best-fit parameters of a model. The χ^2 function used as merit function is defined as

$$\chi^2 = \sum_{i=1}^m \frac{(Y_i - y_i(X_i, a_1, \dots, a_k))^2}{\sigma_i^2}. \quad (4.1)$$

The χ^2 is a bias free estimator, which minimizes the variance. Here, X is the independent variable and Y the dependent and random variable. The measured data points are given by (X_i, Y_i) and the standard deviation σ_i of Y_i is known. The size of the data sample (number of data points) is m . The χ^2 value is determined by the squared difference between the measured value Y_i of the random variable and the value predicted by the model $y_i(X_i, a_1, \dots, a_k)$. The

a_j are the k free parameters of the model. The parameter set leading to the minimum χ^2_{\min} is the best-fit parameter set ($a_{1,\text{best}}, \dots, a_{k,\text{best}}$). The χ^2 is χ^2 -distributed with $m - k$ degrees of freedom (*d.o.f.*). From this distribution the probability p that χ^2 exceeds a certain value of χ^2 by chance, even if the model is correct can be calculated. This p -value is a measure of the goodness-of-fit (this is very similar to hypothesis testing described in Section 4.2.). If the p -value is very small the model is wrong or assumptions made about errors were wrong. As a rule of thumb a reduced chi-square $\chi^2/d.o.f. = 1$ is a good fit, because in this case the difference between measured value and predicted value is on average one standard deviation and the p -value is always ≥ 0.3 .¹ The disadvantage of using χ^2 -fitting is that it is only applicable if the random variables are normally distributed. Otherwise it can still be used to simply compare the values of the data and the model prediction for a quick first estimate, but the p -values will be incorrect.

The matrix of second derivatives of the model function with respect to the free parameters of the model is called Hessian H_{jl} . It measures, evaluated for all data points, how the model responds to changes in parameters (see e.g. Chapter 15.4 in Press et al. 2002). The Hessian matrix is given by

$$H_{jl} = \sum_{i=1}^m \left(\frac{\partial y}{\partial a_j} \frac{\partial y}{\partial a_l} \right) / \sigma_i^2. \quad (4.2)$$

The errors on the best-fit parameters are given by the square root of the diagonal elements of the inverse of the Hessian matrix $\mathbf{C} = \mathbf{H}^{-1}$, called covariance matrix, which is evaluated at the minimum. The off-diagonal elements C_{jk} are the covariances between a_j and a_l and contain information about the correlations/ dependencies between the parameters. The errors are only reliable when the best-fit function gives a good fit to the data.

Is the model function y a linear combination of M specified functions of x (linear model: $y_i = \sum_j a_j f_j(x_i)$) the minimum and the covariance matrix can be calculated analytically. In the none-linear case finding the best-fit parameters and the covariance matrix is an iterative process starting from approximate parameters.

4.1.2 Log-Likelihood-Fitting

χ^2 -fitting is a quick and intuitive method of fitting data. The drawback is that the p -values are not reliable, when the data are not normally distributed. A more general approach is to define a likelihood via the underlying probability distribution $P_i(y_i = Y_i | a_1, \dots, a_k)$, which gives the probability that the value Y_i is measured if the real value is given by the model $y_i(a_1, \dots, a_k)$. The overall probability to measure the random variable data set Y_i for a given model $y(x_i, a_1, \dots, a_k)$ is

$$L = \prod_{i=1}^m P_i(y_i = Y_i | a_1, \dots, a_k). \quad (4.3)$$

¹Careful: This statement is true for high *d.o.f.*, if the reduced χ^2 is exactly 1. But for high *d.o.f.* e.g. *d.o.f.* = 100 a reduced χ^2 of 2 already corresponds to a p -value of $< 10^{-5}$, while for 1 *d.o.f.* a χ^2 of 2 corresponds to a p -value of 0.16. Thus, for high *d.o.f.* a good fit is only given, if the reduced χ^2 is almost exactly 1.

The model fitting the data best corresponds to the parameter set where L reaches its maximum. Often the negative logarithm of the likelihood is used, because the parameter set maximizing the likelihood function also minimizes the negative logarithm of the likelihood function, but it is much easier to find the minimum of an additive function:

$$-2 \ln L = -2 \sum_{i=1}^m \ln(P_i(y_i = Y_i | a_1, \dots, a_k)). \quad (4.4)$$

This function is minimal for exactly the same parameter set that gives the maximum of the likelihood. For normally distributed random variables this treatment leads to a value for $-2 \ln L$, which is identical to the χ^2 defined above. Thus, χ^2 fitting is simply a special case of *log*-likelihood fitting.

4.1.3 Confidence Intervals and Upper Limits

Previously, the best-fit parameter set has been found $(a_{1,\text{best}}, \dots, a_{k,\text{best}})$. However, these are not the true parameter values $a_{j,\text{true}}$ but the ones resulting from one experimental realization of the data set. If the experiment was repeated many times many different realizations of the data set and, thus, of the best-fit parameters would be found. For simplicity let's assume that the model has only one free parameter for now. The best-fit parameter is $a_{1,\text{best}}$ and the true value of the parameter is $a_{1,\text{true}}$. The probability to find a best-fit parameter a_1 in an experimental realization is determined by the probability density function $f(a_1, a_{1,\text{true}})$ giving the probability that the best-fit parameter a_1 is found if the true value is $a_{1,\text{true}}$ ². In reality the true value of the parameter and often also the probability distribution are unknown. Thus, it is assumed that the experimentally measured best-fit parameter $a_{1,\text{best}}$ is a bias free estimator of the true value. The probability that the true value of the parameter is located in an interval $a_{1,L} < a_{1,\text{true}} < a_{1,H}$ (James 2006) is determined by the probability density function $f(a_1, a_{1,\text{best}})$ and given by

$$P(a_{1,L} < a_{1,\text{true}} < a_{1,H}) = \int_{a_{1,L}}^{a_{1,H}} f(a_1, a_{1,\text{best}}) da_1 = \beta. \quad (4.5)$$

Here, a_1 are the possible parameter values of the free parameter. β resembles the probability content of the probability density distribution between the two boundary values $a_{1,L}$ and $a_{1,H}$ and, thus, the probability that the true value of a_1 is located between $a_{1,L}$ and $a_{1,H}$. This definition is also illustrated in the left-hand panel of Figure 4.1. The larger β is chosen the more likely it is that the true value is actually contained in the interval. In practice first the probability content β is chosen and then confidence limits $a_{1,L}$ and $a_{1,H}$ are determined correspondingly. In practice 68.3 % (1 σ), 95.4 % (2 σ) and 99.73 % (3 σ) are commonly used for β . The concept of confidence intervals can be translated to the more general case of many free parameters. Neither in the simple case with one free parameter nor in the more complicated with many free parameters the shape of the confidence region is unique. E.g. in the simple one-dimensional case a line segment can be shifted somewhat to the left and to the

²Instead the probability density distribution f' of the difference between $a_1 - a_{1,\text{true}}$ could be examined. This translation would only move the true value to the origin.

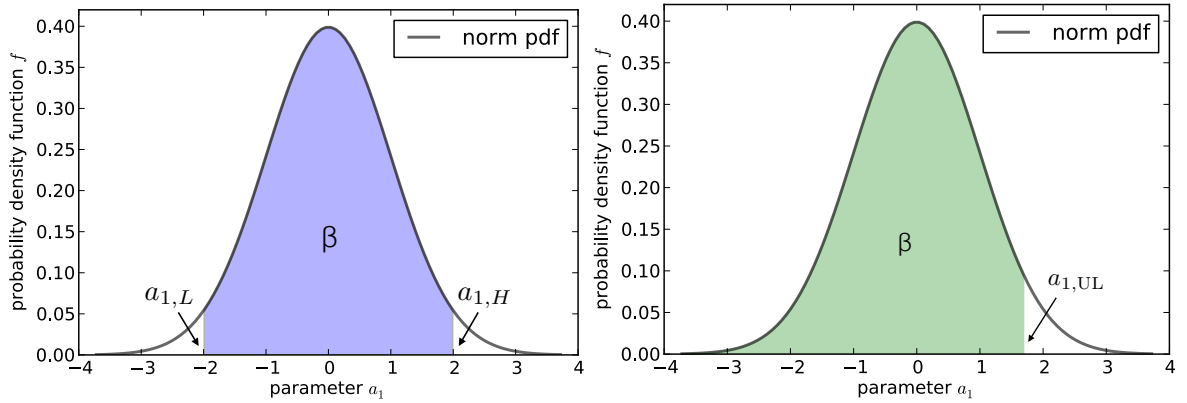


Figure 4.1: An example probability density function is shown. For illustration a normal distribution is used. In the left-hand panel the definition of the confidence limits in a one-dimensional parameter space is illustrated. The blue colored area under the curve illustrates the symmetric confidence limits between which the probability content β is contained. The parameter values at the boundary $a_{1,L}$ and $a_{1,H}$ are also illustrated. In the right-hand panel the definition of upper limits in a one-dimensional parameter space is illustrated. The green colored area under the curve illustrates the area where the probability content β (same as in the left-hand panel) is contained. The upper limit on the parameter a_1 is also illustrated.

right of the best-fit parameter value and overall still contain the chosen probability content β . Since confidence limits are defined to inspire confidence in the measured value of the best-fit parameter in the simple one-dimensional case the chosen line segment is centered on the measured value.

In the multidimensional case ellipses or ellipsoids are most frequently used. In the case of a χ^2 fit the choice of the boundaries for the confidence limits is natural. The χ^2 for the best-fit parameters $a_{i,\text{best}}$ is minimal (χ_{best}^2). Varying the parameters a_j away from the best-fit parameters the χ^2 increases. The value $\Delta\chi^2(a_j) = \chi^2(a_j) - \chi_{\text{best}}^2$ is χ^2 distributed with M d.o.f. Here, M is the number of free parameters that are varied. Thus, a fixed $\Delta\chi^2$ value defines an M -dimensional confidence region containing the chosen probability content β . Is a confidence level chosen for example 95.4% and the number of free parameters is for example 2, the corresponding $\Delta\chi^2$ value is 6.17. Thus, 95.4% of measurements will find best-fit parameters that correspond to a $\Delta\chi^2$ smaller than 6.17. In a multidimensional parameter space the parameter limits are not only two values as in the one-dimensional case but are $(M-1)$ -dimensional planes in the M -dimensional parameter space. Since $(M-1)$ -dimensional planes are difficult to illustrate often only a subset of ν parameters is considered. In that case, the confidence regions are the projections of the M -dimensional regions defined by fixed $\Delta\chi^2$ into the ν -dimensional parameter space.

Instead of using central confidence intervals also upper limits or lower limits are sometimes used. These are extreme none-central intervals where one of the boundaries is set to $-\infty$ or $+\infty$. Upper limits are e.g. often used when a parameter value cannot be negative and is

relatively close to zero. The upper limit in one dimension (see e.g. James 2006) is given by the following formula

$$P(a_{1,\text{true}} < a_{1,\text{UL}}) = \int_{-\infty}^{a_{1,\text{UL}}} f(a_1, a_{1,\text{best}}) da_1 = \beta. \quad (4.6)$$

In this case, the probability that a measured value of a_1 is smaller than $a_{1,U}$ is given by β . The definition of the upper limit is illustrated in the right-hand panel of Figure 4.1. The $\Delta\chi^2$ distribution can be used to set an upper limit on a parameter analogous as done in the case of confidence intervals.

4.2 Hypothesis Testing

The major question after obtaining the result of measurement is whether this result is really significant or occurred just by chance. The most common approach is to test a null hypothesis (corresponding to a null result) against an alternative hypothesis (corresponding to the measurement of a signal). This study is dedicated to the search for an anisotropy in the arrival direction of cosmic-ray electrons, so the null hypothesis would be

- H_0 = Electrons are arriving isotropically at Earth.

The alternative hypothesis is given by

- H_1 = Electrons are arriving anisotropically and are better described by a dipole model.

The second ingredient is a test statistic TS , which reduces the data set to a single numerical value and measures how well either hypothesis fits to the data. The probability of measuring a certain value of the TS for a null result (H_0 is true) is given by the probability distribution/probability density function $p(TS)$ of the TS (example for a χ^2 test statistic in the left-hand panel of Figure 4.2). If the measured TS lies well within this distribution the measured value is compatible with the null hypothesis. The more interesting case occurs when the measured TS value is rather large (less compatible with null). Here, the p -value gives the probability that a system where the null hypothesis is true produces a data set with a TS value at least as extreme as the one found in the measured data set. The smaller the p -value is the more unlikely it is that the null hypothesis is true. A p -value smaller than $2.7 \cdot 10^{-3}$ corresponds to a significance level greater than 3σ ($p\text{-value} < 5.7 \cdot 10^{-7}$ to 5σ).

The p -value can be calculated by using the cumulative distribution function (right-hand panel of Figure 4.2), which gives the probability P that the TS takes on a value smaller than or equal to a certain ts .

$$\text{cdf}(ts) = P(TS \leq ts) = \int_{-\infty}^{ts} p(TS) dTS. \quad (4.7)$$

This value is defined exactly inverse to the definition of the p -value, so that the p -value is given by

$$p = 1 - \text{cdf}(ts). \quad (4.8)$$

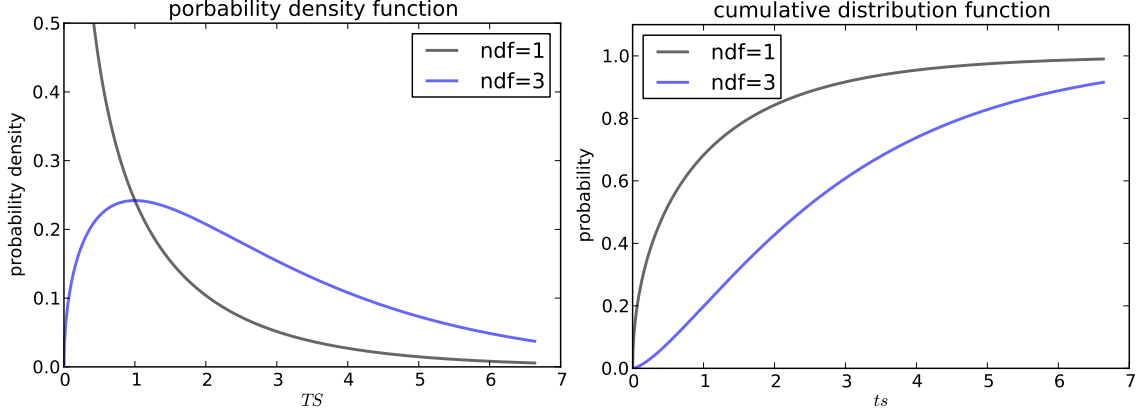


Figure 4.2: Examples of a probability density function (pdf) and the associated cumulative distribution function (cdf). Here, the pdf and the cdf of the χ^2 test statistic are shown. The χ^2 test statistic is shown for two different choices of the number of degrees of freedom (ndf).

The p -value p is connected to the significance level SL via the error function defined as

$$1 - p = \operatorname{erf} \left(\frac{SL}{\sqrt{2}} \right). \quad (4.9)$$

There are several different types of commonly used test statistics. The test statistic must be defined in such a way that it makes a distinction between the null hypothesis and the alternative hypothesis possible. De facto the values of the TS for the alternative hypothesis should be as different from the TS values for the null hypothesis as possible. In principle any kind of function could be a test statistic. The only requirement is that its sampling distribution for the null hypothesis can be exactly calculated or approximated, so that reliable p -values can be derived. Nevertheless, if the TS is not chosen carefully the distributions of the TS may be very similar for both hypotheses making a distinction impossible. In the following a few commonly used types of test statistics are presented. The selection concentrates on test statistics that are used in this study and has not the goal to be complete.

4.2.1 χ^2 - and $\Delta\chi^2$ -Test

The χ^2 -test belongs to a group of hypothesis tests where the test statistic follows a χ^2 -distribution. It is very commonly used in physics, because its definition is very simple and intuitive and often applicable. It compares a measured value of a random variable Y_j (e.g. arrival rate of electrons) to the value expected under the null hypothesis $y_{j,0}$ within m_0 different categories j (e.g. values of arrival rates in dependence on the direction of the sky) and is given by

$$\chi^2 = \sum_j \frac{(Y_j - y_{j,0})^2}{y_{j,0}}. \quad (4.10)$$

Here, the $y_{j,0}$ in the denominator resembles the variance of the underlying Poisson distribution in a counting experiment (Blobel and Lohrmann 1998). If the null hypothesis is true the difference is small, so that the value of χ^2 is also small. It is required that the random variable Y_j follows a normal distribution. This translates directly to a requirement on the sample size in counting experiments. As a rule of thumb the minimum number of events in each category must be 10. In this case, the χ^2 follows a χ^2 -distribution with m_0-1 *d.o.f.*

Often the χ^2 is normalized to the error of each random variable σ_{Y_j} , so that it is defined as

$$\chi^2 = \sum_j \frac{(Y_j - y_{j,0})^2}{\sigma_{Y_j}^2}. \quad (4.11)$$

In the previous definition only the null hypothesis was stated explicitly. The only conclusion that can be drawn from this simple χ^2 -test is whether the null hypothesis can be discarded at a certain confidence level. There is no information about the alternative hypothesis included.

In order to compare two hypotheses (H_0 and H_1) explicitly often the $\Delta\chi^2$ -test is used. The $\Delta\chi^2$ is defined as the difference between the χ^2 s of the null model and the alternative model

$$\Delta\chi^2 = \chi_0^2 - \chi_1^2 = \sum_j \frac{(Y_j - y_{j,0})^2}{\sigma_{Y_j}^2} - \sum_j \frac{(Y_j - y_{j,1})^2}{\sigma_{Y_j}^2}. \quad (4.12)$$

Here, $y_{j,0}$ and $y_{j,1}$ are the predicted values of the null model and the alternative model. The $\Delta\chi^2$ is a measure of how much better H_1 explains the data as compared to H_0 and whether this improvement is significant. Analogue to the χ^2 -test the $\Delta\chi^2$ -test is also only applicable if the random variable Y_j is normally distributed. In physics it is commonly used to test the ability of two models to explain data against each other. In that case H_0 corresponds to a simple model (Model₀ with k_0 fitted parameters) and H_1 to a more complex model (Model₁ with k_1 fitted parameters). If certain conditions (see Section 4.2.3) are fulfilled the $\Delta\chi^2$ is distributed as a χ^2 -distribution with $DF = (m_0 - k_0) - (m_1 - k_1)$ *d.o.f.*, where m_0 and m_1 are the number of data points to which each model is fitted and k_0 and k_1 are the number of free parameters of each model. Usually $m_0 = m_1 = m$ and $k_0 < k_1$.

4.2.2 F-Test

The F -test is commonly used in variance analysis to determine whether the variances of two normally distributed populations (population 1 and population 2) differ. In this case the test statistic is defined as the ratio of the variances of the random variable Y_i of the two populations ($Y_{i,1}$ and $Y_{i,2}$)

$$F_{\text{sample}} = \frac{\frac{1}{n_2-1} \sum_{i=1}^{n_2} (Y_{i,2} - \bar{Y}_2)^2}{\frac{1}{n_1-1} \sum_{i=1}^{n_1} (Y_{i,1} - \bar{Y}_1)^2}. \quad (4.13)$$

\bar{Y}_1 and \bar{Y}_2 are the mean values of the random variable within the two populations. n_1 and n_2 are the sizes of the data samples and must not be identical. The test statistic F_{sample} is F -distributed with $n_2 - 1$ *d.o.f.* in the numerator and $n_1 - 1$ *d.o.f.* in the denominator. The F -distribution from which the p -values are calculated depends on the *d.o.f.* of the numerator and denominator $F(n_1 - 1, n_2 - 1)$. The numerator and denominator are each χ^2 distributed.

In this study the F -test is used in a slightly different form, sometimes called extra sum-of-squares F -test. Similar to the $\Delta\chi^2$ described above it can be used to determine whether a more complex model describes the measured data significantly better than a simple model. In this case there is only one population but two different models, so that we have the predicted values $y_{i,0}$ for the simple Model₀ and $y_{i,1}$ for the more complex Model₁.

The null hypothesis is again that Model₀ describes the data best. The alternative hypothesis is that the introduction of additional free parameters leads to a significant improvement in the description of the data. Following Bevington (2003) the test statistic is defined as follows

$$f = \frac{(\chi_0^2 - \chi_1^2)/(DF_0 - DF_1)}{\chi_1^2/DF_1}. \quad (4.14)$$

f is the ratio between the reduced $\Delta\chi^2$ and the reduced χ^2 of the more complex model. The degrees of freedom are again $DF_0 = m_0 - k_0$ for the simple model and $DF_1 = m_1 - k_1$ for the more complex model. m and k are the sample size of the respective data set and the number of free parameters of the corresponding model. Rewritten, this equation has a similar structure as the F_{sample} distribution and, thus, is also F -distributed with $(DF_0 - DF_1)$ *d.o.f.* in the numerator and DF_1 *d.o.f.* in the denominator

$$f = \frac{\left(\sum_j \frac{(Y_j - y_{j,0})^2}{\sigma_{Y_j}^2} - \sum_j \frac{(Y_j - y_{j,1})^2}{\sigma_{Y_j}^2} \right) / (m_0 - k_0 - m_1 + k_1)}{\sum_j \frac{(Y_j - y_{j,1})^2}{\sigma_{Y_j}^2} / (m_1 - k_1)}. \quad (4.15)$$

If the simple model is a subset of the more complex model there is always a set of parameters of the more complex model that gives the same fit function as the simple model. Consequently, if the more complex model has more free parameters it will always fit the data at least as good as the simple model. This is not taken into account by the $\Delta\chi^2$ -test. There might be a significant improvement, but it does not take into account that possibly the number of degrees of freedom was indefinitely high making the improvement meaningless. In contrast the f test statistic takes into account how many *d.o.f.* both the simple model and the more complex model have. The amount of improvement expected by chance (if the null hypothesis is really true) depends on the number of free parameters and the number of data-points. If the simpler model is true $\Delta\chi^2$ is expected to increase when going from the more complex to the simpler model by the relative change in *d.o.f.* as

$$(\chi_0^2 - \chi_1^2)/\chi_1^2 = (DF_0 - DF_1)/DF_1. \quad (4.16)$$

Thus, if the two models compared have the same number of degrees of freedom using the $\Delta\chi^2$ is perfectly correct, because Equation 4.16 is zero on both sides. But the improvement expected only due to the larger number of *d.o.f.* of the more complex model is considerable for large differences in the *d.o.f.* of the compared models. In this case the $\Delta\chi^2$ -test may be unreliable if there is a large difference in the number of *d.o.f.* and the F -test should be employed.

4.2.3 Requirements on Hypothesis Tests

Mathematically, the $\Delta\chi^2$ -test and the F -test are only applicable when certain boundary conditions are satisfied. These are:

- The random variables Y_i must follow a Gaussian distribution. The sample size must be > 10 .
- The models must be nested, meaning that Model_0 must be a subset of Model_1 .
- The null model should not lie on the boundary of the parameter space of the additional parameters of the complex model.

Previously, the $\Delta\chi^2$ -test and the F -test have commonly been used in physics on many occasions where the last criterion is not fulfilled, e.g. when searching for a line in a spectrum. In that case the null hypothesis is a background model and H_1 is the background model plus an additive line. Thus, Model_0 lies on the boundary of the parameter space of Model_1 . In this case the distribution of the null model is unknown, because it lies outside the defined mathematical theory. Protassov et al. (2002) have shown that applying the $\Delta\chi^2$ -test or the F -test can lead to incorrect results in such cases sometimes underestimating and sometimes overestimating the significance. Protassov et al. (2002) propose a solution using posterior predictive p -values. A more simple approach is to simulate the reference probability distribution of the test statistic of the null model using Monte Carlo simulation techniques. In this case the best-fit parameter values of the null model are used instead of parameters simulated from their posterior distributions (Protassov et al. 2002).

4.2.4 Other Interesting Tests and their Applications

Student's t -test (e.g. Blobel and Lohrmann 1998) is often used to investigate whether the measured mean value of a random variable \bar{Y} is consistent with a theoretical value μ . It can also be employed to resolve the question whether the mean values (\bar{Y}_1, \bar{Y}_2) of two populations are the same, similar to the variance application of the F -test. The value of the t test statistic depends on a scaling term. If this term is known, t follows a normal distribution. If the scaling term is unknown and estimated from data the t test statistic follows a t -distribution.

The Kolmogorov-Smirnoff test (KS test, see e.g. James 2006 or Press et al. 2002) is sensitive to differences in the global form or tendencies of two distributions. The test does not compare the two distributions directly, instead it uses their cumulative distributions. The test can also compare the measured distribution of a random variable to a theoretical distribution. The test is very stable, because it is nonparametric and does not require normality. Thus, it is also applicable if the sample size is small. However, it requires the distribution of the random variable to be continuous.

Instead of using the KS test the Anderson-Darling test (Anderson and Darling 1952) can be used to compare a measured distribution with a theoretical distribution. First the data set is transformed to a uniform distribution by using the theoretical distribution. The test statistic is then given by the distance between the uniform distribution and the transformed, measured distribution. The Anderson-Darling test is more sensitive than the KS test and, thus, often used when testing a distribution for normality, where the KS test is rather insensitive.

4.3 Correlation

4.3.1 Pearson Correlation

The Pearson correlation coefficient is a measure of the linear dependence between two variables (X, Y) . It takes values between -1 and +1. Where a correlation coefficient of +1 or -1 means that the data points of the measurement lie perfectly on a straight line. Notably, a correlation coefficient of 0 does not necessarily mean that the two variables are independent of each other it only means that there is no linear relationship. Thus, independent variables are also always uncorrelated but this statement is not true vice versa. The Pearson product momentum correlation coefficient is defined as the covariance normalized to the product of the standard deviations of X, Y (James 2006)

$$\rho = \text{corr}(X, Y) = \frac{\text{cov}(X, Y)}{\sigma_X \sigma_Y}. \quad (4.17)$$

The mean (expectation value) μ_X , covariance $\text{cov}(X, Y)$ and the standard deviation (variance) σ_X are defined as

$$\begin{aligned} \mu_X &= \int \int X f(X, Y) dX dY = E(X), \\ \sigma_X^2 &= E((X - \mu_X)^2), \\ \text{cov}(X, Y) &= E[(X - \mu_X)(Y - \mu_Y)]. \end{aligned}$$

Here, $f(X, Y)$ is the joint probability density function for X and Y . The expectation value for any function $g(X, Y)$ is defined as $E[g(X, Y)] = \int \int g(X, Y) f(X, Y) dX dY$. The standard deviation and expectation value for Y are defined analogous to those of X . For a data sample the Pearson sample correlation coefficient is obtained by inserting sample values for the standard deviation and mean into Equation 4.18. For two data sets x_i and y_i , both containing n values, the Pearson sample correlation coefficient is calculated as (Press et al. 2002, Chapter 14.5)

$$r = \frac{\sum_{i=1}^n (x_i - \bar{x})(y_i - \bar{y})}{\sqrt{\sum_{i=1}^n (x_i - \bar{x})^2} \sqrt{\sum_{i=1}^n (y_i - \bar{y})^2}}. \quad (4.18)$$

Here, \bar{x} , \bar{y} are the sample means and are given by $\bar{x} = \frac{1}{n} \sum_{i=1}^n x_i$. The correlation coefficient itself is relatively meaningless without a measure of the significance of the result. Thus, a hypothesis test must be performed in order to test the null hypothesis that the true correlation coefficient is really zero, even though a value unequal zero was measured. Different methods for performing such a hypothesis test are applicable, among those are permutation tests, bootstrapping (see e.g. Good 2004) and Student's t -test (Press et al. 2002 Equation 14.5.5., see also Section 4.2.4). Lets assume the correlation is known to be significant. In this case the correlation coefficient can be used as an estimator of the residuals (root mean square deviations) expected when fitting the data by a straight line. In other words there is a relationship between r and the χ^2 calculated when fitting data to a straight line (Press et al. 2002, Equations 15.2.13 - 15.2.14).

4.3.2 Spearman's Rank Correlation

In order to determine whether there is a relationship between two (physical) quantities the correct measure of association must be chosen. Spearman's rank correlation coefficient is a nonparametric measure (using the rank of every value) and is able to detect a monotone relationship between two quantities. Further, there is no requirement made on the probability distribution of the considered quantities. These properties are important for the application (Section 5.3.3) in this study, where the relationship between gamma-like and hadron-like event arrival rates is examined and it is not important that the relationship is linear, but can also be monotone. In contrast to Spearman's rank correlation coefficient the alternative Pearson coefficient is a measure for a linear relationship and the two quantities must be normally distributed. Overall, Spearman's rank correlation coefficient is the more robust choice since also small deviations from normality are less important and associations between the two quantities are still detected.

To calculate Spearman's correlation coefficient ρ_s for every pair of measured quantities (X_i, Y_i) the ranks (\tilde{X}_i, \tilde{Y}_i) are determined. Spearman's rank correlation coefficient depends on the distance between the ranks of each data pair $D_i = \tilde{X}_i - \tilde{Y}_i$ and is 1 if the distance between the ranks of all pairs is zero, so that there is a perfect monotone relationship. For the sample size n Spearman's correlation coefficient (Press et al. 2002 Equation 14.6.4) is given by

$$\rho_s = 1 - \frac{6 \sum_i D_i^2}{n \cdot (n^2 - 1)}. \quad (4.19)$$

Spearman's rank correlation coefficient is technically defined as the Pearson correlation coefficient for the ranked values. The approximation above is only exact if there are no ties in the data set. It is a good approximation if the number of ties is smaller than the sample size n . The significance of the measured correlation coefficient can be computed by employing Student's t -distribution. In this case the t value (Press et al. 2002, Equation 14.6.2) is defined as

$$t = \rho_s \sqrt{\frac{n-2}{1-\rho_s^2}}. \quad (4.20)$$

This way the probability that a value of t is measured at least as big as the measured value of t (and corresponding ρ_s) if the two data sets are really uncorrelated can be calculated from Student's t -distribution. This p -value is a measure for the significance of the measured correlation. Using the t -distribution to test the significance is a robust method, because it does not depend on the underlying distributions of the two quantities.

Chapter 5

Analysis of Cosmic-Ray Electrons

5.1 Data Selection and Reconstruction

5.1.1 Run Quality Selection

In order to guarantee a high quality of the data set analyzed in this study, several run selection criteria have been defined and were applied during the selection process. The criteria are based on the standard run selection in the Paris analysis framework (H.E.S.S. collaboration 2015). The standard selection criteria and applied criteria are summarized in Table 5.1. It contains only the selections that can be applied using the run selection module. Additional selections were also applied. All selection criteria applied are discussed below.

Target selection The diffuse gamma-ray emission from the Galactic plane would cause a considerable background in the analysis of cosmic-ray electrons. Thus, only data taken at a distance of 7° degrees away from the Galactic plane can be used safely in this study.

Telescope tracking selection To minimize systematic effects data taken at zenith angles smaller than 30° are included in this study.

Global run properties Only runs are selected that were taken at a time where all four telescopes were operational. A minimum run duration of 10 minutes is required, to assure sufficient statistics for the determination of the pedestal in the camera pixels.

Trigger selection Standard trigger conditions with a sector threshold of 4 pixels and a pixel threshold of 2.5 p.e. (see Section 3.3.2) were used. Good weather conditions are important in this analysis to minimize systematic effects on the event rate normalization and fluctuations. The event rate depends on the atmospheric conditions at the time of data taking.

Parameter	Standard selection	Applied selection
Global run properties		
Minimum number of working telescopes	3	4
Minimum run duration	5 min	10 min
Trigger		
Pixel threshold	2.5	2.5
Sector threshold	4	4
Zenith corrected average central trigger rate	100-500 Hz	100-500 Hz
Stability	0-4 %	0-4 %
Minimum 2-fold live time fraction	80 %	80 %
Telescope tracking		
Maximum zenith angle	-	30°
Weather quality		
Radiometer stability	0.0 - 0.5 °C	0.0 - 0.5 °C
Minimum number of correct tel.	1	1
Technical quality		
Broken pixel fraction	0 - 10 %	0 - 10 %
Minimum number of correct tel.	3	3

Table 5.1: Run selection criteria applied by using the run selection module provided within the Paris analysis software framework. The standard selection criteria, applied per default, are given in the middle column. The default selections were modified to meet the quality requirements of this study. The actually applied selections are given in the right-hand column.

On longer time scales (weeks to month) the atmospheric transparency changes due to a change in the aerosol concentration, e.g. induced by a higher concentration of dust in the air or by fires typical from August to October. Thus, the zenith corrected average central trigger rate¹ was required to range between 100 and 500 Hz. On shorter time scales (minutes to hours) the atmospheric transparency varies due to clouds passing through the field of view (FoV). This can either lead to a gradual drop of the trigger rate or to trigger rate fluctuations during a run. Thus, it is required that the relative variations of the zenith corrected average central trigger rate during a run are smaller than 4 %.

Following a trigger the signals are digitized and read out by the data acquisition system. During this process an arriving second event cannot be recorded by the camera resulting in a dead time. The dead time of a single telescope or of the telescope system is derived from the distribution of time differences between consecutive events in a run. The two-fold dead time is the dead time of the system with a two-telescope coincidence requirement. The two-fold dead time fraction is defined as the two-fold dead time divided by the run duration. The opposite of the two-fold dead time fraction is the two-fold live time fraction, which gives the time fraction during which the system was able to record arriving events. The two-fold live time fraction was required to be larger than 80 %² to ensure that the dead time of every used run is acceptable.

Weather quality selection Each telescope in the array is equipped with a radiometer measuring the infrared radiation in its FoV (2.9°, paraxial aligned with the telescope). By comparing the observed spectrum to a black-body spectrum the radiative temperature of the sky is determined (see Aye et al. 2003 and Daniel and Chadwick 2015). This temperature is very sensitive to the presence of clouds and water vapor. The radiative temperature of clouds is higher than that of the surrounding atmosphere. The sky temperature can also vary from night to night due to relative humidity and temperature changes. Thus, the radiometer temperature is used to evaluate the amount of clouds present and general weather conditions. Since the radiometer information are not always reliable (they can exhibit a big jump when for example one of the lightning masts enters the FoV) relatively loose selection requirements are applied. During a run the radiometer temperature may not fluctuate by more than 0.5 °C. Only one telescope must pass this requirement.

Technical quality selection There are several sources of hardware and observation related errors in the final estimation of the number of photoelectrons recorded in each pixel, e.g. missing high voltage or a star in the FoV. Pixels with such problems are called broken pixels (Aharonian et al. 2006). Such pixels can lead to incorrect reconstructed showers. In the selection process it is required that only one telescope may have more than 10 % broken pixels.

¹At large zenith angles air showers are observed through a much greater atmospheric column depth. Thus, Cherenkov photons in such showers suffer much more from scattering and absorption. The resulting shower images are dimmer, while the light pool on the ground of showers observed at high zenith angles is larger. In consequence the telescope and central trigger rates both show a smooth monotonic decrease with increasing zenith angle. For the comparison of trigger rates the average trigger rate of a run can be converted to its equivalent at zenith using an empirical formula.

²Note: When using the run selection gui this number is called two-fold dead time fraction. Nonetheless, from the code it is clear that the given number is really the minimum required two-fold live time fraction.

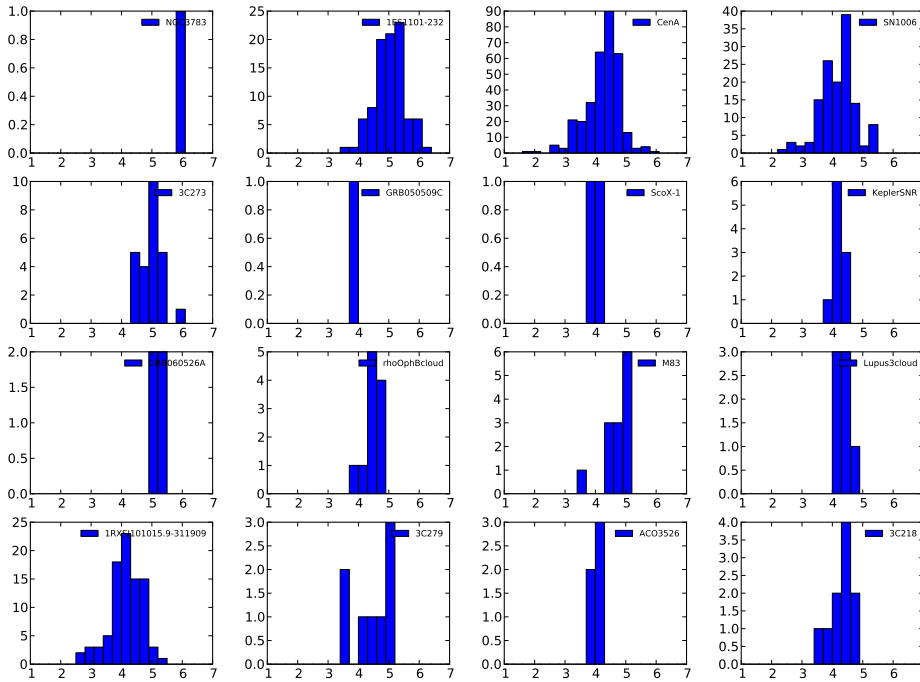


Figure 5.1: Distributions of run-wise measured background (hadron-like) event rates for a selection of pointings. On the x-axis the run-wise measured background rates are given in Hz. On the y-axis the number of runs is given.

Data set The Paris analysis run selection software module was employed to select the runs for the following analysis. The data were taken between 2005 and 2012 with the four H.E.S.S. I telescopes. 3411 runs distributed between 108 sources passed the applied selection requirements. A total observation time³ of 1594 hours corresponding to approximately 1473 hours of live time⁴ is available. Due to incorrect database information 4 runs with pointing positions on the Galactic plane were initially not removed from the data set by the run selection algorithm. Another 4 sources were located very close to the 7° boundary condition. All 8 sources were removed from the data set for the anisotropy analysis in Section 5.3 to avoid any signal due to these pointings.

Stability of background rates Figure 5.1 shows the distribution of the run-wise measured background event rates⁵. The distributions for all other pointings are given in Appendix F. The different observations contain runs giving background rates between 1 and 7 Hz. In the majority of cases the distributions are not Gaussian, but take on a large range of different profiles. The

³This is the timespan between the detection of the first event and last event of the run.

⁴This is the observation time corrected by the previously discussed dead time.

⁵Background events are in this case all events that are defined to be hadron-like events in the gamma-hadron separation procedure discussed in Section 5.1.3. Here, the events with $MSSG > 5$ are used. The event rates for each run are calculated by summing up the background-like events for each run and dividing this number by the total amount of live time of the run.

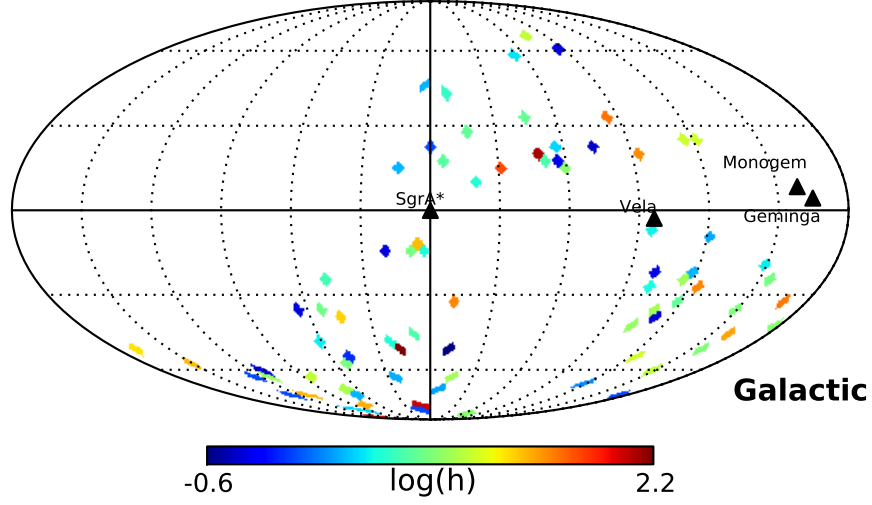


Figure 5.2: Distribution of the available observation time over the sky. Black triangles mark the pulsars Vela, Monogem and Geminga, as well as the Galactic Center SgrA*. The color scale gives the observation time available for each pointing.

different profiles are a result of observations taken under systematically different observation conditions (e.g. zenith angle and optical efficiency distributions differ). As mentioned above there are also shifts in the trigger rate over long time scales due to long term changes of the atmospheric transparency. The stability requirement placed on the central trigger rate does not remove long term variations of the trigger rate from the data set. Further, the cut on the average zenith corrected central trigger rate appears to have been rather loose as can be seen from the analysis of the pointing-wise background rate distributions. In order to select a more homogenous data set it is required that the background event rate for each run j used in anisotropy studies is > 3.5 Hz ($R_{j,BG} > 3.5$ Hz). After this last cut 94 pointings and 2780 runs remain with a total live time of 1178 hours.

Sky exposure The available sky exposure for all 94 sources is shown in Figure 5.2. The data set available for the anisotropy studies (1178 hours) is approximately 5 times the size (239 hours) of the one used previously for the H.E.S.S. electron spectrum (Aharonian et al. 2008). The sources are not equally distributed over the sky, but are restricted to positions that can be observed at low zenith angles with the H.E.S.S. telescopes. The live time per pointing is not equally distributed between pointings. More than 10 % (~ 170 hours) of the available live time was dedicated to PKS 2155-304, while some other pointings were observed for only half an hour.

The available live time is distributed between observations at many different zenith angles, as shown in the left-hand panel of Figure 5.3 with a mean zenith angle of 16° . The aging and optical condition of the telescopes is reflected by the optical (muon) efficiency. The distribution of the live time in dependence on the optical efficiency is shown in the right-hand panel of Figure

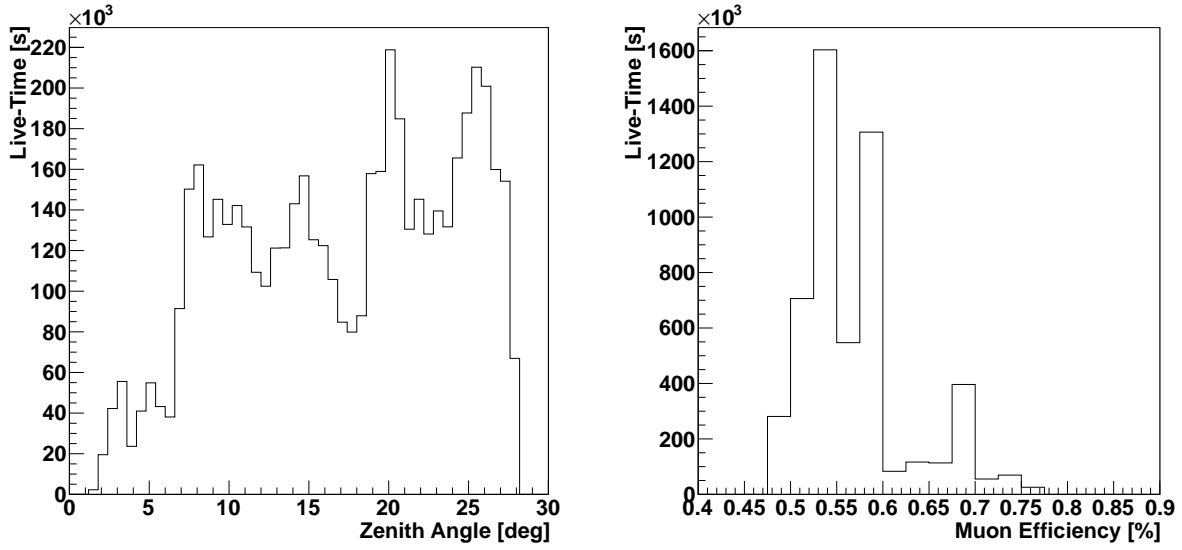


Figure 5.3: Distributions of the live time of observations in dependence on the zenith angle (left-hand panel) and the optical efficiency (right-hand panel). In this plots all 107 pointings were included.

5.3. The optical efficiency ranges from 45 % to 80 %, but most of the observations were taken at 50 % to 60 % optical efficiency.

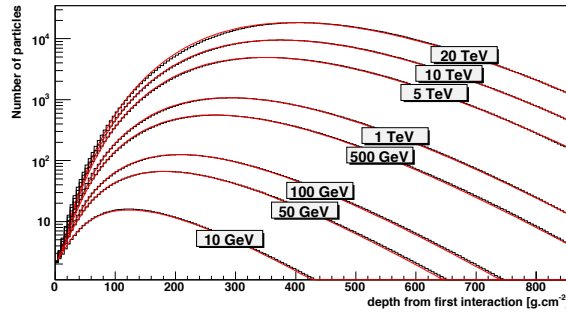


Figure 5.4: Longitudinal shower profile measured from the first interaction point. The number of charged particles in the shower is given in dependence on the distance from the first interaction point for primary particle energies between 10 GeV and 20 GeV. The analytical function for the profile (red) is compared to the results from Monte Carlo simulations (black histogram). Adapted from de Naurois and Rolland (2009).

5.1.2 Shower Reconstruction with Model++: Calibrating the Data

The Model reconstruction technique is presented in de Naurois and Rolland (2009). It is one of the widely used event reconstruction techniques available within the H.E.S.S. collaboration. In this study it was employed for the analysis of the data set. The Model++ algorithm is based on a semi-analytical model of the particle shower in the atmosphere. It was derived by first performing Monte Carlo simulations of air showers initiated by gamma rays. Based on this MC data analytical functions were found that describe the average longitudinal, lateral and angular shower profiles. Figure 5.4 shows such a longitudinal profile function (red line) in comparison to the average longitudinal profile obtained from MC simulations (black histograms).

From the longitudinal, lateral and angular profiles of the particles in the air shower the Cherenkov light density expected in the camera is calculated. Such an intensity distribution is shown in Figure 5.5.

Average intensity distributions from such shower models were calculated for 40 different zenith angles z , 40 impact distances⁶ δ between 0 and $(400 \text{ m})/\cos(z)$, 65 different energies $((50 \text{ GeV})/\cos(z)$ to $(20 \text{ TeV})/\cos(z))$ and 6 first interaction depths from 0 X_0 to 5 X_0 . This produces a database of 2-dimensional shower images in the frame of a perfect camera with a pixel size of 0.01° . From this table shower images for new parameter sets are calculated by interpolating between the generated images on a 4 dimensional parameter space (energy, impact distance, primary interaction depth and zenith angle). The shower direction and the azimuthal angle are taken into account by translating and rotating the camera frame (the original models were obtained for particles at the camera center). Figure 5.6 shows a comparison of the shower image parameters *Length* and *Width* in dependence on the true impact distance produced from camera images generated by simulations or from semi-analytical shower models. The values

⁶The impact distance is the projected (perpendicular) distance of the extrapolated shower track to a telescope (Aharonian et al. 2006).

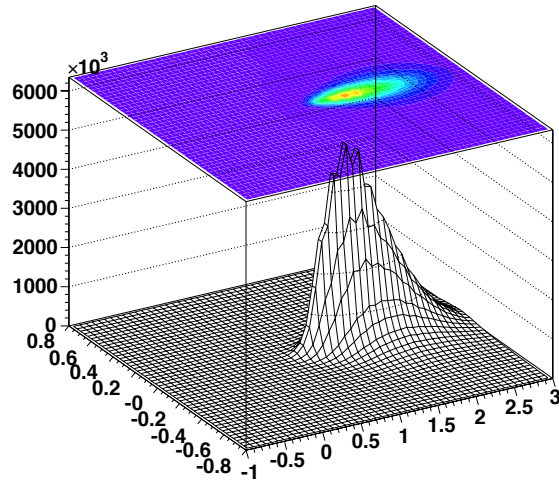


Figure 5.5: Intensity distribution of Cherenkov light in the camera calculated from the semi-analytical shower model for a 1 TeV primary particle started at one radiation length with an impact distance of 250 m. x- and y-axis are given in units of degrees in the camera frame. Adapted from de Naurois and Rolland (2009).

obtained from the semi-analytical shower models are very similar to the corresponding average values from simulations.

In order to obtain the parameter set (energy, direction, impact distance, depth of the first interaction) a *log*-likelihood comparison between the actual shower image and shower images produced from the semi-analytical shower model is performed. For each camera pixel the probability to observe a signal s (in units of photoelectrons) if the expectation value of the pixel is μ follows from the convolution of a Poisson distribution with the Gaussian response of the PMTs and is given by

$$P(s|\mu, \sigma_p, \sigma_\gamma) = \sum_n \frac{\mu^n e^{-\mu}}{n! \sqrt{2\pi(\sigma_p^2 + n\sigma_\gamma^2)}} \exp\left(-\frac{(s-n)^2}{2(\sigma_p^2 + n\sigma_\gamma^2)}\right). \quad (5.1)$$

Here, σ_p is the width of the pedestal. The pedestal is the charge distribution collected in each pixel in the absence of Cherenkov light and, thus, in the absence of a signal as discussed in Section 3.3.4. σ_γ gives the width of a single photoelectron peak representing the resolution of the photomultiplier. Both quantities are specific for each pixel and are measured (see Section 3.3.4). The Poisson distribution gives the probability to measure n photoelectrons if the expectation value is μ . The Poisson distribution is convoluted with the photomultiplier resolution which is well described by a Gaussian with width $\sqrt{\sigma_p^2 + n\sigma_\gamma^2}$. Thus, the Gaussian distribution gives the probability to measure a signal s if the expectation value of the Gaussian distribution is n due to the photomultiplier resolution. The overall probability is given by the sum over all

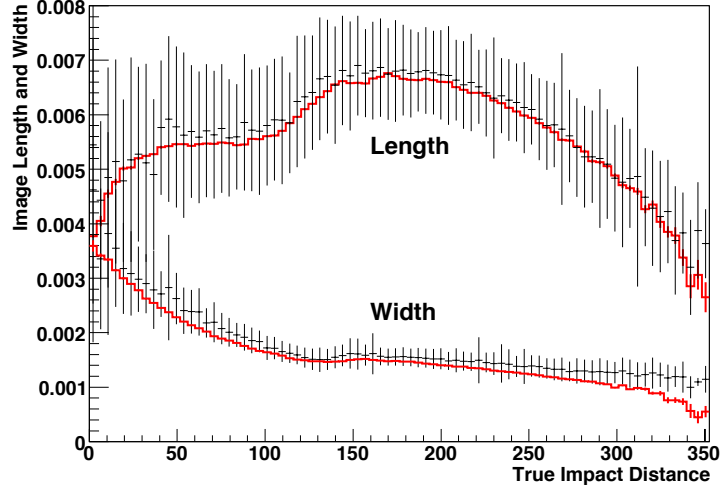


Figure 5.6: Average image length and image width in units of radian of 1 TeV shower images as obtained from simulations (black) and from the semi-analytical shower models (red) in dependence on the impact distance. The parameters were obtained via the standard Hillas parametrization technique. Adapted from de Naurois and Rolland (2009).

possible photoelectron numbers. Thus, a large probability corresponds to a good agreement between measured signal and the expectation value predicted by the semi-analytical shower model.

To get a quantity that behaves asymptotically like a χ^2 -distribution the pixel *log*-likelihood is defined as

$$\ln L_i = -2 \ln P(s_i | \mu_i, \sigma_p, \sigma_\gamma). \quad (5.2)$$

Thus, a large $P(s_i | \mu_i, \sigma_p, \sigma_\gamma)$ value corresponds to a small pixel *log*-likelihood value. The *log*-likelihood for each telescope $\ln L_{\text{tel}}$ is given by

$$\ln L_{\text{tel}} = \sum_{\text{pixel } i} \ln L_i. \quad (5.3)$$

The shower parameters are reconstructed by a pixel per pixel comparison of the actual measured shower images (s_i for each pixel) with the shower images (μ_i for each pixel) predicted by the model. The 6 input shower parameters (energy, depth of the first interaction, two parameters describing the impact, two parameters describing the direction) are varied until the minimum of the *log*-likelihood function and, thus, the parameter set fitting the measured shower best is found. In contrast to the Hillas technique described in Section 3.3.4 all camera pixels are used in the fit and no cleaning procedure identifying the pixels close to the actual image is applied. The output of the fit gives the 6 best-fit shower parameters, the corresponding final *log*-likelihood and the correlation matrix.

In the semi-analytical shower model and the reconstruction of the shower above it was always assumed that the primary particle was a gamma-ray. In fact the shower images are

not only produced by gamma rays but also by other particles, e.g. electrons, hadrons and muons. Thus, it is necessary to separate actual gamma-ray events especially from the hadronic background. It was shown in Figure 3.11 that hadrons produce much broader camera images than gammas, thus, they should produce larger *log*-likelihood values than gamma rays usually would. As a discrimination parameter the *Goodness* of fit is defined for each telescope j

$$G_j = \frac{\sum_{\text{pixel } i} [\ln L(s_i | \mu_i) - \langle \ln L \rangle |_{\mu_i}]}{\sqrt{2 \times \text{NdF}}}. \quad (5.4)$$

Here, $\langle \ln L \rangle |_{\mu_i}$ is the expectation value of the pixel *log*-likelihood function and NdF the number of degrees of freedom of the fit (which is the number of pixels minus the number of fit parameters, here 6). Per construction every pixel *log*-likelihood behaves like an independent variable so that the *Goodness* of fit itself behaves like a normally distributed variable with expectation value $\langle G \rangle = 0$ and width $\sigma^2(G) = 1$.

In the above treatment a Gaussian pedestal was assumed. This assumption is correct if the NSB is much smaller than the electronic noise. In the low-gain channel the pedestal is also approximately Gaussian for higher NSB. In the high-gain channel the approximation holds for high NSB levels above 150 MHz. In the intermediate NSB regime the pedestal exhibits two peaks produced by fractions of single photoelectron pulses falling by chance within the acquisition window. Such a none Gaussian pedestal shape can cause a shift in the *Goodness*. This is solved by rescaling the *Goodness* for each telescope by average *Goodness* $\langle G_{\text{simu}}(q, \delta) \rangle$ values and the variance of the *Goodness* $\sigma_{G, \text{simu}}(q, \delta)$ obtained from simulations. These values are stored in look-up tables in dependence on the impact distance δ and image size q^7 . The *Scaled Goodness* is then given by

$$SG_j = \frac{G(q_j, \delta_j) - \langle G_{\text{simu}}(q_j, \delta_j) \rangle}{\sigma_{G, \text{simu}}(q_j, \delta_j)}. \quad (5.5)$$

The correction tables are only used to calculate the *Scaled Goodness* SG and not during the fit. Finally, the mean value for all telescopes j is calculated as follows

$$MSG = \frac{\sum_j SG_j}{\sqrt{N_{\text{telescopes}}}}. \quad (5.6)$$

$N_{\text{telescopes}}$ is the total number of telescopes.

A variable more sensitive to differences between the model prediction and the actual shower images is defined by using only pixels belonging to the shower to calculate the *Goodness*. These are all pixels with a predicted amplitude > 0.01 p.e. and three rows of neighbors grouped around them. The pixels are selected after the fit procedure. This pixel classification reduces the number of degrees of freedom significantly improving the sensitivity of the variable to differences between model and actual shower image. This quantity is called the *Mean Scaled Shower Goodness* (*MSSG*) and is used in this study to separate gammas from hadrons.

The distribution of the *MSSG* is shown in Figure 5.7 for ON-OFF data (mainly gammas), OFF data containing mainly hadrons and the *MSSG* distribution expected from gamma-ray

⁷The image size is equivalent to the image amplitude.

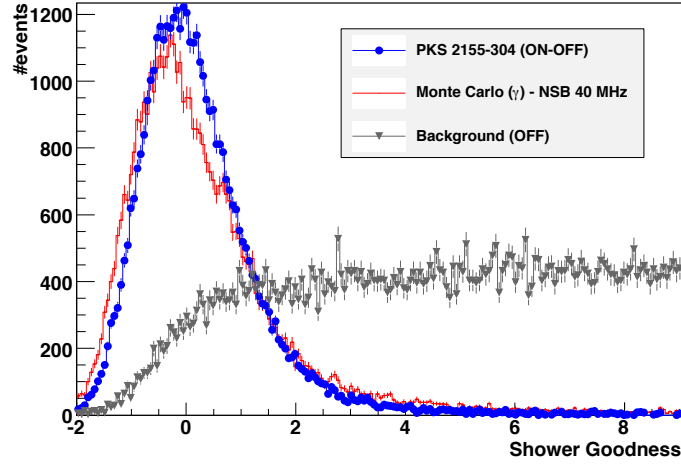


Figure 5.7: *MSSG* (here called only *Shower Goodness*) distribution for data taken of the blazer PKS 2155-304. Blue points mark excess (ON-OFF) events, gray triangles background events (OFF) and the red histogram shows a Monte Carlo gamma-ray distribution obtained at a similar NSB level. Adapted from de Naurois and Rolland (2009).

simulations. As expected the *MSSG* distribution of the simulated gammas and the ON-OFF data follow quite closely a normal distribution around zero, while the *MSSG* distribution of the background (hadrons) looks very different.

The Model analysis is a high performance reconstruction technique obtaining a higher sensitivity and a better resolution than the standard Hillas technique as shown in Figure 5.8. The model reconstruction reaches higher effective areas (except at energies above 10 TeV) and better energy (smaller than 10 % at energies above 300 GeV) and angular resolution (always $< 0.1^\circ$) for all cut choices when compared to comparable Hillas cuts (de Naurois and Rolland 2009).

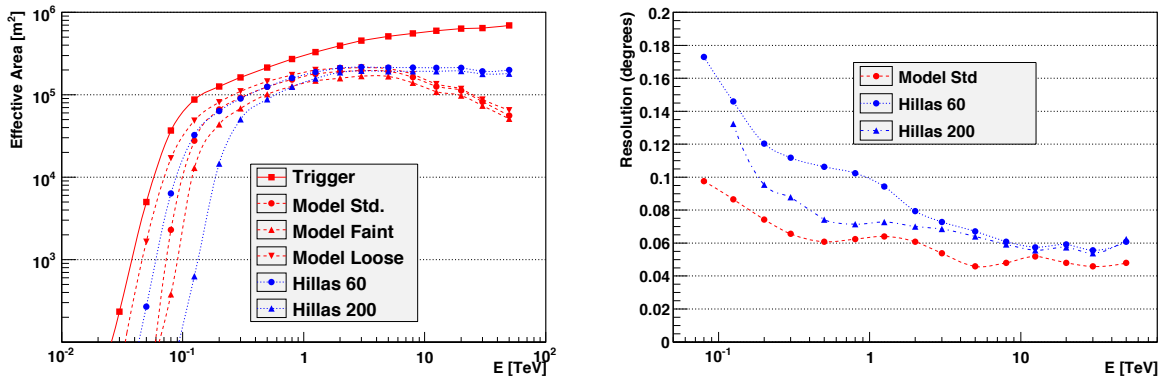


Figure 5.8: Left: Effective Area obtained with different cut choices with the Model++ reconstruction technique and comparable Hillas cuts. Right: Angular resolution obtained with the Model++ reconstruction technique and comparable Hillas cuts. For more details on the definition of the different cut choices and the energy resolution of the Model++ reconstruction technique see de Naurois and Rolland (2009).

5.1.3 Event Selection: Quality Criteria and Gamma-Hadron Separation

For the reliability of the data analysis it is important to solely use well reconstructed shower events. High-quality shower events are selected by requiring that certain quality criteria, called shape cuts, are fulfilled for every shower used in the analysis. The event selection is based on the requirements used for faint sources within the H.E.S.S. collaboration (de Naurois and Rolland 2009), since in this study we search for a faint signal. The used shape cuts, general event selection criteria and the gamma-hadron separation requirement are summarized below.

Shape Cuts on Camera Images

1. A minimum image amplitude per telescope of 120 p.e. was required. In the Model++ analysis the image amplitude is the sum over the charges measured in each pixel in photoelectrons (total image amplitude). In contrast to the Hillas reconstruction technique discussed in Section 3.3.4 no image cleaning procedure is employed before calculating the image amplitude, so that the image amplitudes for Model++ are always slightly larger than the corresponding Hillas analysis amplitudes.
2. The distance of the shower-image barycenter to the camera center (nominal distance) was required to be smaller than 2° for a camera radius of 2.5° . This requirement removes truncated images at the camera edge, that often lead to a miss-reconstruction of the shower direction.
3. All requirements are checked individually for each telescope. Only shower events for which at least two telescopes pass the above criteria are used in the analysis.

Event Selection

1. In order to improve the reconstruction quality of the events it was required that the distance of the shower core⁸ to the center of the telescope array (core distance) must be smaller than 200 m.
2. This study investigates diffuse electrons, thus photons from the source must be excluded from the analysis. Therefore, only events with a reconstructed direction more than 0.4° away from the source are used (angular distance between source position and reconstructed direction of the event $> 0.4^\circ$). This requirement reduces a spill-over of source photons as illustrated in the θ^2 -histogram in Figure 5.9. Figure 5.9 shows the number of source photons (ON-OFF events) in dependence on the squared angular distance from the camera center for the 2006 flare of PKS 2155-304 (Aharonian et al. 2007). For this bright source in its flaring state the number of photons at an angular distance of 0.3° ($\theta^2 = 0.1$) is almost at the null level, but a contribution of a few spill-over photons at an angular distance $> 0.4^\circ$ cannot be excluded. Even though, since the typical source in

⁸The shower core is the position of the intersection of the shower axis with the ground plane (observation level). More precisely, it is the intersection point of the shower axis with a reference x-y plane whose normal vector points towards the zenith.

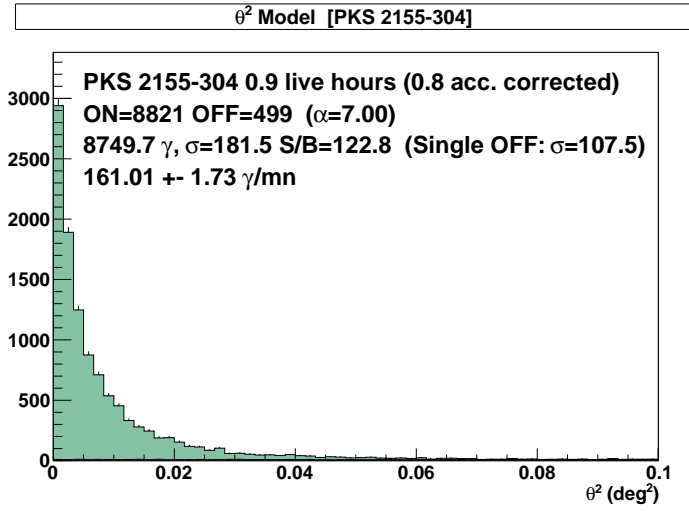


Figure 5.9: θ^2 distribution in an ON-OFF data sample of PKS 2155-304 in its flaring state 2006.

this analysis has a flux a factor 10 to 100 smaller than PKS 2155-304 in its flaring state a contribution of spill-over source photons to the gamma-like events of the used data set is unlikely.

3. In order to avoid systematic effects due to a decreasing acceptance at the edge of the camera only events are used that have been reconstructed at an angular distance less than 1.5° away from the pointing position.

Gamma-Hadron Separation The definition of the *Mean Scaled Shower Goodness* (*MSSG*) ensures that the distribution of the *MSSG* of gamma-like events is normally distributed with an expectation value of 0 and a standard deviation of 1. As shown in Figure 5.7 the distribution of the *MSSG* for hadronic background events is totally different from the *MSSG* distribution of gamma events with background events usually adopting much larger *MSSG* values than gamma events. Thus, in this study the *MSSG* is used to separate gamma events from hadron events. To select gamma-like events normally a cut on the $MSSG < 0.6$ is applied (standard cut). This cut sustains approximately 70% of gamma events⁹. Other cut choices were investigated and the impact on the analysis results is discussed in Section 5.3.5. These selection cuts were a very stringent cut ($MSSG < -0.6$) and an intermediate/complementary cut ($-0.6 < MSSG < 0.6$). For background studies events with $MSSG > 5$ were employed. The impact of using other background event selection choices is also investigated in Section 5.3.5.

⁹For more detailed information on the performance of the gamma-hadron separation cuts in terms of cut efficiencies and quality factor see Section 5.2.2.

5.2 Upper Limit on the Cosmic-Ray Electron Spectrum

5.2.1 Computing the Electron Flux

The quantity measured in (astro)particle physics is usually the number of arriving events respectively the event arrival rate. The number of measured events strongly depends on the setup of the experiment (or the telescope) and, thus, the specifications of the instruments used for detecting the events. In the case of gamma-ray telescopes it depends for example on the size of the light-collection area, the number of telescopes in the array, the employed PMTs and also the observation conditions. In contrast, the physical quantity related to the arrival rates, the flux, is independent from the experimental setup and can, thus, be used to compare results from different experiments.

The differential electron flux¹⁰ $\frac{dF}{dE}$ is defined as the number of electrons at a certain energy $N_{\text{el}}(E)$ divided by the effective area $A_{\text{eff}}(E)$ at this energy, the solid angle element of the fraction of the sky that was simulated $\Delta\Omega$ (this should be as large as the solid angle element covered by the telescope), the width of the energy band in which the events were observed ΔE and the time interval Δt of the observation

$$\frac{dF}{dE} = \frac{N_{\text{el}}(E)}{A_{\text{eff}}(E) \Delta\Omega \Delta E \Delta t}. \quad (5.7)$$

To compute the correct electron flux the measured number of electrons $N_{\text{el}}(E)$ in the considered energy bin ΔE must be precisely known. This is a great challenge for ground-based gamma-ray telescopes. The gamma-hadron separation procedure presented in Section 5.1.2 can suppress a large amount of hadronic background events (for $MSSG < 0.6$ typically 99.5 %). Nevertheless, a certain level of hadronic background remains. In addition, the camera images of gamma ray and electron initiated air showers look almost identical and cannot be separated using the *MSSG*. Thus, the great challenge is to determine the correct amount of background present in the data to be able to calculate the electron spectrum as it was done by Aharonian et al. (2008).

The effective area A_{eff} is the quantity which comprises the instrumental dependence. It is the area over which incoming particles are actually detected by the telescope and depends on the particle type, zenith angle, optical efficiency and energy. The effective area is determined by the means of Monte Carlo (MC) simulations of incoming particles. When considering a diffuse flux it is more appropriate to discuss the exposure $\xi = A_{\text{eff}} \Delta\Omega$, because in the diffuse case the differential flux is given per solid angle element. The exposure is obtained from simulations of electrons distributed over the solid angle element $\Delta\Omega$.

¹⁰More precisely the quantity defined here is an intensity, because the flux discussed originates within the solid angle $\Delta\Omega$ on the sky (see e.g. Longair 2011 and Weigert et al. 2005). Following the common nomenclature in literature concerning cosmic-ray electrons the quantity will be called differential electron flux in this study.

5.2.2 Simulating Diffuse Cosmic-Ray Electrons

For the calculation of the exposure of cosmic-ray electrons a large number of air-shower simulations was performed. First, the air shower initiated by the chosen primary particle (here electrons) is simulated, afterwards the air shower is processed in a simulation of the used detector. The output raw data have the same format as real telescope data. Afterwards, the data are reconstructed analogous to real telescope data with the Model++ reconstruction chain (de Naurois and Rolland 2009) and data summary tables (DSTs) are stored. The important steps are illustrated in Figure 5.10 and described below in more detail.

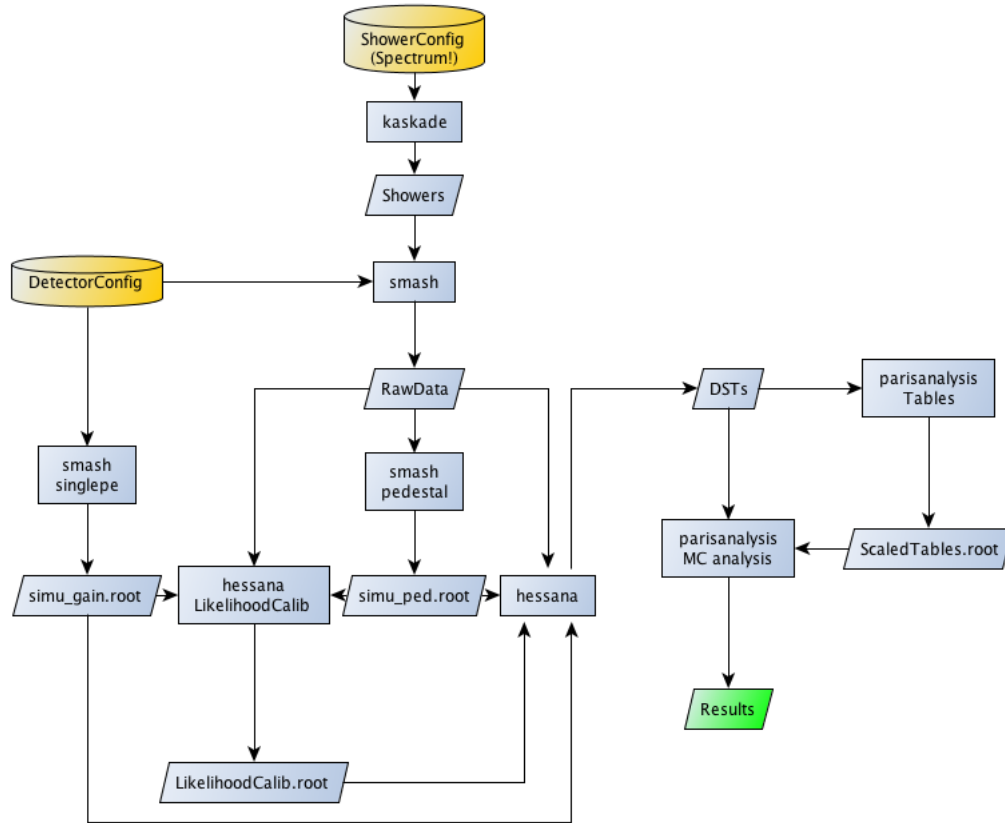


Figure 5.10: Overview chart of the steps necessary to obtain a full shower simulation within the Model++ H.E.S.S. collaboration framework. Shower simulations are performed with KASCADE, detector simulations with Smash and the event reconstruction is done with hessana. The obtained data summary tables (DSTs) can be used in the Paris analysis framework (MC analysis). Image by Anton Jahn.

Shower simulation with KASCADE

When the primary cosmic-ray electron hits the atmosphere, a shower of secondary particles is triggered. KASCADE follows the development of these particles in the atmosphere and models the emission of Cherenkov light emitted by the shower particles. This light is later detected by the telescope. KASCADE (Kertzman and Sembroski 1994) simulates the shower initiated by several different types of primary particles: photons, electrons, muons, protons, helium, and heavier nuclei.

The most important particle interaction processes are included. For electromagnetic air showers (initiated by electrons, photons, electromagnetic sub-showers of hadronic cascades) these are ionization, annihilation processes, Bremsstrahlung, pair production as well as energy losses via several scattering processes (Bhabha, Moeller and Compton scattering). These interactions are well described in the framework of quantum electrodynamics.

In hadronic air showers several scattering processes play an important role for example protons scatter inelastically off atomic nuclei in the Earth's atmosphere producing several types of secondary particles such as nuclear fragments and mesons (mainly pions). These particles scatter again or in the case of unstable pions and kaons decay producing electrons, muons and neutrinos.

Hadronic interaction processes are much more complex and, thus, modeling them is more difficult. There are two different types of hadronic interaction models. Older models usually simply interpolate or extrapolate spline functions between experimental data derived from collider experiments. Recent hadronic interaction models are still of a phenomenological origin, but are based upon an underlying physical theory. The free parameters of such a theory are obtained from experimental collider data. Overall the theoretical descriptions available are strongly model dependent, especially in the forward direction, where it is difficult to obtain experimental data with colliders.

KASCADE uses an interaction model developed by Gaisser et al. (1983). It determines the momenta (parallel and transverse) of the leading particle produced by the interaction as well as the number and momenta of produced mesons. The model is based on data that was obtained from hadron-nucleus and pion-nucleus interaction measurements in an energy range between 20 GeV and 20 TeV and is able to reproduce experimental data (Kertzman and Sembroski 1994). The data available at the highest energies originates from emulsion-chamber experiments measuring cosmic rays.

Further, KASCADE models the emission and propagation of Cherenkov photons by the shower particles. In the atmosphere Cherenkov photons are partially scattered by atoms and molecules (Rayleigh scattering) or by aerosols (Mie scattering). Rayleigh scattering describes the scattering of electromagnetic radiation by particles much smaller than the wavelength of the radiation. It is strongly wavelength dependent ($\sim \lambda^{-4}$) so that shorter wavelengths (blue) are scattered much more efficiently than longer wavelengths (red). Rayleigh scattering of the sunlight, e.g. causes the diffuse sky radiation which is the reason for the blue color of the sky. In contrast Mie scattering describes the scattering of electromagnetic radiation by particles that are of similar size or larger than the wavelength of the light. In the atmosphere Mie scattering is caused by, e.g. pollen, dust, smoke and microscopic water droplets. It occurs mostly in the lower parts of the atmosphere where larger particles are more abundant. Further, it dominates

in cloudy conditions.

The atmosphere is modeled in several layers, each is in thermal equilibrium but with different properties such as the atmospheric density and the number density of aerosols. The atmospheric profile is expressed as a function of atmospheric depth traversed in g/cm^2 . Here, an all-year average atmosphere profile, called Windhoek Average (Konrad Bernlöhner 2001), is used.

This atmospheric profile is based on data of the Windhoek atmosphere recorded with sounding balloons (Konrad Bernlöhner 2001). Sounding balloons carry instruments aloft to measure the atmospheric pressure, temperature, humidity and wind speed. This data provide input values for atmospheric models that are constructed with the commercially available MODTRAN package (Kneizys et al. 1996), which models atmospheric propagation of electromagnetic radiation. Realistic scattering and absorption coefficients were calculated with MODTRAN. The model atmospheres are given in the form of text-format tables. For the simulations of Cherenkov photons, hadrons and muons the atmospheric density values are simply interpolated between the tabulated values. For electron-gamma shower simulations the tabulated values are fit by piece-wise exponential functions (Bernlöhner and H.E.S.S. collaboration 2005).

While the total atmospheric transmission can be measured with optical telescopes using stars, it is impossible to measure the profile of the number densities of molecules and aerosols directly, which is the reason why the MODTRAN package is used to calculate the atmospheric profiles. The molecular density profile (and, thus, Rayleigh scattering) is relatively stable in time and does not introduce large uncertainties in the modeling of the atmospheric transmission. It is much more difficult to model the concentration of aerosols in a realistic way, because it changes on short and long time scales due to, e.g. seasonal changes, bush fires or volcanic eruption. Thus, the main practical problem of modeling the transmission of Cherenkov light in the atmosphere are the properties and the vertical profile of aerosols. For a discussion of the impact of different atmospheric profiles on shower simulations see Bernlöhner (2014).

In addition, KASCADE must be provided with a rough description of the instrument containing size, position, number of telescopes as well as the quantum efficiency of the photo-multipliers used in each telescope. Here, parameters of the H.E.S.S. I array are used and no quantum efficiency is provided (KASCADE Configuration: NoQueffProv). The performance of KASCADE was studied by Guy et al. (2002) who compared the results of KASCADE simulations to the results of the MASS2 balloon experiment (Bellotti et al. 1999 and Circella 1999) and the air shower generator CORSIKA (Heck et al. 1998). It was found that the longitudinal profile of proton, helium and muon fluxes measured with the MASS2 balloon are well reproduced by KASCADE and CORSIKA.

Either point-like or extended/diffuse sources of particles can be simulated with the `kaskade_cpp` software module by adjusting the angular acceptance range (default: minimum and maximum angular acceptance are 0°). The default value is defined for a point-like source and must be adjusted for diffuse simulations. The choice of the maximum accepted angular distance is a compromise of the need to cover the entire FoV of the telescopes for diffuse simulations and to minimize the number of events that are lost, because they are initiated too far away from the telescopes. For these reasons the maximum angular distance of the simulated events was set to 3.2° . Several different azimuth angles (0° , 90° , 180° , 270°) and zenith angles

of the observation can be selected (0° , 18° , 26° , 32° , ..., 70°). The simulations can either be performed at a fixed energy (parameters: energy and maximum impact distance) or for a given energy spectrum (parameters: spectral index and minimum energy).

In this study exposures for cosmic-ray electrons are needed. Consequently, electrons were simulated. For electromagnetic air showers a few hundred thousand simulations are sufficient. The configuration used in this work is summarized below:

- Primary particle: Electron
- Injection depth: 1 g/cm^2
- First interaction height: 0 (interaction height is not fixed)
- Field of View: 7° (half the diameter of virtual telescope FoV)
- KASCADE Configuration: NoQeffProv ($Q_{\text{eff}}=1$)
- Site: Namibia
- Magnetic field: $B_{\text{north}} = 0.12082 \text{ G}$, $B_{\text{east}} = -0.03074 \text{ G}$, $B_{\text{down}} = -0.25906 \text{ G}$
- Observatory altitude: 1800 m
- Telescope layout: HESSPhase1 (4 telescopes)
- Zenith angles: 0° , 18° , 26° , 32°
- Azimuth angle: 180°
- Min. angular acceptance: 0°
- Max. angular acceptance: 3.2°
- Spectral index (integrated): 1 ($N \sim E^{-1}$)
- Minimum energy (spectrum): 0.03 TeV
- Number of simulated showers: 800 000

Detector simulation with Smash

Cherenkov light emitted by particles in the shower is reflected by the mirrors of the telescope onto a camera creating an image of the shower. The detector simulation software Smash (Guy 2003) simulates the detector response to the incident Cherenkov light. First, the incoming photons are propagated from the mirrors to the pixels of the camera. This includes shadowing of the camera and masts, optical properties of the mirrors, acceptance of the pixels/quantum efficiency of the PMTs and loss of photons between mirrors and camera, as well as the reflectivity of the Winston Cones mounted to collect light more efficiently. Afterwards, the electronic signal in the trigger channel is simulated and raw data are calculated, where each pixel contains the

measured number of Analogue-to-Digital Converter (ADC) counts. This includes simulations of the NSB, the used trigger conditions as well as simulations of the electronic noise.

For a full simulation the camera images must be calibrated to relate the measured numbers of ADC counts in each pixel to the correct number of photoelectrons from Cherenkov light. This includes simulating the pedestal and the conversion factor between ADC counts and pixel charge in p.e. for each camera pixel. The pedestal (see Section 3.3.4) is the baseline signal in the cameras due to electronic noise and the NSB and must be subtracted from the total signal. The number of ADC counts above the pedestal value corresponding to one photoelectron is called the conversion factor (see Section 3.3.4) and is necessary to convert the ADC counts in the camera pixels to the correct number of photoelectrons. Thus, the conversion factor can be determined by simulating a single photoelectron run where every pixel in the camera is illuminated with a light intensity of one photoelectron per pixel on average.

The optical efficiency of the instrument, the combination of all instrumental effects described at the beginning of this paragraph, can be determined from images of isolated muon rings in the data. The mean lifetime of muons in their rest frame is only $2.2 \cdot 10^{-6}$ s corresponding to a distance of 660 m travelled. Since the muons are created at an altitude of about 10 km, a non-relativistic muon would decay before reaching the Earth's surface. Only highly relativistic muons can reach the surface of the Earth because of relativistic time dilation (Lorentz factor ≥ 20). These relativistic muons are highly penetrating, undergo virtually no nuclear interactions and suffer only a small amount of ionization losses. For highly relativistic muons the emitted Cherenkov light distribution no more depends on the energy of the muon ($\beta = 1$). Close to the Earth's surface the refractive index and consequently also the Cherenkov angle are relatively constant. Thus, the total number of emitted Cherenkov photons depends only on the distance travelled by the muon. There is a defined maximum height from which Cherenkov photons reach the telescope, which is determined by the Cherenkov angle and the mirror radius of the telescope. It follows that only Cherenkov photons that were emitted a few hundred meters above the ground are detected. Since the Cherenkov angle and the traversed distance are essentially the same for all muons reaching the Earth's surface it is straight forward to calculate the expected Cherenkov light distribution. By propagating this distribution through the detector the expected light intensity of the muon ring is determined and compared to the actual intensity. From the relationship of those two images the current optical efficiency of the instrument is derived.

The typical overall optical efficiency is of the order of 10 %. With time the instrument ages and the mirror reflectivity decreases. In addition, dust affects the instrument. These effects must be taken into account and can also be simulated with Smash. In this study, data taken over several years are used, so that an accurate treatment of the optical efficiency is indispensable. Therefore, the detector was simulated for optical efficiencies between 40 % and 90 % of the optical efficiency of a perfect telescope¹¹.

The CamOptimal_hwtrig_effXX configuration was used to simulate the H.E.S.S. I telescope. The CamOptimal_hwtrig configuration simulates a perfect telescope with a realistic trigger, but without a central trigger and a NSB rate of 0.1 GHz. XX is the optical efficiency in percent. The total configuration used is for example CamOptimal_hwtrig_eff80. In this case

¹¹Note: often this relative value is called optical or muon efficiency. This study will also follow this practice.

the telescope was simulated with a 20 % efficiency drop with respect to a perfect telescope. Muon efficiencies of 40 %, 50 %, 60 %, 70 %, 80 %, 90 % were simulated. The most important configuration parameters are summarized below.

Optical Configuration: HESS1

- Dish radius: 7.0 m
- Focal length: 15.0 m
- Radius of the mirror element: 0.3 m
- Fraction of mirror area effected by the shadows of camera and mast: 0.11
- PSF (standard deviation): 0.017°
- Winston cone efficiency: 73 %
- Global optical collection efficiency: 40 % - 90 %
- Dish Type: Davies Cotton

Electronic Configuration: HESS1

- Duration of the simulated p.e. pulse in trigger and readout channels: 10 ns
- Rise time of the p.e. pulse in the trigger channel (at comparator entrance): 1.5 ns
- FWHM of the p.e. pulse in the trigger channel (at comparator entrance): 2.1 ns
- Width of the time window in which the simulation is performed: 40.0 ns
- Minimum charge over threshold: 7.5 pVs
- Nominal trigger pulse amplitude for a high gain of 80 ADC counts: 25.7 mV
- Rise time of the p.e. pulse in the readout channel: 2.4 ns
- Width of the p.e. pulse in the readout channel: 4.24 ns
- Delay time between trigger signal and start of the read out gate: 6.0 ns
- Width of the readout gate: 16.0 ns
- Delay between start of the background noise simulation and the first shower photon: 10.0 ns
- Number of ADC counts in the high gain channel corresponding to 1 p.e.: 80
- Voltage for one p.e. in pixel threshold: 28 mV
- Voltage for one p.e. in sector threshold: 42 mV

Background Configuration: 0.1 GHz

- Rate of NSB photons: 0.1 GHz

Trigger Configuration: 4-2.5/2

- Telescope multiplicity: 2
- Pixel threshold: 2.5 p.e.
- Sector threshold: 4 pixels
- Voltage for one p.e. in pixel threshold: 28 mV
- Voltage for one p.e. in sector threshold: 42 mV

Shower reconstruction with Hessana

The output of Smash are raw data camera images. Subsequently, the shower is reconstructed to get the direction, impact distance, energy and height of the first interaction. The procedure follows the model reconstruction as described in de Naurois and Rolland (2009). For each camera pixel the pixel *log*-likelihood and for each telescope the telescope *log*-likelihood is calculated. The pixel *log*-likelihood and, thus, the telescope *log*-likelihood depend on the level of NSB. The expectation value of the pixel *log*-likelihood (null-level) must be determined in order to calibrate the found pixel *log*-likelihoods. The null level is derived from simulations of gamma rays with a flat spectrum ($N \sim E^{-1}$) at a zenith angle of 0° . Gamma rays are used because shower pixels can be easily excluded. A correction table containing the null-level information for all camera pixels is produced. The correction is only applied to the final *log*-likelihood values and not during the reconstruction. The output DSTs have the same format as real data DSTs and can be analyzed in the same way as regular H.E.S.S. data.

MC distributions

The final output of the simulations are artificial data sets of diffuse electrons for all combinations of simulated zenith angles and optical efficiencies. Figure 5.11 shows the distribution (histogram with error bars) of the *MSSG* for different zenith angles at an optical efficiency of 60 %. The distributions are always roughly centered on zero, as they should be by definition. However, when going to larger zenith angles the distributions become more asymmetric with a tail towards larger *MSSG* values. In this analysis the standard cut for gamma-like events is $MSSG < 0.6$. This cut retains roughly 69 % of cosmic-ray electrons (for zenith angle = 0°). The more stringent cut $MSSG < -0.6$ however retains only 29 % of diffuse electrons (see the discussion in the last paragraph of this section).

Figure 5.12 shows the ratio of the reconstructed energy of an event and the energy at which the event was originally simulated (true energy) minus one, called relative energy bias, in dependence on the true energy. The relative energy bias presented here was calculated for all electrons (no *MSSG* cut was applied) passing shape and core distance selections discussed in

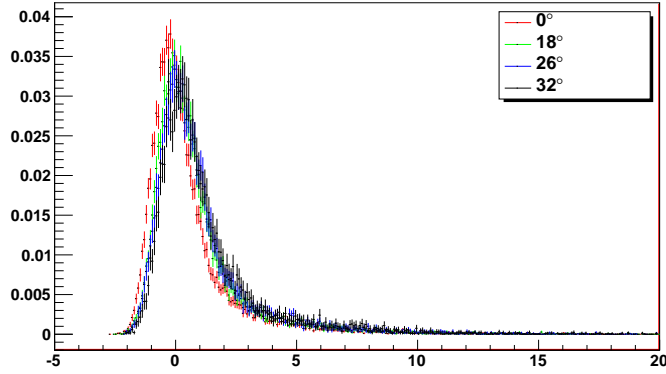


Figure 5.11: Distributions of the $MSSG$ for different zenith angles. The distributions shown were simulated at 60 % optical efficiency. Shape cuts and the core distance cut discussed in Section 5.1.3 were applied. No restrictions on the energy range were applied.

Section 5.1.3. A constant relative energy bias of zero would mean that the event reconstruction works perfectly and the energy is on average correctly reconstructed (without bias). Over a large energy range between approximately 0.4 and 7 TeV the relative energy bias is of the order of a few percent. Above 10 TeV the energy is underestimated, on average, by up to 50 %. In the energy range between 0.64 TeV and 1.04 TeV, which will be used for the anisotropy study, the energy is underestimated by less than 10 % at all zenith angles. At small zenith angles the relative energy bias is smaller than at larger zenith angles. In the energy range between approximately 300 GeV and 10 TeV the relative energy bias is comparable to the one found by de Naurois and Rolland (2009). Differences are found at very small (< 350 GeV) and very large energies ($\gg 10$ TeV) in regimes where the energy bias becomes larger.

At energies below 300 GeV de Naurois and Rolland (2009) find an energy bias smaller than 20 %, while here it was not possible to determine the energy bias below 350 GeV, because the minimum true energy in the MC data sample is 350 GeV. The relatively high energy threshold is probably caused by the choice of the image size cut, which is significantly larger (120 p.e.) than the one used in de Naurois and Rolland (2009) (60 p.e.). This selection removes low energy showers depositing not enough photoelectrons in the cameras from the data sample.

At very high energies de Naurois and Rolland (2009) mention that they find that very high energy showers are reconstructed too close to the telescope with underestimated energies. Here, a similar behavior is found at energies above 10 TeV. The main difference is that the effect is clearly visible at 20 - 30 TeV while it is not in the study of de Naurois and Rolland (2009), where it is only mentioned. The large relative energy bias found in this study is mainly due to $MSSG > 0.6$ electrons, which are included in this study but were excluded in the standard cut selection by de Naurois and Rolland (2009). When applying the $MSSG < 0.6$ cut the large energy bias at a few tenth TeV is removed.

There were further event selections applied that possibly cause minor differences between

the relative energy bias profiles found in this study and in the study of de Naurois and Rolland (2009). The core distance cut that was applied in this study possibly systematically selects distant high energy showers that are reconstructed too close (and consequently with too low energy) to the telescope array. Further, the simulations presented here were calculated at 60 % optical efficiency. Even though, the optical efficiency is taken into account at the reconstruction level and no further energy correction is necessary at a later stage, the optical efficiency of the simulations may influence the energy threshold of the events (in combination with the image size cut). Another trivial difference is the fact that in this study electron simulations were used while de Naurois and Rolland (2009) used gamma-ray simulations.

Efficiencies of gamma-hadron separation cuts

To measure the power of a cut to separate gammas from hadrons the quality factor (Q -factor) is commonly used, which is a quantity describing the gain in significance achieved by different separation algorithms or cut choices. In the analysis concerning cosmic-ray electron anisotropies the Q -factor is of minor importance, because the relative electron rate fluctuations and, thus, the dipole amplitude depends on the relative amount of electrons in the analyzed (gamma-like) event sample called electron fraction and discussed in Section 5.2.5. The electron fraction depends on the gamma-hadron separation parameter cut choice on the one hand and on the spectra of electrons and hadrons on the other hand. If the hadron flux is simply too large the electron fraction may still be too small for an anisotropy search, even though the Q -factor was

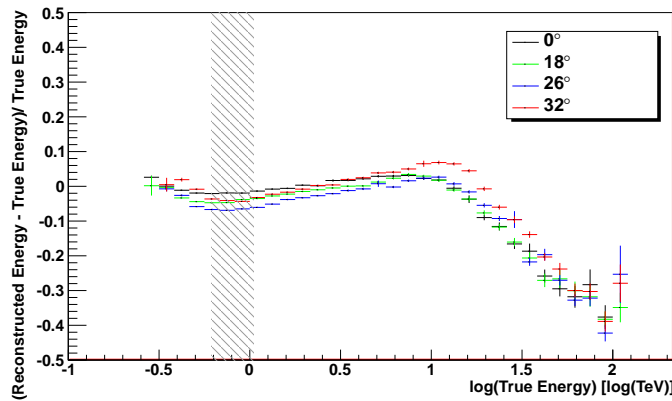


Figure 5.12: Profile of the difference between the reconstructed energy and the true energy normalized to the true energy in dependence on the true energy. The value of this ratio is always the mean value of the ratio for each bin in true energy. The error on the ratio is the standard error on the mean value within each bin in true energy. The black hatched interval indicates the energy range which is used later in the anisotropy studies. The profile shown was calculated from events simulated at 60 % optical efficiency. Shape cuts and core distance cut given in Section 5.1.3 were applied. No *MSSG* cut was applied.

optimized.

Here, the Q -factor is calculated in order to characterize the gamma-hadron separation cut choices used at some point in this study and to allow comparisons with previous and future studies.

The Q -factor is defined as the ratio of the electron efficiency compared to the square root of the hadron efficiency

$$Q = \frac{\text{eff}_{\text{el}}}{\sqrt{\text{eff}_{\text{had}}}}. \quad (5.8)$$

Here, eff_{el} and eff_{had} are the electron and hadron cut efficiencies. In general the cut efficiency for particle species s is defined as

$$\text{eff}_s = \frac{N_{s,\text{MSSGcut}}}{N_s}. \quad (5.9)$$

Here, N_s is the total number of events of species s (after previously applying event quality cuts and an energy cut) and $N_{s,\text{MSSGcut}}$ is the number of events of species s after applying an additional cut on the gamma-hadron separation parameter (here MSSG).

The MSSG cut corresponding to the highest quality parameter corresponds to the cut choice with the best relation between retaining gamma-like events and rejecting hadron-like events¹².

The electron efficiency can be calculated from the distribution of diffuse electron MC events discussed in Section 5.2.2. In this study no hadron MC simulations were performed, instead the cut efficiency is estimated from the MSSG distribution of events from an OFF region (Section 3.3.3). This data sample contains a certain residual amount of diffuse electrons (exactly those particles that we are searching for in this study), but for an estimation of the cut efficiency they are subdominant. The MSSG distribution of OFF-events is shown in Figure 5.13. The data shown is taken from an ON - OFF (ON minus OFF) analysis of 87 PKS 2155-304 runs (a subsample of the whole data set). In addition, the MSSG distribution of the ON region is shown. Both distributions are very similar at high MSSG ($\text{MSSG} > 5$), but in the ON-events a peak around zero is seen, which originates from source photons. Further, a distribution of ON - OFF events is shown, where the ON - OFF distribution for $\text{MSSG} < 0$ was reflected to positive values and fitted by a Gaussian. This approach illustrates the MSSG distribution of source photons, which is very similar to the MSSG distribution obtained for electrons from MC simulations in Section 5.2.2 (remember that gammas and electron initiated air showers look almost identical for gamma-ray telescopes).

Cut efficiencies and the Q -factor in dependence on the maximum allowed MSSG value are shown in the left-hand panel of Figure 5.14. As expected and required the hadron efficiency is much smaller than the electron efficiency. The electron efficiency rises steeply and reaches approximately one at $\text{MSSG} = 1$. In comparison the hadron efficiency rises much slower. In the right-hand panel of Figure 5.14 the development of the electron efficiency and the hadron efficiency relative to each other is shown for different MSSG cuts.

¹²This statement does not necessarily mean that the selected data sample contains more gamma events than hadronic events, because this relative amount is additionally influenced by the flux levels of the two particle types.

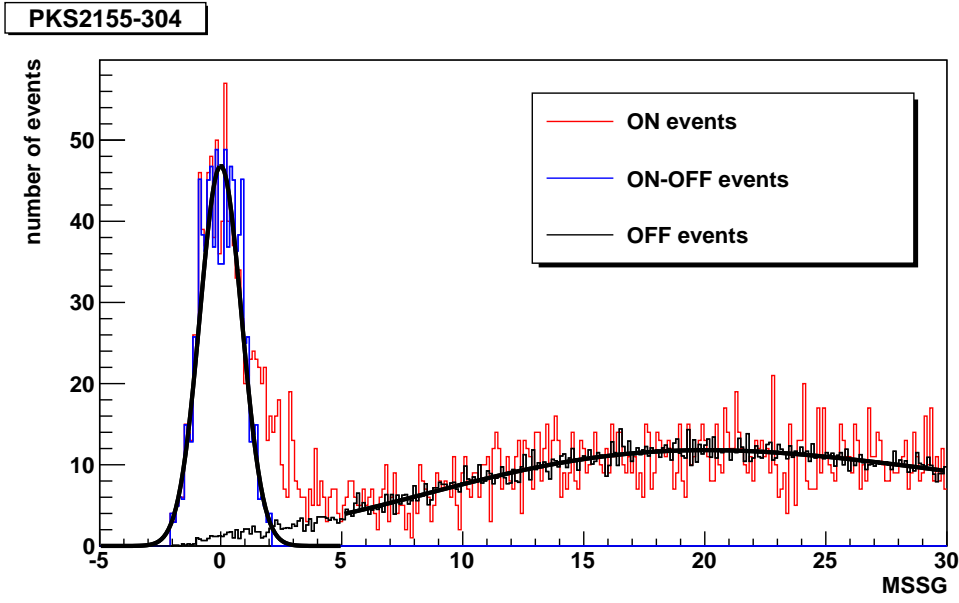


Figure 5.13: Distribution of the $MSSG$ for events in the ON region (red histogram) and OFF region (black histogram) of PKS 2155-304. In addition, a $MSSG$ distribution of ON - OFF events is shown where the ON - OFF distribution for $MSSG < 0$, was reflected on zero to positive values (blues histogram) and fitted by a gaussian (black line). For $MSSG > 5$ also the OFF event sample was fitted by a gaussian (black line). Shape cuts and core distance cut discussed in Section 5.1.3, as well as an energy cut (0.64-1.04 TeV) were applied to the data.

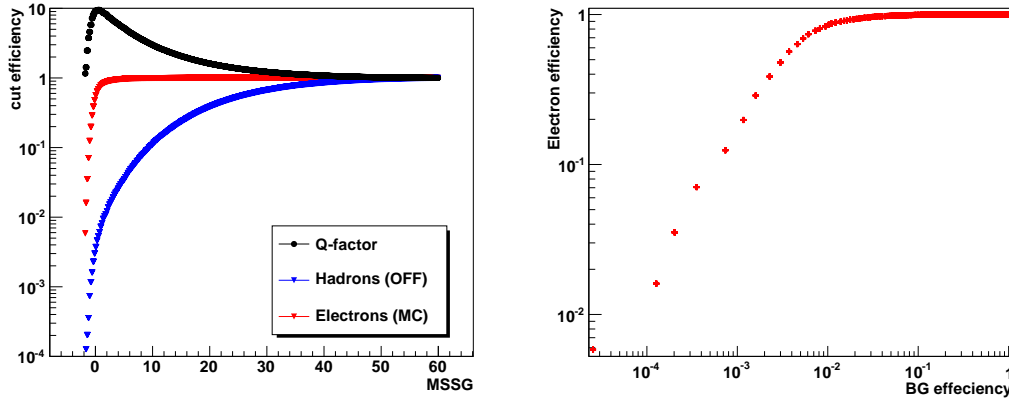


Figure 5.14: Left: Electron and hadron efficiencies as well as the Q -factor in dependence on the choice of the cut on the gamma-hadron separation parameter $MSSG$. Right: Development of the hadron efficiency relative to the electron efficiency. Previously, all shape cuts (see Section 5.1.3, the core distance cut and the energy cut ($0.64 < E < 1.04$ TeV)) were applied to both, OFF data and electron MCs. Electron MCs with a muon efficiency of 60 % and at 0° zenith angles were used.

The resulting electron and hadron efficiencies, as well as the Q -factor are summarized in Table 5.2 for selected $MSSG$ cut choices. The obtained Q -factor of approximately 9 is relatively large when compared to previous calculations by de Naurois and Rolland (2009). While the electron efficiency found in this study is almost equivalent to the gamma efficiency of approximately 70 % (for $MSSG < 0.6$) calculated by de Naurois and Rolland (2009), the hadron efficiencies differ by approximately a factor of 10.

The cuts used for the calculations of the efficiencies and the Q -factor are the same that are used later in the anisotropy search, because the efficiencies and Q -factor characterizing this specific analysis shall be presented here. In consequence there are several differences in the event selection process between the analysis by de Naurois and Rolland (2009) and this study.

In this study a cut on the distance of the shower core to the center of the telescope array (core cut) was applied, but not by de Naurois and Rolland (2009). In addition, only events with energies between 0.64 and 1.04 TeV were used to calculate the Q -factor. The influence of these cut choices on the efficiencies and the Q -factor was investigated by calculating both values, additionally, once without the core cut and once simultaneously without the core cut and without the energy cut. The resulting efficiencies and Q -factors are presented in Appendix A. Further, the Q -factor without the application of the core cut (Q_{NC}) and without the application of the energy cut and the core cut (Q_{NC}) are also given in Table 5.2. From these calculations it is obvious that the hadron efficiencies are more strongly influenced by the additional energy and core cuts than the gamma efficiencies. This results in smaller Q -factors without these cuts applied. Consequently, the discrepancy between the Q -factor found in this study and in de Naurois and Rolland (2009) can be partly explained by the differences concerning the discussed

$MSSG_{\max}$	eff_{el}	$\text{eff}_{\text{had}} = \text{eff}_{\text{OFF}}$	Q -factor	Q_{NC} -factor	Q_{NCE} -factor
1.0	0.778	0.0072	9.1	7.7	6.5
0.6	0.693	0.0053	9.5	8.0	6.7
0.4	0.635	0.0045	9.4	8.0	6.8
0.0	0.565	0.0037	9.3	7.8	6.7
-0.6	0.288	0.0016	7.2	5.9	5.4
-1.0	0.124	0.0007	4.6	4.2	4.3

Table 5.2: Table of electron and hadron efficiencies as well as the corresponding Q -factor for different choices of gamma-hadron separation cuts on the $MSSG$. The efficiencies and the Q -factor were calculated after applying all event selection cuts except the gamma-hadron separation cut ($MSSG$ cut). In addition, the Q -factor is also given without the application of the core cut (Q_{NC}) and without the application of the energy cut and the core cut (Q_{NCE}).

event selection cuts.

The remaining difference may be caused by the discrepancies between the requirements set on the image amplitude (minimum value of 120 p.e. in this study as compared to 60 p.e. used by de Naurois and Rolland 2009). This requirement may increase the relative number of high energy events in the data sample, which will improve the image quality and, thus, the ability of the $MSSG$ to separate gammas from hadrons.

Even though the found discrepancy has not been completely resolved at this point, it is not unlikely that it is caused by the special combination of event selection cuts used in this study. Since the discrepancy is irrelevant for the actual anisotropy analysis it was not investigated in more detail in this study.

5.2.3 Exposure Calculation

In the context of diffuse particle simulations it is not possible to separate the effective area A_{eff} from the solid angle element of the fraction sky that was observed (Ω), so that it is more appropriate to use the exposure where $\xi = A_{\text{eff}} \cdot \Omega$. With this definition the exposure is determined by the fraction of the particles surviving the selection (e.g. quality and gamma-hadron separation cuts) cuts $N_{\text{cuts,weighted}}$ and the total number of simulated particles N_{weighted} multiplied by the surface area A_{MC} in the detector plane on which the events have been randomly simulated and the solid angle element Ω_{MC} within which the electron incidence angle was drawn uniformly in $\cos \vartheta$

$$\xi = A_{\text{MC}} \Omega_{\text{MC}} \frac{N_{\text{MC,cuts,weighted}}}{N_{\text{MC,weighted}}}. \quad (5.10)$$

In the simulations a much flatter spectrum (index = 2.0) than the one expected from cosmic-ray electrons (index = 3.3) was employed in order to increase the accomplishable number of simulated particles at higher energies. In the exposure calculation this is accounted for by weighting every event i with a factor depending on its true simulated energy

$$f_{i,\text{weighting}} = \left(\frac{E_{i,\text{True}}}{0.1 \text{ TeV}} \right)^{-1.3}. \quad (5.11)$$

The index -1.3 in the weighting factor reintroduces the correct spectral shape (index expected in the data) and is given by the difference between the index of the simulated spectrum and the real expected index of cosmic-ray electrons ($I_{\text{weight}} = I_{\text{simulated}} - I_{\text{electrons}} = 2.0 - 3.3 = -1.3$). The true energy is divided by a minimum energy. The minimum energy was chosen below the energy threshold of the simulations ensuring that the weighting factor is always smaller than one. The weighting procedure is applied to both simulated events and events passing the event selection cut of this analysis to generate the particular weighted number of events. The MC area A_{MC} depends on the maximum impact distance (IP_{max}) from which the most energetic events can possibly still be seen with H.E.S.S. The impact parameter as well as the energies that are reasonably simulated depend significantly on the zenith angle as shown in Table 5.3. The MC area is given by $A_{\text{MC}} = \pi \cdot \text{IP}_{\text{max}}^2$.

The solid angle element of the sky Ω_{MC} from within which the electron incidence angle was drawn is given by the angular acceptance range of the simulation, which was set to $[0^\circ, 3.2^\circ]$

Zenith angle [deg]	Energy range [TeV]	IP_{max} [m]
0	0.030-100.000	550
18	0.032-105.146	578
26	0.033-111.260	612
32	0.035-117.918	649

Table 5.3: Dependence of the simulated energy range and the maximum impact distance on the zenith angle.

in order to cover the whole H.E.S.S. FoV of 5 degrees (full opening angle)

$$\Omega_{\text{MC}} = 2\pi(1 - \cos(\theta)) = 0.0098 \text{ sr} \quad \text{with } \theta = 3.2 \text{ deg.} \quad (5.12)$$

Here, θ is defined as half of the opening angle of the view cone. The error on the exposure is determined by the statistical error of the simulated particles

$$\sigma_{\xi} = \sqrt{\left(\frac{A_{\text{MC}} \Omega_{\text{MC}}}{N_{\text{MC,weighted}}} \sigma_{\text{MC,cuts,weighted}}\right)^2 + \left(\frac{A_{\text{MC}} \Omega_{\text{MC}} N_{\text{MC,cuts,weighted}}}{N_{\text{MC,weighted}}^2} \sigma_{\text{MC,weighted}}\right)^2}. \quad (5.13)$$

The error on the events passing the selection cuts $\sigma_{\text{MC,cuts,weighted}} = \frac{\sqrt{N_{\text{MC,cuts}}}}{N_{\text{MC,cuts}}} N_{\text{MC,cuts,weighted}}$ and the error on all simulated events $\sigma_{\text{MC,weighted}} = \frac{\sqrt{N_{\text{MC}}}}{N_{\text{MC}}} N_{\text{MC,weighted}}$ are determined by the corresponding unweighted event number. This way the correct spectrum is inserted correctly simultaneously benefiting from the large statistics at high energies of the simulated flat spectrum.

The exposure $\xi(E, z, \epsilon, d)$ depends on the zenith angle z , the optical efficiency ϵ and slightly on the angular distance between the pointing position and the actual position of the gamma-ray source that has been cut out d .

For each simulated combination of zenith angle and optical efficiency the exposure can be calculated following Equation 5.10. The dependency on the offset can be determined by artificially moving the source position in the camera and selecting only events outside the 0.4° radius around this artificial source position. There is only a weak dependency so that only four different offsets are used to reduce the calculation time. The calculation of the effective exposure valid for the total data set is presented in the following.

1. Zenith angle and offset: The $\xi(E, z_i, \epsilon_j, d_k)$ is interpolated between the available zenith angles z_i to get $\xi(E, z, \epsilon_j, d_k)$. Such an interpolation is shown in Figure 5.15 for $\epsilon = 50\%$ and d between 0 and 0.25.
2. Weighting: The $\xi(E, z, \epsilon_j, d_k)$ is weighted by the relative amount of live time t_{lk} of observations in the total data set (with total live time T_{total}) measured within a certain offset/zenith angle bin lk and integrated (in practice summed up), so that

$$\xi(E, \epsilon_j) = \sum_{l,k} \xi(E, z_l, \epsilon_j, d_k) \cdot \frac{t_{lk}}{T_{\text{total}}}. \quad (5.14)$$

The relative observation time t_{lk}/T_{total} is shown in the right-hand panel of Figure 5.15.

3. Optical efficiency: The exposure $\xi(E, \epsilon_j)$ is interpolated between the different optical efficiency values to get $\xi(E, \epsilon)$ as shown in the left-hand panel of Figure 5.16.

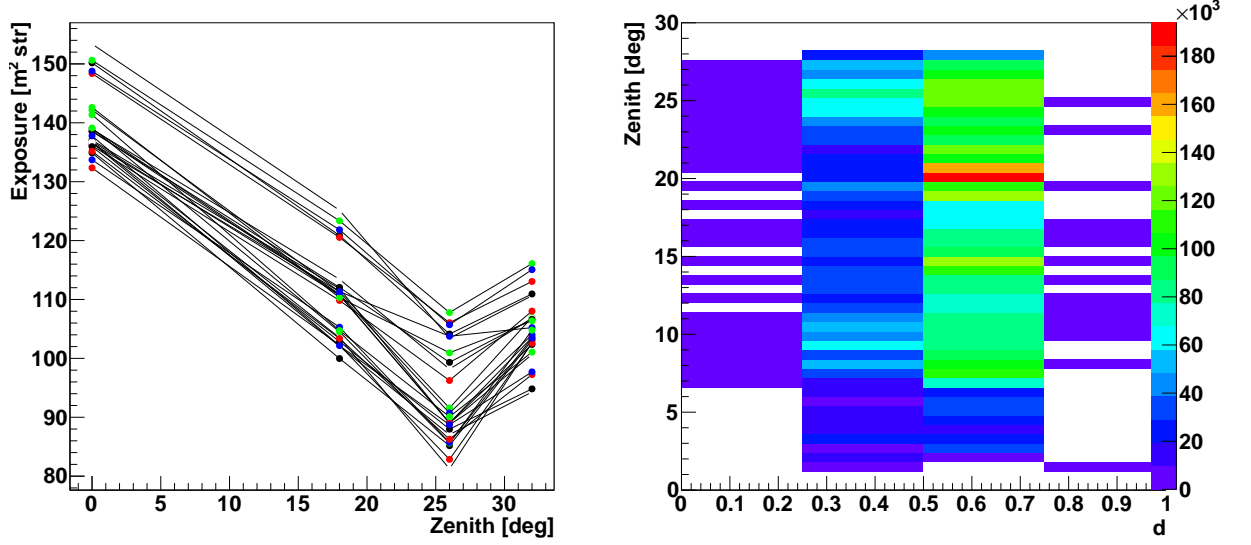


Figure 5.15: Left: Exposure in dependence on the different simulated zenith angles for $\epsilon=50\%$ and d between 0.00 and 0.25 degrees. Right: Live time distribution in the data set in dependence on zenith angle and offset d in degrees. The live time in seconds is given by the color code shown on the z-axis.

4. Weighting: The exposure $\xi(E, \epsilon)$ is weighted by the relative amount of live time t_m of observations in the total data set (with total live time T_{total}) measured within the optical efficiency bin m and integrated. The resulting exposure for the energy band between 0.64 - 1.0 TeV (Fermi energy scale) is given by

$$\xi(E) = \sum_m \xi(E, \epsilon_m) \cdot \frac{t_m}{T_{total}} \quad (5.15)$$

and shown in the right-hand panel of Figure 5.16.

The errors of the interpolated values are calculated by first calculating the error on the intercept and the slope of the regression line from the errors of the two sampling points between which the exposure was interpolated. Afterwards, the error on the interpolated exposure value is obtained via error propagation of the errors on the intercept and the slope of the regression line.

The effective exposure obtained for the entire data set in the energy range between 0.64 and 1.047 TeV is given by $\xi = 108.52 \pm_{11.65}^{11.67} \text{ m}^2 \text{ sr}$ for the $MSSG < 0.6$ cut. The obtained exposure values for all gamma-hadron separation cuts are also shown in Table 5.4 in Section 5.2.5.

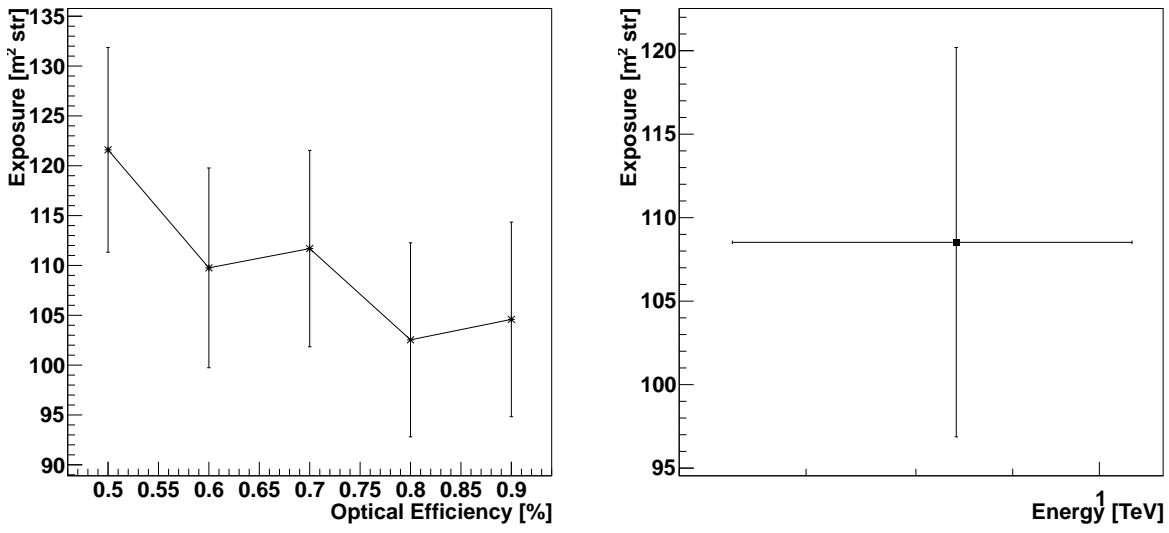


Figure 5.16: Left: Exposure in dependence on the different simulated optical efficiencies. Right: Exposure after being re-weighted with the relative amount of live time of observations within a certain relative optical efficiency band (as shown in the right-hand panel of Figure 5.3)

5.2.4 UL on the Cosmic-Ray Electron Spectrum

Using the H.E.S.S. exposure to diffuse electrons calculated in the previous Section and the total number of events in the electron-like regime (including the residual hadron and photon background) an upper limit (UL) on the electron flux can be determined employing a modified version of Equation 5.7

$$\frac{dF}{dE}_{UL} = \frac{N_{\tilde{\gamma}}(E)}{A_{\text{eff,el,H.E.S.S.}}(E) \Omega \Delta E \Delta t}. \quad (5.16)$$

Here, $N_{\tilde{\gamma}}$ is the total amount of gamma-like events measured (after all cuts).

$A_{\text{eff,el,H.E.S.S.}}(E) \Omega$ is the exposure calculated for electrons in Section 5.2.3. ΔE is the considered energy band and Δt the total live time of the observation. This equation necessarily gives a flux larger than the real electron flux, since the gamma-like event number must be larger than or equal to the number of electrons.

Thus, this method overestimates the electron flux by the amount of wrongly reconstructed background events which are treated like electrons. For the calculation of the UL on the electron flux the more stringent cut ($MSSG < -0.6$) was chosen in order to get as close as possible to the shape of the real cosmic-ray electron spectrum.

The actual electron spectrum was not derived in this study, because of the extensive computational and storage costs proton simulations would have required. Since such simulations were unnecessary for the study of anisotropies in the arrival direction of cosmic-ray electrons, which is the major focus of this thesis, here only an upper limit on the electron spectrum is presented.

In the top panel of Figure 5.17 the UL on the electron spectrum derived in this study is shown in comparison to the *Fermi*-LAT electron spectrum (Ackermann et al. 2010b) rescaled to the H.E.S.S. energy scale with an energy calibration factor obtained from cross calibration as described in Meyer et al. (2010) and the low energy and high energy H.E.S.S. electron spectra (Aharonian et al. 2008, Aharonian et al. 2009).

The arithmetic mean energy of all events contributing to the particular energy bin is used as the energy of the spectral point. The minimum and maximum energies determine the error bars in the x-direction. The error bars on the flux are rather large compared to the ones measured previously by the H.E.S.S. collaboration. The size of the error bars is mainly determined by the small statistics of the simulations in this study. Further, the statistics of the data set are also limited by the very stringent cut chosen for the upper limit ($MSSG < -0.6$) containing approximately 29 % of all electrons.

In the lower energy bins the UL lies above or approximately at the measured values by *Fermi* and H.E.S.S. and, thus, within the rather large error bars of this measurement the results are consistent. At energies above one TeV the UL drops down much faster than the measured H.E.S.S. electron spectrum. Thus, there is a certain tension between the results presented in this study and results from the previously published H.E.S.S. electron spectrum. The UL at higher energies (above approximately 1 TeV) lies far below the H.E.S.S. electron spectrum from Aharonian et al. (2008).

The most obvious difference between the published spectrum and the presented UL is that the spectral points in the published electron spectrum were always set to the arithmetic mean

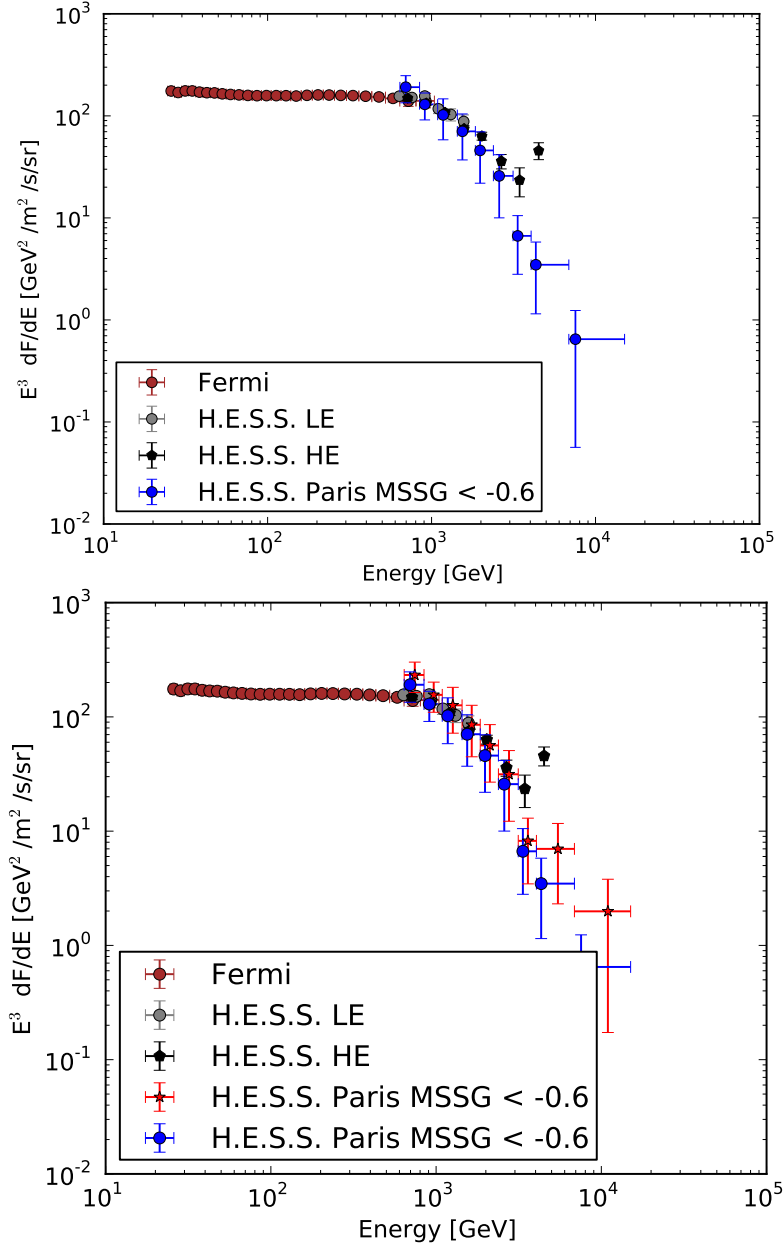


Figure 5.17: The electron spectra measured with H.E.S.S. (black and gray markers) and *Fermi*-LAT (dark red markers) are shown together with the upper limit derived in this study (blue markers). The energy of the spectral points from *Fermi* and H.E.S.S. are the arithmetic mean values of the minimum and maximum energies of the corresponding energy bin. The energies of the *Fermi*-LAT spectrum have been rescaled by an energy calibration factor obtained by Meyer et al. (2010) via cross calibration. For the upper limit the arithmetic mean event energy of all events contributing to the particular bin was used instead (blue markers). For comparison, the UL is additionally shown in the bottom panel using the arithmetic mean of the minimum and maximum energies (red asterisks).

energy of the minimum and maximum of the particular energy bin. This approach does not take into account what the arithmetic mean energy of the particles contributing to this energy bin really was. This influences the resulting spectrum/UL strongly as shown in the bottom panel of Figure 5.17, where the arithmetic mean of the minimum and maximum energies was used for the UL points (red UL) instead of the arithmetic mean event energy (blue UL). This does not only effect the energy values on the x-axis, but because of the chosen representation of the spectra and the UL (differential flux times E^3) also the values on the y-axis. When using the arithmetic mean of the minimum and the maximum as the UL point energy the published spectrum and the UL are already more consistent. In this study the arithmetic mean event energy was used for the UL on the electron spectrum, because this is more realistic.

The average energy bias discussed in Section 5.2.2 is smaller than 10% in both studies and, thus, most likely not responsible for the deviations between the UL and the previously published electron spectrum.

There are several influencing factors that could cause the remaining deviations between the published H.E.S.S. spectrum and the results presented here. Two different reconstruction chains were used, which can lead to differences in the spectra.

Further, hadron interactions at high energies are not well known, because no experimental data from colliders exists at these energies (and in the forward direction, as well as for high energy nuclei interactions), where a large number of neutral pions is produced. Comparisons of different hadronic interaction models have been performed revealing differences of 25 % to 40 % (Spurio 2015). Differences in electron spectra derived employing different interaction models were previously reported by Egberts (2009) and Kolitzus (2015).

In the study of Aharonian et al. 2008 only proton simulations at a zenith angle of 20° were used, which may introduce uncertainties depending on the level of dependence of the proton flux on the zenith angle. Even though, the result of the UL obtained in this study does not depend on proton simulations, the previously published electron spectrum does.

Additionally, the treatment of varying optical efficiencies in this study differs from the approach followed by Aharonian et al. (2008). There, they corrected the gamma-hadron separation parameter distributions and effective areas by a factor depending on the optical efficiency, while the *MSSG* distribution and exposure in this study were obtained directly from MC simulations with different optical efficiencies.

In the case of a not negligible anisotropy the deviating pointing patterns could also cause changes in the spectrum. Difference between spectra obtained from different data sets have been reported by Egberts (2009).

The rise in the published spectrum at high energies could be mimicked by an overestimation of the amount of electrons in the original electron analysis due to too small statistics in certain bins of the gamma-hadron separation parameter at high energies. In this case due to the large error bars it is easy to get a good fit to the data, but also the uncertainties on the fit parameters get larger. Combined with correctly calculated effective exposures for electrons an overestimated amount of electrons could lead to an artificial rise in the resulting electron spectrum.

Deviations between the published electron spectrum and new spectra currently obtained within the H.E.S.S. collaboration were also found by Kolitzus (2014). The major difficulty

appears to be a strong dependence on the optical efficiency when going to larger data samples taken over a long period of time and the subsequent necessity for proton and electron simulations at different optical efficiencies Koltz (2015).

Further, differences were even found reanalyzing the original data set with the original method as used in Aharonian et al. 2008. The only difference was the version of the analysis software used and that the data had been newly calibrated. Thus, the electron spectrum seems to be quite sensitive to small changes in the analysis chain.

In general, the approach employed in this study has the advantage of not depending on possibly unreliable proton Monte Carlo simulations nor on the type of the background particle considered. On the other hand, measured electron spectra, in this case from Fermi-LAT, are used, which are subject to statistical and systematic uncertainties.

5.2.5 The Electron Fraction between 0.64 and 1.04 TeV

The energy range of the *Fermi*-LAT and H.E.S.S. energy spectra overlaps in a small interval (one bin). Figure 5.17 shows the last *Fermi* energy bin between 0.615 TeV and 1.0 TeV (on the *Fermi*-LAT energy scale), which is equivalent to the energy range between 0.64 - 1.04 TeV on the H.E.S.S. energy scale. Since in this energy bin there is a very precise electron and positron flux measurement by *Fermi*-LAT¹³ and the effective exposure of the H.E.S.S. instrument to electrons (previous sections) is known the expected number of electrons can be compared to the actually measured number of gamma-like events in the data sample used in this study. The number of expected electrons for H.E.S.S. is calculated from the known *Fermi*-LAT flux in this energy bin $N_{\text{el}} = N_{\text{pred}}$ and the effective exposures from the previous simulations $A_{\text{eff,el,H.E.S.S.}}(E) \Omega \Delta E \Delta t$.

$$N_{\text{pred}} = N_{\text{el}} = \frac{dF}{dE}_{\text{Fermi-LAT}} A_{\text{eff,el,H.E.S.S.}}(E) \Omega \Delta E \Delta t. \quad (5.17)$$

Here, ΔE is the width of the considered energy bin and Δt the live time of the measurement. The integrated flux between 0.64 and 1.04 TeV measured by *Fermi* is $9.89 \pm_{1.22}^{1.61} \cdot 10^{-5}$ in units of $\text{cm}^{-2}\text{s}^{-1}\text{str}^{-1}$. The total live time of the data sample (all 108 pointings) is $5.3 \cdot 10^6$ seconds.

The actually measured events consist of electrons and background events (mainly protons and photons), so that the real composition is given by

$$N_{\tilde{\gamma}} = N_{\text{el}} + N_{\text{BG}},$$

so that the fraction of electrons ϵ_{el} in the total number of measured gamma-like events is given by

$$\epsilon_{\text{el}} = \frac{N_{\text{el}}}{N_{\tilde{\gamma}}}. \quad (5.18)$$

The error on the electron fraction is governed by the error on the predicted number of electrons and the error on the measured gamma-like event rate and is calculated via Gaussian error propagation

$$\sigma_{\epsilon_{\text{el}}} = \sqrt{\left(\frac{\sigma_{N_{\text{el}}}}{N_{\tilde{\gamma}}}\right)^2 + \left(\frac{N_{\text{el}} \sigma_{N_{\tilde{\gamma}}}}{N_{\tilde{\gamma}}^2}\right)^2}. \quad (5.19)$$

The resulting electron fractions, exposures ξ and numbers of γ -like events for all different gamma-hadron separation cuts used are summarized in Table 5.4.

¹³In principle there is an even better measurement of the electron and positron flux by AMS-02 (Aguilar et al. 2014a). For a discussion see Section 6.

γ -hadron cut	ϵ_{el}	ξ [m ² sr]	N_{γ}
MSSG < 0.6	$0.63 \pm_{0.11}^{0.13}$	$108.52 \pm_{11.65}^{11.67}$	89917 ± 300
- 0.6 < MSSG < 0.6	$0.60 \pm_{0.10}^{0.12}$	$82.28 \pm_{8.33}^{8.38}$	71682 ± 298
MSSG < -0.6	$0.76 \pm_{0.22}^{0.23}$	$26.24 \pm_{6.63}^{6.62}$	18235 ± 135

Table 5.4: Resulting effective exposures, the measured gamma-like event numbers and the electron fractions in the energy band between 0.64 and 1.04 TeV for the three different gamma-hadron separation cuts investigated in this study. The values and corresponding errors are given.

5.3 Search for Anisotropies in Cosmic-Ray Electron Arrival Rates

5.3.1 Electron Arrival Rates

The goal of this study is to evaluate whether cosmic-ray electrons (and positrons) arrive isotropically at Earth or not. This question is closely related to production and propagation mechanisms relevant for cosmic-ray electrons. The flux of cosmic-ray electrons is the physical quantity that must be considered in such a study. Aharonian et al. (2008) (AH08) have shown that it is possible to reconstruct the electron spectrum rather well with IACTs. In AH08 the diffuse electron flux was obtained from data taken from positions all over the sky and possible differences of the electron flux when looking into varying directions were not taken into account. Due to the rather small data sample and additional systematic effects this was a reasonable approach.

This study is dedicated to the search for such variations in the flux depending on the observational direction. It is a continuation of the diploma thesis of Marco Prüser (Prüser 2012), who derived an upper limit on the dipole amplitude based on the data sample already used by AH08 to derive the cosmic-ray electron spectrum.

The available data samples (even with a much larger data set than in the previous analysis) are too small to accurately reconstruct fluxes from every pointing direction. In the approach used in AH08 the simulated distributions of the gamma-hadron separation parameter ζ for electrons and protons were fit to the distribution of this parameter obtained from the measurement (of gamma-like events) in order to retrieve the relative amount of protons and electrons present in the data set. In order to obtain a flux as accurate as the one in AH08 for every direction in the sky the measured distribution of the ζ parameter must be equivalently well known. In other words the same amount of data as in AH08 would have to be available for every investigated direction of the sky. In fact the available data is distributed very inhomogeneous between different directions in the sky making a good flux reconstruction for most directions impossible with the method used in AH08.

Instead, a more direct approach is employed using the measured arrival rate of cosmic-ray electrons. This has the advantage that gamma-like events must not be binned within a distribution but can all be used. The background should consist mainly of protons where the level of anisotropy is of the order of 10^{-3} (see the discussion Section 2.1.2) and, thus, much smaller than the one searched for in this study. Therefore, it is assumed that the background level is constant over the whole sky. Since the electron flux has been well measured by *Fermi*-LAT in the energy range between 0.64 and 1.0 TeV this information was used to obtain the electron fraction in Section 5.2.5 giving a relative amount of electrons ϵ_{el} in the data set of 63 % ($MSSG < 0.6$). Consequently, the relative amount of background particles is given by $1 - \epsilon_{\text{el}}$. Thus, the universal background level can be easily subtracted from the gamma-like event rates employing the electron fraction and the best estimator for the mean gamma-like event rate as will be shown below.

Another advantage of this approach is that it makes use of proton Monte Carlo simulations unnecessary. Those are always an uncertainty factor because the strong interaction physics at TeV energies is not understood (especially in the forward direction most relevant for the development of air showers) at the proton-proton interaction level. In air showers a large num-

ber of particles with small transverse momenta is produced. For such particles perturbative theory is not applicable, because the running coupling constant diverges. Further, only little experimental data is available in the forward direction from collider experiments. Thus, models describing strong interaction physics are usually a mixture of basic theoretical ideas and empirical parameterizations tuned to describe the available experimental data. In regions of the parameter space not yet covered by experimental data, e.g. in the forward direction, the models are based on extrapolations. The understanding of nucleus-nucleus interactions is even worse. The data available from fixed target experiments reaches only up to a few GeV/nucleus. Consequently, several different interaction models exist resembling the large uncertainties that result from the poor understanding of strong interaction physics. In dependence on the different interaction models results may vary between 25% and 40% (Spurio 2015).

The gamma-like event rate ($R_{i,\tilde{\gamma}}$) is determined from the total number of gamma-like events (in this case the number of events left after applying, e.g. the cut $MSSG < 0.6$) measured for each pointing $N_{i,\tilde{\gamma}}$ in the total live time of the observation of each pointing T_i and is given by

$$R_{i,\tilde{\gamma}} = \frac{N_{i,\tilde{\gamma}}}{T_i}. \quad (5.20)$$

In a gaussian approximation (valid for $N_{i,\tilde{\gamma}} \gtrsim 10$) the statistical error (68 % CL) on the gamma-like event rate is given by

$$\sigma_{i,\tilde{\gamma},\text{stat}} = \frac{\sqrt{N_{i,\tilde{\gamma}}}}{T_i}. \quad (5.21)$$

In a simple approach a relative uncertainty ϵ_{syst} is assumed for the treatment of the systematic error. Consequently, the absolute systematic error is defined as follows

$$\sigma_{i,\tilde{\gamma},\text{syst}} = \epsilon_{\text{syst}} R_{i,\tilde{\gamma}}, \quad (5.22)$$

where ϵ_{syst} is determined from the background event Rates ($R_{i,\text{BG}} = \frac{N_{i,\text{BG}}}{T_i}$ here, e.g. for $MSSG > 5$). The derivation of the systematic error will be discussed in Section 5.3.3.

The total error on the gamma-like event rate is then given by

$$\sigma_{i,\tilde{\gamma}}^2 = \sigma_{i,\tilde{\gamma},\text{stat}}^2 + \sigma_{i,\tilde{\gamma},\text{syst}}^2. \quad (5.23)$$

Addition in quadrature is allowed here, because the statistical and systematic errors are independent.

The mean gamma-like event rate $\langle R_{\tilde{\gamma}} \rangle$ over the whole sky can be divided into a mean hadron rate $\langle R_{\text{Had}} \rangle$, a mean photon rate $\langle R_{\text{ph}} \rangle$ and a mean electron rate $\langle R_{\text{el}} \rangle$

$$\langle R_{\tilde{\gamma}} \rangle = \langle R_{\text{Had}} \rangle + \langle R_{\text{ph}} \rangle + \langle R_{\text{el}} \rangle. \quad (5.24)$$

The hadron and photon events make up the background and, thus, together give the mean background rate $\langle R_{\text{BG}} \rangle = \langle R_{\text{Had}} \rangle + \langle R_{\text{ph}} \rangle$. The relative amount of electrons in the total amount of gamma-like events ϵ_{el} was calculated in Section 5.2.5 and amounts to 63 % ($MSSG < 0.6$).

This simultaneously gives the relative amount of background events in the entire gamma-like event sample as $1 - \epsilon_{\text{el}}$. Thus, Equation 5.24 is rewritten as

$$\langle R_{\tilde{\gamma}} \rangle = \langle R_{\text{el}} \rangle + (1 - \epsilon_{\text{el}}) \langle R_{\tilde{\gamma}} \rangle. \quad (5.25)$$

The mean electron rate $\langle R_{\text{el}} \rangle$ is then given by

$$\langle R_{\text{el}} \rangle = \epsilon_{\text{el}} \langle R_{\tilde{\gamma}} \rangle. \quad (5.26)$$

Note: Equation 5.26 can be generalized to all directions of the sky. However, in the case of anisotropy the fraction ϵ_{el} depends on the observation direction and the equation is valid in the following form

$$R_{\text{el}}(\vartheta, \phi) = \epsilon_{\text{el}}(\vartheta, \phi) R_{\tilde{\gamma}}(\vartheta, \phi). \quad (5.27)$$

Here, ϑ and ϕ are spherical coordinates (in this study usually Galactic coordinates are used).

5.3.2 Dipole Model

In previous studies of cosmic-ray anisotropies by, e.g. IceCube (Abbasi et al. 2011) it has been common to calculate an angular power spectrum from the measured sky map. In this study only 94 directions of the sky were probed. The sky coverage available is approximately 1.5% in a none continuous way¹⁴. Such an extreme windowing function¹⁵ has not been investigated in detail yet and may lead to meaningless results when trying to calculate the power spectrum. Several models predict a dominating dipole anisotropy in case of electron and positron acceleration by pulsars (di Bernardo et al. 2011) or even by production via self-annihilating or decaying dark matter (Borriello et al. 2012). Thus, the simple case of a pure dipole anisotropy is studied first. This is done by modeling the electron arrival rates with a simple dipole model. The electron event rate $R_{\text{el}} = R_{\text{el}}(R_{0,\text{el}}, \delta, \cos \vartheta)$ in each direction of the sky for a dipole with amplitude δ and a fixed probed direction of the dipole maximum is modeled by

$$R_{\text{el}} = R_{0,\text{el}} (1 + \delta \cos \vartheta). \quad (5.28)$$

Here, $\cos \vartheta$ is the angular distance between the maximum of the dipole event rate and the present position (e.g. pointing position). Both, δ and $R_{0,\text{el}}$ are free parameters of the model if the direction of the dipole maximum is fixed in advance. If the direction of the maximum of the dipole is not fixed this introduces two more free parameters defining the best-fit dipole position (see below). Thus, the dipole model for finding the *global* best-fit dipole has four free parameters.

A dipole model for the electron event rates translates into the following prediction for gamma-like event rates assuming that hadronic and photon background events are isotropic

¹⁴Calculated for 94 pointings with a solid angle of 2 msr.

¹⁵The windowing function describes the response of an experiment to the power in a particular mode of the underlying fluctuation spectrum. A windowing function often leads to a coupling of the modes. Mathematically, the convolution of the real spectrum with the windowing function gives the measured spectrum.

compared to electrons ($\langle R_{\text{had}} \rangle + \langle R_{\text{ph}} \rangle = (1 - \epsilon_{\text{el}}) R_{0,\tilde{\gamma}}$):

$$\begin{aligned} R_{\tilde{\gamma}}(R_{0,\text{el}}, \delta, \cos \vartheta) &= \langle R_{\text{had}} \rangle + \langle R_{\text{ph}} \rangle + R_{0,\text{el}} (1 + \delta \cos \vartheta) \\ &= (1 - \epsilon_{\text{el}}) R_{0,\tilde{\gamma}} + \epsilon_{\text{el}} R_{0,\tilde{\gamma}} (1 + \delta \cos \vartheta) \\ &= R_{0,\tilde{\gamma}} (1 + \epsilon_{\text{el}} \delta \cos \vartheta). \end{aligned} \quad (5.29)$$

The normalization of the γ -like event rates $R_{0,\tilde{\gamma}}$ is translated into the normalization of the electron event rates

$$R_{0,\text{el}} = \epsilon_{\text{el}} R_{0,\tilde{\gamma}}. \quad (5.30)$$

To calculate the measured electron rate for each pointing, the isotropic arrival rate of hadrons and photons is subtracted from the total γ -like event rate

$$R_{i,\text{el}} = R_{i,\tilde{\gamma}} - (1 - \epsilon_{\text{el}}) R_{0,\tilde{\gamma}}. \quad (5.31)$$

The error of the electron event rate is given by the error of the gamma-like event rate

$$\sigma_{i,\text{el}}^2 = \sigma_{i,\tilde{\gamma}}^2. \quad (5.32)$$

χ^2 -Fitting

For the dipole anisotropy analysis a standard chi-square method for observables with Gaussian-distributed errors is employed

$$\chi^2 = \sum_i \frac{[R_{i,\text{el}} - R_{0,\text{el}} (1 + \delta \cos \vartheta_i)]^2}{\sigma_{i,\text{el}}^2}. \quad (5.33)$$

Applying Equations 5.30 and 5.31 to Equation 5.33 the chi-square function is given by

$$\chi^2 = \sum_i \frac{[R_{i,\tilde{\gamma}} - (1 - \epsilon_{\text{el}}) R_{0,\tilde{\gamma}} - \epsilon_{\text{el}} R_{0,\tilde{\gamma}} (1 + \delta \cos \vartheta_i)]^2}{\sigma_{i,\text{el}}^2}. \quad (5.34)$$

The best-fit parameters for the normalization of the γ -like event rates $R_{0,\tilde{\gamma}}$ and the dipole amplitude δ are found by minimizing the chi-square function. A grid-scan of the parameters $R_{0,\tilde{\gamma}}$ and δ is performed. This procedure, in future called *local fits* for short, finds a minimum χ^2 and corresponding best-fit parameters for each locally probed direction of the sky (fixed directions!).

To find the *global* minimum, that is the direction of the dipole maximum fitting the data best, the procedure of finding the best-fit parameters is the same as in the *local-fits* approach except that the overall minimum of the χ^2 distribution and corresponding best-fit parameters are found. Thus, in this *global fit* two more free parameters, the angular coordinates of the dipole maximum (longitude l and latitude b either in galactic or equatorial coordinates) are involved. The angular distance $\cos \vartheta_i$ ¹⁶ between the dipole maximum (l, b) and the position of

¹⁶The formula for calculating the angular distance between two positions on a sphere was derived in spherical coordinates.

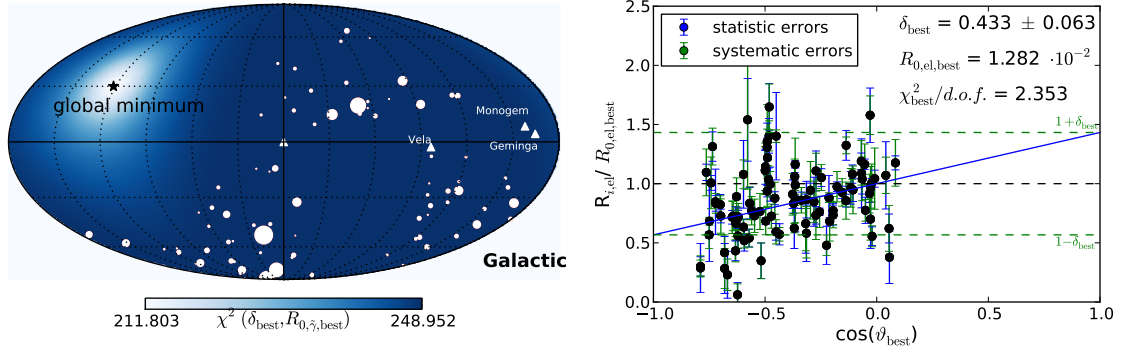


Figure 5.18: Left: Sky map color-coded with the values of χ^2 for each possible direction of the maximum of the electron rate in the sky. The white circles depict the 94 pointings and are scaled with the respective observation time (range from 0.24 to 173 h). The three pulsars Vela, Monogem and Geminga as well as the Galactic Center are also shown and marked by white triangles. The black asterisk indicates the position of the *global* minimum of χ^2 . Right: Graph of electron-arrival rates (black, normalized to the best-fit $R_{0,\text{el,best}}$) relative to the best-fit direction. The statistical (blue error bars) and systematic (green error bars) errors are shown. The dipole model for the best-fit dipole amplitude is represented by the blue line. The green dashed lines represent the minimum and maximum of the predicted electron arrival rates. In addition, information about the χ^2 -fit are given.

pointing i (direction for which to predict the electron arrival rate l_i , b_i) is given by

$$\begin{aligned} \cos \vartheta_i &= \cos(b_i) \cos(l_i) \cos(b) \cos(l) \\ &+ \cos(b_i) \sin(l_i) \cos(b) \sin(l) \\ &+ \sin(b_i) \sin(b). \end{aligned} \quad (5.35)$$

Thus, the dipole model for finding the *global* best-fit dipole has four free parameters.

Figure 5.18 (left-hand panel) shows the result of the χ^2 -fit for every probed direction in the sky (*local fits*) and the result of the *global fit* for the standard MSSG < 0.6 data set. The *global* best-fit direction is located in a direction of the sky where no pointings are located. The *global* minimum $\chi^2_{\text{min}} = 211.80$ corresponds to a reduced *global* chi-square $\chi^2_{\text{min}}/d.o.f. = 2.35$ for 90 *d.o.f.* (94 pointings minus 4 free parameters). As discussed in Section 4.1.1 a good fit requires a reduced χ^2 of approximately one with a correspondingly large p -value. The p -value found here is smaller than 10^{-11} corresponding to a significance larger than 5σ . Consequently, either assumptions made about the errors were wrong or the dipole model is not sufficient to describe the measured arrival rates of cosmic-ray electrons.

In the right-hand panel of Figure 5.18 the electron rates (normalized to $R_{0,\text{el,best}}$) in dependence on their distance to the best-fit direction are shown together with the best-fit dipole model. The rates scatter around the best-fit dipole model. The relative impact of statistical and systematic errors differs between the pointings, since individual statistical and systematic errors have been assigned to each pointing. In most pointings systematic effects dominate the

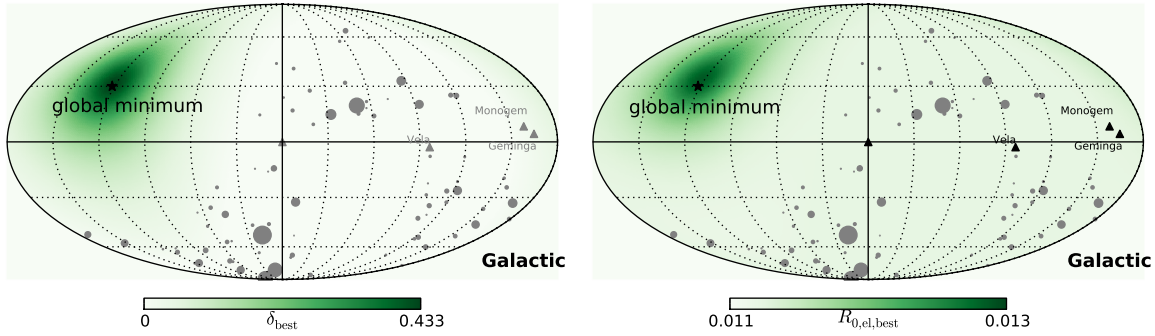


Figure 5.19: Left: Sky map color-coded with the best-fit values for the dipole amplitude δ_{best} for each possible direction of the maximum of the electron rate in the sky. Right: Corresponding map for the best-fit normalization $R_{0,\text{el,best}}$. The gray circles depict the 94 pointings and are scaled with the respective observation time (range from 0.24 to 173 h). The three pulsars Vela, Monogem and Geminga and the Galactic Center are marked by a gray (left) or black (right) triangle. The black asterisk indicates the position of the *global* minimum of the χ^2 -fit.

error, but in some pointings (especially those that have been observed only in a few runs) the statistical error dominates.

The *global* best-fit dipole amplitude and best-fit $R_{0,\text{el,best}}$ are given in the right-hand panel of Figure 5.18. The *global* best-fit dipole amplitude is rather large (43%), while the *global* best-fit $R_{0,\text{el,best}}$ does not differ much from the weighted mean electron rate $\langle R_{\text{el}} \rangle = 1.12 \cdot 10^{-2}$ 1/s. The corresponding best-fit values for the *local fits* are shown in Figure 5.19. It should be noted that the best-fit dipole amplitude δ_{best} is largest in the direction where χ^2 is minimal, while the $R_{0,\text{el,best}}$ are relatively constant and do not vary much over the sky. Nevertheless, they also peak at the *global* best-fit position.

The *global* best-fit position is located in a region of the sky, where no observational data is available. In this region the predicted arrival rates are not constrained by observations so that the free parameters of the fit can obtain relatively large values and consequently relatively better fits to the data, when probing such directions.

The large minimal $\chi^2/d.o.f.$ and the resulting very small p -value point towards large discrepancies between the observational data and the predictions made by the dipole model. Consequently, also the predictive power of the best-fit parameters is impaired and the result cannot be interpreted as the detection of a dipole anisotropy in the arrival direction of cosmic-ray electrons with a dipole amplitude of 43%.

$\Delta\chi^2$ -Test

The chi-square calculated above constitutes a self-consistent way of evaluating how well a dipole model for the arriving electrons can describe the event rates measured with H.E.S.S. To find a statistical measure for the compatibility of the event rates with an isotropic distribution, the chi-square obtained with the dipole model is compared to an isotropic model, which assumes

that the electron arrival rate is identical in all directions of the sky. An unbiased estimator for the isotropic electron rate is calculated employing the relationship in Equation 5.26 from the weighted mean of the gamma-like event rate

$$\langle R_{\tilde{\gamma}} \rangle = \frac{\sum_i R_{i,\tilde{\gamma}} / \sigma_{i,\tilde{\gamma},\text{stat}}^2}{\sum_i 1 / \sigma_{i,\tilde{\gamma},\text{stat}}^2}. \quad (5.36)$$

The isotropic chi-square is given by

$$\chi_{\text{isotropic}}^2 = \sum_i \frac{(R_{i,\text{el}} - \langle R_{\tilde{\gamma}} \rangle)^2}{\sigma_{i,\tilde{\gamma}}^2}, \quad (5.37)$$

with $R_{i,\text{el}} = R_{i,\tilde{\gamma}} - (1 - \epsilon_{\text{el}}) \langle R_{\tilde{\gamma}} \rangle$. The measure of the compatibility of the data with isotropy is given by

$$\Delta\chi_0^2(\delta_{\text{best}}, R_{0,\tilde{\gamma}}) = \chi^2(\delta_{\text{best}}, R_{0,\tilde{\gamma}}) - \chi_{\text{isotropic}}^2. \quad (5.38)$$

The $\Delta\chi^2$ -test is applied here even though, strictly speaking, only the first two criteria discussed in Section 4.2.3 (Gaussian distributed random variables and nested models) are fulfilled. The third criterion is not, but the problem is assessed in more detail in the subsection 'Significance Calculation via Monte Carlo Simulations'. Nonetheless, the method is used here for a simple first approximation.

As discussed in Section 4.1.1 the number of degrees of freedom of the fit is given by the number of data points N_{data} (here equivalent to the number of pointings) minus the number of free parameters. In the case of the isotropic model effectively δ was set to zero, so that only $R_{0,\text{el}}$ is fitted to determine $R_{0,\text{el,best}} = \langle R_{\text{el}} \rangle$ ¹⁷.

In the dipole model with a fixed probed direction of the sky (*local view*) there are two free parameters ($\delta, R_{0,\tilde{\gamma}}$). Consequently, the $\Delta\chi_0^2(\delta_{\text{best}}, R_{0,\tilde{\gamma}})$ is χ^2 distributed with one degree of freedom $DF = (N_{\text{data}} - 1) - (N_{\text{data}} - 2) = 1$. From the χ^2 distribution the p -value for a hypothesis test¹⁸ is calculated as explained in Section 4.2.

For the *global* best-fit dipole the procedure is the same except that the coordinates of the dipole maximum represent two more free parameters, so that the number of free parameters of the fit is four. Thus, the $\Delta\chi_0^2(\delta_{\text{best}}, R_{0,\tilde{\gamma}}, l_{\text{best}}, b_{\text{best}})$ is χ^2 distributed, but with three degrees of freedom $DF = (N_{\text{data}} - 1) - (N_{\text{data}} - 4) = 3$.

Figure 5.20 shows the results of the $\Delta\chi^2$ -test for every probed direction of the sky (*local fits*), as well as for the *global fit*. The sky map in the left-hand panel shows the $\Delta\chi_0^2$ distribution over the sky, while the corresponding *local-fit* p -value distribution is shown in the right-hand panel. Further, the p -value of the *global fit* is given in the right-hand panel (for the calculation and general meaning of p -values see Section 4.2). The minimum of the *local* p -values is not equivalent to the p -value of the *global fit*, because the number of degrees of freedom of the *local* $\Delta\chi_0^2$ s ($DF = 1$) and the *global* $\Delta\chi_0^2$ ($DF = 3$) differ. The *global* p -value ($p = 4.28 \cdot 10^{-8}$) is smaller than $5.7 \cdot 10^{-7}$, which corresponds to a 5σ effect. Thus, the null hypothesis that

¹⁷In fact the weighted mean of the electron arrival rates is equivalent to the best-fit $R_{0,\text{el}}$ parameter for a χ^2 -fit, where only statistical errors are taken into account.

¹⁸The null hypothesis is isotropy and the alternative hypothesis is the dipole model.

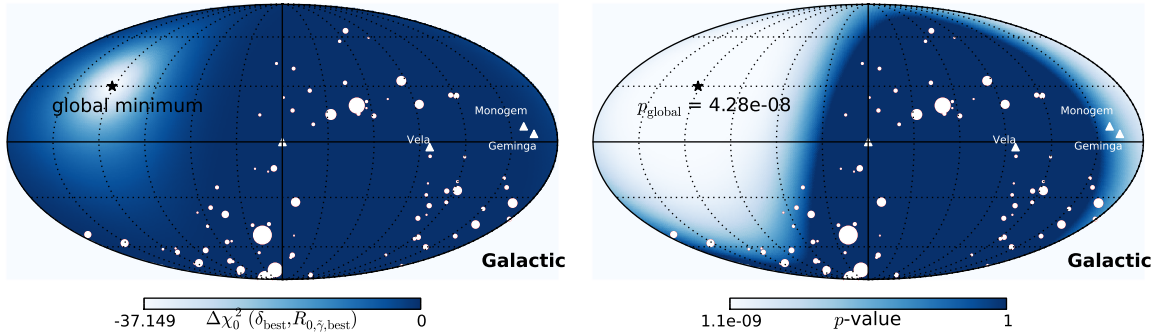


Figure 5.20: Left: Sky map color-coded with the values of $\Delta\chi_0^2$ for each possible direction of the maximum of the electron rate in the sky. Right: Sky map color-coded with the corresponding p -values. In both maps the white circles depict the 94 pointings and are scaled with the respective observation time (range from 0.24 to 173 h). The three pulsars Vela, Monogem and Geminga as well as the Galactic Center are shown and marked by white triangles. The black asterisk indicates the position of the *global* minimum of $\Delta\chi_0^2$.

electrons arrive isotropically can be discarded. The other way around it does not mean that the dipole model is correct. The improvement is simply large enough that the dipole term leads to a significant improvement of the fit, while the fit is not matching the data at a confidence level $> 5\sigma$, neither for the isotropic model nor for the dipole model. Thus, higher orders of multipoles appear to play a significant role¹⁹. Two different strategies to access these higher order anisotropies are presented in Sections 5.3.8 and 5.3.10.

F-Test

The $\Delta\chi^2$ does not take into account that a certain improvement of a fit is always expected when introducing additional free parameters. In this study a complex dipole model with four free parameters (*global fit*) / two free parameters (*local fits*) is compared to a simple isotropic model with one free parameter. The relative increase in the $\Delta\chi^2$ (going from the dipole model to the isotropic model) is expected to equal the relative increase in degrees of freedom (see Section 4.2.2), which is 3 % in the *global view* and 1 % for the *local view*.

In this application, where the reduced χ^2 is relatively large and the fit of the data consequently bad, the *F*-test has another advantage over the $\Delta\chi^2$ -test. Due to the definition of the *f* test statistic it takes the large absolute value of the χ^2 into account. The problem is that if the fit is bad giving a large χ^2 it is easier to achieve large $\Delta\chi^2$ values when adding additional free parameters to the model.

Thus, the *F*-test discussed in Section 4.2.2 is used to resolve the question whether the more complex model fits the data in fact significantly better than the simple isotropic model, or just because of its larger number of free parameters (two as compared to one for *local fits* and four as

¹⁹This conclusion can already be drawn implicitly from the χ^2 -fit result presented in the previous subsection χ^2 -Fitting.

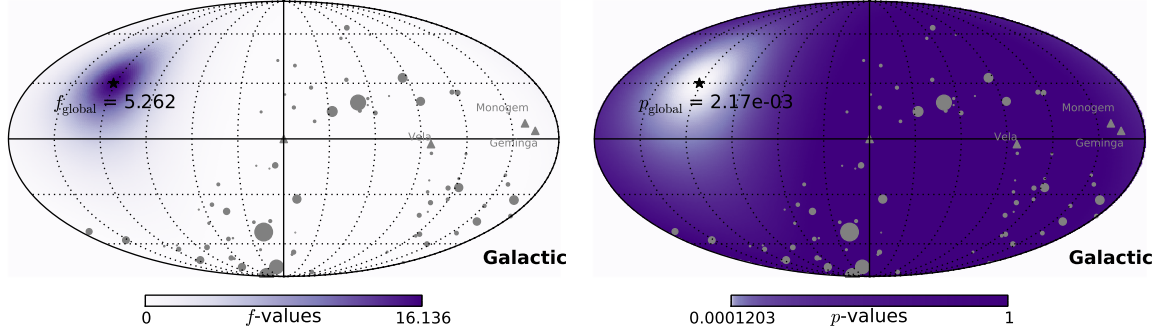


Figure 5.21: Left: Sky map color-coded with the f -values for each possible direction of the maximum of the electron rate in the sky. Right: Sky map color-coded with the corresponding p -values calculated from the F -distribution. In both maps the gray circles depict the 94 pointings and are scaled with the respective observation time (range from 0.24 to 173 h). The pulsars Vela, Monogem and Geminga as well as the Galactic Center are marked by gray triangles. The black asterisk indicates the position of the *global* maximum of f .

compared to one for the *global fit*). The same criteria of applicability that are valid for the $\Delta\chi^2$ -test also apply to the F -test. Again, the first two criteria discussed in Section 4.2.3 are fulfilled (event rates follow a Gaussian distribution and the two models are nested), while the third criterion is strictly speaking not fulfilled, but further discussed in the subsequent subsection ‘Significance Calculation via Monte Carlo Simulations’. The F -statistic is calculated following Bevington (2003)

$$f = \frac{(\chi_{\text{isotropic}}^2 - \chi^2(\delta_{\text{best}}, R_0, \tilde{\gamma})) / (DF_{\text{isotropic}} - DF_{\text{dipole}})}{\chi^2(\delta_{\text{best}}, R_0, \tilde{\gamma}) / DF_{\text{dipole}}}. \quad (5.39)$$

Here, $DF_{\text{isotropic}} = N_{\text{data}} - 1$ are the *d.o.f.* of the isotropic model and $DF_{\text{dipole}} = N_{\text{data}} - 2$ (for *local fits* with fixed directions) or respectively $DF_{\text{dipole}} = N_{\text{data}} - 4$ (for the *global fit*) are the *d.o.f.* of the dipole model. As discussed in Section 4.2 the p -value (p) is calculated using the cumulative distribution function of the F -distribution $F(x, dn, dd)$, where dn are the *d.o.f.* of the nominator ($dn = DF_{\text{isotropic}} - DF_{\text{dipole}}$) and dd the *d.o.f.* of the denominator ($dd = DF_{\text{dipole}}$)

$$p = 1 - F(f, DF_{\text{isotropic}} - DF_{\text{dipole}}, DF_{\text{dipole}}). \quad (5.40)$$

The p -value gives the probability that a system where the null hypothesis (here isotropic electron arrival rates) is true produces a data set with an f -value at least as extreme as the one found in the measured data set due to random fluctuations.

In this context, the resulting f -values and corresponding p -values are shown in the sky maps of Figure 5.21. The f -value for the *global fit* approach is much smaller than the maximum of the f -values of the *local fits* with fixed probed directions. As expected the directions of both maxima are the same. The different f -value magnitudes are caused by the fact that the definition of the f -value itself depends on the *d.o.f.* of the compared models. Analogously, the

minimum of the *local-fit* p -values and the *global* p -value differ by two orders of magnitude. In general, the obtained p -values are 5 orders of magnitude smaller than the p -values calculated from the $\Delta\chi^2$ -test (compare the right-hand panels of Figures 5.20 and 5.21).

In conclusion, the improvement in $\Delta\chi^2$ is most likely only partially caused by a higher number of free parameters. The p -value of the F -test is $2.17 \cdot 10^{-3}$ for the *global fit*, corresponding to a significance larger than 3σ ($p = 2.7 \cdot 10^{-3}$). Therefore, the dipole model explains the data significantly better than the isotropic model at the 3σ level. Consequently, the three additional free parameters, describing the dipole term, should be included in a model of cosmic-ray electron arrival rates. Contrariwise, this does not imply the detection of a dipole anisotropy since the dipole model does not fit the data well (result of χ^2 -test at beginning of this Section) as already discussed in the last subsection concerned with the $\Delta\chi^2$ -test.

Nonetheless, both, the estimation of the significance of the F -test and the $\Delta\chi^2$ -test suffer from significant associated problems. The $\Delta\chi^2$ -test takes neither the absolute value of the χ^2 into account nor accounts it for the improvement that is automatically achieved by introducing additional free parameters. The F -test accounts for both, but is strictly speaking not applicable (as also the $\Delta\chi^2$ -test) because the null value of the additional parameter of the more complex model is at the boundary of the set of possible parameter values, which is mathematically not allowed (Protassov et al. 2002, see also Section 4.2.3). In the case of the dipole model, the additional parameter is the dipole amplitude which is set to zero for the simple model. Since the value range for the dipole amplitude is constrained to $\delta \geq 0$, the additional parameter δ is in fact at the boundary of the possible parameter values.

Nonetheless, the F -test is probably a good measure, because in principle δ could be allowed to obtain negative values, which would just mean that the dipole minimum is located in the pixel direction. This would lead to a symmetric, second minimum in the $\Delta\chi^2$ -value sky distribution and a respective second maximum in the f -value sky distribution. Thus, the F -test should lead to useful results.

To ensure that this argumentation is actually correct simulations of the $\Delta\chi^2$ and f test statistics distributions were performed (for isotropy) and are presented in the next subsection. These simulations can help to estimate the true significance of the result.

Significance Calculation via Monte Carlo Simulations

N simulations of the null hypothesis, in this case isotropy, are performed. The pointing-pattern and live times from the real data set are used. The event rates for every pointing are drawn from a Gaussian probability distribution, where the weighted mean electron rate $\langle R_{\text{el}} \rangle$ is used as the estimate for $R_{0,\text{el}}$ of the null hypothesis and the width of the distribution is determined by the statistical and systematic errors present in the real data set for each pointing.

The dipole analysis ($\Delta\chi^2$ and f -value calculation for every probed direction in the sky and the *global* values) is performed on each simulated data set. It is performed for a sky map with 192 pixels (NSIDE = 4), which is a much smaller resolution than the one used in the previously shown sky maps (NSIDE=64, 49 152 pixel). It was found, that the resulting $-\Delta\chi_0^2 = 33.49$ and $f_{\text{best,global}} = 4.66$ and the minimum of the f -value (*local fits*) sky map $f_{\text{best,min}} = 14.30$ are smaller than the corresponding values obtained with higher resolution maps (which is expected because with a higher resolution also a smaller χ^2 will be reached), but the basic results of the fit are the same. Therefore, it was chosen to use low resolution sky maps for the simulations saving computing time. 10 000 simulations of isotropically arriving electrons were performed. This amount of simulations was a compromise between the desired achievable significance level (here up to p -values of 10^{-4}) and the amount of computational time required. 10 000 simulations took approximately 1 day, so that 100 000 simulations would already require 10 days and 1 million simulations 100 days of computing time²⁰.

From the resulting values of test statistics ($\Delta\chi^2$ and f) two different probability density functions were retrieved:

1. **Global view:** The probability density functions of the *global* $\Delta\chi_{0,\text{global}}^2$ and f_{global} values for the best-fit parameters of the *global fit*.
2. **Best-fit pixel view:** The probability density functions of $\Delta\chi_{0,\text{best}}^2$ and f_{best} values for the overall *best-fit pixel* of the *local fits*. The overall *best-fit pixel* is the pixel where the minimum χ^2 of all *local fits* (probed directions of the sky) was found.

The probability density function ρ is given by the number of simulations within a certain bin of TS -values (test statistic values) $N_{\text{simu},i}$ divided by the total number of simulations $N_{\text{simu,total}}$:

$$\rho_i = N_{\text{simu},i} / N_{\text{simu,total}} \quad (5.41)$$

Figure 5.22 shows the simulated probability density functions for the *global* best-fit $\Delta\chi_{0,\text{global}}^2$ and the $\Delta\chi_{0,\text{best}}^2$ for the *best-fit pixel* of the measurement, as well as the theoretical χ^2 distribution for 3 *d.o.f.* ($\chi^2(3)$) and 1 *d.o.f.* ($\chi^2(1)$), which were the distributions previously used to calculate the p -values of the corresponding $\Delta\chi^2$ -tests (see also Equation 4.8). At small $\Delta\chi_{0,\text{global}}^2$ the theoretical 3 *d.o.f.* probability density function and the corresponding simulated *global* one are very similar, but they start to differ at $\Delta\chi_{0,\text{global}}^2 > 10$, where the theoretical function proceeds steeper than the simulated *global* one. The simulated *best-fit pixel* probability density function $\rho(\Delta\chi_{0,\text{best}}^2)$ lies a little bit below the theoretical $\chi^2(1)$ function. Due to insufficient statistics at $\Delta\chi_{0,\text{best}}^2 > 15$ it is not possible to judge from Figure 5.22 whether

²⁰This time could, in principle, be reduced employing parallel computing.

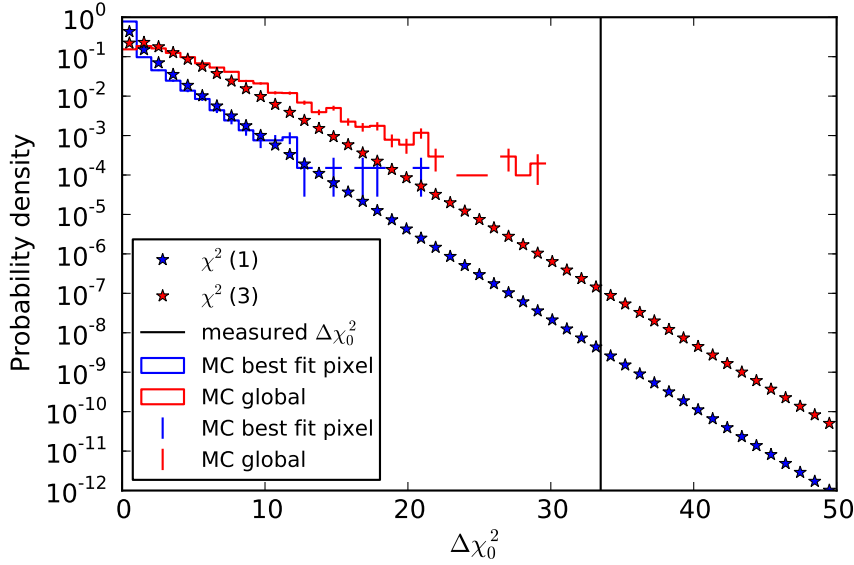


Figure 5.22: Probability density functions for $\Delta\chi_0^2$ are shown. The probability density functions from MC simulations for the *global view* $\rho(\Delta\chi_{0,\text{global}}^2)$ and for the *best-fit pixel* $\rho(\Delta\chi_{0,\text{best}}^2)$ are shown as red and blue histograms. The vertical bars indicate the statistical Poisson error (\sqrt{N}) of the simulations. The corresponding theoretical χ^2 distributions for 3 *d.o.f.* ($\chi^2(3)$) and 1 *d.o.f.* ($\chi^2(1)$) are represented by red and blue markers. The vertical line indicates the measured value of $\Delta\chi_0^2$ (for low resolution).

the two functions evolve away from each other similarly to the *global* functions $\Delta\chi_{0,\text{global}}^2$ and $\chi^2(3)$.

In general, the MC and theoretical probability density functions of the *global fit* lie above the functions for the overall *best-fit pixel* of the *local fits*, except in the very first bin (very small $\Delta\chi_0^2$), where the probability density for the *best-fit pixel* of the *local fits* is much larger than in the respective value of the *global fit*. This means that the probability to find large values of $\Delta\chi_{0,\text{best}}^2$ by chance (in the case of isotropy) is much larger when considering the whole sky (as one would expect).

Figure 5.23 shows the simulated probability density function of the *global* best-fit f_{global} -values and of the f_{best} for the *best-fit pixel* of the measurement (*local fits*), as well as the theoretical f -distributions for $dn = 3$ and $dd = 90$ in the *global view* and $dn = 1$ and $dd = 92$ for *local fits* with a fixed probed direction. These are the probability distributions previously used to calculate the p -values of the corresponding F -tests (see also Equation 4.8). The simulated *global* f_{global} and theoretical $f(3, 90)$ probability density functions differ only mildly. The simulated *best-fit pixel* probability density function lies a little bit below the theoretical function $f(1, 92)$. In this case the $f(1, 92)$ function seems to slightly overestimate the probability to

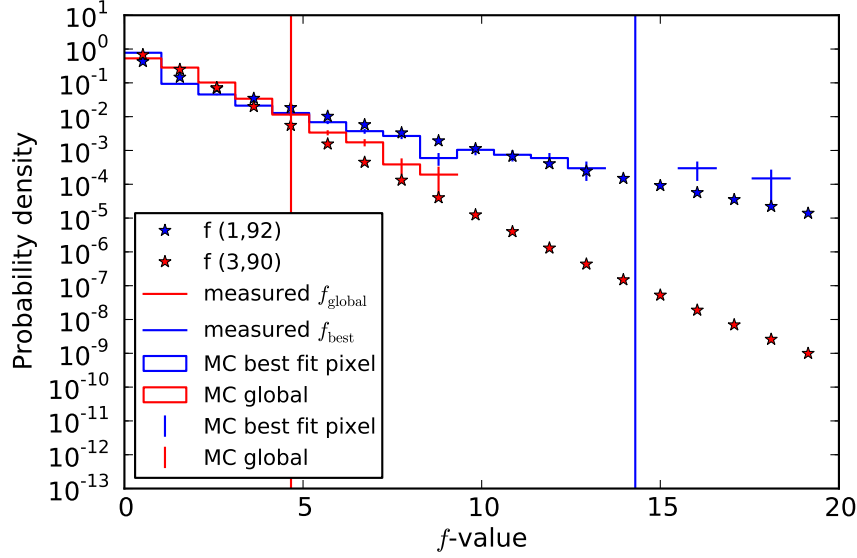


Figure 5.23: Probability density functions for f -values are shown. The probability density functions from MC simulations for the *global view* and for the *best-fit pixel* are shown as red and blue histograms. The vertical bars indicate the statistical Poisson error (\sqrt{N}) of the simulations. The corresponding theoretical f -distributions for $f(3,90)$ and $f(1,92)$ are represented by red and blue markers. The vertical lines indicate the measured values of f_{global} and f_{best} (for low resolution).

find large f -values up to 10^{21} .

The *global* MC probability density function and the corresponding theoretical $f(3,90)$ -distribution show the overall best agreement, while the *global* $\chi^2(3)$ -density function seems to underestimate the probability density function. This explains the relatively small p -values obtained with the $\Delta\chi^2$ -test. The p -value from the F -test, thus, seems to be the more reliable quantity.

The p -value calculated from simulations is given by the number of simulations resulting in a ts larger than the measured ts_{data} ($N(ts_{\text{simu}} \geq ts_{\text{data}})$) divided by the total number of simulations N_{simu} . It is calculated from the MC probability density functions via the following equation:

$$p = N(ts_{\text{simu}} \geq ts_{\text{data}}) / N_{\text{simu}} \quad (5.42)$$

Employing χ^2 statistics the measured values of $\Delta\chi_0^2$ are larger than any value occurring in a MC simulation, making it impossible to calculate actual p -values. In the case of the f statistic the measured f -value of at least the *global view* $f_{\text{global}} = 5.26$ lies within the corresponding MC probability density distribution. Nonetheless, since the *global* MC f -distribution and the

²¹It should be noted that the f -values found in the *global view* and the *best-fit pixel view* are not the same analogously to Section 5.3.2, because their values depend on the numbers of free parameters of the simple model and the complex model (as do the f -distributions).

Test statistic	TS_{global}	p_{global}	$p_{\text{global,MC}}$	TS_{local}	p_{local}	$p_{\text{local,MC}}$
χ^2	211.803	$< 10^{-11}$	-	-	-	-
$\Delta\chi^2$	37.149	$4.28 \cdot 10^{-8}$	$\sim 10^{-4} - 10^{-5}$	37.149	$1.10 \cdot 10^{-9}$	$\sim 10^{-5} - 10^{-6}$
f	5.262	$2.17 \cdot 10^{-3}$	$\sim 10^{-2} - 10^{-3}$	16.136	$1.20 \cdot 10^{-4}$	$\sim 10^{-3} - 10^{-4}$

Table 5.5: Summary of the results of the χ^2 -fit and the different hypothesis tests discussed in this Section. For the χ^2 -test only the p -value derived from the χ^2 -distribution is presented. For the $\Delta\chi^2$ and the f test statistics the p -values derived from the χ^2 and f probability density functions are shown as well as approximate ones from MC simulations.

theoretical $f(3, 90)$ distributions are very similar the previously calculated p -value seems to be a good estimator of the true p -value.

In summary, χ^2 -distribution and f -distribution p -values suggest a wide range of possible p -values between 10^{-3} and 10^{-8} as shown in Table 5.5. From MC simulations of the χ^2 probability density distribution in Figure 5.22 it can be concluded that the theoretical distribution underestimates the probability density function and, thus, also the p -value. Consequently, the $\Delta\chi^2_0$ test statistic is not χ^2 distributed and, thus, the p -values calculated from the χ^2 distribution are unreliable. Most likely there are two reasons responsible for this behavior. First, the $\Delta\chi^2$ distribution does not take the difference between the number of the free parameters of the two models into account. The improvement of the fit due to the larger number of free parameters compulsorily leads to higher $\Delta\chi^2$ values. Second, a large χ^2 (bad fit) of the complex model may also correspond to relatively larger $\Delta\chi^2$ values²². Both aspects are not taken into account by the $\Delta\chi^2$ -test, but they are accounted for by the F -test. Thus, this numerical experiment confirms the presumption that p -values obtained by the F -test are more reliable.

If the probability density function of the χ^2 in the *global view* actually saturates or continues to drop much slower than the theoretical function, the corresponding p -value would possibly be of the order of 10^{-4} to 10^{-5} . Consequently, the real p -value is estimated to be smaller than 10^{-3} and lies probably between 10^{-3} and 10^{-5} .

²²Note: Very small χ^2 values can have the same effect.

5.3.3 Systematic Effects

Since statistics of gamma-like events used in this study are rather small it is difficult to extract reliable information about systematic effects introduced by observational conditions. Gamma-like and hadron-like events were subject to the same observation conditions, e.g. weather and zenith angle distribution. Thus, we can benefit from the large sample of hadron-like (= background) events in order to assess the systematic uncertainties.

Normalized background rates are displayed in the left-hand panel of Figure 5.24. The arithmetic mean of the run-wise background event rates ($\langle R_{i,BG} \rangle = 4.15$ Hz) is three/four orders of magnitude larger than the arithmetic mean of the gamma-like rates ($\langle R_{i,-0.6 < MSSG < 0.6} \rangle = 1.35 \cdot 10^{-2}$ Hz and $\langle R_{i,MSSG < -0.6} \rangle = 3.44 \cdot 10^{-3}$ Hz) shown in the right-hand panel. The normalized background arrival rates are fit reasonably well by a Gaussian illustrated by a green line. Due to the high hadron-like event rates, statistical fluctuations do not play a significant role in their distribution. Therefore, the shape and width of the background distribution is dominated by systematic effects. The distribution of gamma-like event rates is much broader, since it contains significant contributions from both systematic and statistical effects. Additionally, the existence of an anisotropy in the arrival rates of cosmic-ray electrons would introduce further broadening of the gamma-like rate distribution.

The broadening of the gamma-like rate distribution can be characterized by comparing the relative standard deviation of the gamma-like rate distribution $\hat{\sigma}_{\tilde{\gamma}} = \sigma_{\tilde{\gamma}}/\mu_{\tilde{\gamma}}$ to the relative systematic error estimated from the hadron-like event sample $\hat{\sigma}_{BG} = \hat{\sigma}_{\text{syst}} = \sigma_{BG}/\mu_{BG}$ and the statistical error calculated from the mean gamma-like event rate $\mu_{\tilde{\gamma}}$ and the average live time t of a single run $\sigma_{\tilde{\gamma},\text{stat}} = \sqrt{\mu_{\tilde{\gamma}} t}/t$. The average live time of the observations is approximately 25.2 minutes. The relative variance expected from the relative systematic error and the relative statistical error of the gamma-like event rates is given by $\hat{\sigma}_{\tilde{\gamma},\text{stat}}^2 + \hat{\sigma}_{\text{syst}}^2$. All expectation values and standard deviations used are obtained from Gaussian fit functions of the distributions. The relative excess variance is defined by

$$\hat{\sigma}_{\tilde{\gamma},\text{excess}}^2 = \hat{\sigma}_{\tilde{\gamma}}^2 - (\hat{\sigma}_{\tilde{\gamma},\text{stat}}^2 + \hat{\sigma}_{\text{syst}}^2). \quad (5.43)$$

The relative statistical error $\hat{\sigma}_{\tilde{\gamma},\text{stat}}$, the relative systematic error $\hat{\sigma}_{\text{syst}}$, the measured relative standard deviation $\hat{\sigma}_{\tilde{\gamma}}$ and excess variance $\hat{\sigma}_{\tilde{\gamma},\text{excess}}^2$ of the gamma-like rate distribution are summarized in Table 5.6. For all gamma-hadron separation cut choices a relative excess variance that cannot be explained by statistical and systematic variances of 5 % to 9 % remains.

Possible sources of systematic rate fluctuations are the season of the year, the azimuth and zenith angles of the measurement and the year of the observation. Variations of the median, the 68 % percentile width, the mean and the standard deviation are investigated in dependence on these quantities in Figure 5.24. A comparison of the median/68 % percentile width and the mean/standard deviation is useful, because it gives information about the symmetry of the distribution and whether there is for example a tail in the distribution²³.

The right ascension is a measure for the season of the year when the measurement was carried out (second row of Figure 5.24). The standard error as well as the 68 % percentile

²³The mean is more sensitive to a tail, while the median is more stable.

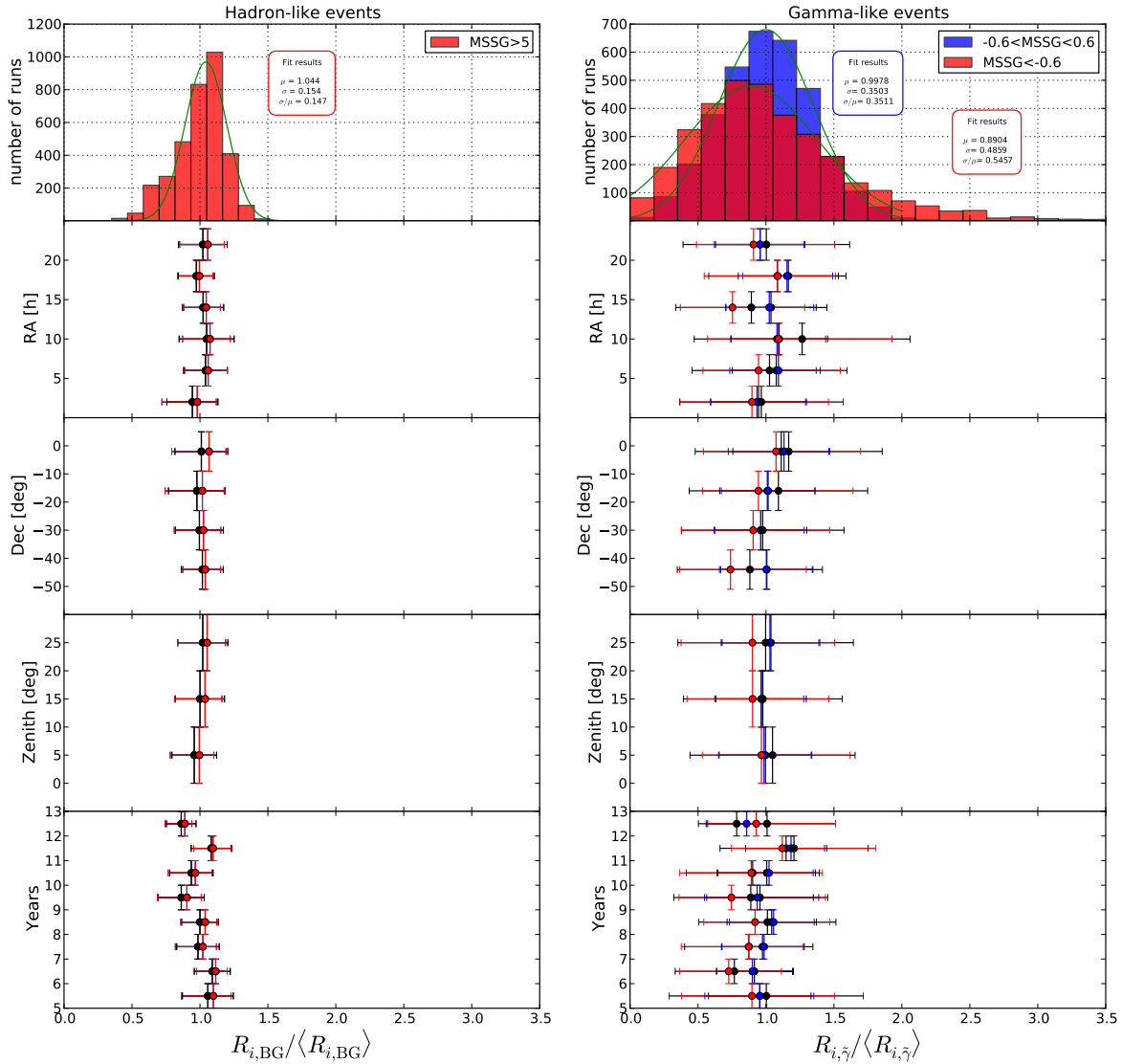


Figure 5.24: First row: Histograms of normalized hadron-like (left-hand panels) and gamma-like (right-hand panels) event rates of all observation runs. For the hadron-like events the standard cut $MSSG > 5$ is shown. For gamma-like events a strict cut $MSSG < -0.6$ and an intermediate cut $-0.6 < MSSG < 0.6$ are shown. The combination of both gives the distribution of the standard-cut sample ($MSSG < 0.6$). The results of Gaussian fits (green lines) of the distributions are shown in the red and blue boxes. In the second to fourth row the dependence of the event rates on the right ascension, the declination, zenith angle and year of the observation run are shown in terms of the median/68 % percentile width (colored) and the mean/standard error (black) of the binned distributions of the event rates.

γ -hadron cut	$\mu_{\tilde{\gamma}}$ [Hz]	$\hat{\sigma}_{\tilde{\gamma}}$	$\hat{\sigma}_{\tilde{\gamma},\text{stat}}$	$\hat{\sigma}_{\text{syst}}$	$\hat{\sigma}_{\tilde{\gamma},\text{excess}}^2$
$MSSG < 0.6$	$1.67 \cdot 10^{-2}$	0.3419	0.1986	0.1423	0.0572
$-0.6 < MSSG < 0.6$	$1.35 \cdot 10^{-2}$	0.5789	0.4770	0.1423	0.0873
$MSSG < -0.6$	$2.91 \cdot 10^{-3}$	0.3501	0.2212	0.1423	0.0534

Table 5.6: The relative statistical error $\hat{\sigma}_{\tilde{\gamma},\text{stat}}$, the relative systematic error $\hat{\sigma}_{\text{syst}}$, the measured relative standard deviation $\hat{\sigma}_{\tilde{\gamma}}$, the relative excess standard deviation $\hat{\sigma}_{\tilde{\gamma},\text{excess}}$ and variance $\hat{\sigma}_{\tilde{\gamma},\text{excess}}^2$ of the gamma-like rate distribution are summarized for all three investigated gamma-hadron separation cut choices. The systematic error is calculated from hadron-like events with $MSSG > 5$.

values lie well within the total width of hadron-like and gamma-like event distributions. No relevant systematic effect with the season is visible in the data, neither for gamma-like nor hadron-like events.

The combination of zenith angle cut ($z < 30^\circ$) and given declination angles constrain the azimuth angles contained within a declination band shown in the third row of Figure 5.24. A small systematic effect in dependence on the declination angle is found for gamma-like events for the strict cut choice. The systematic variation is of the order of 15-20 %, so well within the sensitivity to detect this as major contribution to the excess noise. The variation found in the hadron-like event sample in the left-hand panel of the third row of Figure 5.24 are much smaller and not dominating.

This effect is possibly related to the East-West effect (Olive et al. 2014). Low-energy cosmic rays are deflected by the Earth’s magnetic field, because the presence of the Earth effectively shadows certain trajectories, which are therefore forbidden. In a certain range of momenta and zenith angles positively charged cosmic-ray particles cannot arrive from the East, while they do arrive from the West. This effect should affect electrons more strongly, because their energies are relatively smaller than the energies of the hadrons present in the data sample, so that their gyroradii are also smaller. However, this effect should be subdominant, because showers from east and west are most likely mixed in some of the declination bands.

Another effect, possibly capable of causing the small effect in dependence of the declination angle is the North-South effect. The geomagnetic field influences the shower development and distorts the images of the air showers in the telescopes. The magnetic field vector depends on the location of the site considered. Further, the influence of the magnetic field on the development of a particle shower also depends on the direction from which the particle is approaching. In the case of the H.E.S.S. observatory (southern hemisphere) the vector of the magnetic field and the shower axis are almost parallel for particles approaching from the South and the influence of the magnetic field is negligible. Particles approaching from the North on the contrary experience a Lorentz force and electron-positron pairs in the air shower are deflected. As a consequence the effective area of the H.E.S.S. telescopes is most likely somewhat larger for particles approaching from the South (Krause 2011). On the other hand this effect appears to be disappearing at energies above 100 GeV in the study of Krause (2011). Since particle energies larger than 600 GeV relevant for this analysis were not studied by Krause (2011) it is uncertain whether this effect could account for the observed rate variations. Protons should be

less influenced by this effect, because they initiate air showers deeper in the atmosphere due to their relatively higher energies (in this data sample). Thus, the electron-positron pairs of proton initiated showers would be subject to the influence of the Earth's magnetic field for a shorter period of time.

A very small systematic effect is found in dependence on the zenith angle for background event rates (fourth row of Figure 5.24). The average background arrival rate drops with smaller zenith angle. This behavior is counter intuitive because the effective area and, thus, the trigger rate usually decline with larger zenith angle (except at very high energies of several TeV). However, this effect is still fully reflected in the width of the total background distribution.

The largest variations of gamma-like and background arrival rates are found in dependence on the year of the observation (fifth row of Figure 5.24). These variations appear not to be systematic and are probably due to long term changes in the observation conditions and possibly the optical efficiency of the instrument. These rate variations appear to be similar in background and gamma-like events. Thus, they can be taken into account by estimating these systematic effects from the background event data as explained below.

Spearman's Rank Correlation between Gamma-like and Hadron-like Event Rates

Since gamma-like and hadron-like event rates were obtained under the same observation conditions the minor systematic effects visible in the hadron-like event data should also be present in the gamma-like event data. Thus, there should be a relationship between the measured event rates of both event samples. This implied relationship can be assessed using Spearman's rank correlation coefficient (for a detailed discussion see Section 4.3.2). It was chosen because this study is interested in any kind of monotone relationship without requiring linearity. Spearman's rank correlation coefficient is calculated both, on the run-wise level and on the pointing-wise level between gamma-like event rates $R_{i,\gamma}$ (e.g. $MSSG < 0.6$) and hadron-like background event rates $R_{i,BG}$ ($MSSG > 5$).

Figure 5.25 shows gamma-like and hadron-like event rates as well as the calculated correlation coefficients and the corresponding p -values. Here, the p -value gives the probability that an uncorrelated system produces a correlation coefficient at least as large as the one measured between gamma-like and hadron-like event rates in this study. Thus, it gives information about the significance of the correlation.

On the run-wise level a significant moderate positive correlation of 0.45 with a p -value much smaller than 10^{-7} , corresponding to an effect with a significance larger than 5σ , is found for the standard $MSSG < 0.6$ cut. For the hard $MSSG < -0.6$ cut a low positive correlation of 0.28 with a likewise small p -value and high significance is found.

The correlation coefficients on the pointing and run-wise levels (Figure 5.25) are very similar, while the p -values are much larger on the run-wise level. However, for the standard cut the p -value is still smaller than 10^{-7} (significance larger than 5σ) on the pointing-wise level. Even for the strict cut the significance of the correlation is at the 3σ -level on the pointing-wise level ($p\text{-value} = 3.25 \cdot 10^{-3}$).

The significance on the pointing-wise level generally appears smaller than on the run-wise level, because the p -values are determined via a t -test (Section 4.3.2) and statistical errors are not taken into account. Altogether, it can be concluded that there is a significant monotone re-

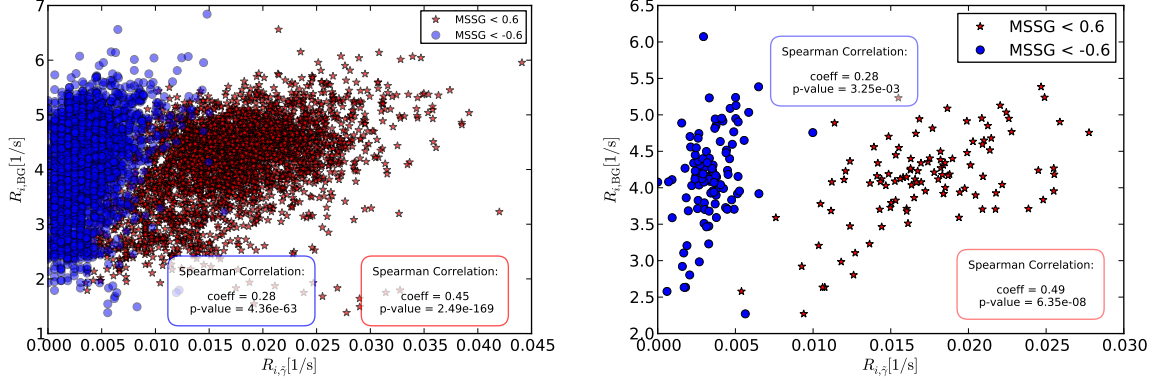


Figure 5.25: Left: Relationship between gamma-like (standard cut: $MSSG < 0.6$ and hard cut: $MSSG < -0.6$) and hadron-like event rates ($MSSG > 5$) on the run-wise level. Spearman's rank correlation coefficients and the corresponding p -values are shown. Right: Relationship between gamma-like (standard cut: $MSSG < 0.6$ and hard cut: $MSSG < -0.6$) and hadron-like event rates ($MSSG > 5$) on the pointing-wise level. Spearman's rank correlation coefficients and corresponding p -values are shown.

relationship/correlation between the two quantities and therefore hadron-like background events can be used to estimate systematic effects in the gamma-like event data.

Calculating the Relative Systematic Error

From cosmic-ray experiments, e.g. Ice Cube and ARGO-YBJ it is known that cosmic rays arrive isotropically at Earth with relative deviations less than 10^{-3} (e.g. Abbasi et al. 2011 and ARGO-YBJ Collaboration 2013). These are the same particles of which the hadron-like event data consists. The level of anisotropy searched for in this study is several orders of magnitude larger so that the hadron-like event arrival rate can be assumed to be perfectly isotropic. By definition systematic effects introduce deviations from this isotropy in the measured hadron-like events. Thus, these deviations must be accounted for in this study. The systematic effects vary between the different pointing positions, because for each pointing a different number of runs is used with different distributions of zenith angles, right ascensions and declinations, and also of inaccessible weather conditions. The relative systematic error is calculated in a two step approach. First, the unbiased estimator of the sample variance of all run-wise measured background rates is calculated for each pointing. The relative sample error of each pointing i is given by

$$\epsilon_{i,\text{sample}} = \frac{\sqrt{\frac{1}{n-1} \sum_{j=1}^n (R_{i,j,BG} - \bar{R}_{i,BG})^2}}{\bar{R}_{i,BG}}. \quad (5.44)$$

Here, n is the number of runs corresponding to each pointing i . $\bar{R}_{i,BG} = \frac{1}{n} \sum_{j=1}^n R_{i,j,BG}$ is the sample mean of the background rates of each pointing. If there is only one run for a pointing

the relative sample error will be set to zero. The relative sample error alone is not sufficient to account for the entire systematic deviations, because it does not account for the fact that the distribution of observation conditions (e.g. zenith angle, optical efficiency and weather conditions) of the runs contributing to each pointing are very different. This leads compulsory to an offset of the sample mean of each pointing from the mean background rate of the entire data set. This offset is accounted for in a second step. The overall relative systematic error for every pointing is calculated by applying a simple χ^2 method. The relative systematic error due to the offset $\epsilon_{i,\text{offset}}$ is raised until the measured hadron event rate is consistent with isotropy for each pointing. If the χ^2 defined below equals one, the hadron-like event rates for each pointing are consistent with the mean measured hadron-like event rate²⁴. The χ^2 used to calculate the systematic error is given by

$$\chi_i^2 = \frac{(R_{i,\text{BG}} - \langle R \rangle_{\text{BG}})^2}{\sigma_{i,\text{BG},\text{stat}}^2 + (\epsilon_{i,\text{sample}} \times R_{i,\text{BG}})^2 + \sigma_{i,\text{BG},\text{offset}}^2} \stackrel{!}{=} 1. \quad (5.45)$$

Here, the weighted mean background rate is given by

$$\langle R \rangle_{\text{BG}} = \sum_i \frac{R_{i,\text{BG}} / (\sigma_{i,\text{BG},\text{stat}}^2 + (\epsilon_{i,\text{sample}} \times R_{i,\text{BG}})^2)}{1 / (\sigma_{i,\text{BG},\text{stat}}^2 + (\epsilon_{i,\text{sample}} \times R_{i,\text{BG}})^2)}. \quad (5.46)$$

The systematic error necessary to account for the offset of the mean sample rates of the pointings from the overall weighted mean rate of the hadron-like events is given by $\sigma_{i,\text{BG},\text{offset}} = \epsilon_{i,\text{offset}} \times R_{i,\text{BG}}$. The total systematic error is consequently given by $\sigma_{i,\text{syst},\text{BG}}^2 = \sigma_{i,\text{BG},\text{offset}}^2 + \sigma_{i,\text{sample},\text{BG}}^2$. Thus, the total relative systematic error is given by $\epsilon_{i,\text{syst}} = \sqrt{\epsilon_{i,\text{offset}}^2 + \epsilon_{i,\text{sample}}^2}$.

Figure 5.26 shows the relative sample error and the final relative systematic error. The difference between both values is given by the relative offset error. Figure 5.26 illustrates how the relative systematic error of pointings with a sample error sufficient to fulfill Equation 5.45 is given by the sample error. Further, pointings for which the relative sample error is small usually have a large offset error.

Figure 5.27 shows the correlation between the statistical error and the sample error, the statistical error and the offset error, and the statistical error and the total systematic error. For the calculation of Spearman's rank correlation coefficient between the statistical error and the sample error (top panel of Figure 5.27) only the pointings for which the sample error was not set to zero were used. A significant moderate negative correlation is found implying that a small statistical error (i.e. a large number of observation runs) corresponds to a large sample error. This behavior can be understood when considering that a small statistical error implies that the pointing has been observed during many runs with many different observation conditions. In the case of a pointing with fewer observation time less different observation conditions contribute. Of course a pointing may have been observed during only a few runs

²⁴In fact, not all of the measured background arrival rates of the different pointings lie in reality exactly one standard deviation away from the mean arrival rate. The systematic error of the ones that lie further away is probably overestimated. The systematic error of the ones that lie very close to the mean rate are accounted for already by the first step of the systematic error calculation. If the statistics of the arrival rate is very small for some reason the statistical error dominates anyway.

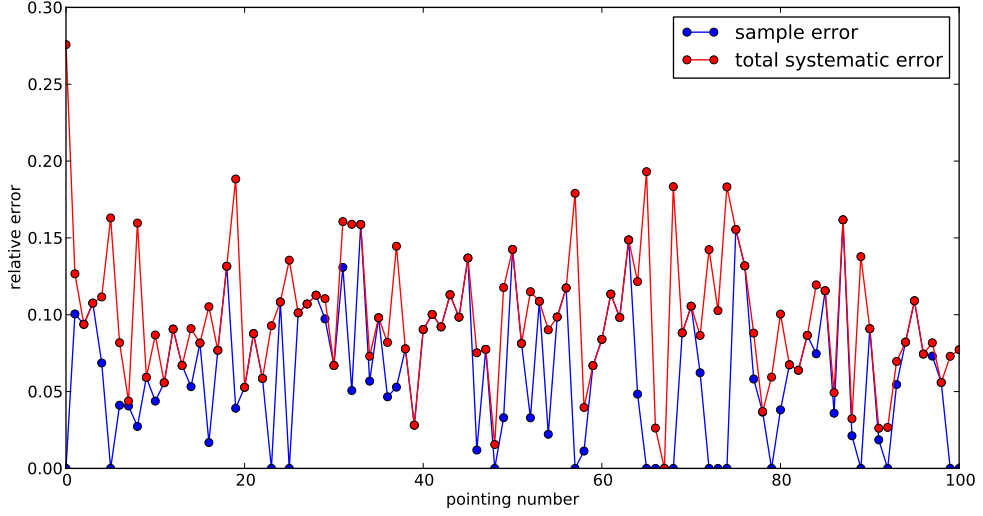


Figure 5.26: Composition of the relative systematic error. The relative sample error and the total systematic error are shown for every pointing. The difference between both is given by the offset error, which is not shown in the diagram for a better presentation.

with very different observation conditions, but often runs observing the same pointing are taken within a short time period. This does of course not apply to sources that are observed very frequently as, e.g. PKS 2155-304.

The correlation between the statistical error and the offset error is shown in the middle panel of Figure 5.27. For the calculation of Spearman's rank correlation coefficient between the statistical error and the offset error only offset errors that were not zero were considered. A slightly positive correlation that is not very significant was found. This positive correlation is mainly caused by pointings with relatively large systematic errors and, thus, zero sample errors. For those pointings only the offset error contributes which is on average larger than for pointings for which also a sample error contributes.

The correlation between the statistical error and the total systematic error is shown in the bottom panel of Figure 5.27. An insignificant negative correlation between the statistical error and the systematic error was found. This is the expected result, since the statistical error should not influence the systematic error.

The relative systematic error obtained from BG events is also applicable to electron/gamma-like event rates, since systematic effects present in BG event rates should also be present in the gamma-like event rates, which was confirmed previously in this Section by showing that gamma-like and BG event rates actually correlate significantly. The absolute systematic error on the gamma-like/electron event rates is calculated by $\sigma_{i,\text{syst,el}} = \epsilon_{i,\text{syst}} \times R_{i,\text{el}}$. The distribution of the resulting relative systematic errors is shown in Figure 5.28. Most relative systematic errors lie between 5 % and 15 %, all are smaller than 30 %. For completeness the distributions of the

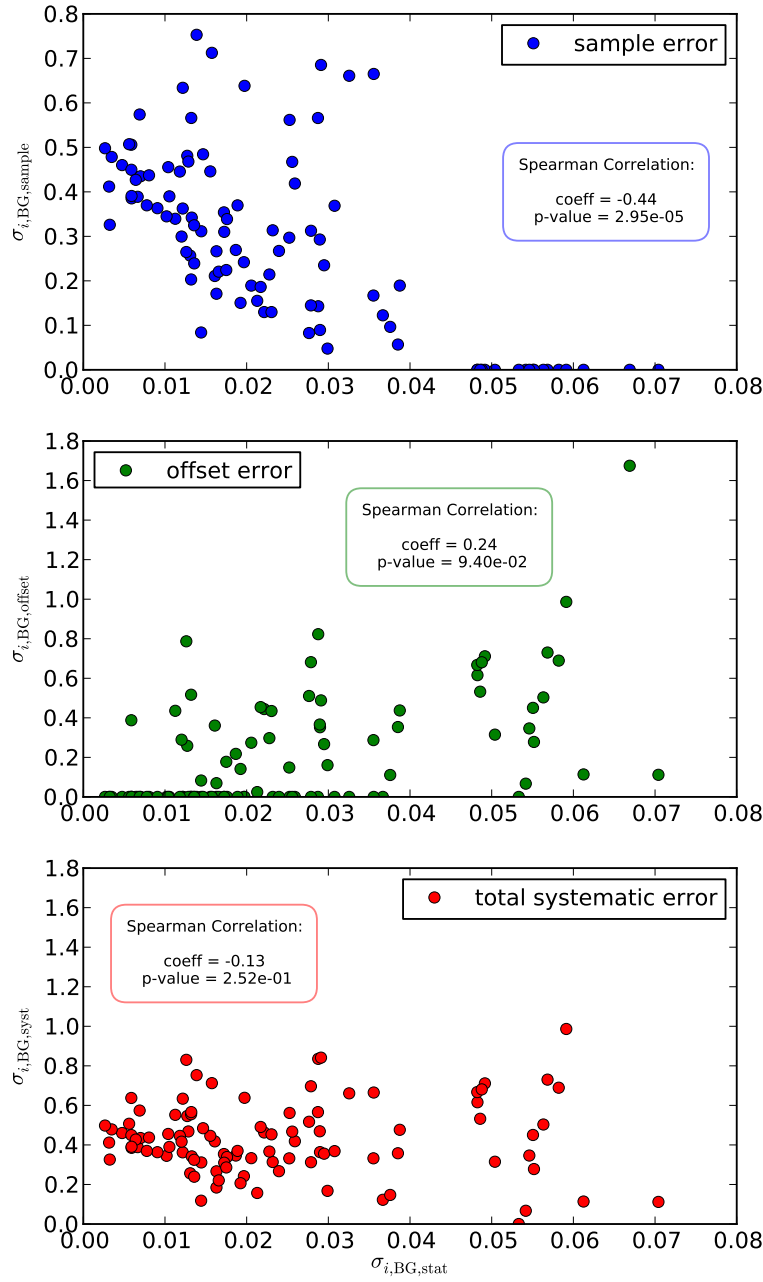


Figure 5.27: Relationship between the statistical error and the sample error, the statistical error and the offset error, and the statistical error and the total systematic error. Spearman's rank correlation coefficient and the corresponding p -value are shown for every pair of errors.

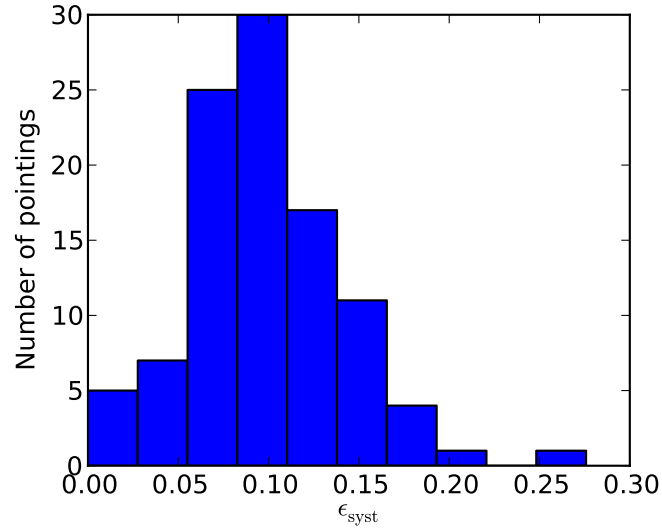


Figure 5.28: Distribution of relative systematic errors ϵ_{syst} .

relative sample errors and the relative offset errors are presented in Figure C.1 in Appendix C.

Discussion of Systematic Errors

The goal of introducing the relative systematic error above is to account for all effects introduced by observation conditions. Thus, when searching for a dipole anisotropy in background data there should be no significant detection of a dipole anisotropy, even if there are systematics in the data set that would lead to a significant non zero dipole amplitude without the introduced systematic error.

The left-hand panel of Figure 5.29 shows the result of the dipole fit to the hadron-like background data without a treatment of systematics. The best-fit $\Delta\chi_0^2$ is larger than 2800, which would be a highly significant effect mimicking a false positive detection. Including the systematic error introduced above the $\Delta\chi_0^2$ becomes smaller than three (right-hand panel of Figure 5.29). For 4 degrees of freedom this corresponds to an effect smaller than 1σ .

Figure 5.30 shows the distribution of BG arrival rates. In the left-hand panel the isotropy model is shown with the corresponding best-fit reduced χ^2 and in the right-hand panel the dipole model is shown with the corresponding best-fit reduced χ^2 and dipole amplitude. The reduced χ^2 is smaller than one indicating that the model indeed accounts for the systematic error. Thus, the BG data is fit well by an isotropic model and, as expected, the improvement obtained when introducing an additional dipole term is insignificant.

From these results it can be concluded that systematic effects present in the hadron-like data set were successfully used to estimate systematic uncertainties which we expect to be present also in the electromagnetic shower sample. The same systematic effects will not lead to significant dipole anisotropies in the gamma-like event sample, since they are accounted for

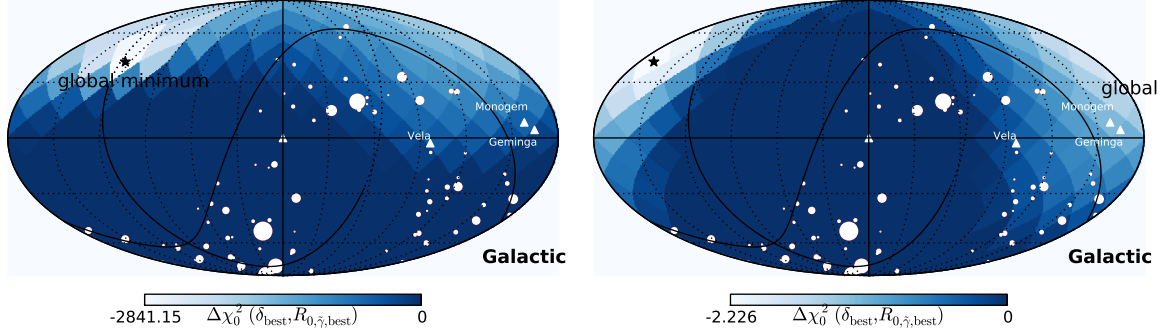


Figure 5.29: Left-hand panel: Result of $\Delta\chi_0^2$ calculation without systematics. Right-hand panel: Result of $\Delta\chi_0^2$ calculation with systematic error calculated following the procedure introduced in the last Section.

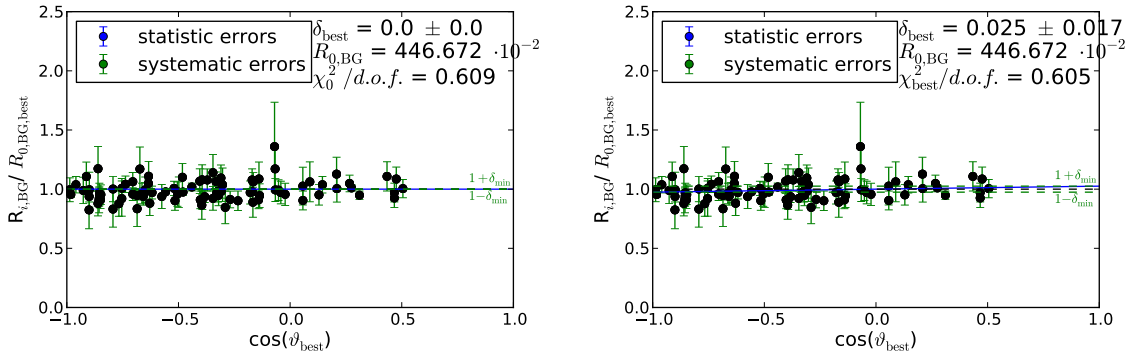


Figure 5.30: Distribution of BG arrival rates (black, normalized to the best-fit $R_{0,BG,best}$) in the best-fit direction of the dipole fit. The statistical (blue error bars) and systematic (green error bars) errors are also shown. In the left-hand panel the best-fit isotropy model is indicated by the blue line. In the right-hand panel the dipole fit for the best-fit dipole amplitude is represented by the blue line. The green dashed lines represent the minimum and maximum of the dipole fit. In addition informations about the χ^2 -fit are given in the upper right corners of the plots.

by applying the same relative systematic error.

5.3.4 Split Analysis

To study further unknown systematic influences on the presented results an extensive systematic study was performed. The data set (all 94 pointings and corresponding runs) was split in dependence on the year, the zenith angle and the optical efficiency of the observations.

Yearly splits Studying the results of the dipole analysis on a yearly basis is useful because the largest variations in the average hadron-like and gamma-like arrival rates were found in dependence on the year of the observation (see Figure 5.24 in Section 5.3.3). Fluctuations of the arrival rate in dependence on the year of the observation may be caused by long-term changes in the observation condition or by the aging of the telescope (especially the mirrors) with time. Every year contains a certain range of run numbers, so that the yearly splits are equivalent to run number splits.

Zenith angle splits The trigger rate of the H.E.S.S. array depends on the zenith angle, because particle showers that are observed at high zenith angles traverse a larger part of the atmosphere. The Cherenkov photons of such showers undergo a larger amount of scattering and, thus, have a larger but dimmer footprint on the ground. This increases the effective energy threshold of the observation. Additionally, a small systematic effect in dependence on the zenith angle was found in Section 5.3.3. Since the dependence of the measured arrival rates on the zenith angle is not corrected in this study it is important to ensure that the measured effects are not caused by zenith angle dependencies. The zenith angles in the data set are distributed between 0° and 30° . At small zenith angles the smallest amount of live time is available, therefore the first zenith angle interval contains observations between 0° and 10° . At higher zenith angles the chosen zenith angle binning is narrower and each bin contains observations from a 5° zenith angle range.

Optical efficiency splits The measured arrival rates may also depend on the optical efficiency of the instrument at the time of data taking. Even though, the optical efficiency is taken into account by Model++ at the reconstruction level a low optical efficiency may alter the energy threshold of the observation and, thus, the arrival rates. An analysis of subsamples of the entire data set with very similar optical efficiencies is used here to ensure that the measured effects are not caused by optical efficiency dependencies. Compared to the live time distribution in dependence on the zenith angle the live time available in dependence on the optical efficiency is distributed even less homogenous, so that the width of the chosen bands contain optical efficiencies between 40 % and 50 %, 50 % and 55 %, 55 % and 60 % and 60 % and 80 %. The split choices have been made in order to retain reasonable amounts of data in each split data set, while being able to study systematic effects.

The previously presented dipole analysis, described in Sections 5.3.2 and 5.3.3, was performed on every split data set. The electron fraction of the whole data set, calculated in Section 5.2.5, was used for fitting all split data sets. This approximation is good enough, because the results do not depend strongly on the assumed electron fraction as shown in Section 5.3.6. It follows

from the definition of the χ^2 -distribution that the sum of independent chi-square variables is also chi-squared distributed. The $\Delta\chi_0^2$ of every split data set is χ^2 -distributed and consequently also the sum of the $\Delta\chi_0^2$. The corresponding number of degrees of freedom of the total $\Delta\chi_{0,\text{total}}^2$ (df_{total}) is given by the sum of the degrees of freedom of the split data sets df_i . Thus, the overall significance ($\Delta\chi_{0,\text{total}}^2$) can be calculated via

$$\Delta\chi_{0,\text{total}}^2 = \sum_{\text{splits } i} \Delta\chi_{0,i}^2 \quad \text{with} \quad df_{\text{total}} = \sum_{\text{splits } i} df_i. \quad (5.47)$$

The stacked $\Delta\chi_{0,\text{total}}^2$ is calculated for every probed direction of the sky.

The results of this split analysis are shown in Figure 5.31. In all three split scenarios the best-fit directions scatter somewhat around the best-fit direction of the global fit. This is

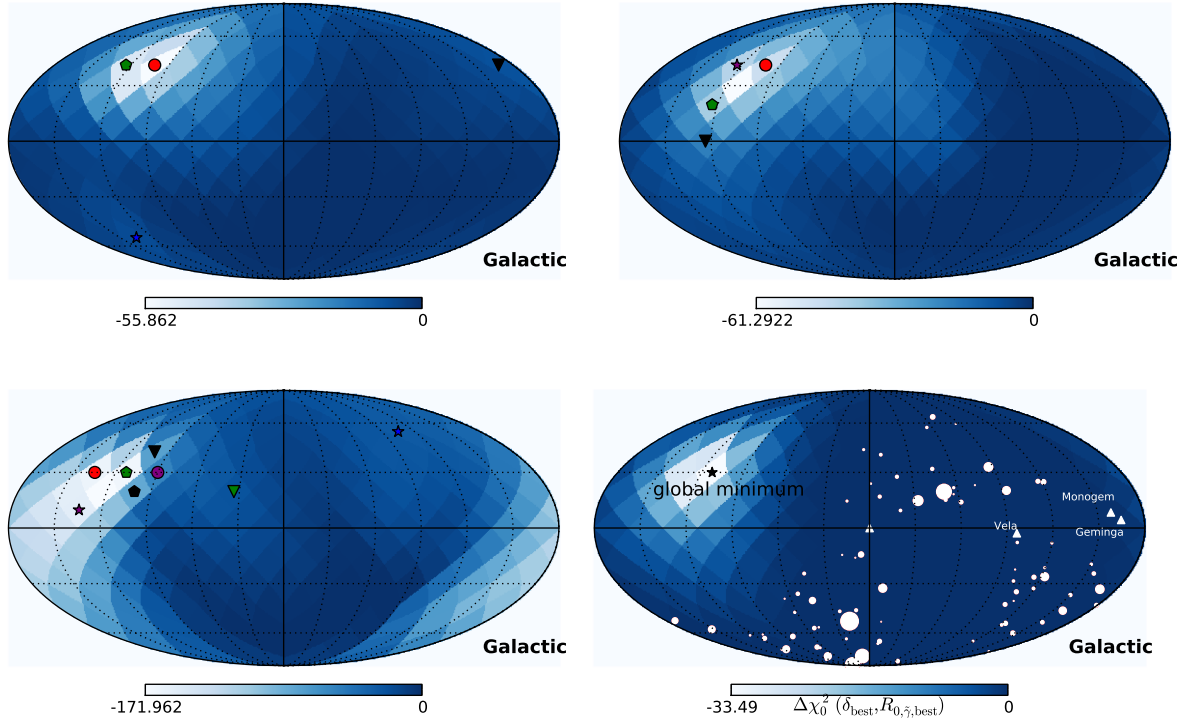


Figure 5.31: Sky maps in galactic coordinates showing the stacked $\Delta\chi_0^2$ for all three split scenarios in optical efficiency (upper left-hand panel), zenith angle (upper right-hand panel) and observation year (lower left-hand panel). The colored markers represent the best-fit directions of the different split analyses. In addition, the result of the analysis of the whole data set (all 94 pointings, no stacking!) is shown in the lower right-hand panel. Here, the black asterisk marks the global best-fit position. The white circles represent the pointing positions and their size scales with the live time available for each pointing (between 0.24 h and 173 h). The pulsars Vela, Monogem and Geminga as well as the Galactic Center are marked by white triangles. In all analyses $\text{NSIDE} = 4$ and $MSSG < 0.6$ holds.

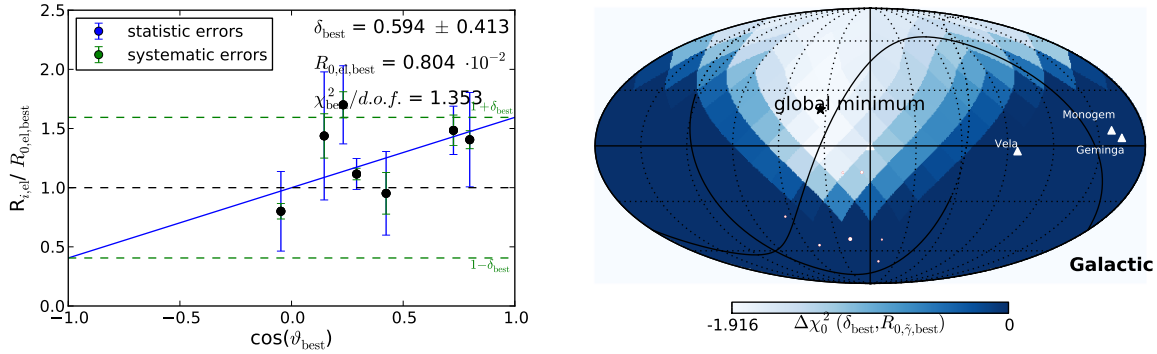


Figure 5.32: Left: Distribution of electron arrival rates (normalized to the mean electron arrival rate) in the best-fit direction for the year 2007. The dipole fit for the best-fit dipole amplitude is represented by the blue line. The green dashed lines represent the minimum and maximum of the dipole. The statistical (blue error bars) and systematic (green error bars) errors are also shown. Right: Sky map color-coded with the values of $\Delta\chi_0^2$ for each possible direction of the maximum of the electron rate in the sky for the year 2007. The white dots depict the pointing positions and are scaled with the respective observation time. The pulsars Vela, Monogem and Geminga as well as the Galactic Center are marked by white triangles. The black asterisk indicates the position of the global minimum of $\Delta\chi_0^2$.

expected since every data set contains only a fraction of the observation time available in the whole data set and, thus, statistical errors are larger. Further, the sky coverage is different in every split and can be very localized in some cases. The most extreme example is shown in Figure 5.32. In this split containing all observations from 2007 only very few pointings are present, which are additionally very localized and contain only a very small amount of observation time. The best-fit parameters obtained from a fit to such a data set are unreliable and have extremely large errors.

The reliability of the individual split analysis results can be estimated by comparing the number of targets in the data sets, the total live times of the data sets and the median of the systematic error of the data sets. Figure 5.33 shows the resulting $\chi^2/d.o.f.$ and $\Delta\chi_0^2$ values for every split analysis, the best-fit dipole amplitudes, the number of targets in the data set, the live time and the median of the systematic error distribution for each split analysis for the optical efficiency splits. Figures D.1 and D.2 in the Appendix show the same quantities for the yearly and zenith angle splits. The pointing pattern is the only information relevant for evaluating the reliability of the fit results that could not be included in these summary tables. However, if necessary this information is included in the $\Delta\chi_0^2$ sky maps for every split data set (an example sky map is shown in Figure 5.32).

In general, the reduced χ^2 obtains values between 1.5 and 8 except for splits where the available observation time is very small and, thus, statistical errors dominate. The p -value of each fit depends on the χ^2 and the number of $d.o.f.$ Thus, the p -values are not necessarily the same for two splits with the same reduced χ^2 . For a typical number of 50 data points

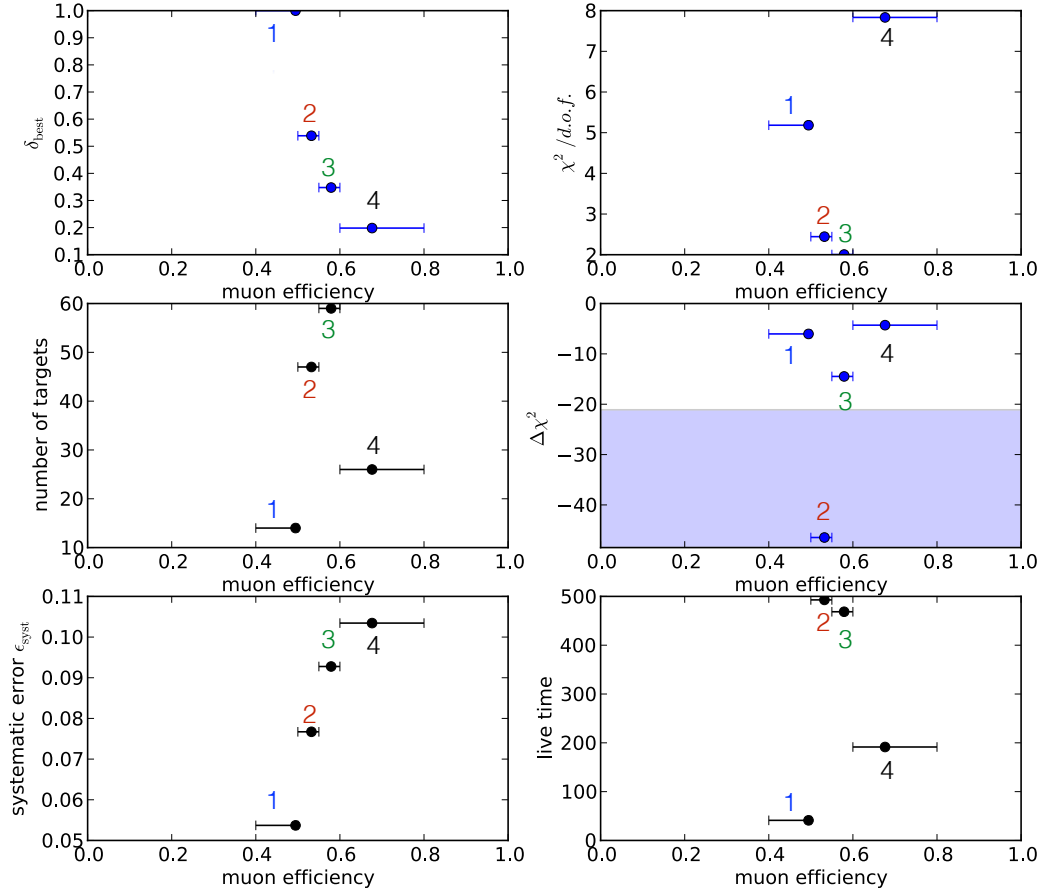


Figure 5.33: Summary figure for the optical efficiency split scenario. The best-fit dipole amplitude (upper left-hand panel), the resulting global $\chi^2/d.o.f.$ (upper right-hand panel), the number of pointings (middle left-hand panel), the global $\Delta\chi_0^2$ (middle right-hand panel), the median of the systematic errors (lower left-hand panel) and the total live time in hours (lower right-hand panel) are shown for every split data set. A bin number was assigned to every optical efficiency bin. The bin number is shown above or below every data point and was assigned the same color in every panel. The number of *d.o.f.* for the global dipole fit is given by the number of pointings minus 4. The blue band in the middle right-hand panel depicts the improvements in the fit represented by $\Delta\chi_0^2$ that are more significant than 4σ .

(pointings) available in a split data set the p -value for a reduced χ^2 ($d.o.f. = 46$) of 1.5 is 0.015 and for a reduced χ^2 of 2 it is 6.6×10^{-5} . For a larger number of data points the p -value is even smaller, e.g. for $\chi^2/d.o.f. = 2$ and 56 $d.o.f.$ the p -value is 1.3×10^{-5} . For a smaller number of data points the p -value is larger, e.g. for $\chi^2/d.o.f. = 2$ and 26 $d.o.f.$ the p -value is 1.8×10^{-3} . Thus, the dipole model does not fit the data well in most split data sets and the probability that the measured χ^2 is found if the dipole model is true is always smaller than approximately 10^{-2} .

As expected a smaller amount of live time and a smaller number of targets reduces the absolute value of $\Delta\chi_0^2$ as can be seen in Figure 5.33. In zenith angle and yearly splits the effects are not quite as obvious, since also the pointing pattern and the systematic error influence the resulting $\Delta\chi_0^2$. The influence of the systematic error is most obvious in the 4th zenith angle bin of Figure D.1 in the Appendix. Here, the 4th zenith angle bin contains the most live time which is distributed between the most sources, but still the corresponding $\Delta\chi_0^2$ is relatively small. This could be caused by the fact that the median systematic error is also rather large in this split, which reduces the significance of the result. The large systematic error is possibly caused by the large range of observation conditions in the data set due to the large number of runs contributing. However, also the distribution of the live time between the pointings will have an additional effect on the results.

Overall the results of all split scenarios confirm the previous results. In most split data sets, especially in those containing a reasonable amount of statistics, the data is not fit well by a dipole model. The improvement of the fit by introducing a dipole term evaluated by calculating $\Delta\chi_0^2$ even corresponds to effects up to 4σ in individual data sets (blue band in the middle right-hand panel of Figure 5.33), when employing $\Delta\chi^2$ statistics. The stacked scenarios find the same best-fit positions and larger total $\Delta\chi_0^2$ compared to the results found in the analysis of the full data set. In the stacked yearly split scenario the total $\Delta\chi_0^2$ is even an order of magnitude larger than in the analysis of the total data set. There are three reasons for the discrepancy between the $\Delta\chi_0^2$ of the total data set and the $\Delta\chi_{0,\text{total}}^2$ of the stacked split analysis results. These are:

- As mentioned above, the number of degrees of freedom of the stacked data $\chi_{0,\text{total}}^2$ is given by the sum of the degrees of freedom of the subsamples. Each split $\Delta\chi_0^2$ has three degrees of freedom. Thus, the number of degrees of freedom of the stacked $\chi_{0,\text{total}}^2$ is given by the number of split samples times three. Consequently, the number of degrees of freedom of the stacked $\chi_{0,\text{total}}^2$ is much larger than of the $\Delta\chi_0^2$ of the whole data set. Therefore, it is understandable that the $\chi_{0,\text{total}}^2$ of the split scenarios are larger than $\Delta\chi_0^2$ of the total data set.
- The systematic errors are calculated individually for every split data set. Thus, the same pointing may have different systematic errors in dependence on the runs used in each split sample. In general it is likely that they are smaller, since the split data samples should be more homogenous at least with respect to the attribute (e.g. year) by which they were defined.
- The best-fit parameters of the fits of the different data samples are not the same. Consequently, the $\Delta\chi_0^2$ are stacked for different best-fit models.

Rate-Adjustment Method The results are also confirmed by employing a second, very different method, of treating systematics. In this method called rate adjustment, the γ -like event rates are corrected run-wise by a factor derived from the hadron-like event rate distribution. First, the adjustment factor is calculated for every run j

$$f_{j,\text{corr}} = \frac{\langle R_{\text{BG}} \rangle - R_{j,\text{BG}}}{R_{j,\text{BG}}}. \quad (5.48)$$

Here, $\langle R_{\text{BG}} \rangle$ is the mean hadron-like event rate of all runs and $R_{j,\text{BG}}$ the hadron-like event rate of every single run. This definition ensures that the gamma-like event rates are scaled to smaller values if the hadron-like event rate of a run is larger than the mean hadron-like event rate. The corrected gamma-like event rates are given by

$$R_{j,\tilde{\gamma},\text{corr}} = R_{j,\tilde{\gamma}} + f_{j,\text{corr}} \cdot R_{j,\tilde{\gamma}}. \quad (5.49)$$

Figure 5.34 shows how the distributions of γ -like events for different background event rates are corrected/adjusted to very similar mean values. Before the correction there appears to be an almost linear relationship between the mean values of the gamma-like event rates and the hadron-like event rates (upper right-hand panel of Figure 5.34). After the correction this relationship vanishes (lower right-hand panel of Figure 5.34). Applying the dipole fit procedure to the adjusted rates confirms the previous results in the split analysis with the main difference that the results are more significant (see Figure D.3 in the Appendix), which is caused by the fact that no systematic error is introduced. Since variations of the mean corrected gamma-like event rate in dependence on the observation year were still found after adjusting the rates, the rate-adjustment method was only used as a cross-check in the split analysis, but not as the standard treatment of systematics.

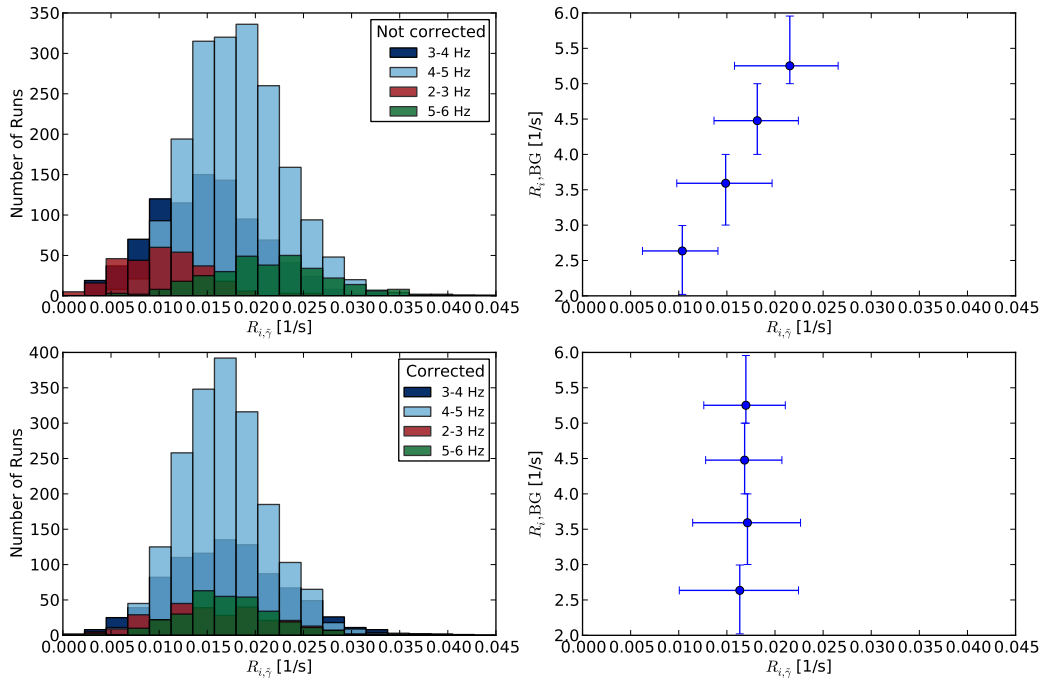


Figure 5.34: The left-hand panels show the distributions of the gamma-like event rates in bins of the hadron-like event rates before (upper left-hand panel) and after (lower left-hand panel) correcting the gamma-like event rates. In the right-hand panels the mean gamma-like event rates in dependence on the mean hadron-like event rates before (upper right-hand panel) and after correcting the gamma-like event rates by the hadron-like event rates (lower right-hand panel). The error bars give the 18 % and 82 % percentiles.

5.3.5 Dependency on Gamma-Hadron Separation Cuts

A detailed study was performed in order to evaluate the dependence of the results on the choice of gamma-hadron separation cuts. In the first step the dependence of Spearman's rank correlation coefficient between gamma-like and hadron-like event rates and the corresponding significance (p -value) on the gamma-hadron separation cut choice was investigated at the run-wise level.

The background (BG) cuts were varied in eight steps from $MSSG > 3$ to $MSSG > 20$. The $MSSG > 20$ data sample contains the smallest amount of events. In contrast applying $MSSG > 3$ the hadron-like event sample contains much more statistics, but is possibly slightly contaminated by electrons (see Figure 5.11). However, the contribution should be negligible. In the $MSSG > 20$ data set no contamination by electrons is expected (Figure 5.11).

The gamma-like event cut was varied between $MSSG < 1.0$ which retains most electrons (approximately 78 %, see Table 5.2), but also eventually a comparably large amount of background events (approximately one percent of the total hadron-like events are left after this cut, see Figure 5.14), and $MSSG < -0.6$ a very stringent cut, where only approximately 29 % electrons and one in thousand background events survive.

The dependency of Spearman's rank correlation coefficient between gamma-like and hadron-like event rates on the gamma-like and BG cuts is illustrated in Figure 5.35. Spearman's rank correlation coefficient ranges from 0.2 to 0.5, while all correlation coefficients are significant with p -values smaller than 10^{-7} .

Spearman's rank correlation coefficient gets smaller when going to larger $MSSG_{\min}$ BG event cuts (top left-hand panel of Figure 5.35). This is understandable as the shape of the image and the air shower development tends to differ more from the electromagnetic shower type with increasing $MSSG$ (e.g. longitudinal development, sampling of different parts of the atmosphere etc.). Further, the significance gets smaller going to larger $MSSG_{\min}$ BG event cuts (larger p -value) as shown in the bottom left-hand panel of Figure 5.35. This is due to the fact that with a more stringent cut on the $MSSG$ in the BG event sample, also the number of events and, thus, the available statistic is reduced.

In the right-hand panels of Figure 5.35 it is shown that the correlation coefficient gets larger and the p -value smaller (significance larger) with a less stringent (larger $MSSG_{\max}$) gamma-like event cut choice. This is caused by better statistics in the gamma-like event sample. Further, a gamma-like event sample with a less stringent cut on the $MSSG$ will also contain more BG events, naturally causing a larger correlation. The closer the cut choices of the gamma-like and hadron-like event sample are to each other the larger is the background contamination by events really belonging to the other species, which causes larger correlations. Nonetheless, even for the cut combination separating gamma-like ($MSSG < -0.6$) and BG ($MSSG > 20$) events most efficiently there is still a significant correlation found between the arrival rates. This finding supports the previous conclusion that there is a significant correlation between gamma-like and hadron-like event rates as suggested in Section 5.3.3.

For further investigations three gamma-hadron separation cut choices were selected. The standard $MSSG < 0.6$ cut dipole analysis results were compared to the results obtained with the very stringent $MSSG < -0.6$ data sample and the intermediate $-0.6 < MSSG < 0.6$ data sample. The last two data samples are absolutely independent gamma-like event samples. The

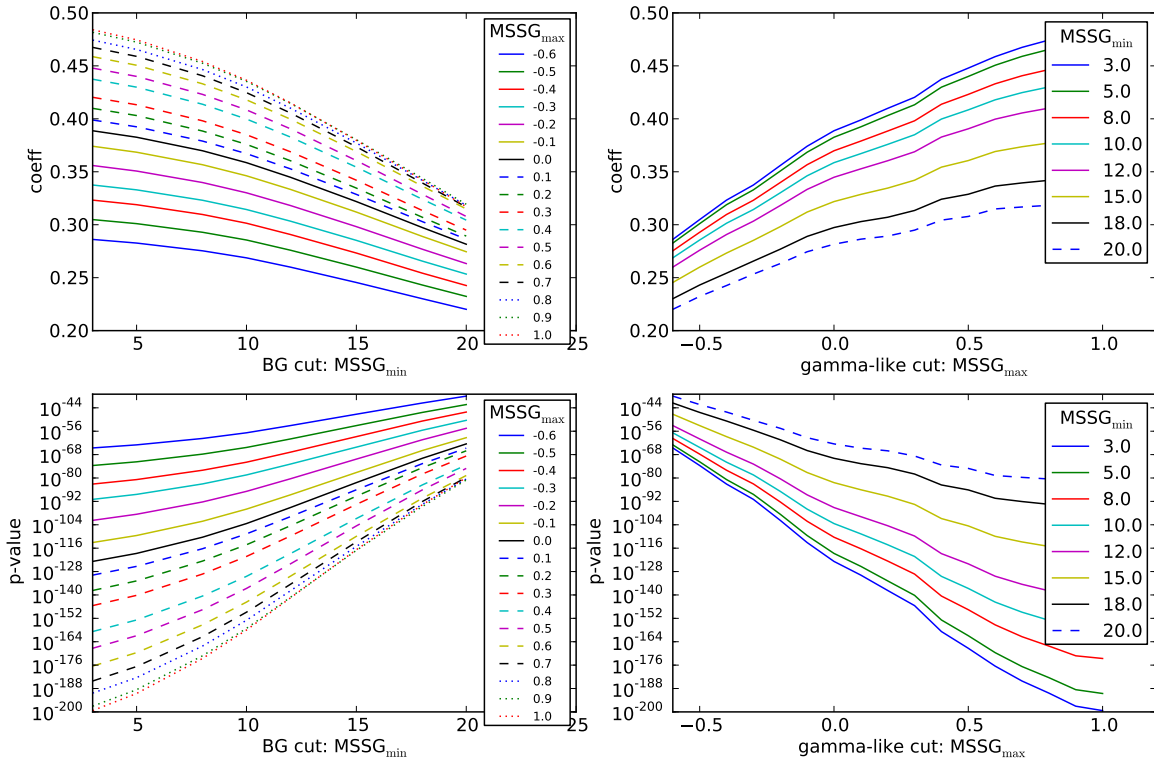


Figure 5.35: Dependency of Spearman's rank correlation coefficient between gamma-like and hadron-like event rates on the choice of the gamma-like cut (this is the cut usually used to separate gammas from hadrons) and BG cuts. Spearman's rank correlation coefficients (top panels) and corresponding p -values (bottom panels) are shown. In the left-hand panels the dependencies are shown for changing BG cut choices for several different fixed gamma-like cut choices. In the right-hand panels the dependencies of the correlation coefficient and the p -value are shown for varying gamma-like cut choices for several fixed BG cut choices.

entirety of the last two data sample gives the standard $MSSG < 0.6$ data sample containing most events (largest statistic).

In Section 5.2.2 it was shown that the $MSSG < 0.6$ cut corresponds to the cut choice with the best quality factor, giving the choice with the best relation between preserving the largest possible amount of electrons while eliminating as much BG events as possible. For the dipole analysis the electron fraction calculated in Section 5.2.5 is more relevant. The most stringent cut $MSSG < -0.6$ contains the fewest number of events and, thus, the smallest statistics, while it is the cleanest electron sample with an electron fraction of 0.76. The intermediate event sample serves as a cross-check sample and contains the smallest amount of electrons (only 60%). The standard $MSSG < 0.6$ contains the sum of all events from the two other data samples with a corresponding electron fraction of $\epsilon_{el} = 0.63$.

In the left-hand panels of Figure 5.36 the $\Delta\chi_0^2$ plots for all three cut choices are shown. The best-fit positions are compatible, while the shape of the $\Delta\chi_0^2$ distribution over the sky of the standard $MSSG < 0.6$ cut appears to be a superposition of the two other cut choices.

Likewise, the improvement of the fit by introducing the dipole term represented by the $\Delta\chi_0^2$ obtained in the standard data sample appears to be a mixture of the improvements in the stringent and intermediate data samples. In the stringent data sample the obtained $\Delta\chi_0^2$ is much larger than in the intermediate data sample, implying that the rate fluctuations are also larger in the stringent cut data sample.

Further, the best-fit dipole amplitudes and the reduced χ^2 ($\chi^2/d.o.f.$) are shown in the right-hand panel of Figure 5.36. Again, the values found in the standard data sample originate from the superposition of the values of the subsamples (stringent cut and intermediate cut samples). For example, the $\chi^2/d.o.f. = 2.75$ of the stringent cut sample is significantly larger than the $\chi^2/d.o.f. = 1.98$ found in the intermediate data sample. This indicates that the rate fluctuations in the stringent data sample are larger than in the intermediate data sample. Consequently, the $\chi^2/d.o.f. = 2.35$ of the standard sample lies in between the other values because the standard sample contains all events from the subsamples.

Since the stringent cut data sample contains the largest amount of electrons and apparently also the largest amount of rate fluctuations the results indicate that the measured rate fluctuations²⁵ originate from the electron component.

²⁵Here, we refer to rate fluctuations that are not present in the BG data and consequently not accounted for by the systematic error.

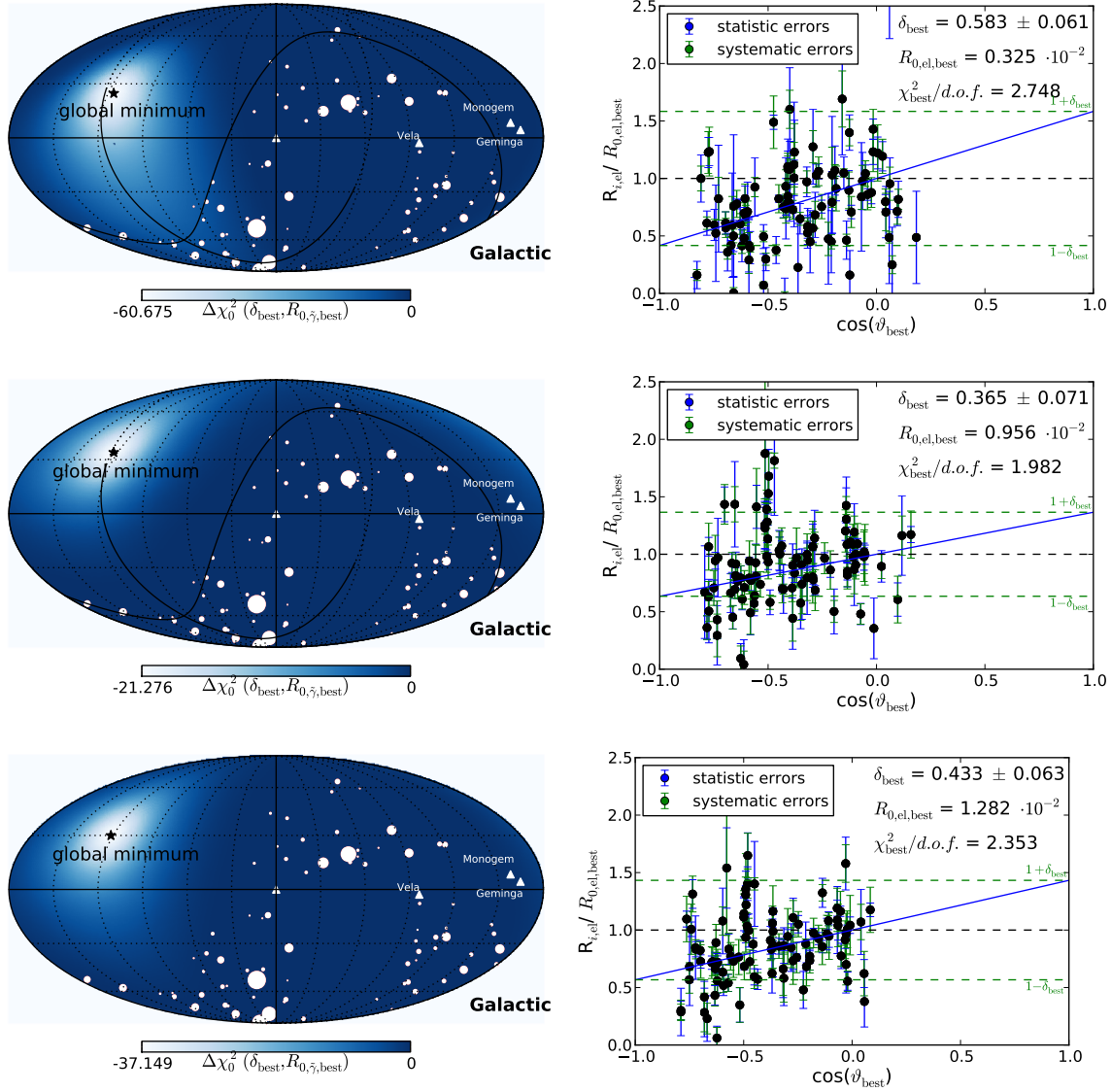


Figure 5.36: Sky maps color-coded with the values of $\Delta\chi_0^2$ for each possible direction of the maximum of the electron rate in the sky (left-hand panels) and the distribution of electron arrival rates (normalized to the mean electron arrival rate) in the best-fit direction (right-hand panels) for all three investigated cut choices ($MSSG < -0.6$ in the upper panels, $-0.6 < MSSG < 0.6$ in the middle panels, $MSSG < 0.6$ in the bottom panels). The white dots depict the pointing positions and are scaled with the respective observation time. The pulsars Vela, Monogem, Geminga and the Galactic Center are marked by white triangles. The black asterisk indicates the position of the global minimum of $\Delta\chi_0^2$. In the right-hand panels the dipole fit for the best-fit dipole amplitude is represented by the blue line. The green dashed lines represent the minimum and maximum of the dipole. The statistical (blue bars) and systematic (green bars) errors are also shown.

5.3.6 Dependency on the Electron Fraction

In order to investigate the dependence of the results of the dipole fit ($\Delta\chi^2$, R_0 , δ_{best} and best-fit position) on the electron fraction, the dipole analysis was performed for electron fractions between 0 % and 95 %. The improvement of the fit in terms of $\Delta\chi^2$ depends on the electron fraction as well as the best-fit parameters, i.e. the dipole amplitude δ_{best} , the rate normalization $R_{0,\text{best}}$ and the best-fit direction, which is represented by the number of the best-fit pixel ($\text{pixel}_{\text{best}}$). The dependencies of these parameters on the electron fraction are illustrated in Figure 5.37.

It is shown in the upper left-hand panel of Figure 5.37 that the improvement of the fit represented by the $\Delta\chi^2$ is constant above an electron fraction of approximately 20 %. Below this value the γ -like events are fit by a dominating isotropic component and a small amount of electrons. In the dipole model the electron component is described by a monopole term and a dipole term. For very small electron fractions the dipole term is also small and does not contribute significantly (see Equation 5.29). With growing electron fraction the dipole term contributes more and more strongly to the predicted electron arrival rate and, thus, a better fit of the data is possible. This interrelation can nicely be seen from a reformulated version of Equation 5.34 given by

$$\chi^2 = \sum_i \frac{[R_{i,\tilde{\gamma}} - (R_{0,\tilde{\gamma}}(\delta) + \epsilon_{\text{el}} R_{0,\tilde{\gamma}}(\delta) \delta \cos(\vartheta_i))]^2}{\sigma_{i,\text{el}}^2}. \quad (5.50)$$

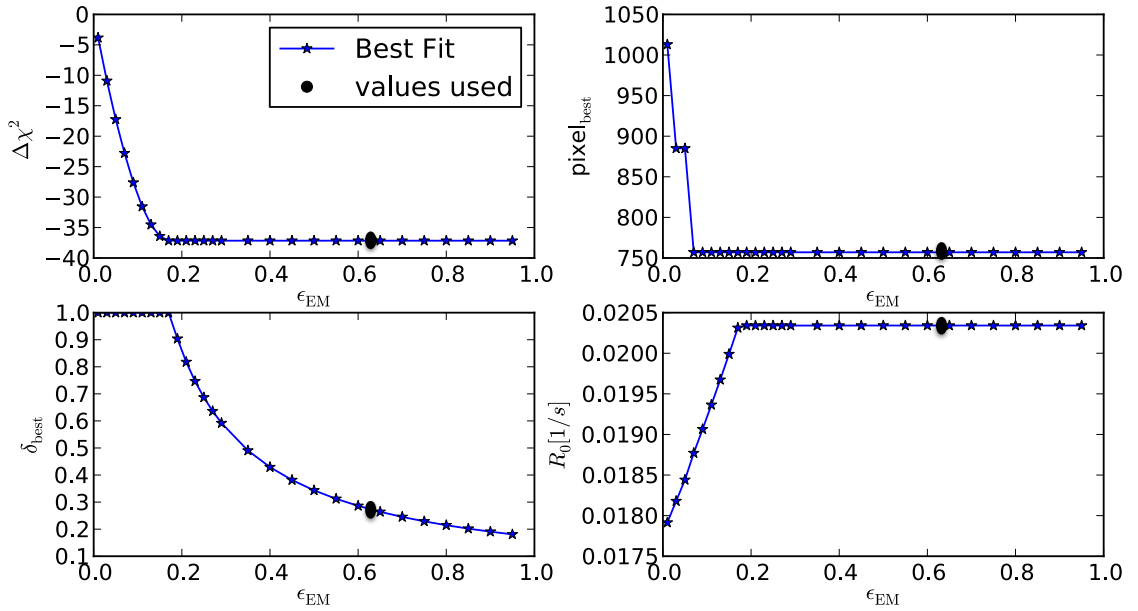


Figure 5.37: Dependencies of the global $\Delta\chi^2$ and corresponding best-fit parameters of the dipole model on the electron fraction. The black circle shows the value of the electron fraction used in this study (standard cut choice).

In the bottom left-hand panel of Figure 5.37 it is shown that the dipole amplitude remains constant at 100 % below an electron fraction of 20 %, while the best-fit normalization gets larger (see bottom right-hand panel of Figure 5.37) and the best-fit pixel position converges towards the overall best-fit position (see top right-hand panel of Figure 5.37). Above an electron fraction of 20 % the $\Delta\chi^2$ saturates, as does the best-fit normalization parameter $R_{0,\text{best}}$. In contrast the best-fit dipole amplitude starts to decline. This behavior can be understood by remembering the dipole term formula given in Equation 5.29. The dipole term depends on $\epsilon_{\text{el}} \cdot \delta$. While ϵ_{el} is artificially changed in this analysis, δ is a free parameter of the fit. After the best-fit $\epsilon_{\text{el}} \cdot \delta$ has been reached by the fit procedure an artificial change in the electron fraction is compensated in the fit by a change of the best-fit dipole amplitude. Thus, the best-fit $\epsilon_{\text{el}} \cdot \delta$ also grows below an electron fraction of 20 % and saturates above.

In conclusion the evaluation of the significance of the improvement of the description of the data by introducing a dipole term in the electron component does not require exact knowledge of the electron fraction. However, it influences the magnitude of the resulting best-fit dipole amplitude and influences, thus, also the error on the dipole amplitude.

5.3.7 Cross Check

Within the scope of this study it was not possible to obtain a full cross check of the presented results within a reasonable period of time. Such a cross check would have to include the following steps:

- Calibrating and reconstructing the data sample using an analysis chain other than the chain used in this study (e.g. a Hillas based chain).
- Determination of the residual background level including electron Monte Carlo simulations and the calculation of the effective exposure.
- Calculation of electron and background arrival rates.
- Reimplementation of the statistical analysis starting with the isotropic and dipole models.

These steps should be taken in the course of an independent analysis. Given the limited capacity of the H.E.S.S. collaboration, a cross check is still pending.

Instead another route was taken here to inspire confidence in the presented results. Within the H.E.S.S. collaboration the only other analysis concerning cosmic-ray electrons was the calculation of the H.E.S.S. electron spectrum (Aharonian et al. 2008 and Aharonian et al. 2009). Thus, this data sample is used to inspect at least parts of the analysis chain. The data sample used in Aharonian et al. 2008 is a subsample of the large data sample analyzed in this study so that it can be employed to check the obtained results at least for a fraction of the whole data sample.

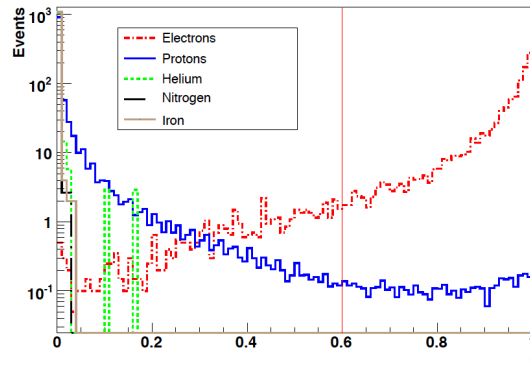


Figure 5.38: Distributions of the gamma-hadron separation parameter ζ for simulations of electrons (red), protons (blue), helium (green), nitrogen (black) and iron (brown) in the energy range between 1 - 4 TeV. The vertical line illustrates the ζ range that was used for the background determination fit for the determination of the electron spectrum by Egberts (2009). This is not the gamma-hadron separation cut used in this study. The Figure was adapted from Egberts (2009).

The cross-check data sample contains data taken in 29 different directions of the sky and amounts to 239 hours of live time. The residual background level for this data set was calculated by Prüser (2012) using the best-fit distributions of hadron and electrons presented in Figure 3.9 of Egberts (2009). The energy range (0.616 - 1.047 TeV) for which the distributions are available differs slightly from the energy range used in this study (0.64 - 1.04 TeV). The derived fraction of electromagnetic air showers is given by approximately 53 %.

Further, the measured distribution of the depth of the shower maximum was fit to simulated distributions of electrons, protons and photons. It was found that photons do most likely not account for more than 10 % of electromagnetic showers (Egberts 2009). Thus, the electron fraction is given by $\epsilon_{\text{el}} = 0.53 \times 0.9 = 0.477$. In Aharonian et al. 2008 a Random Forest machine learning algorithm using the Hillas moments of the camera images as input parameters was employed (here called Hillas RF method). The Random Forest converts the image information into a single parameter ζ , which is used for gamma-hadron separation.

The distribution of the ζ parameter is shown in Figure 5.38 for simulated electrons, protons, helium, nitrogen and iron. A stringent cut on $\zeta > 0.9$ was chosen in this cross check to select gamma-like events. This choice ensures that the residual background for this cut does not dominate the event sample. Hadron-like events are given by $\zeta < 0.1$.

The same subsample was also analyzed with Model++. The electron fraction of the subsample for the Model++ analysis chain was estimated to be approximately the same as for the entire data set $\epsilon_{\text{el}} = 0.63$ for $MSSG < 0.6$. This approximation should not strongly influence the results since it was shown in Section 5.3.6 that the results remain the same as long as the electron fraction is larger than 20 %.

Spearman's rank correlation coefficient was calculated between gamma-like and hadron-like event rates obtained with Model++ ($MSSG < 0.6$ and $MSSG > 5$) and Hillas RF ($\zeta > 0.9$ and $\zeta < 0.1$). The correlation coefficient was calculated on run-wise and pointing-wise granularity levels. In Figure 5.39 the correlation between gamma-like/hadron-like event rates obtained with the two different analysis chains is obvious. Relatively large correlation coefficients of approximately 0.63 are found on the pointing-wise level for both gamma-like and hadron-like event samples and on the run-wise level for hadron-like events. The statistics available on the run-wise level for gamma-like events is extremely small which leads to a much smaller correlation coefficient of 0.23. However, since the correlation coefficient on the pointing-wise level is also of the order of 0.63, including much more statistics, the larger correlation is reasonable. The corresponding p -value is much larger on the run-wise level, because its calculation does not take the actual statistical errors into account, but instead depends on the size of the data sample (Section 4.3.2).

In addition to the direct comparison of the hadron-like and gamma-like event arrival rates the dipole model analysis results were obtained for the event rates calculated with both methods. Figure 5.40 show the χ^2 sky maps, the $\Delta\chi^2$ sky maps and the best-fit direction graph. The best-fit position is found approximately in the same direction of the sky for both reconstruction chains. Furthermore, the best-fit dipole amplitudes are compatible within their errors. There is a large discrepancy between the goodness-of-fit of the results. While the reduced χ^2 for the Hillas RF method is smaller than 1 indicating that systematic errors may have been somewhat over estimated, the reduced χ^2 with Model++ is almost twice as big. The difference between

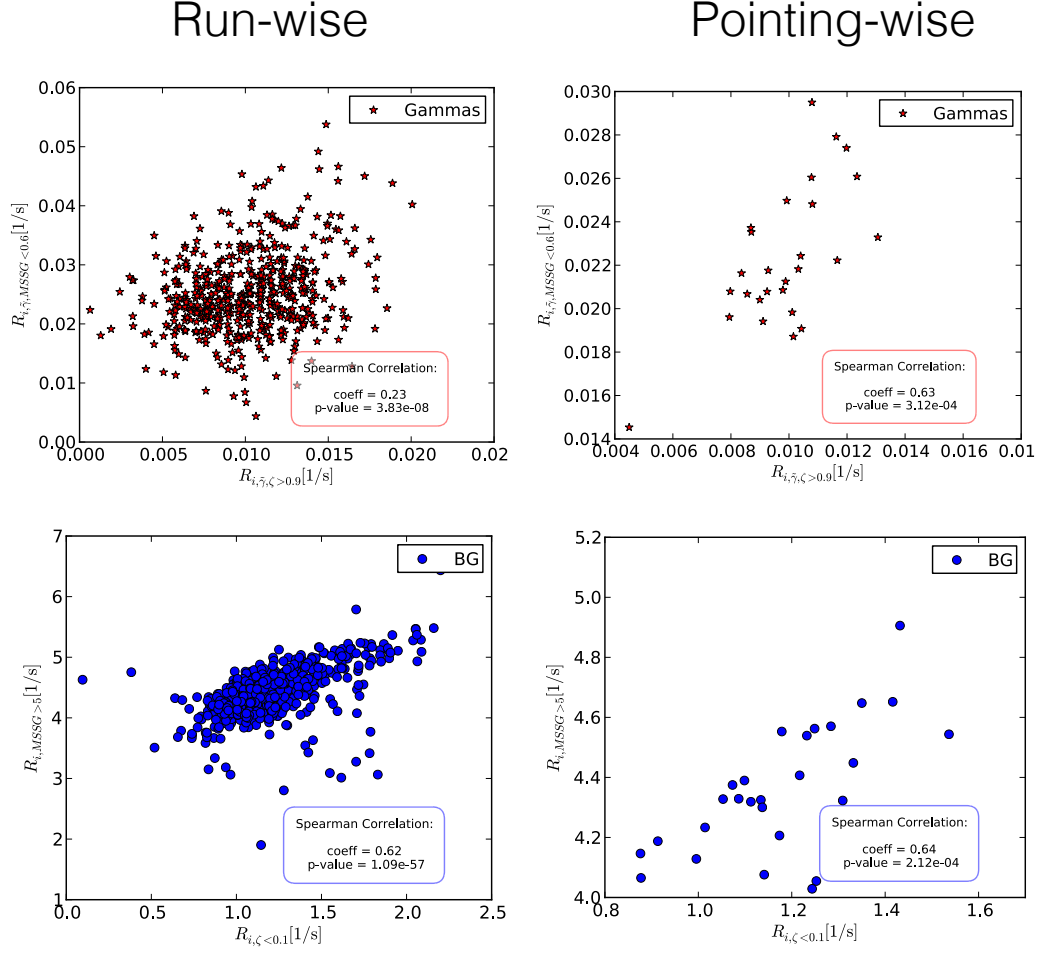


Figure 5.39: Spearman's rank correlation coefficients calculated for gamma-like (top panels) and hadron-like (bottom panels) event rates obtained with two different reconstruction techniques (Model++ and Hillas RF). In the left-hand (right-hand) panel the correlations are shown for run-wise (pointing-wise) calculated event rates. The Model++ gamma-hadron separation parameter is the Mean Scaled Shower Goodness ($MSSG$) and the Hillas RF separation parameter is the output parameter of the Random Forrest called ζ .

the two data samples is that the Hillas RF sample is much smaller than the one obtained with Model++. Thus, in the Model++ data sample fluctuations are not dominated by statistics, so that the correct estimation of the systematic error is even more important. As in the large data sample the fluctuations cannot be explained with statistical and systematic uncertainties²⁶.

Upper limits on the dipole amplitude obtained with both methods are shown in Figure 5.41. Even with the extremely small data sample analyzed with the Hillas RF method upper limits

²⁶ Again the systematic error was calculated from the background events analogous to the procedure used for the large data sample.

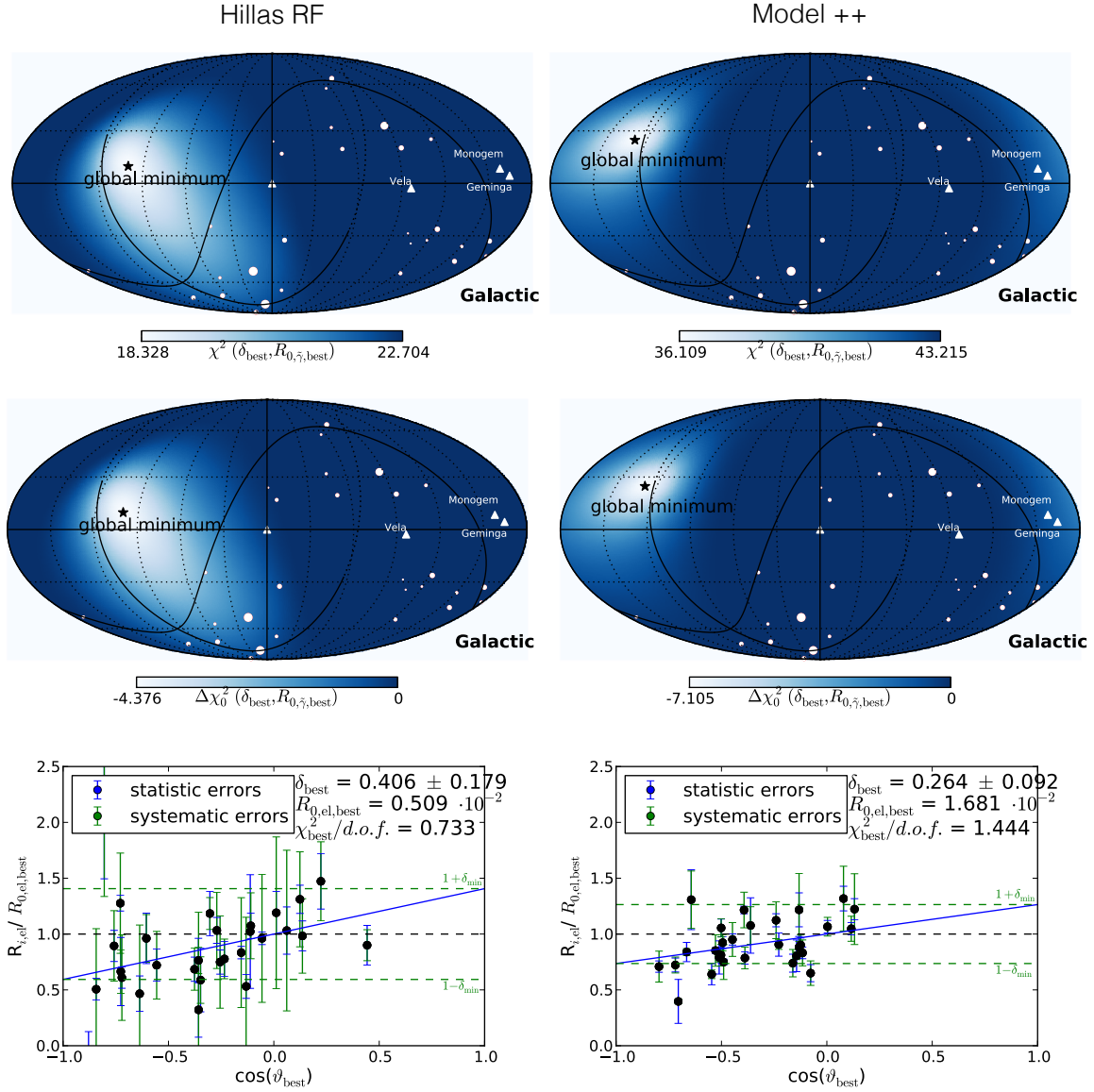


Figure 5.40: Top and middle panels: Sky map color-coded with the values of χ^2 (top panels) and $\Delta\chi_0^2$ (middle panels) for each possible direction of the maximum of the electron rate in the sky. In all maps the white circles depict the 29 pointings and are scaled with the respective observation time. The three pulsars Vela, Monogem and Geminga as well as the Galactic Center are marked by a white triangle. The black asterisk indicates the position of the global minimum of χ^2 and $\Delta\chi_0^2$. Bottom panels: Graphs of electron arrival rates (black, normalized to the best-fit $R_{0,\text{el,best}}$) relative to the best-fit direction. The statistical (blue error bars) and systematic (green error bars) errors are shown. The dipole fit function for the best-fit dipole model is represented by the blue line. The green dashed lines represent the minimum and maximum rate values of the dipole fit. In addition, information about the χ^2 -fit are given. In the left-hand panels the graphs are shown for the Hillas RF method and in the right-hand panels for the Model++ method.

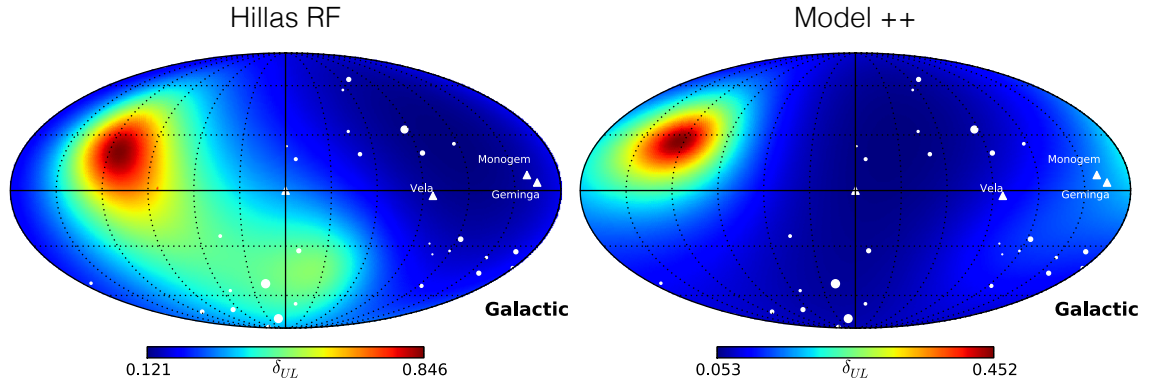


Figure 5.41: Sky map in galactic coordinates showing the upper limits derived on the dipole amplitude of cosmic-ray electrons for each possible direction of the dipole maximum based on the small subsample data set. The white circles depict the 29 pointings and are scaled with the respective observation time. The pulsars Vela, Monogem, Geminga and the Galactic Center are also shown and marked by a white triangle. In the left-hand panel the map is shown for the Hillas RF method and in the right-hand panel for the Model++ method.

on the dipole amplitude between 12 % and 85 % are obtained. They are less stringent than the limits obtained with the Model++ method due to smaller statistics. It should be noted that the constraint on the dipole amplitude with the larger data set is only more stringent by a factor up to two most likely due to overall larger systematic effects in the large data set.

5.3.8 Multipole Fits

In the previous sections it was found that neither an isotropic nor a dipole model fit the measured H.E.S.S. electron event rates well. Nonetheless, the rate fluctuations of gamma-like (or electron) events are much larger than the respective values for background events. This is already obvious when considering the unbiased sample variance and the statistically weighted mean of the data samples. The statistically weighted mean of the gamma-like event rates of all pointings is $\langle R_{\tilde{\gamma}} \rangle = 1.78 \cdot 10^{-2} \text{ Hz}$ ($MSSG < 0.6$). For cosmic-ray electron arrival rates it is $\langle R_{\text{el}} \rangle = 1.12 \cdot 10^{-2} \text{ Hz}$ and for background-like event rates it is 4.41 Hz ($MSSG > 5$). The unbiased sample variance is the same for gamma-like and electron event rates and is given by $\text{var}(R_{i,\tilde{\gamma}}) = \text{var}(R_{i,\text{el}}) = 1.53 \cdot 10^{-5} \text{ Hz}^2$. For background-like events the variance is $\text{var}(R_{i,\text{BG}}) = 0.15 \text{ Hz}^2$. The square root of the variances gives the standard deviations of the measured event rates from the expectation value of the sample (in this case the statistically weighted mean event rates). The standard deviation is a measure of the scatter of the measured event rates around their expectation value. In order to compare the rate fluctuations in the data samples the relative standard deviation, also called coefficient of variation, is calculated. The relative standard deviation ($\text{var}K$) is obtained by dividing the standard deviation by the corresponding statistically weighted mean event rate. The relative standard deviation of gamma-like event rates is $\text{var}K(R_{i,\tilde{\gamma}}) = 22.0\%$, for electron events it is $\text{var}K(R_{i,\text{el}}) = 34.9\%$ and for background events $\text{var}K(R_{i,\text{BG}}) = 8.8\%$. While the rate fluctuations in background events were sufficiently accounted for by statistical and systematic errors (as discussed in Section 5.3.3), the rate fluctuations seen in gamma-like events and, consequently, also in electron events cannot account for all rate fluctuations (as long as the relative amount of cosmic-ray electrons in the gamma-like event sample is indeed larger than 20 % as shown in Section 5.2.5).

This Section aims at further characterizing the rate fluctuations in the cosmic-ray electron arrival rates by investigating multipole models up to $l = 4$. The fluctuations of the electron event rates can be described by the multipole expansion of any angular distribution over a sphere $I(\mathbf{n})$ (analogous to definitions often used in CMB analysis see e.g. Peacock 1999, Bunn 1995 and Tojeiro 2006)

$$I(\mathbf{n}) = \sum_{l=0}^{\infty} \sum_{m=-l}^l a_{lm} Y_{lm}(\mathbf{n}). \quad (5.51)$$

Here, \mathbf{n} is a unit vector pointing to a position on the sphere (depending on polar angle θ and azimuthal angle ϕ). $I(\mathbf{n})$ represents the fluctuations of the electron events rates $I(\mathbf{n}) = \frac{R(\mathbf{n}) - \langle R_{\text{el}} \rangle}{\langle R_{\text{el}} \rangle}$. $Y_l^m(\mathbf{n})$ are the spherical harmonic functions defined on a unit sphere (see e.g. Bronstein et al. 1999)

$$Y_l^m = \sqrt{\frac{2l+1}{4\pi} \frac{(l-m)!}{(l+m)!}} P_l^m(\cos \theta) e^{im\phi}. \quad (5.52)$$

Here, l is a none negative integer taking values between $l = 0, 1, 2, \dots, \infty$. l is the multipole and represents a given angular scale π/l in radians. The parameter m is an integer and takes values between $-l$ and $+l$. The functions $P_l^m(\cos \theta)$ are the associated Legendre polynomials (e.g. Bronstein et al. 1999). A real basis of spherical harmonics Y_{lm} can be defined in terms of their complex analogues. These functions have the same orthonormality properties as the complex

ones. The coefficients a_{lm} are connected to the spherical harmonics and rate fluctuations via

$$a_{lm} = \int_{\theta=0}^{\pi} \int_{\phi=0}^{2\pi} I(\mathbf{n}) Y_{lm}^*(\mathbf{n}) d\Omega. \quad (5.53)$$

Using real spherical harmonics the dipole model is given by

$$\begin{aligned} I(d, \alpha)_{\text{dip}} &= m_0 + p_x \cos(d) \cos(\alpha) + p_y \cos(d) \sin(\alpha) + p_z \sin(d) \\ &= m_0 + \mathbf{p} \cdot \mathbf{n} \end{aligned} \quad (5.54)$$

$$= m_0 + |\mathbf{p}| \cos(\vartheta). \quad (5.55)$$

Here, d is the latitude and α the longitude. They are connected via $d = \pi/2 - \theta$ and $\alpha = \phi$ to the spherical coordinates used above. The constants m_0, p_x, p_y, p_z correspond to the multipole coefficients a_{lm} for $l = 0$ and $l = 1$. \mathbf{p} is the vector of the dipole moment and \mathbf{n} the unit vector pointing to a position on the sphere. $\cos(\vartheta)$ is the cosine of the angular distance between the considered position on the sphere and the direction of the maximum dipole amplitude. It can be shown that Equation 5.54 and Equation 5.28 used previously are equivalent. The dipole amplitude δ and the rate normalization $R_{0,\text{el}}$ are connected to the multipole coefficients and the mean electron rate: $\delta = \frac{|\mathbf{p}|}{1+m_0}$ and $R_{0,\text{el}} = \langle R_{\text{el}} \rangle (1 + m_0)$. Likewise, models for higher multipoles are defined. In this study multipoles up to $l = 4$ are considered, since data from only 94 directions in the sky are available. The general form of this model is given by:

$$\begin{aligned} I(d, \alpha) &= M(m_0) + D(d, \alpha, p_x, p_y, p_z) + Q(d, \alpha, q_0, q_1, q_2, q_3, q_4, q_5) \\ &+ O(d, \alpha, o_0, o_1, o_2, o_3, o_4, o_5, o_6, o_7) \\ &+ H(d, \alpha, h_0, h_1, h_2, h_3, h_4, h_5, h_6, h_7, h_8, h_9) + \dots \end{aligned} \quad (5.56)$$

Here, M, D, Q, O and H are functions including the different terms of the multipole expansion in Equation 5.51 for the different multipoles l expressed by real spherical harmonics. Thus, $M = m_0$ and $D(d, \alpha, p_x, p_y, p_z) = p_x \cos(d) \cos(\alpha) + p_y \cos(d) \sin(\alpha) + p_z \sin(d)$. The spherical harmonic functions for higher multipoles are given in Appendix E.

The different multipole functions were fitted to the data by minimizing

$$\chi^2 = \sum \frac{(R_{i,\text{el}} - (\langle R_{\text{el}} \rangle + \langle R_{\text{el}} \rangle \cdot I(d, \alpha)))^2}{\sigma_{i,\text{el}}^2} \quad (5.57)$$

using MINUIT package routines for python called PyMinuit (James 1998).

Here, the electron rate is calculated from the gamma-like event rate $R_{i,\tilde{\gamma}}$ and is given by $R_{i,\text{el}} = R_{i,\tilde{\gamma}} - (1 - \epsilon_{\text{el}}) \langle R_{\tilde{\gamma}} \rangle$ and the mean electron event rate is given by $\langle R_{\text{el}} \rangle = \epsilon_{\text{el}} \langle R_{\tilde{\gamma}} \rangle$. $\langle R_{\tilde{\gamma}} \rangle$ is the weighted mean of the gamma-like event rates as defined in Equation 5.36. Different models were fit to the data by consecutively adding higher multipole moments to the model. The highest multipole considered is the hexadecapole ($l = 4$). In this model 25 free parameters are fit to the data. Figure 5.42 shows the electron rate predictions obtained by including consecutively higher and higher multipoles in the model (dipole: $l_{\text{max}} = 1$, quadrupole: $l_{\text{max}} = 2$, octupole: $l_{\text{max}} = 3$, hexadecapole: $l_{\text{max}} = 4$). In the model with $l_{\text{max}} = 4$, an additional requirement

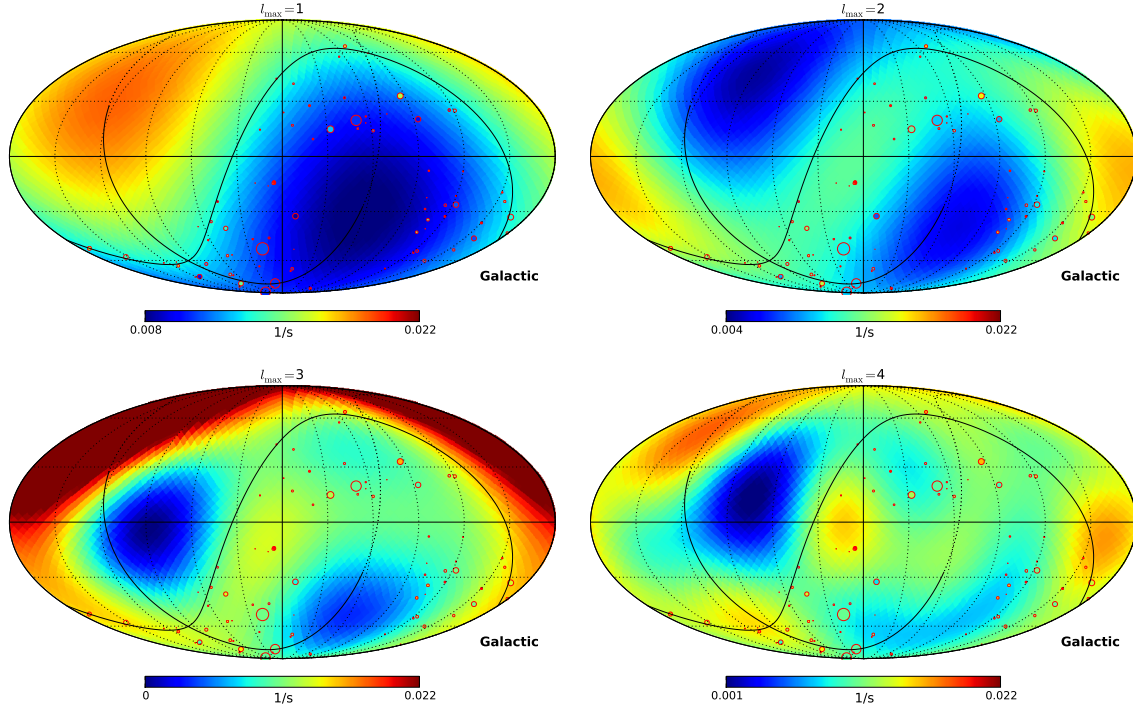


Figure 5.42: Electron rate prediction sky maps for the best-fit multipole models including multipoles up to the dipole ($l_{\max} = 1$, upper left-hand panel), quadrupole ($l_{\max} = 2$, upper right-hand panel), octupole ($l_{\max} = 3$, lower left-hand panel) and hexadecapole ($l_{\max} = 4$, lower right-hand panel) are illustrated.

l_{\max}	χ^2_{best}	N_{para}	$d.o.f.$	$\chi^2_{\text{best}} / d.o.f.$	p -value
0	248.69	1	93	2.67	3.89×10^{-16}
1	209.24	4	90	2.32	1.72×10^{-11}
2	182.80	9	85	2.15	4.03×10^{-09}
3	164.09	16	78	2.10	4.43×10^{-08}
4	150.94	25	69	2.19	4.72×10^{-08}

Table 5.7: Results of the fits of the multipole functions to electron arrival rates. The table contains the maximum multipole l_{\max} included in the model function, the corresponding best-fit χ^2_{best} , number of free parameters (N_{para}), number of degrees of freedom of the fit ($d.o.f.$), corresponding reduced chi-square ($\chi^2_{\text{best}}/d.o.f.$) and p -value.

$l_{\text{simple}} - l_{\text{comp}}$	$\Delta\chi^2$	$d.o.f.$	p -value
0 - 1	39.45	3	1.40×10^{-08}
1 - 2	26.43	5	7.35×10^{-05}
2 - 3	18.72	7	9.10×10^{-03}
3 - 4	13.15	9	1.56×10^{-01}

Table 5.8: Results of $\Delta\chi^2$ -tests of consecutive multipole fit functions. First, the multipoles of the simple model l_{simple} and the more complex model l_{comp} are given. Further, corresponding $\Delta\chi^2$ values, the number of degrees of freedom ($d.o.f.$) and p -values are given.

forcing the predicted electron rates to be positive was included. This was necessary, because the fit otherwise converges to parameter values predicting unphysical (negative) electron rates. This leads to a best-fit model that has a much larger χ^2 than without the constraint.

Table 5.7 shows a summary of the obtained best-fit χ_{best}^2 values, numbers of free parameters, numbers of degrees of freedom, the corresponding $\chi_{\text{best}}^2/d.o.f.$ and p -values. The best-fit parameters of every fit are not given explicitly, because these are up to 25 values. Instead, the best-fit model is illustrated by showing the electron rate predictions of the model (Figure 5.42).

The dipole model serves as a cross-check model to the previous results in Section 5.3.2. Previously, the dipole fit was carried out for every probed direction in the sky. The models were calculated on a finite-dimensional grid with smaller or larger resolution. The overall best-fit model approximately gives the same results that are found in the global fit done in this Section. The χ^2 values are 209.24 as compared to 211.80. The best-fit parameters of m_0 , p_x , p_y , p_z were translated to a dipole amplitude $\delta = 0.425 \pm 0.049$ and rate normalization $R_{0,\text{el}} = 1.35 \times 10^{-2}$. These values are similar to the ones calculated before. From the left-hand panel in Figure 5.42 it can be seen that also the directions of the dipole maxima for the best-fit models are compatible.

For all considered models the $\chi_{\text{best}}^2/d.o.f.$ is much larger than 1. The corresponding p -values get larger when including additional multipoles, but even for the hexadecapole the p -value is still of the order of 10^{-8} . Here, the p -value gives the probability that such a large χ_{best}^2 is found if the considered model is correct (null hypothesis). Since this probability is very small, none of the models is sufficient to explain the data.

Further, the improvement of the fit achieved by subsequently examining more complex models by including more multipoles was studied. For this, both, the $\Delta\chi^2$ -test and the F -test were employed. The results of the $\Delta\chi^2$ -test are shown in Table 5.8, while the results of the F -test are shown in Table 5.9. Here, the p -value gives the probability that the $\Delta\chi^2$ (or F) value is found if the simple model is correct. Thus, a small p -value means that it is unlikely to find such a large $\Delta\chi^2$ (or F) value if the simple model is correct and that the additional parameters should, consequently, be included in the model. Employing the $\Delta\chi^2$ -test the improvements are significant at the order of 5 σ going from the isotropy model to the dipole model, larger than 3 σ going from dipole to quadrupole and larger than 2 σ going from quadrupole to octupole. The improvement when going to the hexadecapole is not significant

$l_{\text{simple}} - l_{\text{comp}}$	f	p -value
0 - 1	5.66	1.35×10^{-03}
1 - 2	2.46	3.95×10^{-02}
2 - 3	1.27	2.75×10^{-01}
3 - 4	0.67	7.35×10^{-01}

Table 5.9: Results of F -tests of consecutive multipole fit functions. First the multipoles of the simple model l_{simple} and the more complex model l_{comp} are given. Further, corresponding f -values and p -values are given.

at any considerable level. The p -values given by the F -test are comparably larger, because the F -test takes into account that a certain amount of improvement of the fit is always expected when introducing more free parameters. With the F -test only the improvement going from monopole to dipole and from dipole to quadrupole are significant at the much smaller 2σ level.

5.3.9 Power Spectrum

The assumption of isotropy implies that the harmonic coefficients a_{lm} are on average zero. The variance of the harmonic coefficients a_{lm} gives a power spectrum of the measured fluctuations. This variance taken over many ensembles is given by

$$\langle a_{lm} a_{l'm'}^* \rangle = \delta_{ll'} \delta_{mm'} C_l. \quad (5.58)$$

In other words the a_{lm} s are independent Gaussian random variables with mean zero and variance C_l . Since there is only one universe available it is only possible to measure $2l+1$ m -modes for each multipole. Thus, the maximum-likelihood estimator of the C_l s is called power spectrum and given by

$$C_l = \frac{1}{2l+1} \sum_{m=-l}^l |a_{lm}|^2. \quad (5.59)$$

Assuming the rate fluctuations were measured with full-sky coverage and with negligible noise and the a_{lm} s are independent identically distributed Gaussian random fields the C_l s are χ^2 distributed and the variance of C_l is given by

$$\frac{\text{Var}(C_l)}{C_l} = \frac{2}{2l+1}. \quad (5.60)$$

This is the unavoidable minimum uncertainty of C_l in the case of perfect measurement conditions (called cosmic variance). In realistic setups the variance and, thus, the uncertainty of C_l gets larger with declining sky coverage (roughly anti-proportional to the fraction of the sky covered). It is important to realize that every theory predicts the expectation values of the C_l s

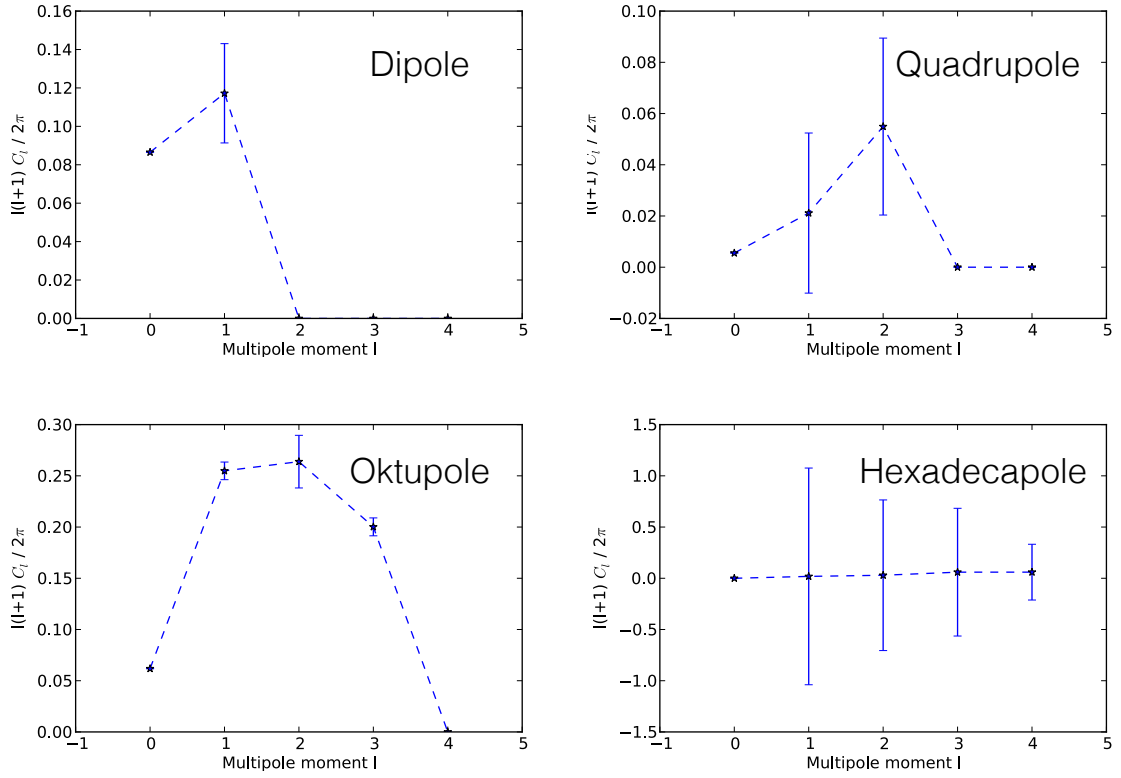


Figure 5.43: Power spectra of the best-fit multipole models including multipoles up to the dipole ($l_{\max} = 1$, upper left-hand panel), the quadrupole ($l_{\max} = 2$, upper right-hand panel), the octupole ($l_{\max} = 3$, lower left-hand panel) and the hexadecapole ($l_{\max} = 4$, lower right-hand panel) are shown. The error on C_0 has always been set to zero because it is often so large that displaying it would make it impossible to read the Figure. C_l s and corresponding errors of multipoles that are not included in the model are also set to zero.

and our sky gives one realization of these C_l s. Thus, it will never be possible to distinguish between models that predict differences in the C_l s smaller than the cosmic variance.

Figure 5.43 shows the power spectra for the best-fit $l_{\max} = 1$ to $l_{\max} = 4$ models. The errors of the fit parameters are given by the square root of the diagonal elements of the covariance matrix. The covariance matrix was found by first applying the MIGRAD algorithm and then applying the HESSE algorithm both included in the MINUIT software package (James 1998). The minimization algorithm implemented in MIGRAD is a stable variation of the Davidon-Fletcher-Powell variable-metric algorithm (James 2004). This algorithm converges to the correct error matrix as it converges to the function minimum. It can happen that the function converges too quickly to its minimum for the algorithm to find a good estimate of the error matrix. In this case HESSE should be invoked, which calculates the full second-derivative matrix by finite differences and inverts it. This appears to happen in case of the octupole model, where MIGRAD found extremely small errors of the order of 10^{-9} . However, even after using HESSE the error bars became larger, but were still relatively small. Additionally, the covariance matrix was artificially forced to be positive definite. This can be caused by one of three reasons. A region of the parameter space with unphysical behavior was traversed, the system was under-determined or numerical inaccuracies occurred (James 1998). In any case, the resulting minimum is suspicious and the errors are unreliable. Consequently, the results of the octupole fit are unreliable.

In general, the errors on parameters of the more complicated model are expected to be larger for a certain parameter than the error bars for the same parameter in a less complex model (a model where effectively some of the parameters for higher multipoles were set to zero). This is due to the fact that correlations between the parameters contribute to the errors on the parameters. Thus, if one of the parameters is fixed its correlation with other parameters is gone and does not contribute to the error of the other parameters anymore (James 2004).

The error bars of the C_l s were calculated via Gaussian error propagation from the diagonal elements of the variance matrix calculated by PyMinuit. In a more complete examination also the off-diagonal elements (= covariance) must be considered, because in this study only a very small fraction of the sky is covered, which should lead to degeneracies (dependencies/correlations) between the multipoles and, thus, the C_l s (Scott and Smoot 2004). In Figure 5.43 the error for $l = 0$ is always set to zero artificially, because it is often so large that an illustration is impossible. Instead, the values for m_0 and its error are shown in Table 5.10 for all models. Further, the values of C_l s for multipoles that are not included in the considered model are also set to zero in Figure 5.43.

The C_l s derived from different multipole fit functions are quite different, which implies that also the best-fit parameters for the same multipole vary strongly between the different functions. Thus, when introducing more and more free parameters, also the free parameters that were already included in simpler models vary into other regions of their parameter spaces when searching for the best-fit parameter set. This implies that the parameters of the model are not strictly constrained by the data. In other words, systematic and statistical errors on the data appear to be too large to draw any definite conclusions on actual model parameters and, thus, the actual power at a given multipole. This is consistent with the bad fit between data and model, which also implies that the best-fit models considered in this study are not

l_{\max}	m_0	σ_{m_0}
0	-0.010	0.019
1	0.210	0.040
2	-0.053	0.174
3	0.175	0.007
4	0.001	4.45

Table 5.10: The best-fit m_0 parameter and corresponding error σ_{m_0} for all considered multipole models.

sufficient to explain the data.

Further, the shape of the resulting best-fit rate predictions appears to be strongly dominated by regions where no experimental data was available. Minima and maxima of the best-fit rate prediction functions are always located in regions of the sky without data. If the electron arrival rates are not constrained in extended regions of the sky the predicted rates in those directions can become arbitrarily large or small.

Conclusion In conclusion, the rate fluctuations in the electron-arrival rates considered in this study cannot be described sufficiently by isotropy or large scale anisotropy models. The angular scales at which the rate fluctuations occur appear to be much smaller than the angular scales considered in this study. However, the amount of data available and distribution over the sky makes it impossible to investigate such small scale anisotropies with H.E.S.S. at this point. The only conclusion that can be drawn from this study is that neither isotropy nor large scale anisotropies alone can account for the observed electron rate fluctuations provided that systematic effects were sufficiently taken into account.

5.3.10 The Two-Point-Correlation Function

In Section 5.3.2 it was found that neither isotropy nor a simple dipole model can explain the H.E.S.S. I measurement of electron arrival rates. It has been suggested that higher order anisotropies may play an important role. In Fig 5.44 a visualization of the measured arrival rates of cosmic-ray electrons (with a 20° smoothing radius) is shown in the top panel and the cosmic-ray anisotropies measured with IceCube-22 (Abbasi et al. 2010) and Tibet-III (Amenomori and Tibet AS γ Collaboration 2006) are shown in the bottom panel. In contrast to all previous plots the sky maps are now shown in equatorial coordinates.

The amplitudes of the measured fluctuations are found at very different scales (fluctuations at the order of 10^{-3} in cosmic rays compared to fluctuations at the order of a few times 10^{-1} in cosmic-ray electrons). This visualization is not a statistical analysis, and the smoothing of the electron sky map was simply done by calculating a weighted average of the measured electron arrival rates within 20° of a sky map pixel.

Besides fitting multipole models to the data and calculating a power spectrum from the fit coefficients as it was done in Sections 5.3.8 and 5.3.9 it is possible to perform an analysis of the two-point-correlation function (TPC function) in order to evaluate the power of anisotropies at different angular scales. Analogous to the definition common in investigations of CMB anisotropies the correlation function is given by the expectation value of the correlation of the fluctuations of the electron arrival rates²⁷ $I_i = \frac{R_{i,\text{el}} - \langle R_{\text{el}} \rangle}{\langle R_{\text{el}} \rangle}$ between two points in the sky with angular distance $\cos \theta$. The correlation function is connected to the angular power spectrum C_l by the following relation

$$\langle I(\hat{\mathbf{n}}) \cdot I(\hat{\mathbf{n}}') \rangle = \frac{1}{4\pi} \sum_{l=0}^{\infty} C_l P_l(\cos \theta). \quad (5.61)$$

Here, the C_l s are the coefficients of the angular power spectrum and the P_l s are the Legendre polynomials. As before l is called the multipole and represents the given angular scale. It is obvious from Equation 5.61 that the values of the TPC function for points at a given angular distance $\hat{\mathbf{n}} \cdot \hat{\mathbf{n}}' = \cos \theta$ contain contributions from different multipoles in contrast to the power spectrum, where every C_l only gives the angular power exactly at the multipole l (at least in the case of an all sky coverage). This makes the interpretation of the TPC function more challenging than the interpretation of the power spectrum. On the other hand both functions equivalently contain the complete information about the anisotropies. An additional analysis of the TPC function of a cosmic-ray anisotropy sky map can also help to understand the TPC function of cosmic-ray electrons better, by investigating for example what imprints certain features (e.g. hot spots) can have in the TPC function and answering the question whether these imprints can have an obvious effect. In the power spectrum approach the effects might be distributed between the C_l s of different multipoles, while they are concentrated in one angular distance bin for the TPC function (see the subsequent subsection discussing the ARGO-YBJ TPC function and power spectrum).

²⁷In the case of the CMB the temperature is used instead see, e.g. Peacock 1999, Bunn 1995 and Tojeiro 2006.

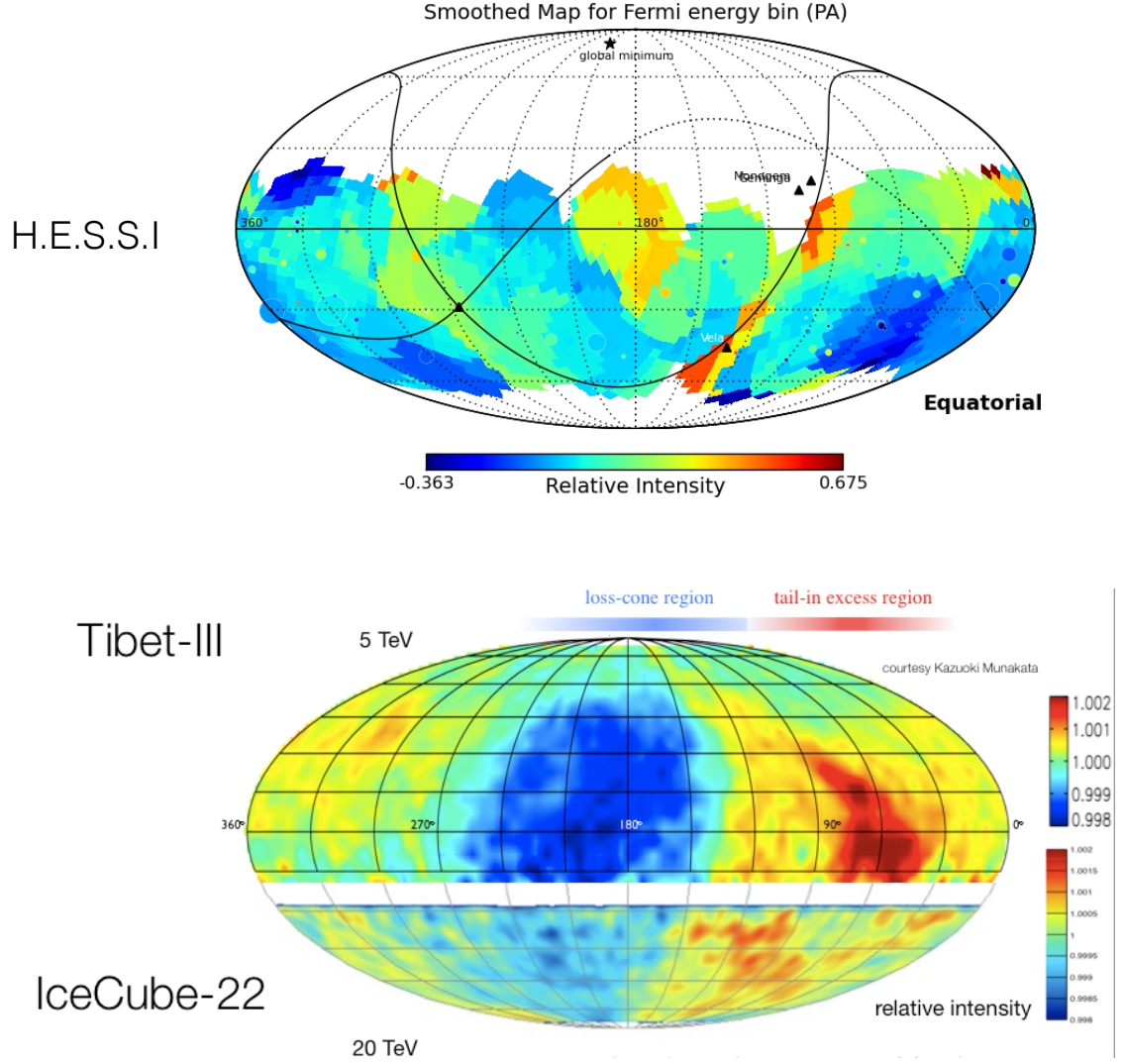


Figure 5.44: Top: Sky map of cosmic-ray electron event rates with 20° smoothing radius. In each pixel the weighted mean of the measured electron arrival rate fluctuations of all pointings within 20° distance is shown. In addition the pointings are marked by a circle with a radius corresponding to the live time of the observations of every pointing. The colors of the circles are scaled with the corresponding electron arrival rate value. Bottom: Sky maps of the cosmic-ray anisotropies measured with IceCube22 (Abbasi et al. 2010) and Tibet-III (Amenomori and Tibet AS γ Collaboration 2006). Adapted from Desiati 2012.

The TPC function is determined by the fluctuation of the measured electron event rates (with $R_{i,\text{el}} = R_{i,\tilde{\gamma}} - (1 - \epsilon_{\text{el}})\langle R_{\tilde{\gamma}} \rangle$ and $\langle R_{\text{el}} \rangle = \epsilon_{\text{el}}\langle R_{\tilde{\gamma}} \rangle$) for every possible pair of pointings (i, j) in dependence on their angular separation $\cos\theta$. The average of this value is taken within distinct $\cos\theta$ bins. The TPC function C_1 is given by

$$C_1(\theta) = \left\langle \frac{R_{i,\text{el}} - \langle R_{\text{el}} \rangle}{\langle R_{\text{el}} \rangle} \cdot \frac{R_{j,\text{el}} - \langle R_{\text{el}} \rangle}{\langle R_{\text{el}} \rangle} \right\rangle_{\cos\theta}. \quad (5.62)$$

An alternative definition of the TPC function can also be employed. Here, the absolute rate fluctuations are compared to the error on the corresponding electron event rate $\sigma_{i,\text{el}} = \sigma_{i,\tilde{\gamma}}$. The TPC function C_2 is defined similarly to C_1 and given by

$$C_2(\theta) = \left\langle \frac{R_{i,\text{el}} - \langle R_{\text{el}} \rangle}{\sigma_{i,\text{el}}} \cdot \frac{R_{j,\text{el}} - \langle R_{\text{el}} \rangle}{\sigma_{j,\text{el}}} \right\rangle_{\cos\theta}. \quad (5.63)$$

For both definitions of the TPC function the power of the TPC function is large for large fluctuations around the mean independent from correlation or anti-correlation. The C_2 definition has the advantage that rate fluctuations are observed relative to the error on the measured rate. Consequently, it also gives an information about the strength of the fluctuation compared to the magnitude of the errors and takes statistical and systematic errors into account. Both definitions of the TPC function should give similar results.

The significance of all quantities is determined by the means of MC simulations, since the underlying probability distribution is unknown. The procedure is comparable to the approach used in Section 5.3.2. With the difference that now the TPC functions are calculated for every simulated data set and the probability of getting the measured value of $C_1(\theta)$ and $C_2(\theta)$ in the isotropy simulations is determined for every $\cos\theta$ bin.

Instead of using the expectation value of the relative rate fluctuations also Spearman's rank correlation coefficient can be used. Both relative intensity definitions can be employed

$$I_{i,1} = \frac{R_{i,\text{el}} - \langle R_{\text{el}} \rangle}{\langle R_{\text{el}} \rangle} \text{ or } I_{i,2} = \frac{R_{i,\text{el}} - \langle R_{\text{el}} \rangle}{\sigma_{i,\text{el}}}. \quad (5.64)$$

For each angular distance bin $\cos\theta$ all k possible pairs $P_k=(I_i, I_j)$ of pointings (i, j) with relative intensities I_i and I_j are built. Thus, two data samples are generated, where the first sample X contains the first of the two values in each pair so that $X_k=I_i$ and the second sample contains the second of the two values in each pair $Y_k=I_j$. The corresponding ranked data samples are calculated $x_k=\text{Rank}(I_i)$ and $y_k=\text{Rank}(I_j)$ and Spearman's rank correlation coefficient $\rho_s = \text{spear}(X, Y)$ is calculated as explained in Section 4.3.2. With this method the p -value and, thus, the significance of Spearman's rank correlation coefficient can be calculated via Student's t -test and is, consequently, independent from MC simulations and any assumption made concerning systematic errors. Here, it is used for cross checking the results of the previous methods.

Likewise, the TPC functions and ρ_s are calculated from the hadron-like event samples. In this case electron event rates and corresponding errors are simply replaced by the corresponding hadron-like (BG) event rates and errors.

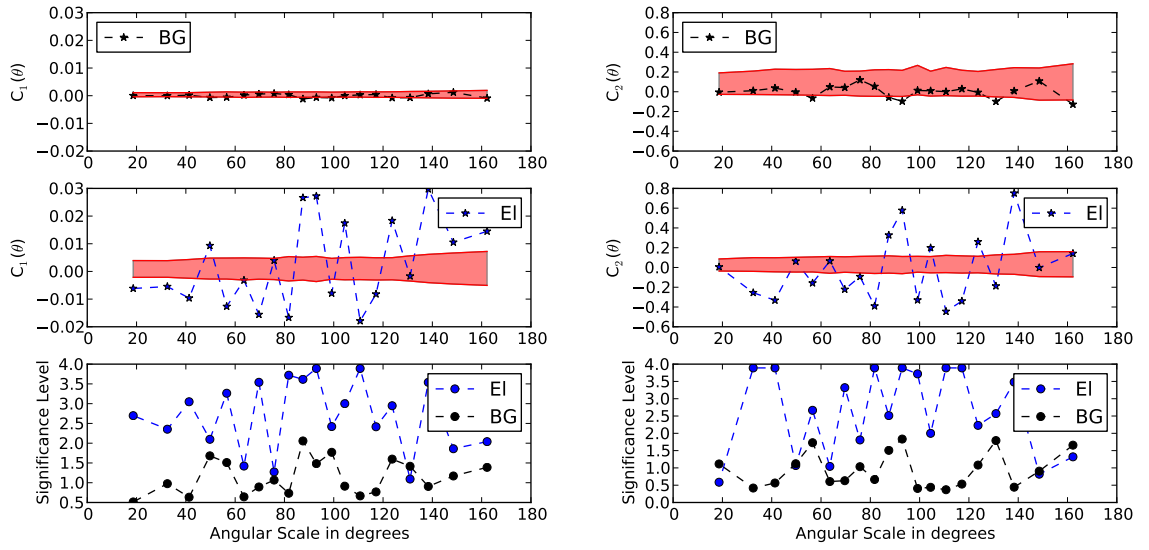


Figure 5.45: Top panels: C_1 (left) and C_2 (right) calculated from the measured BG event rates (black markers). Middle panels: C_1 (left) and C_2 (right) calculated from the measured electron event rates (blue markers). The boundaries of the red bands depict the 16 % and 84 % percentiles from the probability density distributions of the corresponding simulated TPC function values. Consequently, 68 % of the simulations generate TPC function values within this band. Bottom panels: The significance given in units of Gaussian sigma calculated from the simulated probability density functions for each measured TPC function value for the electron (blue markers) and BG (black markers) rates for C_1 (left) and C_2 (right).

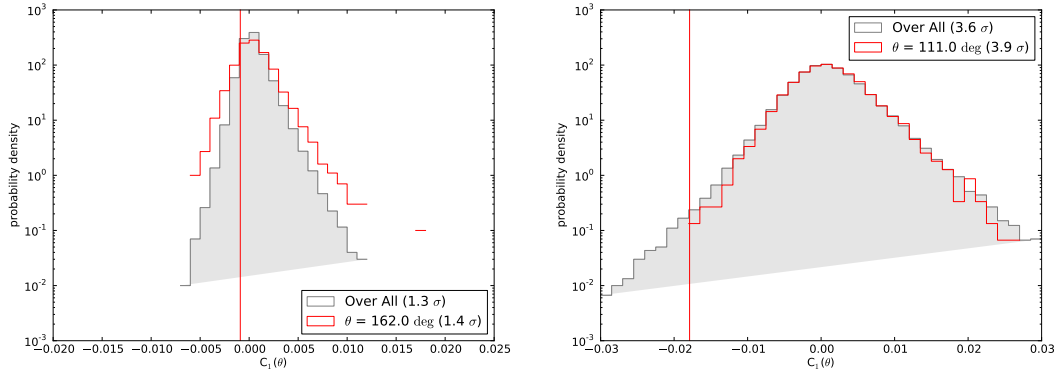


Figure 5.46: Example probability density function for C_1 obtained via MC simulations for BG event rates (left-hand panel) and electron event rates (right-hand panel). The red histograms show the probability density functions found for one example $\cos\theta$ bin for BG rates (left-hand panel) and electron rates (right-hand panel). The corresponding measured values in this $\cos\theta$ bin are marked by a red line. The gray histogram contains the corresponding probability density function for all $\cos\theta$ bins combined. The significances of the measured values considering the probability density function of the chosen $\cos\theta$ bin and the combined function are shown.

Figure 5.45 shows the results of the calculation of $C_1(\theta)$ and $C_2(\theta)$. Corresponding results from MC simulations are superimposed as a grey band, which contains 68 % of the simulations (boundaries are given by the 16 % and 84 % percentiles). For both TPC function definitions the TPC function values calculated from the hadron-like (BG) data ($MSSG > 5$) and electron event data ($MSSG < 0.6$) are shown in the top and middle panels of Figure 5.45. The measured TPC function values for, both, electron and BG rates fluctuate around zero. The amplitudes of the TPC function values are much smaller for BG rates than for electron rates (for both C_1 and C_2). Even though, the shapes of C_1 and C_2 are not identical, the largest minima and maxima in the functions can be found in both definitions (for electrons and BG events). Due to the different definitions of C_1 and C_2 the absolute function values of C_1 and C_2 cannot be compared. Via construction C_2 adopts values between approximately -1 and +1, while the amplitudes of C_1 depend on the amplitudes of the event rates themselves.

In addition to the measured TPC function a band of the TPC function values obtained via isotropy simulations is shown. The boundaries of this band correspond to the 16 % and 84 % percentiles from the probability density distributions of simulated TPC function values. Consequently, the simulation bands in Figure 5.45 contain the innermost 68 % of the TPC function values obtained via simulations. The probability density distribution of TPC function values is shown in the left-hand panel of Figure 5.46 for BG events and in the right-hand panel for electron events for one example $\cos\theta$ bin of C_1 .

The BG events for both TPC function definitions lie mostly within this 68 % band showing qualitatively that the distribution of BG event rates in the sky is compatible with isotropy at all angular distances considered. This is in agreement with the dipole analysis before. The measured electron TPC function values acquire values located significantly outside the 68 %

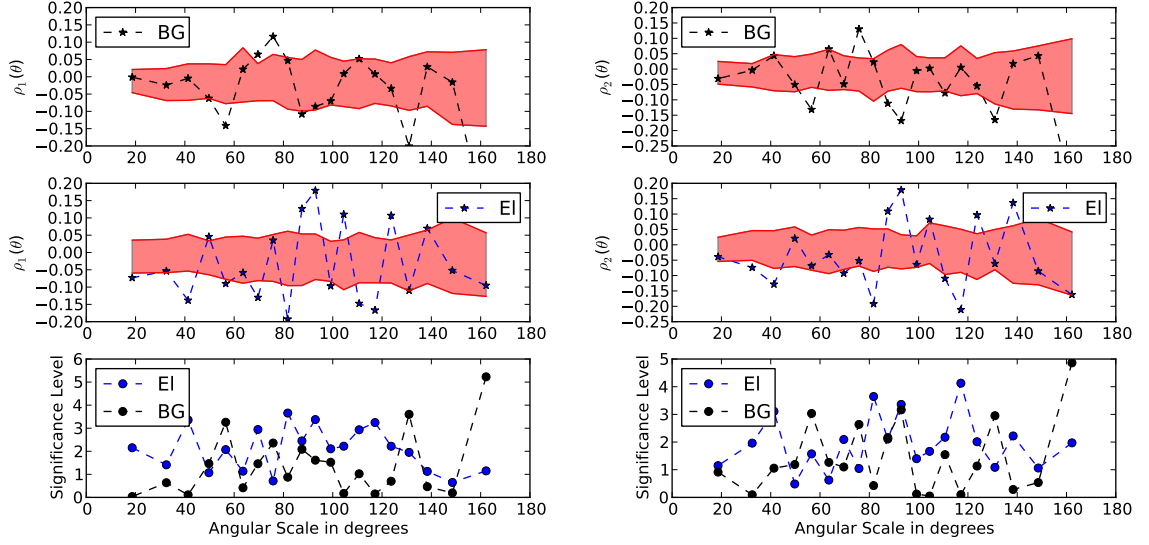


Figure 5.47: Top panel: Spearman's rank correlation coefficients ρ_1 (left) and ρ_2 (right) calculated from the measured BG event rates (black markers). Middle panels: Spearman's rank correlation coefficients ρ_1 (left) and ρ_2 (right) calculated from the measured electron event rates (blue markers). The boundaries of the red bands depict the 16 % and 84 % percentiles from the probability density distributions of the corresponding simulated ρ_s values. 68 % of the simulations generate ρ_s values within this band. Bottom panels: The significance given in units of Gaussian sigma calculated from the t -distribution for the electron (blue markers) and BG (black markers) rates.

band. This behavior suggests qualitatively that they are much less compatible with isotropy. Thus, the probability (p -value) that a TPC function value greater than or equal to the measured value is found by chance is calculated from the probability density distributions of the TPC function values for each $\cos \theta$ bin. From the p -value the corresponding significance in each $\cos \theta$ bin is calculated following Equation 4.9. A large significance means that the probability to find a TPC function value at least as extreme as the measured value, just by chance, is very small if cosmic-ray electrons really arrive isotropically at Earth. The results of the significance calculations are shown in the bottom panels of Figure 5.45. The significance of the TPC function values for the BG events is smaller than 2σ for all $\cos \theta$ bins. For electrons the deviation from isotropy is much more significant with a significance $\geq 4 \sigma$ in many $\cos \theta$ bins. The maximum resolution of the simulations corresponds to a maximum achievable significance of 4σ , because only 10 000 simulations were performed.

These results are verified by the corresponding results employing Spearman's rank correlation coefficient shown in Figure 5.47. The shapes of the functions ρ_1 and ρ_2 are similar to the shapes of C_1 and C_2 . In particular, the most prominent minima and maxima of ρ_1 and ρ_2 shown in Figure 5.45 correspond to the minima maxima found in C_1 and C_2 shown in Figure 5.47.

In Figure 5.47 the 68 % bands are obtained via simulations, but the significances in the third panel are calculated via Student's t -test (remember Equation 4.20 in Section 4.3.2). This method of calculating the significance does not take statistical and systematic errors into account as simulations do, but solely depends on the values of ρ_s and the shape of the t -distribution. Thus, it gives a significance estimate more independent from the estimation of systematics. The significance for the coefficients ρ_1 and ρ_2 calculated from the BG event rates is somewhat larger than the significances calculated for C_1 and C_2 , but usually $< 3 \sigma$, apart from the last $\cos \theta$ bin. Here, an outlier is found. For electrons the maximum significance obtained with this method is comparable to the significance found for C_1 and C_2 (up to 4σ).

ARGO-YBJ TPC and Power Spectrum

As mentioned before, the interpretation of the TPC function is much less straight forward compared to the interpretation of the angular power spectrum, because the TPC function contains contributions from all multipoles at every angular distance. The idea is to learn from an anisotropy sky map what imprints or signatures small to medium scale features (e.g. hot spots) would have on the TPC function. In other words: Do large electron arrival rates make the power at a certain angular scale larger? How do such features look like in a TPC function and can they be identified?

For such studies the ARGO-YBJ collaboration provided us with the original cosmic-ray anisotropy sky maps (signal and background maps) that were used to calculate the published total sky map shown Figure 5.48 (ARGO-YBJ Collaboration 2013). The ARGO-YBJ sky maps are of special interest for such an analysis for several reasons. First, even though H.E.S.S. observes the southern hemisphere and ARGO-YBJ the northern hemisphere there is a certain overlap between the regions of the sky observed with both experiments. Second, the cosmic-ray electrons measured with H.E.S.S. should contribute to the data set and consequently possibly also the anisotropies measured with ARGO-YBJ. Further, the ARGO-YBJ sky maps contain medium to small scale anisotropies of the type that might also be present in the electron data. Thus, these sky maps are suitable to study the behavior of the TPC function.

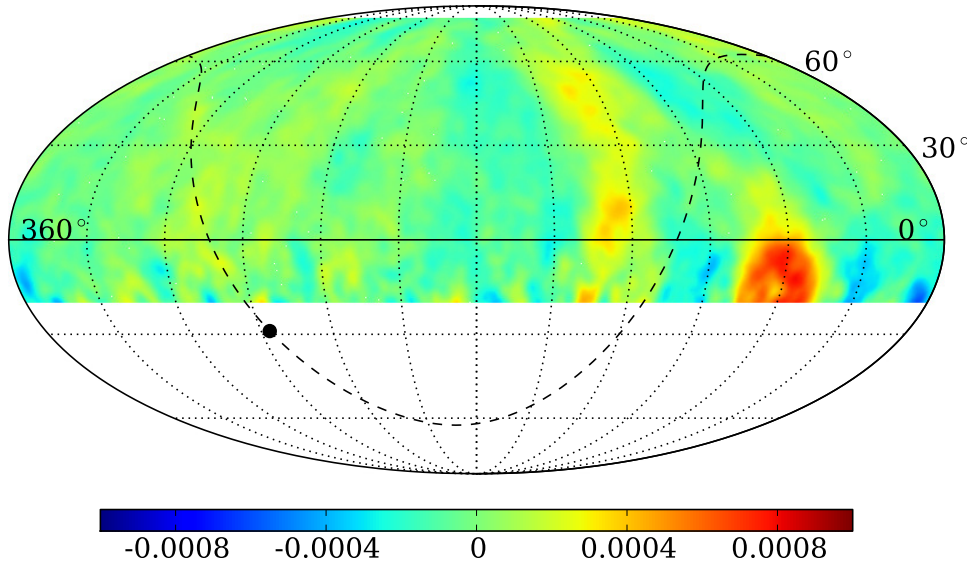


Figure 5.48: Published ARGO-YBJ cosmic-ray anisotropy sky map in equatorial coordinates for all events with a stripe multiplicity larger than 25. The relative excess with respect to the background events is shown. A Gaussian beam smoothing has been applied with an angle corresponding to the PSF of the detector. The galactic plane is shown as a black dashed line and the Galactic Center marked by the black circle. Figure adapted from ARGO-YBJ Collaboration 2013.

Stripe-multiplicity interval	Number of events	E_p^{50} [TeV]
25 - 40	1.41673×10^{11} (38 %)	0.55
40 - 100	1.75695×10^{11} (48 %)	1.4
100 - 250	3.80812×10^{10} (10 %)	3.5
250 - 360	1.09382×10^{10} (3 %)	7.3
> 360	4.34442×10^9 (1 %)	20

Table 5.11: Table of the used multiplicity intervals, the corresponding measured event numbers and the corresponding median energy E_p^{50} from cosmic-ray proton MC simulations. The values were taken from ARGO-YBJ Collaboration 2013.

ARGO-YBJ²⁸ does not apply any gamma-hadron separation algorithm. Thus, the shown map does not only contain protons but possibly also photons and electrons. Further, it is not possible to reconstruct the energy of an individual cosmic-ray particle. Instead, the data set was split into five multiplicity intervals in order to investigate the energy dependence of the cosmic-ray anisotropies. Via Monte Carlo simulations of protons the median energy E_p^{50} of every multiplicity interval was determined (ARGO-YBJ Collaboration 2013). The used stripe multiplicity intervals, the number of events measured in this interval and the corresponding median energy from proton MC simulations are shown in Table 5.11. Since the particles detected with ARGO-YBJ are assumed to be protons, cosmic-ray electrons of 600 GeV would be counted as protons of roughly 1 TeV (Iuppa 2014). The ratio of the electron flux at 600 GeV (Ackermann et al. 2010b) and protons at 1 TeV (Adriani et al. 2011b) is $\phi_{\text{el}}(600\text{GeV})/\phi_{\text{proton}}(1\text{TeV}) \approx 10^{-3}$. Thus, 1 electron for every 1000 protons is expected in the data set at 1 TeV. Depending on the amount of anisotropy really existing in cosmic-ray electrons the anisotropy measured with ARGO-YBJ may also contain an electron contribution. Electrons with energies between 0.64 and 1.04 TeV would, thus, contribute to the lowest two multiplicity interval data sets.

In this study only the first four multiplicity interval sky maps, corresponding to median proton energies up to 7.3 TeV, were used, because the last one contains not enough statistics. All four relative intensity ($\text{RelInt}_{\text{ARGO}} = N_{\text{signal}} - N_{\text{BG}}/N_{\text{BG}}$) sky maps are shown in Figure 5.49. To every map a Gaussian beam smoothing with a full-width-half-maximum (fwhm) corresponding to the individual point spread function (PSF) estimated from Bartoli et al. (2011) was applied. For the lowest energy map a $\text{fwhm} = 4^\circ$ of the Gaussian beam was used, while for the map with the highest median energies only a $\text{fwhm} = 2.5^\circ$ was used.

The TPC function for the ARGO-YBJ sky maps is defined a little bit different from the previous definition given in Equation 5.62, because here we have a signal and a background

²⁸The ARGO-YBJ detector is located at an altitude of 4300 m above sea level at the YangBaJing Cosmic Ray Observatory in Tibet. ARGO-YBJ uses resistive-plate chambers (RPCs) to detect air showers induced by cosmic rays and gamma rays. The RPCs are operated in streamer mode and cover a total area of 5600 m². Each RPC is read out by 80 external strips (in total there are 146880 strips). The multiplicity is the number of fired strips and is connected to the energy of the primary particle. The charged particles in an air shower are detected with an efficiency larger than 98 %. The energy threshold of the instrument is approximately 100 GeV. The highest primary particle energies detectable without significant saturation is 200 TeV. For more information on the ARGO-YBJ experiment see, e.g. Bartoli et al. 2011 and Aielli et al. 2012.

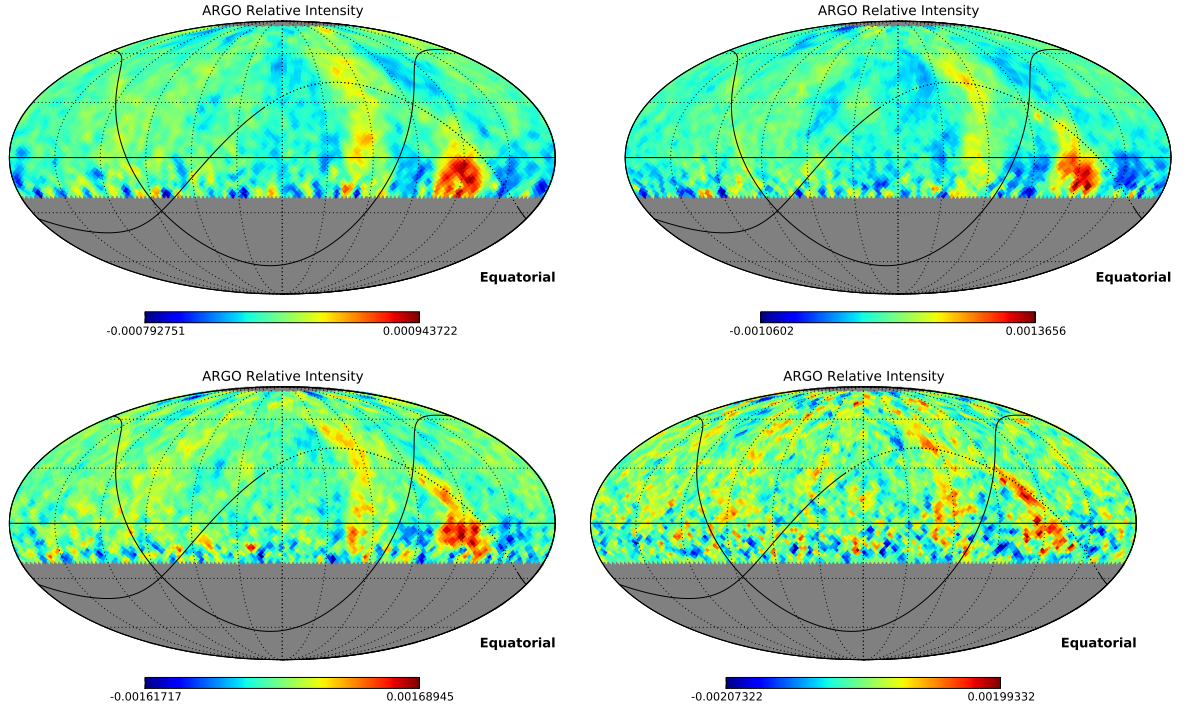


Figure 5.49: ARGO-YBJ relative intensity sky maps in equatorial coordinates. A Gaussian beam smoothing was applied to every sky map with a smoothing radius corresponding to the individual point spread function (PSF). The maps for different pairs of E_p^{50} and fwhm are shown for $E_p^{50} = 0.66$ TeV and fwhm = 4° in the upper left-hand panel, for $E_p^{50} = 1.4$ TeV and fwhm = 3° in the upper right-hand panel, for $E_p^{50} = 3.5$ TeV and fwhm = 3° in the lower left-hand panel and for $E_p^{50} = 7.3$ TeV and fwhm = 2.5° in the lower right-hand panel.

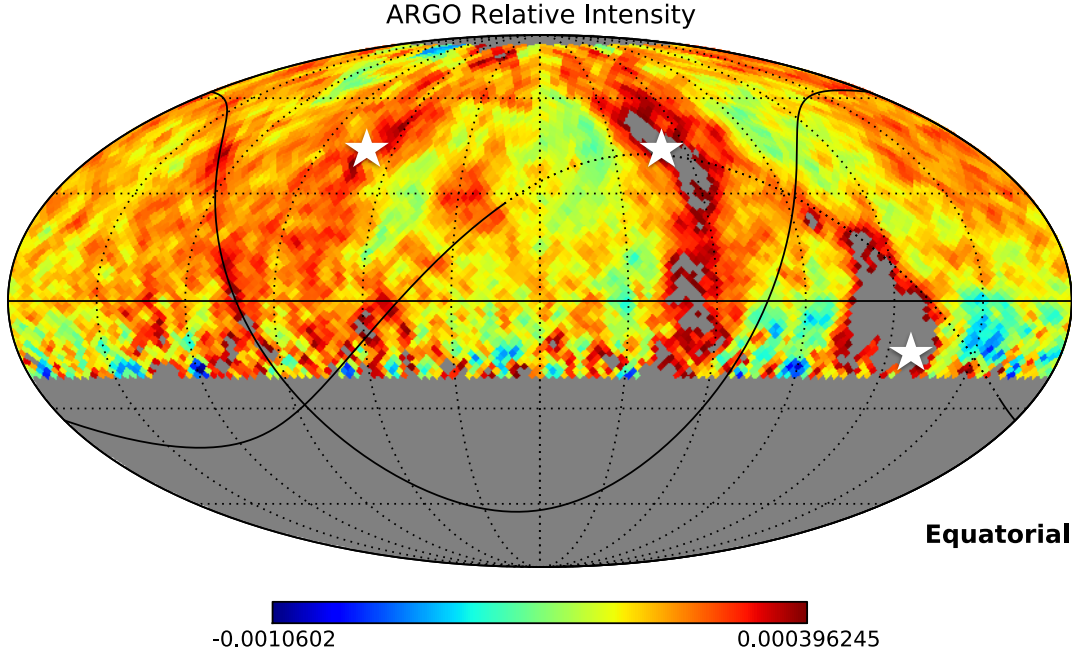


Figure 5.50: Example relative intensity sky map in equatorial coordinates where the 5 % highest relative intensity pixels have been removed. The positions of three hot spots are marked by white asterisks.

map available. The relative intensity fluctuations in each pixel i are given by the number of signal events $N_{i,\text{signal}}$ minus the number of background events $N_{i,\text{BG}}$ and normalized to the number of background events. Thus, the TPC is defined as follows

$$\tilde{C}_1(\theta) = \left\langle \frac{N_{i,\text{signal}} - N_{i,\text{BG}}}{N_{i,\text{BG}}} \cdot \frac{N_{j,\text{signal}} - N_{j,\text{BG}}}{N_{j,\text{BG}}} \right\rangle_{\cos \theta}. \quad (5.65)$$

This function is similar to C_1 (see Equation 5.62), so that it is called \tilde{C}_1 . The resulting TPC functions for the three maps with the lowest median energies (map₀: $E_p^{50} = 0.66$ TeV, map₁: $E_p^{50} = 1.4$ TeV and map₂: $E_p^{50} = 3.5$ TeV) are shown in the left-hand panel of Figure 5.51. They all are qualitatively and quantitatively very similar. Minima and maxima of the functions seem to shift somewhat to smaller angular scales with higher median energies, while the amplitudes of the minima and maxima seem to get larger with higher energy. This is reasonable since also the minimum and maximum of the relative intensity maps get larger with higher median energy. As expected the TPC function values are fluctuating around zero, while the function itself is much smoother than the corresponding H.E.S.S. I TPC function shown in Figure 5.45. This is expected because in the ARGO TPC not only 94 positions in the sky were probed, but a sky map covering a large area of the sky was used. If considering that only a few positions in the sky were used, the shape of the H.E.S.S. I TPC function of electrons seems reasonable.

In order to investigate the impact that prominent features can have on the TPC function

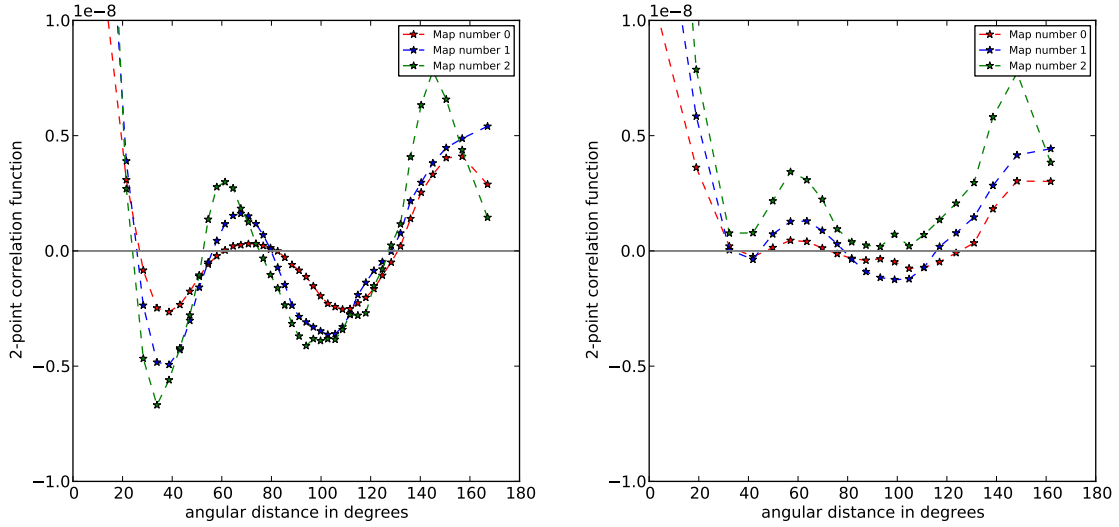


Figure 5.51: In the left-hand panel the TPC functions of the three maps with the lowest median energies (map₀: $E_p^{50} = 0.66$ TeV, map₁: $E_p^{50} = 1.4$ TeV and map₃: $E_p^{50} = 3.5$ TeV) are shown. In the right-hand panel the 5 % highest relative intensity pixels have been removed from these sky maps before the TPC functions were calculated.

the 5 % highest relative intensity pixels (with the goal to remove the two largest hot spot areas) have been removed from the sky maps (example map is shown in Figure 5.50) and the corresponding resulting TPC function is shown in the right-hand panel of Figure 5.51. After removing the 5 % highest relative intensity pixels the TPC function has obviously changed. While there is only a small influence on the maxima, the minima have become much smaller. Also the shift between the minima and maxima has been removed.

In order to investigate the impact of removing hot spots from the sky maps on the power spectrum, the power spectra of the sky maps are calculated using the anafast algorithm as it is implemented in the HealPy²⁹/HealPix³⁰ software package (Górski et al. 2005). The resulting power spectra are shown in Figure 5.52 before (left-hand panel) and after (right-hand panel) removing the highest 5 % relative intensity pixels. In the power spectrum the differences are much less obvious than they were in the TPC function. The most prominent changes are that the power in the $l = 0$ multipole is somewhat larger, as well as the power at $l > 30$. In between the power seems to be a little bit reduced.

Overall the impact is much less striking than in the TPC function, because in the power spectrum the effect seems to be distributed between the C_l s of all multipoles, while the effect concentrates on certain angular scales in the TPC function. Thus, the TPC function appears to be the more useful tool to investigate the possible existence of hot spots. It could be argued that the existence of prominent minima in a TPC function may hint to the existence of hot

²⁹<http://healpy.readthedocs.org>

³⁰<http://healpix.sourceforge.net>

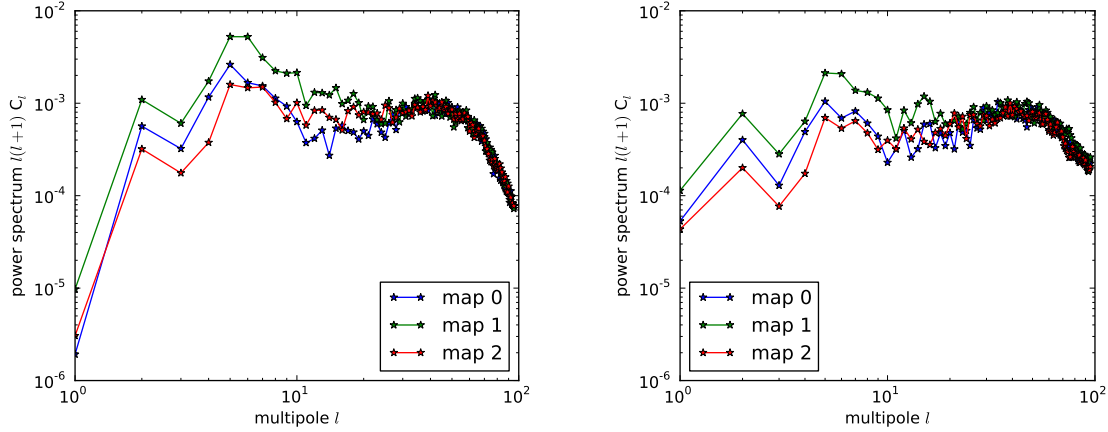


Figure 5.52: In the left-hand panel the power spectra of the three maps with the lowest median energies (map₀: $E_p^{50} = 0.66$ TeV, map₁: $E_p^{50} = 1.4$ TeV and map₃: $E_p^{50} = 3.5$ TeV) are shown. In the right-hand panel the 5 % highest relative intensity pixels have been removed from the sky maps before the power spectra were calculated.

spots in the sky (e.g. the two prominent minima in TPC of cosmic-ray electrons as shown in Figure 5.45). From the angular scale at which the minima occur it might be possible to derive the average angular distance between hot spots from the TPC function, while no information about where exactly these hot spots would be located can be derived.

As mentioned before, cosmic-ray electrons may contribute to the cosmic-ray anisotropy maps measured with ARGO-YBJ. Therefore, the Pearson correlation coefficient and Spearman's rank correlation coefficient were calculated between the relative intensity fluctuations of the H.E.S.S. I pointings and the corresponding ARGO sky pixels. For this analysis ARGO-YBJ relative intensity sky maps were downgraded in their resolution to a pixel size approximately as large as the solid angle area of the H.E.S.S. I measurement (half angle of 2°). Figure 5.53 shows the used ARGO-YBJ relative intensity sky map superimposed with all pointings of the H.E.S.S. I electron analysis. It is obvious that not all of the H.E.S.S. I pointings have a corresponding ARGO-YBJ sky patch. Figure 5.54 shows the results of the Pearson and Spearman's rank correlation coefficients and corresponding p -values. A mild anti-correlation is suggested by the data. The results of the two coefficients are similar. Spearman's correlation coefficient is somewhat larger indicating that the relationship is more likely monotone than linear. The corresponding p -values are rather large so that the result is not significant.

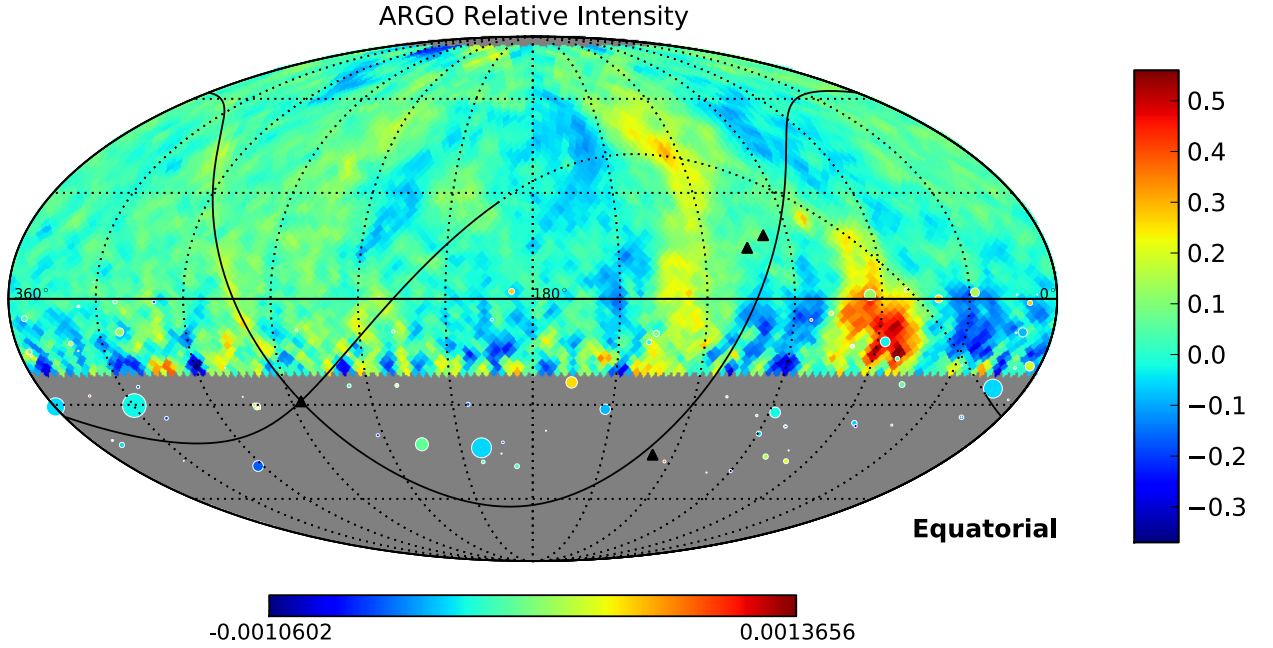


Figure 5.53: ARGO-YBJ sky map (NSide = 32) of the $E_p^{50} = 1.4$ TeV energy bin. The relative intensity of cosmic rays is color coded in the map. On the bottom the corresponding color bar is shown. Additionally, H.E.S.S. 1 pointings used in this study are depicted. The relative intensities of the electron arrival rates determine the colors of the circles depicting all 94 pointings. The color bar on the right-hand side of the map gives the color scale of electron intensities. Further, the circles are scaled with the respective observation time. The Galactic Center Sgr A* and pulsars Vela, Monogem and Geminga are shown and marked by black triangles. The map is given in equatorial coordinates.

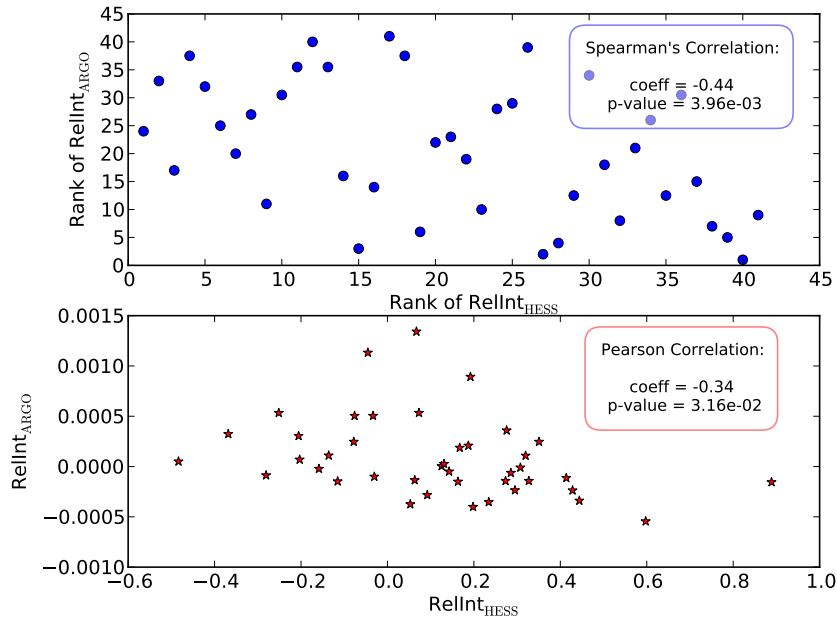


Figure 5.54: Top: Ranks of ARGO-YBJ relative intensities of cosmic rays compared to H.E.S.S.I relative intensities of cosmic-ray electrons. Spearman's rank correlation coefficient and corresponding p -value are shown. Bottom: ARGO-YBJ relative intensities of cosmic rays compared to H.E.S.S.I relative intensities of cosmic-ray electrons. The Pearson correlation coefficient and the corresponding p -value are shown.

Conclusion Overall, the analysis of the TPC functions showed that the TPC function values were not compatible with isotropy at the 4σ level confirming the results of the previous Sections. The interpretation of the TPC function beyond this statistical statement is difficult. Even though, the analysis of a medium to small scale anisotropy sky map provided by the ARGO-YBJ collaboration showed that imprints of hot spots are more prominent in the TPC function as compared to the power spectrum. No correlation between H.E.S.S. rate fluctuations and data from the same positions in the sky derived from the ARGO-YBJ sky map was found.

5.3.11 Upper Limit on the Dipole Amplitude

In the previous sections it was found that the measured electron arrival rate data could neither be fit well by a dipole model nor by models including higher order multipoles. Nonetheless, the fitted models can be used to constrain the model parameter space. Confidence intervals (Section 4.1.3) of the model parameters can be calculated, in principle, using planes of constant χ^2 . In this study the models involved have a large number of free parameters. Consequently, this method would unlikely give useful, connected regions of the parameter space. Instead, the H.E.S.S. data are employed to derive an upper limit (Section 4.1.3) on the dipole component.

Previously, *Fermi*-LAT and AMS-02 have set upper limits on the dipole amplitude of the cosmic-ray electron plus positron flux and the ratio of positron to electron flux respectively (Ackermann et al. 2010a, Aguilar et al. 2013 and Cangas 2013-2014). The upper limits were set in energy regions below the energies considered in this study. They are shown in the bottom panel of Figure 5.55. The AMS-02 upper limit, which was set on the dipole amplitude of pure electrons, was translated into an upper limit on the electron plus positron dipole amplitude using the electron and positron fluxes given by Aguilar et al. 2014b.

The H.E.S.S. upper limit on the electron flux was derived for every probed direction of the sky by fixing $R_{0,\text{el}}$ to its best-fit value ($R_{0,\text{el,best}}$) and then varying δ . The following requirement on $\Delta\chi^2(\delta)$ is valid for a 95 % CL upper limit and one varied parameter

$$\Delta\chi^2(\delta) = \chi^2(R_{0,\text{el,best}}, \delta) - \chi_{\text{best}}^2 \stackrel{!}{=} 4. \quad (5.66)$$

Here, $\chi_{\text{best}}^2 = \chi^2(R_{0,\text{el,best}}, \delta_{\text{best}})$ is the best-fit χ^2 of the dipole model discussed in Section 5.3.2. The dipole amplitude fulfilling the criterion defined in Equation 5.66 gives the upper limit on the dipole amplitude.

In the top panel of Figure 5.55 the sky map of upper limits is shown. This sky map gives the upper limit on the dipole amplitude always assuming that the maximum of the dipole is pointing into the probed direction of the sky. The derived upper limits reach from 2.5 % to 56 % in dependence on the direction of the observation. The dipole amplitude is least constrained in the direction of the sky where no data was available and much more constrained in directions where cosmic-ray electron data from H.E.S.S. is available.

In the bottom panel of Figure 5.55 the currently available upper limits on the dipole amplitude are summarized. The upper limits derived in this study depend on the considered direction in the sky and are, thus, illustrated by a blue band. In the regions of the sky most efficiently covered by H.E.S.S. observations the upper limits derived in this study are comparable or even below the upper limits from *Fermi*-LAT.

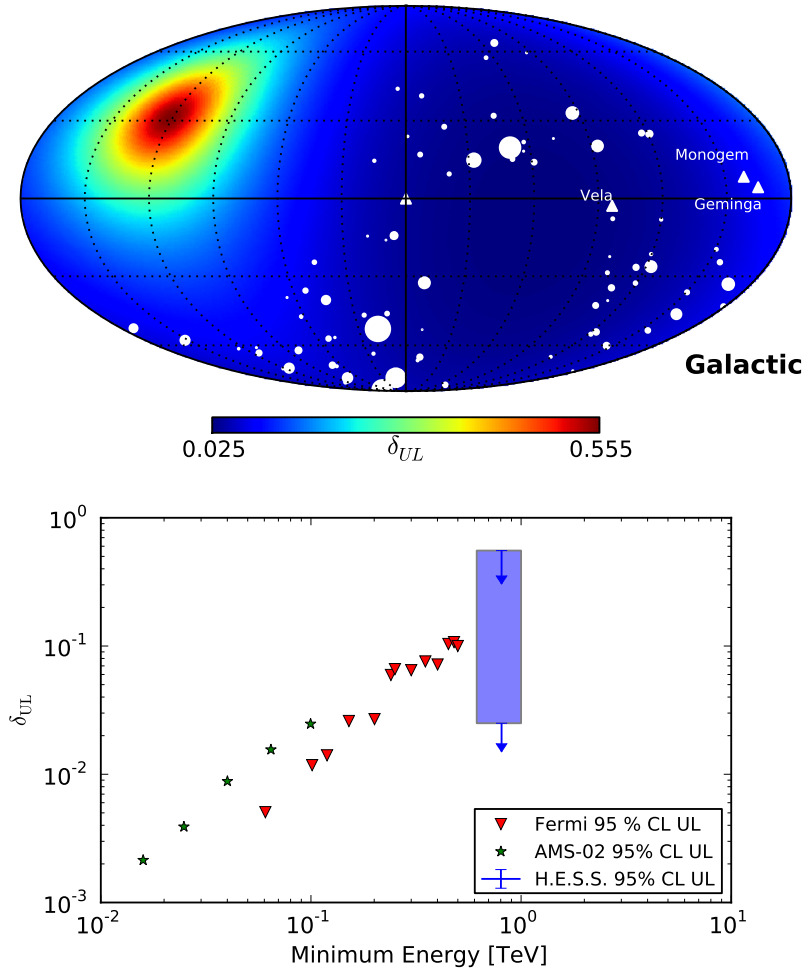


Figure 5.55: Top: Sky map in galactic coordinates showing the upper limits derived from H.E.S.S. data on the dipole amplitude of cosmic-ray electrons for each possible direction of the dipole maximum. The white circles depict the 94 pointings and are scaled with the respective observation time (range from 0.24 to 173 h). The pulsars Vela, Monogem, Geminga and the Galactic Center are also shown and marked by a white triangle. Bottom: 95 % CL upper limits on the dipole amplitude δ_{UL} derived with *Fermi*-LAT (Ackermann et al. 2010a), AMS-02 (Cangas 2013-2014) and H.E.S.S. The AMS-02 upper limits were set on the ratio of positron to electron flux. In dependence of the electron and positron fluxes they were translated to electron plus positron upper limits for comparison. The *Fermi*-LAT and AMS-02 upper limits are given in dependence on the minimum energy of the used events. The H.E.S.S. upper limits were calculated in a defined energy bin. For H.E.S.S. a blue band of upper limits is illustrated since the sky is only partially covered by observations and, thus, the upper limits vary strongly between the different assumed directions.

Chapter 6

Conclusion: Summary and Outlook

The analysis presented in this study is one of the first investigations of anisotropies in the arrival directions of cosmic-ray electrons with an Imaging Atmospheric Cherenkov Telescope (IACT). The analysis is based on an unprecedented, high-quality data set of 1178 hours of observation time distributed between 94 positions in the sky measured with the four 12 m H.E.S.S. I telescopes between 2005 and 2012.

Residual Background The first major challenge faced when analyzing cosmic-ray electrons with IACTs is the determination of the residual background (hadrons and photons). In this study a data driven approach was chosen. The residual background was approximated over the whole data set by employing the electron flux measured with *Fermi*-LAT and the effective electron exposure of H.E.S.S. The fraction of electrons in the selected event sample was estimated to be 63 % for the standard gamma-hadron separation cut choice ($MSSG < 0.6$). Additionally, an upper limit on the electron spectrum was derived using the effective electron exposure. This upper limit represents the first cross check of the electron spectrum measured with H.E.S.S. obtained with an advanced event reconstruction technique based on a semi-analytical shower model. At low energies (< 1 TeV) the upper limit lies, as expected, above the previously measured electron spectrum. At energies above 1 TeV the two spectra are in tension, because the upper limit obtained in this study falls down much steeper than the published spectrum. Possible reasons for the differences were discussed in detail.

Systematic Effects The second major challenge was the fact that the statistics available in many directions of the sky are not sufficient to calculate individual fluxes for every position in the sky. Instead, the electron arrival rates (gamma-like event rates minus the residual background) were directly used in the anisotropy analysis. Differences in observation conditions, e.g. zenith angle, optical efficiency and weather conditions, were taken into account by defining a systematic error large enough to account for such systematic rate variations. In a unique approach, the systematic error was estimated taking advantage of the high statistics in the hadron-like event sample, in which systematic variations should be clearly visible. It was shown that the hadron-like event sample was consistent with isotropy when using the obtained systematic errors. The same relative systematic error was also applied to the electron analysis

ensuring that all systematic effects comprised in the hadron-like event sample could not lead to significant effects in the electron anisotropy search.

Anisotropy Search In the first step an extensive search for a dipole anisotropy was performed. Several different methods were employed including χ^2 -fitting, $\Delta\chi^2$ -test, and f -test hypothesis testing as well as Monte Carlo simulations. It was found that neither isotropy ($\chi^2/d.o.f.=2.67$) nor a dipole model ($\chi^2/d.o.f.=2.32$) was sufficient to explain the data. The improvement of the fit when including the dipole term was significant at approximately 5σ with the $\Delta\chi^2$ -test and 3σ with the f -test. Further, the data set was split into several subsamples on the basis of zenith angle, optical efficiency and year of data taking. Except in subsamples with very small statistics again neither isotropy nor a dipole model fit the data well. These results indicate that higher order anisotropies (smaller scale structures) must be present in the data.

Multipole Models Higher order multipole functions up to the hexadecapole ($l_{\max} = 4$) were fit to the data sample. It was found, that none of the models fit the data sufficiently well (p -value $< 10^{-8}$ for all fits) indicating that even smaller scale structures play an important role. Fits including succeeding multipoles up to the quadrupole give significantly better results ($> 3\sigma$ with $\Delta\chi^2$ -test), while the improvements gained by including the octupole and hexadecapole terms are not significant ($< 2\sigma$). Since in all cases the best-fit model did not describe the data well the errors on the best-fit parameters were very large making a detailed characterization of the anisotropies impossible.

Two-Point-Correlation Function A second method was employed to investigate medium to small scale anisotropies. The two-point-correlation function (TPC function) gives the power of correlation at different angular scales. A few clear peaks and minima were visible. It was found that the values of the TPC function at some angular scales were not compatible with isotropy at the 4σ level. This result confirms the previous interpretation of the existence of medium to small scale anisotropies. Beyond this conclusion, the interpretation of the TPC function appeared difficult, since it contains contributions from different multipoles in each angular distance bin. For a better understanding of the TPC function a cosmic-ray anisotropy sky map containing small and medium scale anisotropies provided by the ARGO-YBJ collaboration was studied. The imprint of hot spots is much more obvious in the TPC function than in the power spectrum. Hence, the observation of prominent minima in a TPC function may hint towards the existence of prominent hot spots. From the angular scale of peaks and minima in the TPC function it might be possible to draw conclusions about the distance between hot spots, while no information about their exact location can be obtained.

Upper Limits The only two other experiments previously searching for cosmic-ray electrons, the *Fermi*-LAT and AMS-02 experiments, published upper limits on the dipole amplitude. Since no significant dipole anisotropy was found in this analysis an upper limit was set on the dipole amplitude for all directions in the sky. The upper limit is derived for the energy bin between 0.64 and 1.04 TeV accessing an energy range higher than *Fermi*-LAT and AMS-02.

The 95 % CL upper limits range from 2.5 % to 56 % and are one of the first upper limits obtained on the dipole amplitude in this energy range and with an IACT.

Discussion The analysis summarized above found evidence for rate fluctuations in cosmic-ray electrons that are significantly larger than the fluctuations found in associated hadron events. It was indirectly shown that these fluctuations are not most prominent on large angular scales (dipole to hexadecapole), but on smaller angular scales. The cause for this anisotropy signal cannot be ultimately resolved. Two scenarios are possible.

First, the signal could be of physical origin. In this case the anisotropy would be a result of the location and distribution of the sources of cosmic-ray electrons and the deflections from the galactic magnetic field electrons undergo on their way to Earth. In this case a better determination of the shape of anisotropy would be useful to discriminate between electron production and propagation models. The magnitude of the anisotropies found in this analysis and the upper limit derived on the dipole amplitude might already provide a tool to constrain such models.

Second, the assumption that the systematic error derived from hadrons does also describe the systematic effects present in electron rates correctly is not valid. Additional systematic effects regarding only electrons may exist. Such effects would increase the systematic uncertainty on the electron rates only. This would impair the significance of the results found in this study.

Such a systematic effect could be due to the East-West effect or the North-South effect discussed in Section 5.3.3, which would influence electron initiated showers more strongly than hadronic showers. An imprint of these effects may be seen in the systematic variations of the gamma-like rates in dependence on the declination angle of the observation. Even though, these effects are most likely not strong enough to explain the measured variations of the electron rates.

Another possible scenario would be that electron initiated air showers are more strongly influenced by seasonal variations of the atmosphere than hadrons. Electrons and hadrons in the data sample probe different parts of the atmosphere. Absorption of photons in particular by aerosols depends strongly on the height of the part of the atmosphere the air shower traverses. Thus, absorption processes influence electron and hadron initiated showers possibly in different ways due to a change of the aerosol concentration in certain parts of the atmosphere. Such a change may be induced by, e.g. bush fires. Nonetheless, the effect of such an event on the hadronic arrival rates should be strong, so that the applied selection criteria should have removed these runs from the data sample. Moreover, this argument is disfavored by the good correlation between gamma-like and hadron-like event rates on the run-by-run basis as demonstrated in Sections 5.3.3 and 5.3.4.

Further, unresolved sources in the field of view (FoV) may cause fluctuations in the event rates. However, this effect would most likely be isotropic, because unresolved sources are not expected to appear predominantly in a certain direction.

In any case, the systematic error would have to be approximately 2 times the size or have an offset of 10 % of the systematic error obtained in this study, to make the data compatible

with isotropy¹.

Systematics causing rate fluctuations of the magnitude found in this analysis, would also concern previous results found by the H.E.S.S. experiment, because the same magnitude of systematic effects would also apply to gamma rays. For flux measurements with H.E.S.S. a systematic uncertainty of 20% was estimated by Aharonian et al. (2006). The absolute flux calibration depends on uncertainties concerning the camera response, the optical response and the interactions of particles and light in the atmosphere (MC simulations). Major contributions arise from the uncertainty of the atmospheric models used in MC simulations (10 %), the choice of selection cut (8 %), the effects caused by broken pixels (5 %) and the run-by-run variability (15 %)². The run-by-run variability is attributed to variations in the atmosphere. In this study the uncertainties that only concern the absolute flux level are irrelevant, since the arrival rates are used directly. Thus, uncertainties arising from MC simulations or cut selection choices should not be present in the data. Only systematics due to individual observation conditions of the runs (e.g. atmospheric conditions and broken pixels), which should overall be of the order of 15 – 16 % according to Aharonian et al. (2006), contribute to this measurement. Consequently, the systematic error due to individual observation conditions would have to be larger than assumed previously to explain the results found in this study.

Outlook Even though, this analysis has been carried out with care and a high level of precision an independent cross check of the data set with a different event reconstruction technique is pending. Within the scope of this work only a subsample of the data set was cross checked.

Further, the AMS-02 electron spectrum indicates a lower electron flux at high energies than *Fermi*, this would imply that the electron fraction is also smaller. The principle results of this analysis would not change as long as the electron fraction is above 20 %. A lower flux would change the obtained upper limits on the dipole amplitude towards higher values.

Altogether, this analysis of cosmic-ray electrons was just the very first step in the quest of understanding the distribution of arrival directions of cosmic-ray electrons. The picture, as for hadronic cosmic rays, may be more complicated than what was predicted by the isotropic diffusion approximation. The distribution of cosmic-ray electron sources, either of dark matter or pulsar origin, and the effects of the propagation of the particles through the turbulent magnetic field will play an important role.

In any case, for a better understanding, it is mandatory to collect more data, both, with direct and indirect measurement techniques. A very good understanding of systematic effects will be crucial for the analysis of very large amounts of data collected over a long period of time at very different observation conditions. Additionally, a combination of data taken with a telescope in the northern hemisphere, e.g. MAGIC or Veritas, should be performed. This way, the problem that either telescope has blind spots in some parts of the sky would be avoided.

¹Note: Also a homogenous systematic error of 20 % would make the data set compatible with isotropy. In all three cases the $\Delta\chi^2$ when going from the isotropic model to the dipole model would be of the order of 10 to 12.

²Note: The run-by-run variability found in flux measurements of the Crab of 15 % is very similar to the standard deviation found in hadron-like rates.

Further, even though IACTs such as H.E.S.S. are in principle sensitive to large scale anisotropies, e.g. the dipole (or extremely small anisotropies within a single FoV) with an irregular observation pattern, they cannot detect medium or small scale anisotropies in this observation mode. To access those anisotropies it might be necessary to perform all-sky surveys (or in reality probably part-sky surveys). Also in such an observation mode combining data from different instruments in the northern and southern hemispheres will be necessary to deduce a complete picture.

In any case, it will probably take several more years of scientific work for this just now emerging puzzle to be resolved.

Bibliography

- M. G. Aartsen, R. Abbasi, Y. Abdou, M. Ackermann, J. Adams, J. A. Aguilar, M. Ahlers, D. Altmann, K. Andeen, J. Auffenberg, and et al. Observation of Cosmic-Ray Anisotropy with the IceTop Air Shower Array. *Astrophys. J.*, 765:55, March 2013. doi: 10.1088/0004-637X/765/1/55.
- R. Abbasi, Y. Abdou, T. Abu-Zayyad, J. Adams, J. A. Aguilar, M. Ahlers, K. Andeen, J. Auffenberg, X. Bai, M. Baker, and et al. Measurement of the Anisotropy of Cosmic-ray Arrival Directions with IceCube. *Astrophys. J., Letters*, 718:L194–L198, August 2010. doi: 10.1088/2041-8205/718/2/L194.
- R. Abbasi, Y. Abdou, T. Abu-Zayyad, J. Adams, J. A. Aguilar, M. Ahlers, D. Altmann, K. Andeen, J. Auffenberg, X. Bai, and et al. Observation of Anisotropy in the Arrival Directions of Galactic Cosmic Rays at Multiple Angular Scales with IceCube. *Astrophys. J.*, 740:16, October 2011. doi: 10.1088/0004-637X/740/1/16.
- R. Abbasi, Y. Abdou, T. Abu-Zayyad, M. Ackermann, J. Adams, J. A. Aguilar, M. Ahlers, M. M. Allen, D. Altmann, K. Andeen, and et al. Observation of Anisotropy in the Galactic Cosmic-Ray Arrival Directions at 400 TeV with IceCube. *Astrophys. J.*, 746:33, February 2012. doi: 10.1088/0004-637X/746/1/33.
- R. U. Abbasi, T. Abu-Zayyad, M. Allen, J. F. Amman, G. Archbold, and et al. First Observation of the Greisen-Zatsepin-Kuzmin Suppression. *Physical Review Letters*, 100(10):101101, March 2008a. doi: 10.1103/PhysRevLett.100.101101.
- R. U. Abbasi, T. Abu-Zayyad, M. Allen, J. F. Amman, and High Resolution Fly’s Eye Collaboration. Search for correlations between HiRes stereo events and active galactic nuclei. *Astroparticle Physics*, 30:175–179, November 2008b. doi: 10.1016/j.astropartphys.2008.08.004.
- A. A. Abdo, B. Allen, T. Aune, D. Berley, E. Blaufuss, and et al. Discovery of Localized Regions of Excess 10-TeV Cosmic Rays. *Physical Review Letters*, 101(22):221101, November 2008. doi: 10.1103/PhysRevLett.101.221101.
- A. A. Abdo, M. Ackermann, M. Ajello, W. B. Atwood, M. Axelsson, L. Baldini, and et al. Measurement of the Cosmic Ray $e^+ + e^-$ Spectrum from 20GeV to 1TeV with the Fermi Large Area Telescope. *Physical Review Letters*, 102(18):181101, May 2009. doi: 10.1103/PhysRevLett.102.181101.

- J. Abraham, P. Abreu, M. Aglietta, C. Aguirre, D. Allard, I. Allekotte, J. Allen, P. Allison, J. Alvarez-Muñiz, M. Ambrosio, and et al. Observation of the Suppression of the Flux of Cosmic Rays above 4×10^{19} eV. *Physical Review Letters*, 101(6):061101, August 2008a. doi: 10.1103/PhysRevLett.101.061101.
- J. Abraham, P. Abreu, M. Aglietta, C. Aguirre, D. Allard, I. Allekotte, J. Allen, P. Allison, J. Alvarez-Muñiz, and et al. Correlation of the highest-energy cosmic rays with the positions of nearby active galactic nuclei. *Astroparticle Physics*, 29:188–204, April 2008b. doi: 10.1016/j.astropartphys.2008.01.002.
- J. Abraham, P. Abreu, M. Aglietta, E. J. Ahn, D. Allard, I. Allekotte, J. Allen, J. Alvarez-Muñiz, M. Ambrosio, L. Anchordoqui, and et al. Measurement of the Depth of Maximum of Extensive Air Showers above 10^{18} eV. *Physical Review Letters*, 104(9):091101, March 2010. doi: 10.1103/PhysRevLett.104.091101.
- A. Abramowski, F. Acero, F. Aharonian, A. G. Akhperjanian, G. Anton, A. Barnacka, U. Barres de Almeida, A. R. Bazer-Bachi, Y. Becherini, J. Becker, B. Behera, K. Bernlöhr, A. Bochow, and et al. Search for a Dark Matter Annihilation Signal from the Galactic Center Halo with H.E.S.S. *Physical Review Letters*, 106(16):161301, April 2011. doi: 10.1103/PhysRevLett.106.161301.
- Attila Abramowski. private communication, June 2015.
- L. Accardo, M. Aguilar, D. Aisa, B. Alpat, A. Alvino, G. Ambrosi, K. Andeen, and et al. High Statistics Measurement of the Positron Fraction in Primary Cosmic Rays of 0.5 - 500 GeV with the Alpha Magnetic Spectrometer on the International Space Station. *Phys. Rev. Lett.*, 113:121101, Sep 2014. doi: 10.1103/PhysRevLett.113.121101. <http://link.aps.org/doi/10.1103/PhysRevLett.113.121101>.
- M. Ackermann, M. Ajello, W. B. Atwood, L. Baldini, J. Ballet, and et al. Searches for cosmic-ray electron anisotropies with the Fermi Large Area Telescope. *Phys. Rev. D*, 82(9):092003, November 2010a. doi: 10.1103/PhysRevD.82.092003. arXiv:1008.5119 [astro-ph.HE].
- M. Ackermann, M. Ajello, W. B. Atwood, and et al. Fermi LAT observations of cosmic-ray electrons from 7 GeV to 1 TeV. *Phys. Rev. D*, 82(9):092004, November 2010b. doi: 10.1103/PhysRevD.82.092004.
- M. Ackermann, M. Ajello, A. Allafort, W. B. Atwood, and et al. Measurement of Separate Cosmic-Ray Electron and Positron Spectra with the Fermi Large Area Telescope. *Physical Review Letters*, 108(1):011103, January 2012. doi: 10.1103/PhysRevLett.108.011103.
- M. Ackermann, M. Ajello, A. Allafort, L. Baldini, J. Ballet, and et al. Detection of the Characteristic Pion-Decay Signature in Supernova Remnants. *Science*, 339:807–811, February 2013. doi: 10.1126/science.1231160.
- O. Adriani, G. C. Barbarino, G. A. Bazilevskaya, R. Bellotti, M. Boezio, and et al. An anomalous positron abundance in cosmic rays with energies 1.5-100 GeV. *Nature*, 458:607–609, April 2009. doi: 10.1038/nature07942.

- O. Adriani, G. C. Barbarino, G. A. Bazilevskaya, R. Bellotti, M. Boezio, and PAMELA Collaboration. PAMELA Results on the Cosmic-Ray Antiproton Flux from 60 MeV to 180 GeV in Kinetic Energy. *Physical Review Letters*, 105(12):121101, September 2010. doi: 10.1103/PhysRevLett.105.121101.
- O. Adriani, G. C. Barbarino, G. A. Bazilevskaya, R. Bellotti, M. Boezio, and et al. Cosmic-Ray Electron Flux Measured by the PAMELA Experiment between 1 and 625 GeV. *Physical Review Letters*, 106(20):201101, May 2011a. doi: 10.1103/PhysRevLett.106.201101.
- O. Adriani, G. C. Barbarino, G. A. Bazilevskaya, R. Bellotti, and et al. PAMELA Measurements of Cosmic-Ray Proton and Helium Spectra. *Science*, 332:69–, April 2011b. doi: 10.1126/science.1199172.
- O. Adriani, G. C. Barbarino, G. A. Bazilevskaya, and et al. Measurement of the Isotopic Composition of Hydrogen and Helium Nuclei in Cosmic Rays with the PAMELA Experiment. *Astrophys. J.*, 770:2, June 2013. doi: 10.1088/0004-637X/770/1/2.
- M. Aguilar, G. Alberti, B. Alpat, A. Alvino, G. Ambrosi, K. Andeen, H. Anderhub, L. Arruda, P. Azzarello, A. Bachlechner, and et al. First Result from the Alpha Magnetic Spectrometer on the International Space Station: Precision Measurement of the Positron Fraction in Primary Cosmic Rays of 0.5–350 GeV. *Physical Review Letters*, 110(14):141102, April 2013. doi: 10.1103/PhysRevLett.110.141102.
- M. Aguilar, D. Aisa, B. Alpat, A. Alvino, G. Ambrosi, K. Andeen, L. Arruda, N. Attig, P. Azzarello, A. Bachlechner, and et al. Precision Measurement of the ($e^+ + e^-$) Flux in Primary Cosmic Rays from 0.5 GeV to 1 TeV with the Alpha Magnetic Spectrometer on the International Space Station. *Physical Review Letters*, 113(22):221102, November 2014a. doi: 10.1103/PhysRevLett.113.221102.
- M. Aguilar, D. Aisa, A. Alvino, G. Ambrosi, K. Andeen, L. Arruda, N. Attig, P. Azzarello, A. Bachlechner, F. Barao, and et al. Electron and Positron Fluxes in Primary Cosmic Rays Measured with the Alpha Magnetic Spectrometer on the International Space Station. *Physical Review Letters*, 113(12):121102, September 2014b. doi: 10.1103/PhysRevLett.113.121102.
- F. Aharonian, A. G. Akhperjanian, K.-M. Aye, and et al. Calibration of cameras of the H.E.S.S. detector. *Astroparticle Physics*, 22:109–125, November 2004. doi: 10.1016/j.astropartphys.2004.06.006.
- F. Aharonian, A. G. Akhperjanian, A. R. Bazer-Bachi, and et al. Observations of the Crab nebula with HESS. *Astronomy and Astrophysics*, 457:899–915, October 2006. doi: 10.1051/0004-6361:20065351.
- F. Aharonian, A. G. Akhperjanian, A. R. Bazer-Bachi, B. Behera, and et al. An Exceptional Very High Energy Gamma-Ray Flare of PKS 2155–304. *Astrophys. J., Letters*, 664:L71–L74, August 2007. doi: 10.1086/520635.

- F. Aharonian, A. G. Akhperjanian, U. Barres de Almeida, A. R. Bazer-Bachi, and et al. Energy Spectrum of Cosmic-Ray Electrons at TeV Energies. *Physical Review Letters*, 101 (26):261104, December 2008. doi: 10.1103/PhysRevLett.101.261104.
- F. Aharonian, A. G. Akhperjanian, G. Anton, U. Barres de Almeida, A. R. Bazer-Bachi, and et al. Probing the ATIC peak in the cosmic-ray electron spectrum with H.E.S.S. *Astronomy and Astrophysics*, 508:561–564, December 2009. doi: 10.1051/0004-6361/200913323.
- G. Aielli, C. Bacci, B. Bartoli, and et al. Highlights from the ARGO - YBJ experiment. *Nuclear Instruments and Methods in Physics Research A*, 661:50–55, 2012.
- E. Aliu, H. Anderhub, L. A. Antonelli, P. Antoranz, M. Backes, C. Baixeras, J. A. Barrio, H. Bartko, D. Bastieri, and MAGIC Collaboration. Observation of Pulsed γ -Rays Above 25 GeV from the Crab Pulsar with MAGIC. *Science*, 322:1221, November 2008. doi: 10.1126/science.1164718.
- G. Allen. Evidence of 10-100 TeV Electrons in Supernova Remnants. *International Cosmic Ray Conference*, 3:480, August 1999.
- R. Aloisio. Ultra High Energy Cosmic Rays: A Short Review. *ArXiv e-prints*, November 2012. arXiv:1211.2004 [astro-ph.HE].
- M. Amenomori and Tibet AS γ Collaboration. Anisotropy and Corotation of Galactic Cosmic Rays. *Science*, 314:439–443, October 2006. doi: 10.1126/science.1131702.
- M. Amenomori and Tibet AS γ Collaboration. Modeling of the high-energy galactic cosmic-ray anisotropy. *Astrophysics and Space Sciences Transactions*, 6:49–52, December 2010. doi: 10.5194/astra-6-49-2010.
- M. C. Anderson and L. Rudnick. The deceleration powering of synchrotron emission from ejecta components in supernova remnant Cassiopeia A. *Astrophys. J.*, 441:307–333, March 1995. doi: 10.1086/175357.
- T.W. Anderson and D.A. Darling. Asymptotic theory of certain "goodness-of-fit" criteria based on stochastic processes. *Annals of Mathematical Statistics*, 23:193–212, 1952.
- W. D. Apel, J. C. Arteaga-Velázquez, K. Bekk, M. Bertaina, J. Blümer, H. Bozdog, I. M. Brancus, and et al. KASCADE-Grande measurements of energy spectra for elemental groups of cosmic rays. *ArXiv e-prints*, June 2013. arXiv:1306.6283 [astro-ph.HE].
- ARGO-YBJ Collaboration. Medium scale anisotropy in the TeV cosmic ray flux observed by ARGO-YBJ. *Phys. Rev. D*, 88(8):082001, October 2013. doi: 10.1103/PhysRevD.88.082001.
- E. Armengaud. Search for large-scale anisotropies with the Auger Observatory. *International Cosmic Ray Conference*, 4:175–178, 2008. arXiv:0706.2640 [astro-ph].
- J. Arons and E. T. Scharlemann. Pair formation above pulsar polar caps - Structure of the low altitude acceleration zone. *Astrophys. J.*, 231:854–879, August 1979. doi: 10.1086/157250.

- A. M. Atoyan, F. A. Aharonian, and H. J. Völk. Electrons and positrons in the galactic cosmic rays. *Phys. Rev. D*, 52:3265–3275, September 1995. doi: 10.1103/PhysRevD.52.3265.
- W. B. Atwood, A. A. Abdo, M. Ackermann, W. Althouse, B. Anderson, M. Axelsson, L. Baldini, J. Ballet, D. L. Band, G. Barbiellini, and et al. The Large Area Telescope on the Fermi Gamma-Ray Space Telescope Mission. *Astrophys. J.*, 697:1071–1102, June 2009. doi: 10.1088/0004-637X/697/2/1071. arXiv:0902.1089 [astro-ph.IM].
- W. I. Axford, E. Leer, and G. Skadron. Acceleration of cosmic rays by shock waves. In V. A. Dergachev and G. E. Kocharov, editors, *Cosmophysics*, pages 125–134, 1978.
- K.-M. Aye, P. M. Chadwick, C. Hadjichristidis, and et al. Atmospheric Monitoring for the H.E.S.S. Project. *International Cosmic Ray Conference*, 5:2879, July 2003.
- W. Baade and F. Zwicky. Remarks on Super-Novae and Cosmic Rays. *Physical Review*, 46: 76–77, July 1934. doi: 10.1103/PhysRev.46.76.2.
- K. J. Bae and B. Kyae. PAMELA/ATIC anomaly from exotic mediated dark matter decay. *Journal of High Energy Physics*, 5:102, May 2009. doi: 10.1088/1126-6708/2009/05/102.
- M. G. Baring. High-energy emission from pulsars: the polar cap scenario. *Advances in Space Research*, 33:552–560, 2004. doi: 10.1016/j.asr.2003.08.020.
- B. Bartoli, P. Bernardini, and et al. Observation of the cosmic ray moon shadowing effect with the ARGO-YBJ experiment. *Phys. Rev. D*, 84(2):022003, July 2011. doi: 10.1103/PhysRevD.84.022003.
- A. R. Bell. The acceleration of cosmic rays in shock fronts. I. *Monthly Notices of the Royal Astronomical Society*, 182:147–156, January 1978.
- R. Bellotti, F. Cafagna, M. Circella, C. N. de Marzo, R. L. Golden, S. J. Stochaj, and et al. Balloon measurements of cosmic ray muon spectra in the atmosphere along with those of primary protons and helium nuclei over midlatitude. *Phys. Rev. D*, 60(5):052002, September 1999. doi: 10.1103/PhysRevD.60.052002.
- E. G. Berezhko. Maximum energy of cosmic rays accelerated by supernova shocks. *Astroparticle Physics*, 5:367–378, October 1996. doi: 10.1016/0927-6505(96)00037-0.
- D. Berge, S. Funk, and J. Hinton. Background modelling in very-high-energy γ -ray astronomy. *Astronomy and Astrophysics*, 466:1219–1229, May 2007. doi: 10.1051/0004-6361:20066674.
- K. Bernlöhr. Simulations of detector arrays and the impact of atmospheric parameters. *ArXiv e-prints*, February 2014. arXiv:1402.5081 [astro-ph.IM].
- K. Bernlöhr, O. Carrol, R. Cornils, S. Elfahem, and et al. The optical system of the H.E.S.S. imaging atmospheric Cherenkov telescopes. Part I: layout and components of the system. *Astroparticle Physics*, 20:111–128, November 2003. doi: 10.1016/S0927-6505(03)00171-3.
- Konrad Bernlöhr and H.E.S.S. collaboration. *sim_hessarray Reference Manual*, August 2005.

- H. Bethe and W. Heitler. On the Stopping of Fast Particles and on the Creation of Positive Electrons. *Royal Society of London Proceedings Series A*, 146:83–112, August 1934. doi: 10.1098/rspa.1934.0140.
- P. R. Bevington. *Data reduction and error analysis for the physical sciences*. McGraw-Hill Higher Education, 3rd edition, 2003. ISBN 0-07-247227-8.
- R. D. Blandford and J. P. Ostriker. Particle acceleration at astrophysical shocks. *Astrophys. J., Letters*, 221:L29–L32, April 1978. doi: 10.1086/182658.
- R. D. Blandford and J. P. Ostriker. Supernova shock acceleration of cosmic rays in the Galaxy. *Astrophys. J.*, 237:793–808, May 1980. doi: 10.1086/157926.
- P. Blasi and E. Amato. Diffusive propagation of cosmic rays from supernova remnants in the Galaxy. II: anisotropy. *Journal of Cosmology and Astroparticle Physics*, 1:011, January 2012. doi: 10.1088/1475-7516/2012/01/011.
- V. Blobel and E. Lohrmann. *Statistische und numerische Methoden der Datenanalyse*. B.G. Teubner Stuttgart · Leipzig, 1998. doi: 10.1007/978-3-663-05690-4. ISBN 3-519-03243-0.
- H. Blümer and K.-H. Kampert. Die Suche nach den Quellen der kosmischen Strahlung. *Physikalische Blätter*, 56:39–45, March 2000. doi: 10.1002/phbl.20000560311.
- J. Blümer, R. Engel, and J. R. Hörandel. Cosmic rays from the knee to the highest energies. *Progress in Particle and Nuclear Physics*, 63:293–338, October 2009. doi: 10.1016/j.pnpnp.2009.05.002.
- D. Borla Tridon. Measurement of the cosmic electron spectrum with the MAGIC telescopes. *International Cosmic Ray Conference*, 6:47, 2011. doi: 10.7529/ICRC2011/V06/0680. arXiv:1110.4008 [astro-ph.HE].
- E. Borriello, L. Maccione, and A. Cuoco. Dark matter electron anisotropy: A universal upper limit. *Astroparticle Physics*, 35:537–546, March 2012. doi: 10.1016/j.astropartphys.2011.12.001.
- Ilja N Bronstein, Konstantin A Semendjajew, Gerhard Musiol, and Heiner Mühlig. *Taschenbuch der Mathematik*. Verlag Harri Deutsch, 4 edition, 1999.
- E. F. Bunn. *Statistical Analysis of Cosmic Microwave Background Anisotropy*. PhD thesis, UNIVERSITY OF CALIFORNIA, BERKELEY, January 1995.
- Ignacio Cernuda Cangas. *Cosmic-Ray Positron Fraction Measurement with the AMS-02 Detector*. PhD thesis, UNIVERSIDAD COMPLUTENSE DE MADRID, 2013-2014.
- I. Cernuda. Cosmic-ray electron anisotropies as a tool to discriminate between exotic and astrophysical sources. *Astroparticle Physics*, 34:59–69, September 2010. doi: 10.1016/j.astropartphys.2010.05.003.

- J. Chang, W. K. H. Schmidt, J. H. Adams, H. S. Ahn, G. Bashindzhagyan, K. E. Batkov, M. Christl, A. R. Fazely, O. Ganel, R. M. Gunasingha, T. G. Guzik, J. Isbert, K. C. Kim, E. Kouznetsov, M. Panasyuk, A. Panov, E. S. Seo, N. Sokolskaya, J. Z. Wang, J. P. Wefel, J. Wu, and V. Zatsepin. The Electron Spectrum above 20 GeV Measured by ATIC-2. *International Cosmic Ray Conference*, 3:1, 2005.
- J. Chang, J. H. Adams, H. S. Ahn, G. L. Bashindzhagyan, M. Christl, O. Ganel, T. G. Guzik, J. Isbert, K. C. Kim, E. N. Kuznetsov, M. I. Panasyuk, A. D. Panov, W. K. H. Schmidt, E. S. Seo, N. V. Sokolskaya, J. W. Watts, J. P. Wefel, J. Wu, and V. I. Zatsepin. An excess of cosmic ray electrons at energies of 300-800GeV. *Nature*, 456:362–365, November 2008. doi: 10.1038/nature07477.
- K. S. Cheng, C. Ho, and M. Ruderman. Energetic radiation from rapidly spinning pulsars. I - Outer magnetosphere gaps. II - VELA and Crab. *Astrophys. J.*, 300:500–539, January 1986. doi: 10.1086/163829.
- M. Circella. A measurement of the proton and helium components in the atmosphere. *International Cosmic Ray Conference*, 7:359, 1999.
- A. H. Compton. A Quantum Theory of the Scattering of X-rays by Light Elements. *Physical Review*, 21:483–502, May 1923. doi: 10.1103/PhysRev.21.483.
- R. Cornils, S. Gillessen, I. Jung, W. Hofmann, M. Beilicke, and et al. The optical system of the H.E.S.S. imaging atmospheric Cherenkov telescopes. Part II: mirror alignment and point spread function. *Astroparticle Physics*, 20:129–143, November 2003. doi: 10.1016/S0927-6505(03)00172-5.
- M. K. Daniel and P. M. Chadwick. Atmospheric monitoring with an infrared radiometer. In *European Physical Journal Web of Conferences*, volume 89 of *European Physical Journal Web of Conferences*, page 3005, March 2015. doi: 10.1051/epjconf/20158903005.
- J. M. Davies and E. S. Cotton. Design of the quartermaster solar furnace. *Solar Energy*, 1: 16–22, April 1957. doi: 10.1016/0038-092X(57)90116-0.
- M. de Naurois and L. Rolland. A high performance likelihood reconstruction of γ -rays for imaging atmospheric Cherenkov telescopes. *Astroparticle Physics*, 32:231–252, December 2009. doi: 10.1016/j.astropartphys.2009.09.001.
- P. Desiati and A. Lazarian. Anisotropy of TeV Cosmic Rays and Outer Heliospheric Boundaries. *Astrophys. J.*, 762:44, January 2013. doi: 10.1088/0004-637X/762/1/44.
- Paolo Desiati. <http://icecube.wisc.edu/%7EDesiati/activity/anisotropy/large/>, January 2012.
- G. di Bernardo, C. Evoli, D. Gaggero, D. Grasso, L. Maccione, and M. N. Mazziotta. Implications of the cosmic ray electron spectrum and anisotropy measured with Fermi-LAT. *Astroparticle Physics*, 34:528–538, February 2011. doi: 10.1016/j.astropartphys.2010.11.005.

- J. Diemand, M. Kuhlen, P. Madau, M. Zemp, B. Moore, D. Potter, and J. Stadel. Clumps and streams in the local dark matter distribution. *Nature*, 454:735–738, August 2008. doi: 10.1038/nature07153.
- L. O. ’. Drury and F. A. Aharonian. The puzzling MILAGRO hot spots. *Astroparticle Physics*, 29:420–423, July 2008. doi: 10.1016/j.astropartphys.2008.04.007. arXiv:0802.4403 [astro-ph].
- R. Durrer and A. Neronov. Cosmological magnetic fields: their generation, evolution and observation. *The Astronomy and Astrophysics Review*, 21:62, June 2013. doi: 10.1007/s00159-013-0062-7.
- Kathrin Egberts. *The Energy Spectrum of Cosmic-Ray Electrons Measured with H.E.S.S.* PhD thesis, Ruperto-Carola Universität Heidelberg, March 2009.
- A. Einstein. Über einen die Erzeugung und Verwandlung des Lichtes betreffenden heuristischen Gesichtspunkt. *Annalen der Physik*, 322:132–148, 1905. doi: 10.1002/andp.19053220607.
- A. D. Erlykin and A. W. Wolfendale. The origin of cosmic rays. *Journal of Physics G Nuclear Physics*, 31:1475–1498, December 2005. doi: 10.1088/0954-3899/31/12/009.
- Y.-Z. Fan, B. Zhang, and J. Chang. Electron/positron Excesses in the Cosmic Ray Spectrum and Possible Interpretations. *International Journal of Modern Physics D*, 19:2011–2058, November 2010. doi: 10.1142/S0218271810018268.
- E. Fermi. On the Origin of the Cosmic Radiation. *Physical Review*, 75:1169–1174, April 1949. doi: 10.1103/PhysRev.75.1169.
- S. Funk, G. Hermann, J. Hinton, D. Berge, K. Bernlöhr, W. Hofmann, P. Nayman, F. Toussenel, and P. Vincent. The trigger system of the H.E.S.S. telescope array. *Astroparticle Physics*, 22:285–296, November 2004. doi: 10.1016/j.astropartphys.2004.08.001.
- T. K. Gaisser, R. J. Protheroe, and T. Stanev. Nuclear Target Effects and Interpretation of Cosmic Ray Cascades. *International Cosmic Ray Conference*, 5:174, August 1983.
- S. Ghigna, B. Moore, F. Governato, G. Lake, T. Quinn, and J. Stadel. Dark matter haloes within clusters. *Monthly Notices of the Royal Astronomical Society*, 300:146–162, October 1998. doi: 10.1046/j.1365-8711.1998.01918.x.
- G. Giacinti and G. Sigl. Local Magnetic Turbulence and TeV-PeV Cosmic Ray Anisotropies. *Physical Review Letters*, 109(7):071101, August 2012. doi: 10.1103/PhysRevLett.109.071101.
- A. Giuliani, M. Cardillo, M. Tavani, Y. Fukui, S. Yoshiike, and et al. Neutral Pion Emission from Accelerated Protons in the Supernova Remnant W44. *Astrophys. J., Letters*, 742:L30, December 2011. doi: 10.1088/2041-8205/742/2/L30.
- P. Goldreich and W. H. Julian. Pulsar Electrodynamics. *Astrophys. J.*, 157:869, August 1969. doi: 10.1086/150119.

- Phillip I. Good. *Permutation, Parametric and Bootstrap Tests of Hypotheses: A Practical Guide to Resampling Methods for Testing Hypotheses: 3rd (Third) edition*. Springer-Verlag New York, LLC, 12 2004. URL <http://amazon.com/o/ASIN/B0085AYWCY/>.
- K. M. Górski, E. Hivon, A. J. Banday, B. D. Wandelt, F. K. Hansen, M. Reinecke, and M. Bartelmann. HEALPix: A Framework for High-Resolution Discretization and Fast Analysis of Data Distributed on the Sphere. *Astrophys. J.*, 622:759–771, April 2005. doi: 10.1086/427976.
- K. Griest. The Nature of the Dark Matter. In S. Bonometto, J. R. Primack, and A. Provenzale, editors, *Dark Matter in the Universe*, page 343, 1996.
- J. Guy. *Thèse de doctorat*. PhD thesis, Université Paris VI,, 2003.
- J. Guy, P. Vincent, J. P. Tavernet, and M. Rivoal. Comparison of simulated longitudinal profiles of hadronic air showers with MASS2 balloon data. *Astroparticle Physics*, 17:409–414, July 2002. doi: 10.1016/S0927-6505(01)00168-2.
- A. K. Harding, J. V. Stern, J. Dyks, and M. Frackowiak. High-Altitude Emission from Pulsar Slot Gaps: The Crab Pulsar. *Astrophys. J.*, 680:1378–1393, June 2008. doi: 10.1086/588037.
- X.-G. He. Dark Matter Annihilation Explanation for e^\pm Excesses in Cosmic Ray. *Modern Physics Letters A*, 24:2139–2160, 2009. doi: 10.1142/S0217732309031740. arXiv:0908.2908 [hep-ph].
- D. Heck, J. Knapp, J. N. Capdevielle, G. Schatz, and T. Thouw. *CORSIKA: a Monte Carlo code to simulate extensive air showers*. Forschungszentrum Karlsruhe GmbH, Karlsruhe (Germany), February 1998.
- W. Heitler. Quantum theory of radiation. *Oxford University Press*, 1944.
- V. F. Hess. Über Beobachtungen der durchdringenden Strahlung bei sieben Freiballonfahrten. *Physikalische Zeitschrift*, 13:1084–1091, 1912.
- H.E.S.S. collaboration. Paris run quality documentation, 2015. URL <http://11r.in2p3.fr/sites/hess/hess-documentation/parisrunquality/>.
- A. M. Hillas. Cerenkov light images of EAS produced by primary gamma. *International Cosmic Ray Conference*, 3:445–448, August 1985.
- A. M. Hillas. TOPICAL REVIEW: Can diffusive shock acceleration in supernova remnants account for high-energy galactic cosmic rays? *Journal of Physics G Nuclear Physics*, 31:95, May 2005. doi: 10.1088/0954-3899/31/5/R02.
- A. M. Hillas. Cosmic Rays: Recent Progress and some Current Questions. *ArXiv Astrophysics e-prints*, July 2006. arXiv:astro-ph/0607109.

- A. Hoecker, P. Speckmayer, J. Stelzer, J. Therhaag, E. von Toerne, and et al. TMVA - Toolkit for Multivariate Data Analysis. *ArXiv Physics e-prints*, March 2007. arXiv:physics/0703039 [physics.data-an].
- W. Hofmann and H.E.S.S. Collaboration. Status of the H.E.S.S. project. *International Cosmic Ray Conference*, 7:2785, August 2001.
- W. Hofmann, I. Jung, A. Konopelko, H. Krawczynski, H. Lampeitl, and G. Pühlhofer. Comparison of techniques to reconstruct VHE gamma-ray showers from multiple stereoscopic Cherenkov images. *Astroparticle Physics*, 12:135–143, November 1999. doi: 10.1016/S0927-6505(99)00084-5.
- D. Hooper. TASI 2008 Lectures on Dark Matter. *ArXiv e-prints*, January 2009. arXiv:0901.4090 [hep-ph].
- D. Hooper, P. Blasi, and P. Dario Serpico. Pulsars as the sources of high energy cosmic ray positrons. *Journal of Cosmology and Astroparticle Physics*, 1:025, January 2009. doi: 10.1088/1475-7516/2009/01/025. arXiv:0810.1527 [astro-ph].
- J. R. Hörandel. The composition of cosmic rays at the knee. *Nuovo Cimento B Serie*, 120:825, June 2005. doi: 10.1393/ncb/i2005-10124-2.
- J. R. Hörandel. The composition of cosmic rays at the knee. In J. F. Ormes, editor, *American Institute of Physics Conference Series*, volume 1516 of *American Institute of Physics Conference Series*, pages 185–194, February 2013. doi: 10.1063/1.4792566. arXiv:1212.0739 [astro-ph.HE].
- Arpad Horvath. Cherenkov, März 2006. URL <http://en.wikipedia.org/wiki/File:Cherenkov.svg>.
- Hyperphysics. Hadronic cosmic ray shower, 2015. URL <http://hyperphysics.phy-astr.gsu.edu/hbase/astro/cosmic.html>.
- Roberto Iuppa. private communication, June 2014.
- Constance Jahn. *Systematic Studies of an ON-OFF-Analysis of H.E.S.S. data in Search for a Signal from the Dark Matter Halo of the Milky Way*. PhD thesis, Friedrich-Alexander-Universität Erlangen-Nürnberg, September 2013.
- F. James. *MINUIT Reference Manual*. CERN, cern program library long writeup d506 edition, 1998.
- F. James. *The interpretation of Errors*. CERN, cern program library long writeup d506 edition, 2004.
- Frederick James. *Statistical Methods in Experimental Physics: 2nd Edition*. World Scientific Publishing Company, 2nd edition, November 2006. ISBN 9789812705273.

- C. C. H. Jui and Telescope Array Collaboration. Cosmic Ray in the Northern Hemisphere: Results from the Telescope Array Experiment. *Journal of Physics Conference Series*, 404 (1):012037, December 2012. doi: 10.1088/1742-6596/404/1/012037.
- G. Jungman, M. Kamionkowski, and K. Griest. Supersymmetric Dark Matter. *Physics Reports*, 267:195–373, March 1996. doi: 10.1016/0370-1573(95)00058-5.
- K.-H. Kampert. Methods of determination of the energy and mass of primary cosmic ray particles at extensive air shower energies. *Journal of Physics G Nuclear Physics*, 27:1663–1673, July 2001. doi: 10.1088/0954-3899/27/7/321.
- V. M. Kaspi, M. S. E. Roberts, and A. K. Harding. *Isolated neutron stars*, pages 279–339. Cambridge University Press, April 2006. ISBN 978-0-521-82659-4, arXiv:astro-ph/0402136.
- M. P. Kertzman and G. H. Sembroski. Computer simulation methods for investigating the detection characteristics of TeV air Cherenkov telescopes. *Nuclear Instruments and Methods in Physics Research A*, 343:629–643, April 1994. doi: 10.1016/0168-9002(94)90247-X.
- F.X. Kneizys, L.W. Abreu, G.P. Anderson, and et al. *The MODTRAN 2/3 Report and LOW-TRAN 7 MODEL*. Phillips Laboratory, Geophysics Directorate, Hanscom AFB, MA 01731-3010, U.S., November 1996.
- T. Kobayashi, Y. Komori, K. Yoshida, and J. Nishimura. The Most Likely Sources of High-Energy Cosmic-Ray Electrons in Supernova Remnants. *Astrophys. J.*, 601:340–351, January 2004. doi: 10.1086/380431.
- Hermann Kolanoski. Vorlesung: Einführung in die Astroteilchenphysik, February 2006. <http://www-zeuthen.desy.de/%7Ekolanosk/astro0506/skript.html>.
- David Kolitzus. Cosmic-ray electron spectrum - status report. H.E.S.S. collaboration AWG SeeVogh Meeting 2014, November 2014.
- David Kolitzus. Cosmic-ray electron spectrum - status report. H.E.S.S. collaboration AWG SeeVogh Meeting 2015, März 2015.
- Konrad Bernlöhr. *CORSIKA and sim_hessarray – Simulation of the imaging atmospheric Cherenkov technique for the H.E.S.S. experiment*, september 26, 2012 edition, May 2001. Internal Note.
- Maria Krause. Studies of the influence of the geomagnetic field on the sensitivity of gamma-ray observatories. Master’s thesis, Brandenburgische Technische Universität Cottbus, Politechnika Poznanńska, 2011.
- G. F. Krymskii. A regular mechanism for the acceleration of charged particles on the front of a shock wave. *Akademiia Nauk SSSR Doklady*, 234:1306–1308, June 1977.
- P. O. Lagage and C. J. Cesarsky. The maximum energy of cosmic rays accelerated by supernova shocks. *Astronomy and Astrophysics*, 125:249–257, September 1983.

- L. Landau. On the energy loss of fast particles by ionization. *J. Exp. Phys. (USSR)*, 8(201), 1944.
- A. Lazarian and P. Desiati. Magnetic Reconnection as the Cause of Cosmic Ray Excess from the Heliospheric Tail. *Astrophys. J.*, 722:188–196, October 2010. doi: 10.1088/0004-637X/722/1/188.
- M. Lemoine-Goumard, B. Degrange, and M. Tluczykont. Selection and 3D-reconstruction of gamma-ray-induced air showers with a stereoscopic system of atmospheric Cherenkov telescopes. *Astroparticle Physics*, 25:195–211, April 2006. doi: 10.1016/j.astropartphys.2006.01.005.
- T. Linden and S. Profumo. Probing the Pulsar Origin of the Anomalous Positron Fraction with AMS-02 and Atmospheric Cherenkov Telescopes. *Astrophys. J.*, 772:18, July 2013. doi: 10.1088/0004-637X/772/1/18.
- M. S. Longair. *High Energy Astrophysics*. Cambridge University Press, The Edinburgh Building, Cambridge CB2 8RU, UK, February 2011. ISBN 978-0-521-75618-1.
- M. A. Malkov, P. H. Diamond, L. O’C. Drury, and R. Z. Sagdeev. Probing Nearby Cosmic-ray Accelerators and Interstellar Medium Turbulence with MILAGRO Hot Spots. *Astrophys. J.*, 721:750–761, September 2010. doi: 10.1088/0004-637X/721/1/750.
- R. N. Manchester and J. H. Taylor. *Pulsars*. San Francisco : W. H. Freeman, 1977.
- C. Y. Mao and C. S. Shen. Anisotropy and diffusion of cosmic ray electrons. *Chinese Journal of Physics*, 10:16–28, 1972.
- M. Meyer, D. Horns, and H.-S. Zechlin. The Crab Nebula as a standard candle in very high-energy astrophysics. *Astronomy and Astrophysics*, 523:A2, November 2010. doi: 10.1051/0004-6361/201014108. arXiv:1008.4524 [astro-ph.HE].
- I. V. Moskalenko and A. W. Strong. Production and Propagation of Cosmic-Ray Positrons and Electrons. *Astrophys. J.*, 493:694–707, January 1998. doi: 10.1086/305152.
- D. Müller. Cosmic-ray electrons and positrons. *Advances in Space Research*, 27:659–668, 2001. doi: 10.1016/S0273-1177(01)00107-7.
- NASA. LAT structure, 2015. URL <http://hyperphysics.phy-astr.gsu.edu/hbase/astro/cosmic.html>.
- S. Nikolić, G. van de Ven, K. Heng, D. Kupko, B. Husemann, J. C. Raymond, J. P. Hughes, and J. Falcón-Barroso. An Integral View of Fast Shocks Around Supernova 1006. *Science*, 340:45–48, April 2013. doi: 10.1126/science.1228297.
- L. O’C. Drury. The problem of small angular scale structure in the cosmic ray anisotropy data. *ArXiv e-prints*, May 2013. arXiv:1305.6752 [astro-ph.HE].

- S. Ohm, C. van Eldik, and K. Egberts. γ /hadron separation in very-high-energy γ -ray astronomy using a multivariate analysis method. *Astroparticle Physics*, 31:383–391, June 2009. doi: 10.1016/j.astropartphys.2009.04.001.
- K. A. Olive, Agashe, K., and Particle Data Group. Review of Particle Physics. *Chinese Physics C*, 38(9):090001, August 2014. doi: 10.1088/1674-1137/38/9/090001.
- A. D. Panov. Electrons and Positrons in Cosmic Rays. *Journal of Physics Conference Series*, 409(1):012004, February 2013. doi: 10.1088/1742-6596/409/1/012004.
- A. D. Panov, V. I. Zatsepin, N. V. Sokolskaya, J. H. Adams, Jr., H. S. Ahn, G. L. Bashindzhagyan, J. Chang, M. Christl, T. G. Guzik, J. Isbert, K. C. Kim, E. N. Kouznetsov, M. I. Panasyuk, E. B. Postnikov, E. S. Seo, J. Watts, J. P. Wefel, and J. Wu. Possible structure in the cosmic ray electron spectrum measured by the ATIC-2 and ATIC-4 experiments. *Astrophysics and Space Sciences Transactions*, 7:119–124, April 2011. doi: 10.5194/astra-7-119-2011.
- J. A. Peacock. *Cosmological Physics*. Cambridge University Press, 1st edition, January 1999. ISBN 052141072X.
- P. Picozza, A. M. Galper, G. Castellini, O. Adriani, F. Altamura, and et al. PAMELA A payload for antimatter matter exploration and light-nuclei astrophysics. *Astroparticle Physics*, 27:296–315, April 2007. doi: 10.1016/j.astropartphys.2006.12.002.
- Pierre Auger Collaboration, J. Abraham, P. Abreu, M. Aglietta, C. Aguirre, D. Allard, I. Allekotte, J. Allen, P. Allison, C. Alvarez, and et al. Correlation of the Highest-Energy Cosmic Rays with Nearby Extragalactic Objects. *Science*, 318:938–, November 2007. doi: 10.1126/science.1151124.
- W. H. Press, S. A. Teukolsky, W. T. Vetterling, and B. P. Flannery. *Numerical recipes in C++ : the art of scientific computing*. CAMBRIDGE UNIVERSITY PRESS, The Edinburgh Building, Cambridge CB2 2RU, UK, 2002. ISBN 0-521-75033-4.
- S. Profumo. An observable electron-positron anisotropy cannot be generated by dark matter. *Journal of Cosmology and Astroparticle Physics*, 2:043, February 2015. doi: 10.1088/1475-7516/2015/02/043.
- R. Protasov, D. A. van Dyk, A. Connors, V. L. Kashyap, and A. Siemiginowska. Statistics, Handle with Care: Detecting Multiple Model Components with the Likelihood Ratio Test. *Astrophys. J.*, 571:545–559, May 2002. doi: 10.1086/339856.
- Marco Prüser. Suche nach Dipolanisotropien in der elektromagnetischen Komponente der kosmischen Strahlung mit den H. E. S. S. Cherenkov Teleskopen. Master’s thesis, Institut für Experimentalphysik Universität Hamburg, 2012.
- V. S. Ptuskin, F. C. Jones, E. S. Seo, and R. Sina. Effect of random nature of cosmic ray sources Supernova remnants on cosmic ray intensity fluctuations, anisotropy, and electron energy spectrum. *Advances in Space Research*, 37:1909–1912, 2006. doi: 10.1016/j.asr.2005.08.036.

- Michael Punch, A. Abramowski, and H.E.S.S. Collaboration. H.E.S.S.II: expansion of H.E.S.S. for higher sensitivity and lower energy. In *Towards a network of atmospheric Cherenkov detectors VII, Palaiseau, April 27-29, 2005*, pages 379–392. HESS, 2005.
- R. Ramaty and R. E. Lingenfelter. Gamma-ray line astronomy. *Nature*, 278:127–132, March 1979. doi: 10.1038/278127a0.
- S. P. Reynolds and D. M. Gilmore. Radio observations of the remnant of the supernova of A.D. 1006. I - Total intensity observations. *Astronomical Journal*, 92:1138–1144, November 1986. doi: 10.1086/114244.
- M. A. Ruderman and P. G. Sutherland. Theory of pulsars - Polar caps, sparks, and coherent microwave radiation. *Astrophys. J.*, 196:51–72, February 1975. doi: 10.1086/153393.
- D. Scott and G. Smoot. Cosmic Background Radiation Mini-Review. *ArXiv Astrophysics e-prints*, June 2004. arXiv:astro-ph/0406567.
- P. Slane. Particle Acceleration in Supernova Remnants and Pulsar Wind Nebulae. *ArXiv Astrophysics e-prints*, May 2002.
- V. Springel, J. Wang, M. Vogelsberger, A. Ludlow, A. Jenkins, A. Helmi, J. F. Navarro, C. S. Frenk, and S. D. M. White. The Aquarius Project: the subhaloes of galactic haloes. *Monthly Notices of the Royal Astronomical Society*, 391:1685–1711, December 2008. doi: 10.1111/j.1365-2966.2008.14066.x. arXiv:0809.0898 [astro-ph].
- M. Spurio. *Particles and Astrophysics*. Springer (Cham, Switzerland), 2015. doi: 10.1007/978-3-319-08051-2. ISBN 978-3-319-08050-5.
- A. W. Strong and I. V. Moskalenko. Propagation of Cosmic-Ray Nucleons in the Galaxy. *Astrophys. J.*, 509:212–228, December 1998. doi: 10.1086/306470.
- A. W. Strong, I. V. Moskalenko, and V. S. Ptuskin. Cosmic-Ray Propagation and Interactions in the Galaxy. *Annual Review of Nuclear and Particle Science*, 57:285–327, November 2007. doi: 10.1146/annurev.nucl.57.090506.123011.
- J. Swain. Anisotropies in Ultrahigh Energy Cosmic Rays. In M. Novello, S. Perez Bergliaffa, and R. Ruffini, editors, *The Tenth Marcel Grossmann Meeting. Proceedings of the MG10 Meeting held at Brazilian Center for Research in Physics (CBPF), Rio de Janeiro, Brazil, 20-26 July 2003, Eds.: Mário Novello; Santiago Perez Bergliaffa; Remo Ruffini. Singapore: World Scientific Publishing, in 3 volumes, ISBN 981-256-667-8 (set), ISBN 981-256-980-4 (Part A), ISBN 981-256-979-0 (Part B), ISBN 981-256-978-2 (Part C), 2006, XLVIII + 2492 pp.: 2006, p.721*, page 721, February 2006. doi: 10.1142/9789812704030_0043.
- S. I. Syrovatskii. The Distribution of Relativistic Electrons in the Galaxy and the Spectrum of Synchrotron Radio Emission. *Soviet Astronomy*, 3:22, February 1959.
- A. P. S. Tang, J. Takata, J. J. Jia, and K. S. Cheng. A Revisit of the Phase-resolved X-Ray and Gamma-Ray Spectra of the Crab Pulsar. *Astrophys. J.*, 676:562–572, March 2008. doi: 10.1086/527029.

- Rita Tojeiro. Understanding the cosmic microwave background temperature power spectrum. http://www.roe.ac.uk/ifa/postgrad/pedagogy/2006_tojeiro.pdf, March 2006.
- P. A. Čerenkov. Visible Radiation Produced by Electrons Moving in a Medium with Velocities Exceeding that of Light. *Physical Review*, 52:378–379, August 1937. doi: 10.1103/PhysRev.52.378.
- P.V. Vavilov. Ionization losses of high energy heavy particles. *Soviet Physics JETP*, 5(749), 1957.
- P. Vincent, J.-P. Denanca, J.-F. Huppert, P. Manigot, de Naurois, and H.E.S.S. Collaboration. Performance of the H.E.S.S. Cameras. *International Cosmic Ray Conference*, 5:2887, July 2003.
- H. J. Völk and K. Bernlöhr. Imaging very high energy gamma-ray telescopes. *Experimental Astronomy*, 25:173–191, August 2009. doi: 10.1007/s10686-009-9151-z.
- Alfred Weigert, Heinrich J. Wendker, and Lutz Wisotzki. *Astronomie und Astrophysik: Ein Grundkurs*. Wiley-VCH Verlag GmbH Co. KGaA, 4th edition, 2005.
- P.-F. Yin, Q. Yuan, J. Liu, J. Zhang, X.-J. Bi, S.-H. Zhu, and X. Zhang. PAMELA data and leptonically decaying dark matter. *Phys. Rev. D*, 79(2):023512, January 2009. doi: 10.1103/PhysRevD.79.023512.
- K. Yoshida, S. Torii, T. Yamagami, T. Tamura, H. Kitamura, J. Chang, I. Iijima, A. Kadokura, K. Kasahara, Y. Katayose, T. Kobayashi, Y. Komori, Y. Matsuzaka, K. Mizutani, H. Murakami, M. Namiki, J. Nishimura, S. Ohta, Y. Saito, M. Shibata, N. Tateyama, H. Yamagishi, and T. Yuda. Cosmic-ray electron spectrum above 100 GeV from PPB-BETS experiment in Antarctica. *Advances in Space Research*, 42:1670–1675, November 2008. doi: 10.1016/j.asr.2007.04.043.
- J. Zavala, M. Vogelsberger, T. R. Slatyer, A. Loeb, and V. Springel. Cosmic X-ray and gamma-ray background from dark matter annihilation. *Phys. Rev. D*, 83(12):123513, June 2011. doi: 10.1103/PhysRevD.83.123513.
- V. Zirakashvili. Role of reverse shocks for the production of galactic cosmic rays in SNRs. *International Cosmic Ray Conference*, 6:167, 2011. doi: 10.7529/ICRC2011/V06/0837.
- V. N. Zirakashvili and F. A. Aharonian. Radioactivity and electron acceleration in supernova remnants. *Phys. Rev. D*, 84(8):083010, October 2011. doi: 10.1103/PhysRevD.84.083010.

Appendix A

Q -factor

$MSSG_{\text{max}}$	eff_{el}	$\text{eff}_{\text{had}} = \text{eff}_{\text{OFF}}$	$Q_{\text{NC-factor}}$
1.0	0.810	0.0114	7.7
0.6	0.760	0.0093	8.0
0.4	0.693	0.0075	8.0
0.0	0.592	0.0057	7.8
-0.6	0.267	0.0025	5.9
-1.0	0.155	0.0014	4.2

Table A.1: Table of electron and hadron efficiencies as well as the corresponding Q -factors without previously applying the core cut for different choices of gamma-hadron separation cuts on the $MSSG$. The shape cuts including a cut on the image amplitude and a cut on the energy of the particles (0.64 - 1.04 TeV) were applied before calculating the efficiencies.

$MSSG_{\max}$	eff_{el}	$\text{eff}_{\text{had}} = \text{eff}_{\text{OFF}}$	$Q_{\text{NCE-factor}}$
1.0	0.800	0.0152	6.5
0.6	0.745	0.0122	6.7
0.4	0.666	0.0094	6.8
0.0	0.560	0.0069	6.7
-0.6	0.289	0.0028	5.4
-1.0	0.160	0.0013	4.3

Table A.2: Table of electron and hadron efficiencies as well as the corresponding Q -factors for different choices of gamma-hadron separation cuts on the $MSSG$ without previously applying the core cut and the energy range constraint (0.64 -1.04 TeV). The shape cuts including a cut on the image amplitude were applied before the calculation of the efficiencies.

Appendix B

Electron Spectrum

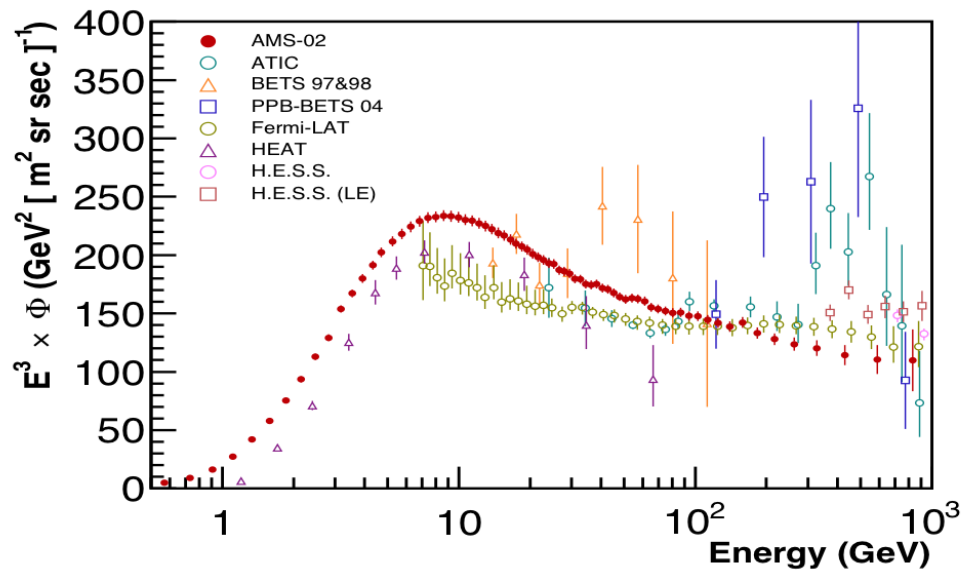


Figure B.1: Differential spectrum of cosmic-ray electrons plus positrons up to 1 TeV as observed by several experiments at Earth. The Figure was adapted from Aguilar et al. 2014a.

Appendix C

Systematic Error

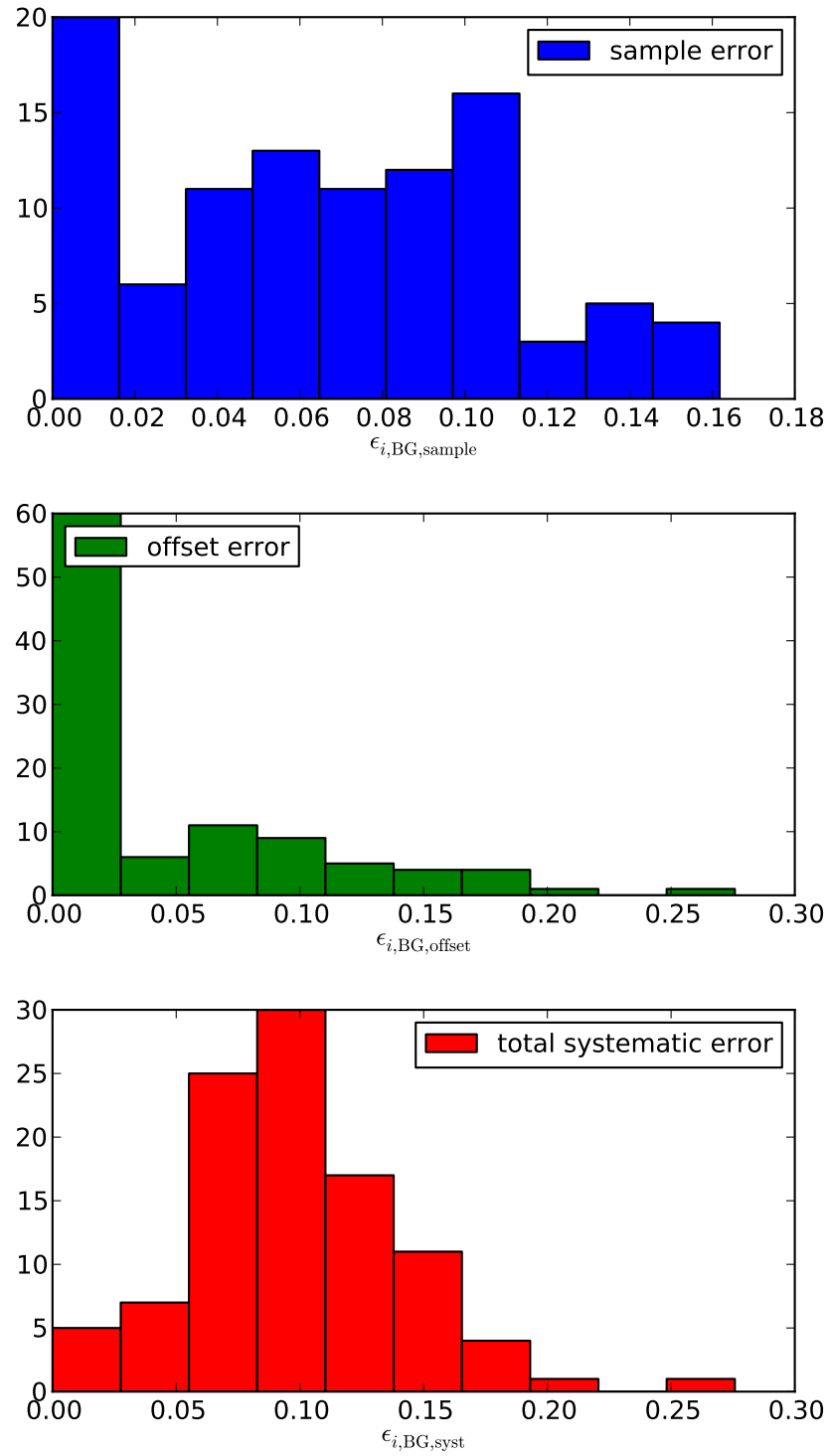


Figure C.1: Distributions of the sample error, the offset error and the total systematic error.

Appendix D

Split Analysis

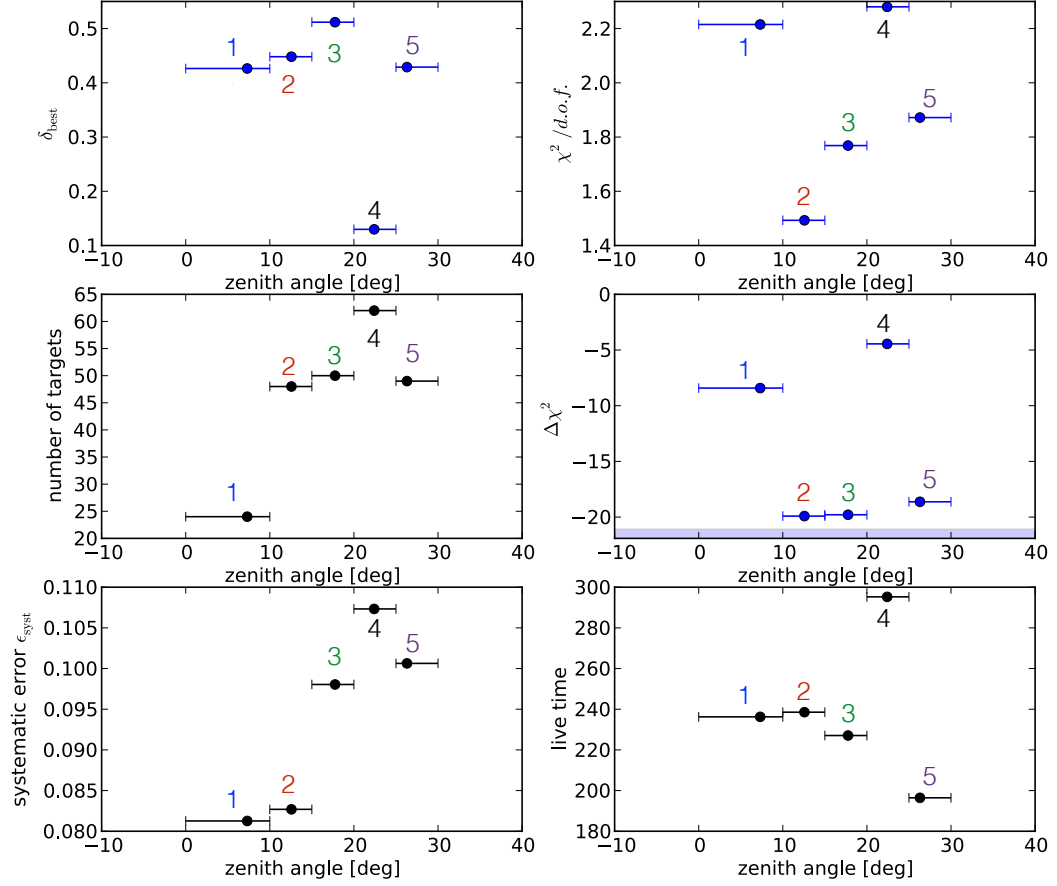


Figure D.1: Summary Figure for the zenith angle split scenario. The best-fit dipole amplitude (upper left-hand panel), the resulting global $\chi^2/d.o.f.$ (upper right-hand panel), the global $\Delta\chi_0^2$ (middle right-hand panel), the number of pointings (middle left-hand panel), the total live time in hours (lower right panel) and the median of the systematic errors (lower left-hand panel) are shown for every split data set. A bin number was assigned to every zenith angle bin. The bin number is shown above or below every data point and was assigned the same color in every panel. The number of *d.o.f.* for the global dipole fit is given by the number of pointings minus 4. The blue band in the middle right-hand panel depicts the improvements in the fit represented by $\Delta\chi_0^2$ that are more significant than 4σ .

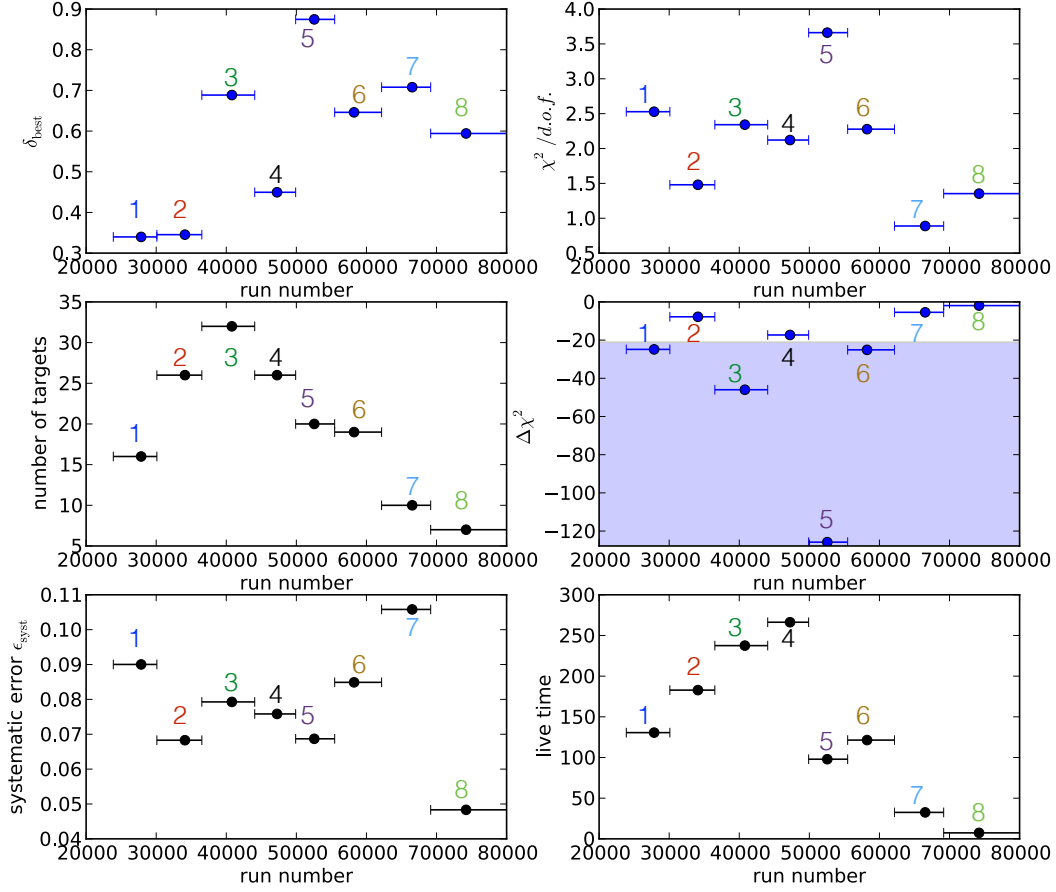


Figure D.2: Summary Figure for the yearly/run number split scenario. The best-fit dipole amplitude (upper left-hand panel), resulting global $\chi^2/d.o.f.$ (upper right-hand panel), global $\Delta\chi_0^2$ (middle right-hand panel), the number of pointings (middle left-hand panel), the total live time in hours (lower right-hand panel) and the median of the systematic errors (lower left-hand panel) are shown for every split data set. A bin number was assigned to every run number bin. The bin number is shown above or below every data point and was assigned the same color in every panel. The number of $d.o.f.$ for the global dipole fit is given by the number of pointings minus 4. The blue band in the middle right-hand panel depicts the improvements in the fit represented by $\Delta\chi_0^2$ that are more significant than 4σ .

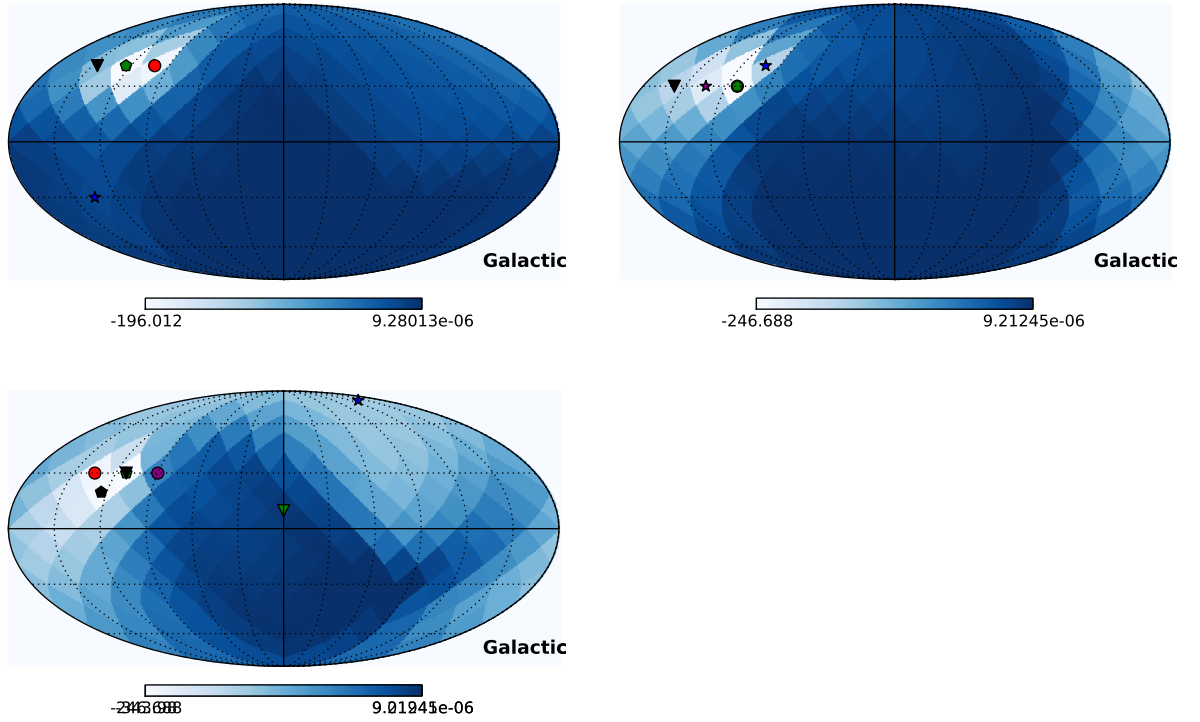


Figure D.3: Sky maps in galactic coordinates showing the stacked $\Delta\chi_0^2$ for all three split scenarios in optical efficiency (upper left-hand panel), zenith angle (upper right-hand panel) and observation year (lower left-hand panel) for the dipole analysis with adjusted gamma-like event rates. The colored markers represent the best-fit directions of the different split analysis. In all analysis $\text{NSIDE} = 4$ and $MSSG < 0.6$.

Appendix E

Multipole Fits

Spherical harmonics are given in terms of cartesian coordinates below. The cartesian coordinates x, y, z are related to the spherical coordinates r, θ, ϕ through the following transformation:

$$x = r \sin \theta \cos \phi \quad (\text{E.1})$$

$$y = r \sin \theta \sin \phi \quad (\text{E.2})$$

$$z = r \cos \theta \quad (\text{E.3})$$

The real spherical harmonics are given from the monopole $l = 0$ up to the hexadecapole $l = 4$.

l = 0 :

$$Y_{00} = s = Y_0^0 = \frac{1}{2} \sqrt{\frac{1}{\pi}} \quad (\text{E.4})$$

l = 1 :

$$Y_{1,-1} = p_y = i \sqrt{\frac{1}{2}} (Y_1^{-1} + Y_1^1) = \sqrt{\frac{3}{4\pi}} \cdot \frac{y}{r} \quad (\text{E.5})$$

$$Y_{10} = p_z = Y_1^0 = \sqrt{\frac{3}{4\pi}} \cdot \frac{z}{r} \quad (\text{E.6})$$

$$Y_{11} = p_x = \sqrt{\frac{1}{2}} (Y_1^{-1} - Y_1^1) = \sqrt{\frac{3}{4\pi}} \cdot \frac{x}{r} \quad (\text{E.7})$$

l = 2 :

$$Y_{2,-2} = d_{xy} = i\sqrt{\frac{1}{2}} (Y_2^{-2} - Y_2^2) = \frac{1}{2}\sqrt{\frac{15}{\pi}} \cdot \frac{xy}{r^2} \quad (\text{E.8})$$

$$Y_{2,-1} = d_{yz} = i\sqrt{\frac{1}{2}} (Y_2^{-1} + Y_2^1) = \frac{1}{2}\sqrt{\frac{15}{\pi}} \cdot \frac{yz}{r^2} \quad (\text{E.9})$$

$$Y_{20} = d_{z^2} = Y_2^0 = \frac{1}{4}\sqrt{\frac{5}{\pi}} \cdot \frac{-x^2 - y^2 + 2z^2}{r^2} \quad (\text{E.10})$$

$$Y_{21} = d_{xz} = \sqrt{\frac{1}{2}} (Y_2^{-1} - Y_2^1) = \frac{1}{2}\sqrt{\frac{15}{\pi}} \cdot \frac{zx}{r^2} \quad (\text{E.11})$$

$$Y_{22} = d_{x^2-y^2} = \sqrt{\frac{1}{2}} (Y_2^{-2} + Y_2^2) = \frac{1}{4}\sqrt{\frac{15}{\pi}} \cdot \frac{x^2 - y^2}{r^2} \quad (\text{E.12})$$

l = 3 :

$$Y_{3,-3} = f_{y(3x^2-y^2)} = i\sqrt{\frac{1}{2}} (Y_3^{-3} + Y_3^3) = \frac{1}{4}\sqrt{\frac{35}{2\pi}} \cdot \frac{(3x^2 - y^2)y}{r^3} \quad (\text{E.13})$$

$$Y_{3,-2} = f_{xyz} = i\sqrt{\frac{1}{2}} (Y_3^{-2} - Y_3^2) = \frac{1}{2}\sqrt{\frac{105}{\pi}} \cdot \frac{xyz}{r^3} \quad (\text{E.14})$$

$$Y_{3,-1} = f_{yz^2} = i\sqrt{\frac{1}{2}} (Y_3^{-1} + Y_3^1) = \frac{1}{4}\sqrt{\frac{21}{2\pi}} \cdot \frac{y(4z^2 - x^2 - y^2)}{r^3} \quad (\text{E.15})$$

$$Y_{30} = f_{z^3} = Y_3^0 = \frac{1}{4}\sqrt{\frac{7}{\pi}} \cdot \frac{z(2z^2 - 3x^2 - 3y^2)}{r^3} \quad (\text{E.16})$$

$$Y_{31} = f_{xz^2} = \sqrt{\frac{1}{2}} (Y_3^{-1} - Y_3^1) = \frac{1}{4}\sqrt{\frac{21}{2\pi}} \cdot \frac{x(4z^2 - x^2 - y^2)}{r^3} \quad (\text{E.17})$$

$$Y_{32} = f_{z(x^2-y^2)} = \sqrt{\frac{1}{2}} (Y_3^{-2} + Y_3^2) = \frac{1}{4}\sqrt{\frac{105}{\pi}} \cdot \frac{(x^2 - y^2)z}{r^3} \quad (\text{E.18})$$

$$Y_{33} = f_{x(x^2-3y^2)} = \sqrt{\frac{1}{2}} (Y_3^{-3} - Y_3^3) = \frac{1}{4}\sqrt{\frac{35}{2\pi}} \cdot \frac{(x^2 - 3y^2)x}{r^3} \quad (\text{E.19})$$

$l = 4 :$

$$Y_{4,-4} = g_{xy(x^2-y^2)} = i\sqrt{\frac{1}{2}} (Y_4^{-4} - Y_4^4) = \frac{3}{4}\sqrt{\frac{35}{\pi}} \cdot \frac{xy(x^2-y^2)}{r^4} \quad (\text{E.20})$$

$$Y_{4,-3} = g_{zy^3} = i\sqrt{\frac{1}{2}} (Y_4^{-3} + Y_4^3) = \frac{3}{4}\sqrt{\frac{35}{2\pi}} \cdot \frac{(3x^2-y^2)yz}{r^4} \quad (\text{E.21})$$

$$Y_{4,-2} = g_{z^2xy} = i\sqrt{\frac{1}{2}} (Y_4^{-2} - Y_4^2) = \frac{3}{4}\sqrt{\frac{5}{\pi}} \cdot \frac{xy \cdot (7z^2 - r^2)}{r^4} \quad (\text{E.22})$$

$$Y_{4,-1} = g_{z^3y} = i\sqrt{\frac{1}{2}} (Y_4^{-1} + Y_4^1) = \frac{3}{4}\sqrt{\frac{5}{2\pi}} \cdot \frac{yz \cdot (7z^2 - 3r^2)}{r^4} \quad (\text{E.23})$$

$$Y_{40} = g_{z^4} = Y_4^0 = \frac{3}{16}\sqrt{\frac{1}{\pi}} \cdot \frac{(35z^4 - 30z^2r^2 + 3r^4)}{r^4} \quad (\text{E.24})$$

$$Y_{41} = g_{z^3x} = \sqrt{\frac{1}{2}} (Y_4^{-1} - Y_4^1) = \frac{3}{4}\sqrt{\frac{5}{2\pi}} \cdot \frac{xz \cdot (7z^2 - 3r^2)}{r^4} \quad (\text{E.25})$$

$$Y_{42} = g_{z^2xy} = \sqrt{\frac{1}{2}} (Y_4^{-2} + Y_4^2) = \frac{3}{8}\sqrt{\frac{5}{\pi}} \cdot \frac{(x^2 - y^2) \cdot (7z^2 - r^2)}{r^4} \quad (\text{E.26})$$

$$Y_{43} = g_{zx^3} = \sqrt{\frac{1}{2}} (Y_4^{-3} - Y_4^3) = \frac{3}{4}\sqrt{\frac{35}{2\pi}} \cdot \frac{(x^2 - 3y^2)xz}{r^4} \quad (\text{E.27})$$

$$Y_{44} = g_{x^4+y^4} = \sqrt{\frac{1}{2}} (Y_4^{-4} + Y_4^4) = \frac{3}{16}\sqrt{\frac{35}{\pi}} \cdot \frac{x^2(x^2 - 3y^2) - y^2(3x^2 - y^2)}{r^4} \quad (\text{E.28})$$

Appendix F

Run Selection

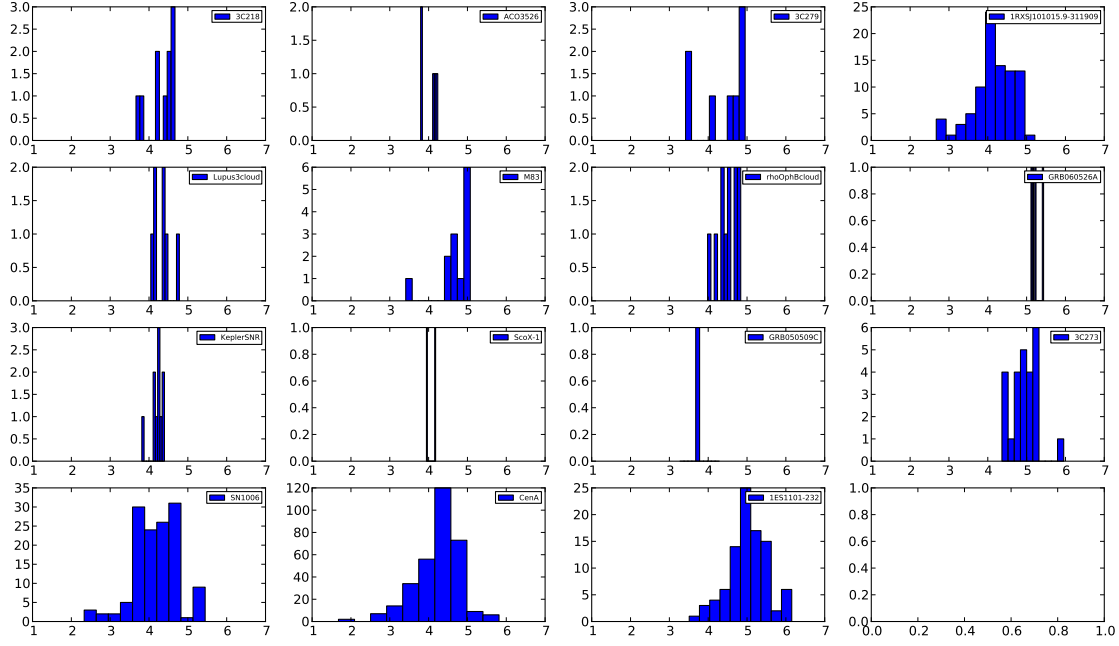


Figure F.1: Distributions of run-wise measured background (hadron-like) event rates for a selection of pointings. On the x-axis the run-wise measured background rates are given in Hz. On the y-axis the number of runs is given.

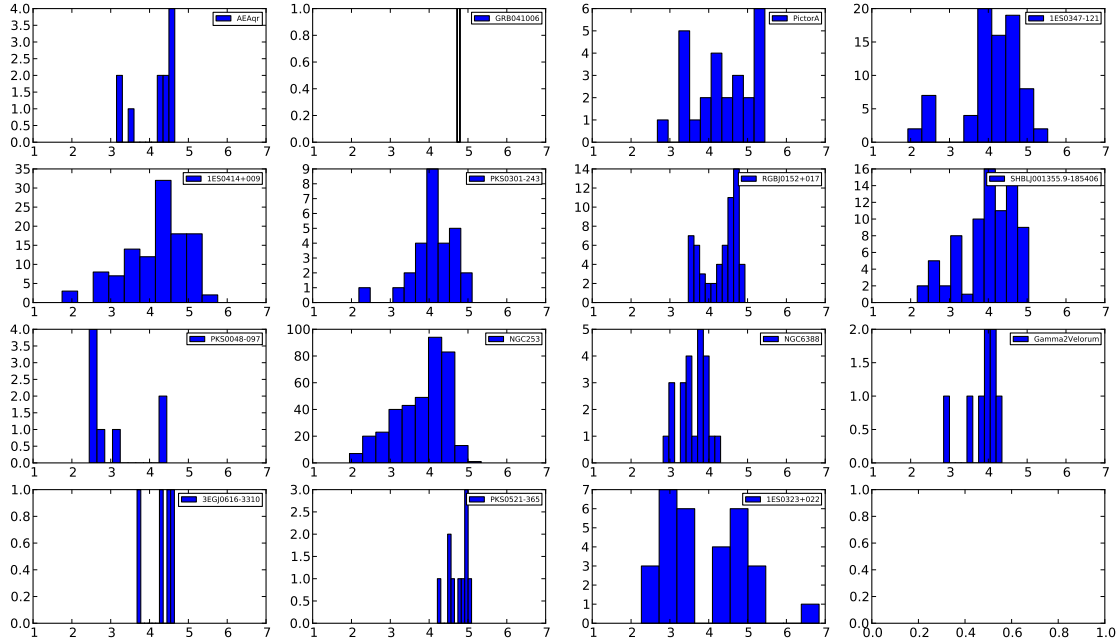


Figure F.2: Distributions of run-wise measured background (hadron-like) event rates for a selection of pointings. On the x-axis the run-wise measured background rates are given in Hz. On the y-axis the number of runs is given.

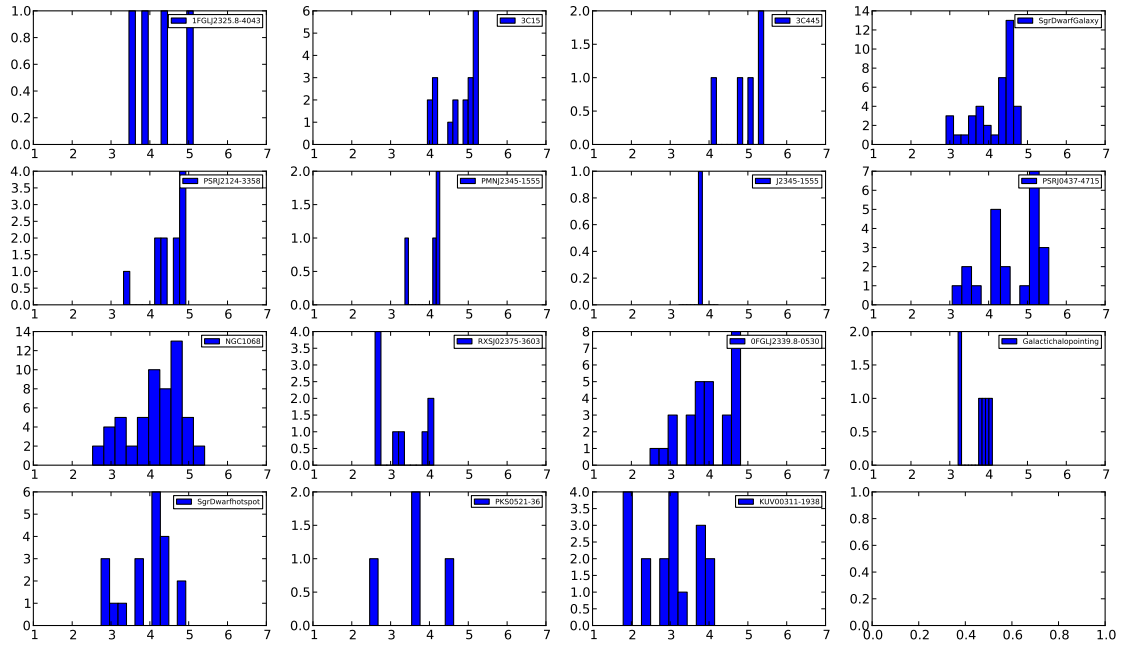


Figure F.3: Distributions of run-wise measured background (hadron-like) event rates for a selection of pointings. On the x-axis the run-wise measured background rates are given in Hz. On the y-axis the number of runs is given.

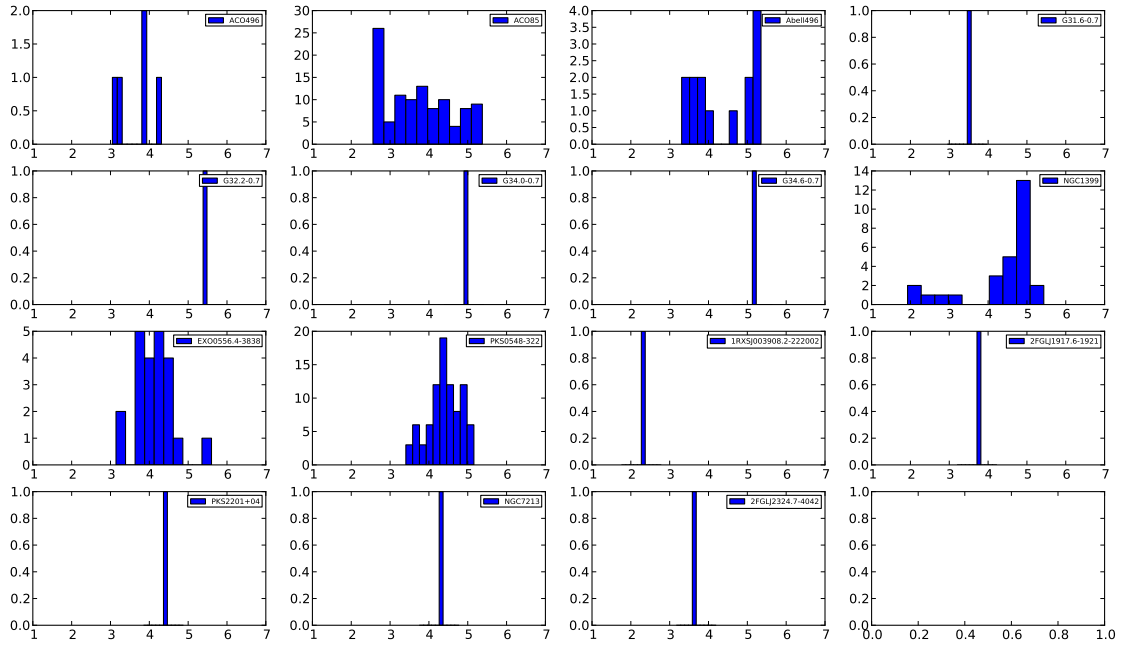


Figure F.4: Distributions of run-wise measured background (hadron-like) event rates for a selection of pointings. On the x-axis the run-wise measured background rates are given in Hz. On the y-axis the number of runs is given.

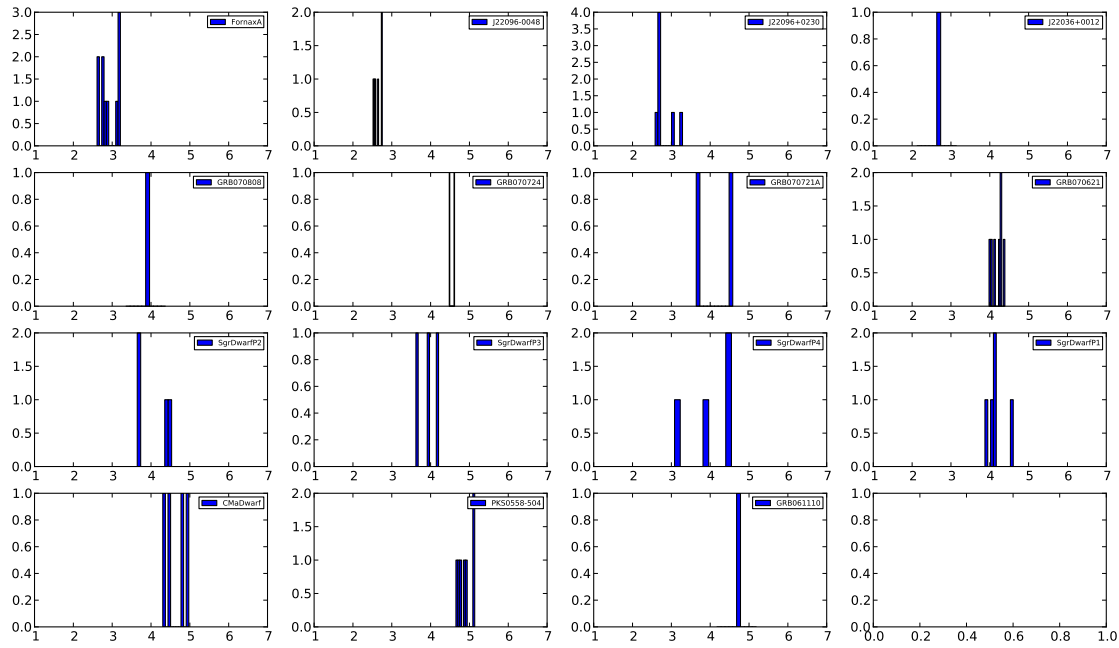


Figure F.5: Distributions of run-wise measured background (hadron-like) event rates for a selection of pointings. On the x-axis the run-wise measured background rates are given in Hz. On the y-axis the number of runs is given.

Comment to the List of my Publications

During my PhD I was a member of the H.E.S.S. collaboration. During this time about 28 collaboration papers were published where I contributed in form of discussions at several collaboration and working-group meetings. Further, I gave comments at different stages of the manuscript. All the papers presented below are H.E.S.S. collaboration paper.

List of my Publications

- ABRAMOWSKI, A., ACERO, F., AHARONIAN, F., AIT BENKHALI, F., AKHPERJANIAN, A. G., ANGÜNER, E., ANTON, G., BALENDERAN, S., BALZER, A., BARNACKA, A., & ET AL. 2013. Constraints on axionlike particles with H.E.S.S. from the irregularity of the PKS 2155-304 energy spectrum. *Physical Review D*, **88**(10), 102003.
- ABRAMOWSKI, A., AHARONIAN, F., AIT BENKHALI, F., AKHPERJANIAN, A. G., ANGÜNER, E. O., BACKES, M., BALENDERAN, S., BALZER, A., BARNACKA, A., BECHERINI, Y., & ET AL. 2014a. Diffuse Galactic gamma-ray emission with H.E.S.S. *Physical Review D*, **90**(12), 122007.
- ABRAMOWSKI, A., AHARONIAN, F., AIT BENKHALI, F., AKHPERJANIAN, A. G., ANGÜNER, E. O., BACKES, M., BALENDERAN, S., BALZER, A., BARNACKA, A., BECHERINI, Y., & ET AL. 2014b. Discovery of the Hard Spectrum VHE γ -Ray Source HESS J1641-463. *Astrophys. J., Letters*, **794**(Oct.), L1.
- ABRAMOWSKI, A., AHARONIAN, F., BENKHALI, F. A., AKHPERJANIAN, A. G., ANGÜNER, E., ANTON, G., BALENDERAN, S., BALZER, A., BARNACKA, A., BECHERINI, Y., & ET AL. 2014c. HESS J1640-465 - an exceptionally luminous TeV γ -ray supernova remnant. *Monthly Notices of the Royal Astronomical Society*, **439**(Apr.), 2828–2836.
- ABRAMOWSKI, A., AHARONIAN, F., AIT BENKHALI, F., AKHPERJANIAN, A. G., ANGÜNER, E. O., BACKES, M., BALENDERAN, S., BALZER, A., BARNACKA, A., BECHERINI, Y., & ET AL. 2015a. Constraints on an Annihilation Signal from a Core of Constant Dark Matter Density around the Milky Way Center with H.E.S.S. *Physical Review Letters*, **114**(8), 081301.
- ABRAMOWSKI, A., AHARONIAN, F., AIT BENKHALI, F., AKHPERJANIAN, A. G., ANGÜNER, E. O., BACKES, M., BALENDERAN, S., BALZER, A., BARNACKA, A., BECHERINI, Y., & ET AL. 2015b. The 2012 Flare of PG 1553+113 Seen with H.E.S.S. and Fermi-LAT. *Astrophys. J.*, **802**(Mar.), 65.
- ALIU, E., ARCHAMBAULT, S., AUNE, T., BEHERA, B., BEILICKE, M., BENBOW, W., BERGER, K., BIRD, R., BOUVIER, A., BUCKLEY, J. H., & ET AL. 2014. Long-term TeV and X-Ray Observations of the Gamma-Ray Binary HESS J0632+057. *Astrophys. J.*, **780**(Jan.), 168.
- H. E. S. S. COLLABORATION, ABRAMOWSKI, A., AHARONIAN, F., AIT BENKHALI, F., AKHPERJANIAN, A. G., ANGÜNER, E., ANTON, G., BALENDERAN, S., BALZER, A.,

- BARNACKA, A., & ET AL. 2014a. HESS J1818-154, a new composite supernova remnant discovered in TeV gamma rays and X-rays. *Astronomy and Astrophysics*, **562**(Feb.), A40.
- H. E. S. S. COLLABORATION, ABRAMOWSKI, A., AHARONIAN, F., AIT BENKHALI, F., AKHPERJANIAN, A. G., ANGÜNER, E., ANTON, G., BALENDERAN, S., BALZER, A., BARNACKA, A., & ET AL. 2014b. H.E.S.S. observations of the Crab during its March 2013 GeV gamma-ray flare. *Astronomy and Astrophysics*, **562**(Feb.), L4.
- H. E. S. S. COLLABORATION, ABRAMOWSKI, A., AHARONIAN, F., AIT BENKHALI, F., AKHPERJANIAN, A. G., ANGÜNER, E., ANTON, G., BACKES, M., BALENDERAN, S., BALZER, A., & ET AL. 2014c. Search for extended γ -ray emission around AGN with H.E.S.S. and Fermi-LAT. *Astronomy and Astrophysics*, **562**(Feb.), A145.
- H. E. S. S. COLLABORATION, ABRAMOWSKI, A., AHARONIAN, F., AIT BENKHALI, F., AKHPERJANIAN, A. G., ANGÜNER, E. O., BACKES, M., BALZER, A., BECHERINI, Y., BECKER TJUS, J., & ET AL. 2015a. Discovery of variable VHE γ -ray emission from the binary system 1FGL J1018.6-5856. *Astronomy and Astrophysics*, **577**(May), A131.
- H. E. S. S. COLLABORATION, ABRAMOWSKI, A., AHARONIAN, F., AIT BENKHALI, F., AKHPERJANIAN, A. G., ANGÜNER, E. O., BACKES, M., BALENDERAN, S., BALZER, A., BARNACKA, A., & ET AL. 2015b. H.E.S.S. detection of TeV emission from the interaction region between the supernova remnant G349.7+0.2 and a molecular cloud. *Astronomy and Astrophysics*, **574**(Feb.), A100.
- H. E. S. S. COLLABORATION, ABRAMOWSKI, A., AHARONIAN, F., AIT BENKHALI, F., AKHPERJANIAN, A. G., ANGÜNER, E. O., BACKES, M., BALENDERAN, S., BALZER, A., BARNACKA, A., & ET AL. 2015c. H.E.S.S. detection of TeV emission from the interaction region between the supernova remnant G349.7+0.2 and a molecular cloud (Corrigendum). *Astronomy and Astrophysics*, **580**(Aug.), C1.
- H. E. S. S. COLLABORATION, ABRAMOWSKI, A., AHARONIAN, F., AIT BENKHALI, F., AKHPERJANIAN, A. G., ANGÜNER, E. O., BACKES, M., BALENDERAN, S., BALZER, A., BARNACKA, A., & ET AL. 2015d. H.E.S.S. reveals a lack of TeV emission from the supernova remnant Puppis A. *Astronomy and Astrophysics*, **575**(Mar.), A81.
- H. E. S. S. COLLABORATION, ABRAMOWSKI, A., AHARONIAN, F., AIT BENKHALI, F., AKHPERJANIAN, A. G., ANGÜNER, E., ANTON, G., BACKES, M., BALENDERAN, S., BALZER, A., & ET AL. 2015e. Probing the gamma-ray emission from HESS J1834-087 using H.E.S.S. and Fermi LAT observations. *Astronomy and Astrophysics*, **574**(Feb.), A27.
- H.E.S.S. COLLABORATION, ABRAMOWSKI, A., ACERO, F., AHARONIAN, F., AIT BENKHALI, F., AKHPERJANIAN, A. G., ANGÜNER, E., ANTON, G., BALENDERAN, S., BALZER, A., & ET AL. 2013. Discovery of very high energy γ -ray emission from the BL Lacertae object PKS 0301-243 with H.E.S.S. *Astronomy and Astrophysics*, **559**(Nov.), A136.

- H.E.S.S. COLLABORATION, ABRAMOWSKI, A., AHARONIAN, F., AIT BENKHALI, F., AKHPERJANIAN, A. G., ANGÜNER, E., ANTON, G., BALENDERAN, S., BALZER, A., BARNACKA, A., & ET AL. 2014a. Erratum: HESS J1640-465 - an exceptionally luminous TeV γ -ray supernova remnant. *Monthly Notices of the Royal Astronomical Society*, **441**(July), 3640–3642.
- H.E.S.S. COLLABORATION, ABRAMOWSKI, A., AHARONIAN, F., AIT BENKHALI, F., AKHPERJANIAN, A. G., ANGÜNER, E., ANTON, G., BALENDERAN, S., BALZER, A., BARNACKA, A., & ET AL. 2014b. Flux upper limits for 47 AGN observed with H.E.S.S. in 2004-2011. *Astronomy and Astrophysics*, **564**(Apr.), A9.
- H.E.S.S. COLLABORATION, ABRAMOWSKI, A., AHARONIAN, F., AIT BENKHALI, F., AKHPERJANIAN, A. G., ANGÜNER, E. O., BACKES, M., BALENDERAN, S., BALZER, A., BARNACKA, A., & ET AL. 2014c. Long-term monitoring of PKS 2155-304 with ATOM and H.E.S.S.: investigation of optical/ γ -ray correlations in different spectral states. *Astronomy and Astrophysics*, **571**(Nov.), A39.
- H.E.S.S. COLLABORATION, ABRAMOWSKI, A., AHARONIAN, F., AIT BENKHALI, F., AKHPERJANIAN, A. G., ANGÜNER, E., ANTON, G., BALENDERAN, S., BALZER, A., BARNACKA, A., & ET AL. 2014d. Search for TeV Gamma-ray Emission from GRB 100621A, an extremely bright GRB in X-rays, with H.E.S.S. *Astronomy and Astrophysics*, **565**(May), A16.
- H.E.S.S. COLLABORATION, ABRAMOWSKI, A., AHARONIAN, F., BENKHALI, F. A., AKHPERJANIAN, A. G., ANGÜNER, E., ANTON, G., BALENDERAN, S., BALZER, A., BARNACKA, A., & ET AL. 2014e. TeV γ -ray observations of the young synchrotron-dominated SNRs G1.9+0.3 and G330.2+1.0 with H.E.S.S. *Monthly Notices of the Royal Astronomical Society*, **441**(June), 790–799.
- HESS COLLABORATION, ABRAMOWSKI, A., ACERO, F., AHARONIAN, F., AIT BENKHALI, F., AKHPERJANIAN, A. G., ANGÜNER, E., ANTON, G., BALENDERAN, S., BALZER, A., & ET AL. 2015. Discovery of the VHE gamma-ray source HESS J1832-093 in the vicinity of SNR G22.7-0.2. *Monthly Notices of the Royal Astronomical Society*, **446**(Jan.), 1163–1169.
- H.E.S.S. COLLABORATION, ABRAMOWSKI, A., AHARONIAN, F., AIT BENKHALI, F., AKHPERJANIAN, A. G., ANGÜNER, E. O., BACKES, M., BALENDERAN, S., BALZER, A., BARNACKA, A., & ET AL. 2015a. The exceptionally powerful TeV γ -ray emitters in the Large Magellanic Cloud. *Science*, **347**(Jan.), 406–412.
- H.E.S.S. COLLABORATION, ABRAMOWSKI, A., AHARONIAN, F., AIT BENKHALI, F., AKHPERJANIAN, A. G., ANGÜNER, E., ANTON, G., BACKES, M., BALENDERAN, S., BALZER, A., & ET AL. 2015b. The high-energy γ -ray emission of AP Librae. *Astronomy and Astrophysics*, **573**(Jan.), A31.

Danksagung

An dieser Stelle möchte ich mich herzlich bei allen bedanken, die zum Gelingen dieser Arbeit beigetragen haben. Zu allererst möchte ich mich bei Prof. Dr. Horns für die interessante Aufgabenstellung und die sorgfältige Betreuung der vorliegenden Arbeit bedanken. Insbesondere für seine Bereitschaft diese Doktorarbeit auch aus der Ferne zu Ende zu betreuen.

Ebenfalls gilt mein besonderer Dank Prof. Dr. Günter Sigl für die Aufnahme und Betreuung dieser Arbeit im Rahmen der Forschungsprojekts "Astroparticle Physics with Multiple Messengers". Ich möchte mich bei beiden oben genannten Personen für die Möglichkeit zur Teilnahme an der Sommerschule in Heidelberg und viele weitere Reisen bedanken.

Des Weiteren möchte ich mich bei Prof Dr. Ullrich Katz dafür bedanken, dass dieser mich als Gastwissenschaftlerin am ECAP in Erlangen aufgenommen hat und mir zudem die dortigen Rechnerkapazitäten zur Verfügung stellte.

Bei der gesamten H.E.S.S. Kollaboration bedanke ich mich für 4 Jahre der kollegialen Zusammenarbeit mit vielen fruchtbaren Diskussionen.

Ich bedanke mich bei Roberto Iuppa und der gesamten ARGO-YBJ Kollaboration für die freundliche Aufnahme bei meinem Gastvortrag und für das zur Verfügung stellen der ARGO-YBJ Himmelskarten.

Natürlich bedanke ich mich auch bei meiner Arbeitsgruppe in Hamburg, die mir stets mit Rat und Tat zur Seite stand. Ich habe die gemeinsamen wissenschaftlichen und nichtwissenschaftlichen Diskussionen immer sehr genossen. Namentlich möchte ich hier insbesondere Alexander Gewering-Peine, Dr. Milton Fernandes, Dr. Hannes Zechlin, Dr. Björn Opitz, Max Kastendieck, Attila Abramowski, Dr. Manuel Meyer, Dr. Martin Tluczykont, Andrei Lobanov, Rayk Nachtigall und Maike Kunas erwähnen.

Ein weiterer besonderer Dank geht an meine Kollegen und Kolleginnen in Erlangen, insbesondere an Susanne Raab und Dr. Anton Jahn für eine wirklich tolle Unterstützung bei der Nutzung der Parisanalyse. Ich hatte zudem in Erlangen die Ehre mit dem kürzlich verstorbenen Dr. Friedrich Stinzing zusammen zu Arbeiten. Unsere lebhaften Diskussionen haben mir sehr viel Freude bereitet.

Ein ungewöhnlicher Dank geht zudem an meinen Abteilungsleiter Dr. Daniel John und meine Arbeitskollegen bei der HUK Coburg, die es mir in den letzten eineinhalb Jahren ermöglicht haben Privatleben, Doktorarbeit und den Beruf unter einen Hut zu bekommen.

Nicht zuletzt möchte ich mich bei meinem Ehemann Andreas Spies, meinen Freunden und

meiner Familie für die Unterstützung während meiner Doktorarbeit bedanken.

Erklärung

Hiermit erkläre ich, Franziska Spies, an Eides statt, dass ich die vorliegende Dissertationsschrift selbst verfasst und keine anderen als die angegebenen Quellen und Hilfsmittel benutzt habe.

Coburg, den 30.09.2015
Franziska Spies